Tectonic Investigation of The Northern San Gregorio Fault, San Mateo County, California.

Project Report of Dec 2021 by Hudson Washburn,

Volunteer Researcher in Kimberly Blisniuk's Group, San Jose State University Geology Dept:

Table of Contents:

Abstract 2
Introduction, Tectonic Setting 3
Methods 11
Results: Mapping 13
Stratigraphy 19
Dating Sediments 25
Middle Strand Exposures 29
Fault Behavior in Qmt 38
Middle Strand Fault Sequence 48
Offset and Slip Rate Estimate 53
Conclusions and Discussion 63
Acknowledgements 67
Appendix A 69
    Geotechnical Mapping Compilation
Appendix B 74
    Simple Demonstration of Folding at a Restraining Bend
Appendix C 76
    Aseismic Creep Evidence
Appendix D 82
    Folding Model
Appendix E 100
    Half Moon Bay
Appendix F 110
    Magnetic Anomalies
References 125
List of Figures 131
End 142

Abstract:

The San Gregorio Fault is the western-most component of the right-lateral strike-slip San Andreas Fault System. It lies predominantly offshore and comes ashore in only two locations, the one analyzed here is along a restraining double bend at Pillar Point Bluff and the Seal Cove area of Moss Beach in San Mateo County, California. A component of its eastern strand, referred to here as the Middle Strand, mapped tentatively by Pampeyan, 1994, is confirmed to trend down the middle of Pillar Point Bluff, exhibit significant oblique slip, and play a more prominent active tectonic role, including in local mass wasting, than previously understood.

Several components of the Middle Strand are traced from the Pliocene Purisima fm bedrock into the unconformably overlying late Pleistocene marine sedimentary layers by excavating new fault exposures along a landslide headscarp more than 100 m in length and up to 10 m in height. Findings include fault gouge zones up to 1.7 m wide in Purisima with numerous faults propagating into the marine terrace sediments, a few traced to the surface. These faults are combined with extensive mapping of surface shears, fault bounded ridges, consultant's trench-identified faults and magnetic anomaly mapping throughout the Pillar Point Bluff and Seal Cove areas, to map out a positive flower structure along a restraining bend along the southern part of Pillar Point Bluff which transitions to a negative flower structure along a releasing duplex in the northern part. Together these comprise the main strike-slip components of the eastern strand of the San Gregorio Fault. One strand proceeds northwest from Seal Cove and a second path progresses through a series of releasing faults and connects to an eastern strand. The currently most active releasing bend fault aligns with a strike-slip fault previously reported by Simpson et al, 1997, and continues to a well-exposed shoreline fault gouge and breccia zone in the Fitzgerald Marine Reserve in the process producing a pull-apart graben. With the current mapping right-lateral strike-slip faulting is traced the length of Pillar Point Bluff and matched to previously identified faults without recourse to the prominent eastern scarp, called the Seal Cove Fault, SCF, which was long considered the main eastern component of the strike-slip San Gregorio Fault in this area, but for which only east-vergent thrust faulting has been confirmed by Koehler et al, 2005 and here mapping, slickensides, and magnetic anomaly data suggests the SCF is predominantly dip-slip. Montara Granodiorite bedrock appears to have translated into the SGF-E path deflecting the SGF-E into the current restraining bend which caused a compressive force producing the prominent folding visible offshore west of the fault and the uplift of Pillar Point Bluff while at the same time forming an extensive force on the eastern side south of the granitic contact that produced the Half Moon Bay syncline. North of the granitic contact the Moss Beach Syncline, a frequently studied plunging syncline in the surf zone northeast of the Fitzgerald fault exposure, was formed by compression of Purisima against the granite obstruction.

Pillar Point Bluff consists of an uplifted marine terrace deposited unconformably on a wave-cut platform cut into Purisima fm bedrock. The marine terrace deposits are here dated to 49.7 ka (41.8 – 57.9, 95% probability limits) by combining CRN and IRSL dating results. A change in bedrock dip occurs along this section of Pillar Point Bluff due to the offshore folding and records a landward rotation of bedrock slope with distance into the restraining bend of about 23 degree per km of translation. This slope dependence along with a measured change in the bedrock angle of 7.6 ± 1.2° implies an offset of 326 m (205 – 466 m) since the wavecut platform was abandoned. Combined with the sediment dating this implies a late Quaternary horizontal slip rate of 6.5 mm/yr (4.0 – 9.7) along with a maximum vertical uplift rate of 2 ± 0.5 mm/yr. The latter is higher than typical for marine terraces along the central California coast, but consistent with this restraining bend's compression. The event recurrence interval since abandonment of the marine terrace, estimated by counting faults in the marine terrace sediment, is estimated to be in the range of 200 to 700 years.

Introduction, Tectonic Setting:

The San Gregorio Fault (SGF) system is the western-most component of the right-lateral strike-slip San Andreas Fault System in Northern California, Figure 1. The SGF is an active northwest trending right-lateral strike-slip fault that lies offshore over most of its length from south of Monterey Bay north to near Bodega Bay. It is generally considered to merge with the Hosgri Fault to the south (e.g. Dickinson et al, 2005, Johnson et al, 2018) to form a continuous, mostly offshore, western limit of the San Andreas Fault System, SAF, south to the Transverse Ranges. On the northern end near Bodega Bay it merges with the main San Andreas Fault (Brun et al, 2002). The SGF comes onshore in only two locations: from Ano Nuevo to San Gregorio and from Pillar Point to Moss Beach. At Ano Nuevo it consists of at least five sub-parallel faults over a width of about 3 km (Weber and Cotton, 1981). The Pillar Point section, Figure 2, the subject of this report, is where the SGF traverses Pillar Point Bluff and the Seal Cove area of Moss Beach. The western component of the SGF, the Frijoles Fault, that lies offshore at this latitude, is not studied here. Locally, and often in the literature, the northern on-land section of the SGF, generally assumed to be the trace that runs along the prominent eastern scarp of Pillar Point Bluff, is referred to as the Seal Cove Fault, SCF, (e.g. Pampeyan, 1994, Ryan et al, 2008). More faults are here mapped on this on-land section of the SGF, Figure 2, and it is proposed to maintain the Seal Cove Fault designation for only the prominent eastern scarp, the fault currently traced by the California Alquist-Priolo lines.

This eastern component of the SGF consists of an ~ 4 km long restraining double bend, the SGF-E, Figure 2; the southeastern bend being about 13^{o} and two (as will be developed below) northwestern bends 17 - 19^{o}. The on-land portion of the SGF-E traverses the length of the 3 km long Pillar Point Bluff and extends into the unincorporated Seal Cove area of Moss Beach on the northern end. The main bluff is here referred to as Pillar Point Bluff although it is sometimes referred to as Seal Cove Bluffs in the literature. The bluff reaches elevations up to 55 m and a width of 200 to 400 m. Seal Cove is cut into the northwest corner of this bluff and much of the bluff and fault path lie within the James E. Fitzgerald Marine Reserve. To aid identification, in Figure 2 “Seal Cove Lowlands” refers to the area that Simpson et al, 1997 call a wind gap, a lower lying area between Pillar Point Bluff and the elevated NW corner of Fitzgerald Marine Reserve that is here referred to as the “Fitzgerald Bluff”, and “Seal Cove Highlands” refers to the mostly developed section of Pillar Point Bluff that is adjacent and south of the Lowlands, with the two separated roughly along Los Banos Avenue.

The SGF is an active right-lateral strike-slip fault included in California's Alquist-Priolo Special Studies Zone (Bedrossian, 1979, and California Geological Survey, 2018) which requires geotechnical investigation for new construction within a certain proximity to the AP-designated faults. For that reason, and because the SGF is the western-most component of the San Andreas Fault System in the San Francisco Bay area, it is important to understand its contribution to seismic hazards and to accurately locate and characterize the active components of the SGF-E. An objective of this report is to map and characterize the faults along this onshore section of the SGF-E. Geotechnical trenching reports are abundant for properties along the AP-designated SCF and are used here to help constrain the location of faults in the area. A Middle Strand, mapped by Pampeyan, 1981, as a "photo-lineament most likely controlled by faults", Figure 3, extends from the southern end of Pillar Point Bluff to a large landslide area and follows a subtle scarp down the middle of the bluff and a more prominent ravine on the southern end. This fault is not currently part of the Alquist Priolo Zone and it is noteworthy that several properties which lie along the here-mapped extension of that Middle Strand were developed without geotechnical trenching studies. Leighton et al, 1971, mapped three faults from photo lineations on the northern end of Pillar Point Bluff that were also included by Pampeyan, 1981, 1994, Figure 3, two of which agree with mapping results presented here, Figures 2 and 4. The sea cliff recession has been documented to be on the order of 1 ft/yr in the Holocene and has generally been assigned to cliff-side landsliding without reference to a tectonic contribution, Leighton et al, 1971 and Cotton et al, 1980. In this report it is suggested there is a tectonic contribution.

A sea cliff fault exposure (now covered by riprap) in the Fitzgerald Marine Reserve, Figure 5, (Wylie, 1984), referred to as the Fitzgerald Fault in Figure 2, is an oft noted marker of the northern end of the on-land portion of the SGF. An about 10 m wide gouge zone expressed in the intertidal zone and a prominent syncline, known as the Moss Beach Syncline (Pampeyan, 1994), Figure 3, or informally as the Bathtub Syncline, adjacent the gouge zone and extending into the surf zone on the northeast side have been the subject of numerous field trips and reports (e.g. May et al, 1976, Lohr et al, 2009). The fault exposure was of marine terrace deposit on the northeast emplaced against Purisima fm sandstone on the southwest side with slickensides plunging 10° SE confirming predominantly strike-slip motion with west side up. This exposure is roughly in-line with an extrapolation of the prominent, up to about 30 m high, scarp along the northeastern side of Pillar Point Bluff, the SCF, which has long been assumed to represent the main right-lateral SGF-E on-shore strand which comes ashore on the southern end at Pillar Point Marsh (Pampeyan, 1994, Koehler et al, 2005). That assumption is here disputed. Lohr et al (2009) identified hydrocarbons in the fault gouge in the approximately 10 m wide Fitzgerald Fault zone which was suggested to follow the gouge up from a lower lying Monterey fm. They suggested hydrocarbons in such a wide fault gouge zone implies the fault may not sustain high stress.

Simpson et al, 1997, using a paleoseismic trench, found strike-slip fault evidence expressed in the marine terrace west of a straight-line extrapolation across the Seal Cove Lowlands between the prominent scarp and the sea-cliff exposure and proposed a small loop in the SCF path to accommodate their observation noting that the loop also followed a slight geomorphic curvature in the scarp. Their 37 m long and 3 to 4 m deep trench did not extend down to bedrock but did expose an erosional unconformity between lower marine terrace deposits and unconformably overlying Holocene pond deposits and soil developments plus Paleo-Indian midden deposits. They lithostratigraphically identified three marine terrace sections offset vertically as well as horizontally by two sets of faults about 20 m apart. The western set of faults, those around their 12 – 15 m location, contained a component extending into the soil A-horizon, but not into the root zone, which displayed crosscutting relationships that allowed them to identify it as the most recent earthquake, MRE, striking 341°. Using archaeological dating of offset midden deposits and historical records they constrained the MRE to after 1270 to 1400 CE and before 1775 CE. Based on midden distributions they estimated a lateral displacement of about 5 (-2, +6) m for the MRE resulting in an estimated magnitude greater than M7. The eastern set of faults, around their 34.5 m location, contained what they identified as the penultimate event (which extended up to but not into the surficial soil A-horizon) and had a strike of 326°. The penultimate event was radiocarbon dated to have probably occurred between 620 CE and 1400 CE. The penultimate event had a displaced wedge component across the trench which, based on certain assumed geometries, allowed them to calculate a 3 ± 0.2 m displacement and an estimated M7 for that event. They also found that the western terrace section tilted eastward indicating preunconformity deformation. Their drawings, without a defined precision, indicate a northeast-dipping tilt angle from about 8 to 13° in the marine terrace deposit layers compared to about 1° or less in the unconformably overlying soil layers. Noller et al, 1995, estimate a slip rate from this study of 4.5 to 11 mm/yr.

Table I: Summary of tectonic events from earlier reports.

Parameter	Simpson et al, 1997	Koehler et al, 2005
Fault Location	Seal Cove Lowlands, off the Seal Cove Fault. Proposed loop to include it.	Seal Cove Fault, Pillar Point Marsh.
Most Recent Event	After 1270 – 1400 CE Before 1725 CE	After 1515 CE
MRE displacement	5 m (-2, +6)	-
Strike-slip confirmed?	Yes	No
Penultimate Event	After 620 CE Before 1400 CE	After 1330 BCE inferred Before 1060 BCE
PE displacement	3 m (± 0.2)	-
Other Events	Likely multiple Holocene events	After 2080 BCE Before 1350 BCE
Recurrence Interval	~< 1100 years inferred	1037 – 2205 years
MRE Magnitude est	Order M7 or higher	-
Slip Rate	4.5 - 11 mm/yr	Not constrained

Koehler et al, 2005, studied sedimentary strata in Pillar Point marsh, adjacent the southern end of Pillar Point Bluff, under the assumption the Middle Strand and the fault forming the prominent eastern scarp, the Seal Cove Fault, formed a right-stepping pull-apart basin in which the marsh sits (although to point out the obvious; the southern side of this pull-apart basin is the ocean shore without a notable rise, making the basin not well defined). They found evidence of sudden subsidence resulting in several peaty soil layers about 20 cm or less thick in the marsh that they assigned to tectonic subsidence in the pull-apart basin. Using radiometrically dated layers and a criteria matrix following Nelson et al (1996) and Knudsen et al (2002), they identified two to four tectonic events the most recent of which was consistent with the MRE dated by Simpson et al, 1997. They also performed trenching along the base of the eastern scarp of Pillar Point Bluff where they identified east-vergent thrust faulting but were unable to confirm a strike-slip component. Table I lists some key findings of the Simpson et al, 1997, and the Koehler et al, 2005, reports.

No earthquakes had been reported during recorded history along this section of the SGF-E at the time of the above studies, which fact is the basis of the Simpson et al upper limit for their MRE. Ryan et al, 2008, did assign an M5 event from 1999 to this component of the SGF very near where it merges with the SAF in the northern San Francisco Bay, this is the star labeled 1999 in Figure 6, approximately 40 km north of the study area. If it was on the SGF it likely had little impact at this study location. Cotton et al, 1980, assign two earthquakes of Richter magnitude 6.1 from 1926 approximately 90 km south of the study area in Monterey Bay to the San Gregorio Fault.

Bryant and Cluett (1999) state the slip rate on this northern section of the SGF-E is unknown although they do list various estimates. There is very limited onshore exposure and no good piercing points had then been identified. Clark (1997) estimated overall SGF-E slip rates based on total displacement of various features along the full SGF over long time intervals and found a late Miocene slip rate of 25 to 30 mm/yr which decreased to 16 mm/yr in the late Pliocene and to 6 mm/yr by the Holocene. Bryant and Cluett (1999) summarize a range of reported estimates, from 1 to 11 mm/yr, for Pleistocene slip rates. Dickinson et al, 2005, in a review of available data, claim the most likely best Holocene estimate is around 8 mm/yr obtained from offset marine terraces (Weber, 1990).

Pillar Point Bluff is an uplifted marine terrace (Glenn, 1959 and Pampeyan, 1981). The terrace sediment, variously 0 to about 20 m or more thick, unconformably overlies Purisima formation sandstone/siltstone. The Purisima formation is an upper Miocene to upper Pliocene marine sedimentary rock layer that occurs from south of Santa Cruz to possibly as far north as

Point Reyes west of the San Andreas Fault and outcrops prominently along the coast (Glenn, 1959, Cummings et al, 1968, and Powell et al, 1998). In our study area the exposed Purisima northeast of the SGF-E was identified by Glenn (1959) to be from the upper Purisima formation and deposited at less than 50m ocean depth while two samples “southwest of the fault” (as then mapped) he found to be from lower in the Purisima and deposited at bathyal depths. In this study we propose a modification to the SGF-E fault path such that both bathyal depth samples collected by Glenn were between two paths of the proposed faults on the northern end of PPB and would have been west of one but not both of the here proposed fault paths. His B-4792 at 37^{o}, 31’, 15.5” N; 122^{o}, 30’, 56.5” W lies between the two northwestern going continuations of the SGF-E at this latitude. His other sample, B-4791, is between the main Middle Strand and the here mapped West Wall fault, it is at about 37^{o}, 29’, 59” N, 122^{o}, 29’, 45.6” W (which are not the coordinates listed by Glenn, which place it near the middle of the marsh east of the fault where there are no Purisima exposures, rather it matches his description of it being 1850’ along the beach from the southwestern-most pier in Princeton and is west of the Seal Cove fault as he states). Recently, Richard Stanley (2019, personal communication) identified a change in the Purisima lithology and paleontology from where Glenn chose his B-4792 sample and that west of the more westerly fault extension here identified, so we anticipate there will be more to learn from the paleontology of the Purisima along the coast and particularly from that west of all the eastern branches of the SGF.

In this area Montara Mountain Granodiorite, a Salinian remnant (e.g. Dickinson, 2005) abuts the Purisima to the northeast and possibly lies beneath the Purisima formation particularly along its eastern extent (Leighton et al 1971, Pampeyan 1994). Pampeyan (1994) shows the Montara Granodiorite underlying the Purisima beneath Pillar Point Bluff. Leighton et al, 1971, reported finding granite bedrock in drill cores west of the Seal Cove Fault but east of one of the crossing faults reported here with only sandstone bedrock in cores west of that fault, this is discussed below with reference to Figure 65 and in Appendix E. Whether Montara granite underlies Purisima sandstone anywhere in the bluff is here considered unknown.

Offshore from Pillar Point Bluff the Purisima formation is eroded and exposed on the sea floor where it displays a pronounced eroded fold pattern with its topology recorded by bathymetry data (Bretz et al, 2014), Figure 2. The offshore pattern indicates an eroded exposure of an anticline-syncline-anticline sequence with the furthest offshore anticline and the syncline plunging to the SE adjacent the southern end of Pillar Point Bluff, Figure 4, (Pampeyan, 1994 shows the near-shore anticline plunging to the NW), the folding transitions to a simple northeast-dipping section along the northern end. Most of the folded section near shore is not included in the bathymetry data because it is at depths too shallow to record, (10 meters sea depth was needed for the bathymetry measurement) but its prominent resistant layers are observable in Google Earth and other near-shore aerial photography and from shore at low tide and are added in Figures 2 and 4. This folding results in a systematic increase in dip as the plate moves into the restraining bend that is used below to estimate the lateral offset associated with a given dip angle change. The folding has been frequently commented on, and strike and dip have been measured by students around the shoreline and offshore (E. Miller personal communication to K. Blisniuk, 2017) but has not previously been used to characterize the behavior of the SGF-E. This folding is used here along with the bathymetry data in Bretz el al, 2014, to improve the precision of the slope in bedrock angle along the Middle Strand.

In the following sections, after a discussion of methods, new fault mapping is combined with a reevaluation of prior work to revise the SGF-E strike-slip fault map. Stratigraphy is briefly discussed followed by dating of the marine terrace sediment by Cosmogenic Radioactive Nuclide, CRN, and Infrared Stimulated Luminescence, IRSL, techniques. Recent fault exposures that have been traced in both marine terrace deposits and down into Purisima bedrock are then detailed and an analysis of the fault style progression as interpreted from faults in the marine terrace deposits is included. Horizontal fault offset since the abandonment of the wavecut platform is then estimated by a measure of the change in dip along the fault and that is combined with the terrace age to obtain a probability density function of the slip rate. Other more conventional but less well constrained piercing points are also discussed. Fault progressions in both the Qmt layers and overall along PPB are outlined. Appendices include details of the consultant-identified subsurface faults, a simple demonstration of folding at a restraining bend, details of a folding model used to improve the offset estimate, magnetic anomaly measurements that further characterize the faults, and the implications of the restraining bend for the formation of the Half Moon Bay Syncline and the Moss Beach Syncline east of the SGF-E.

Methods:

Sources of information for this report include much previous work, scarps, shears in asphalt roadbeds, offsets of linear features, consolidation of a large number of geotechnical consultant reports, faults exposed in walls of unconsolidated sediment as well as Purisima fm bedrock, magnetic anomaly profile scans, and folds in ocean eroded bedrock layers combined with a folding model. Prior reports, some dating back to 1971, which have been done partly in response to concerns of the ground movement effect on development in much of the area have contributed information to this review. Exposure of fault gouge by a recent landslide was seminal in confirming the path of the Middle Strand down the middle of Pillar Point Bluff and lead to additional exposures and faults along a headscarp about 100 m long with a cliff face height of up to 10 m. Manual excavations followed the faults, bedrock, and terrace deposit layers as needed to clarify their structure which resulted in the exposed configurations being quite three-dimensional. The faults and strata measured on walls oriented at various azimuths using surveyed locations, elevations, strikes, and dips were extrapolated to one vertical plane normal to the 319° trend of the Middle Strand, Figure 9, to get a layout in one dimension based on the measured trends of each feature. While this extrapolation inherently includes dimensional uncertainties the structure and trends are believed to reasonably reflect the structural layout at this latitude. Magnetic anomaly profiles were used to confirm and characterize faults and were found to provide supporting information on bedrock configuration.

Adjacent the most prominent fault (the “Middle Fault”, MF, component of the Middle Strand which displays a wide fault gouge and vertical offset in Purisima bedrock and significant lithology offset in Qmt) a series of contiguous fault planes representing a progression of the fault in Qmt were measured to orient them and combined with an assumed fault trend to determine the changing fault plunge over time. Slickensides were also recorded in clay fault gouge foliated layers, and found consistent with calculated recent plunge angles although the slickensides are not considered as precise or informative as the series of fault planes for determining a sequence of fault plunge as discussed below in section “Fault Behavior in Qmt”.

Mapping of other geomorphic features, including ridges with both downhill and uphill facing scarps, identified initially as gravity spreading ridges, now believed to be part of releasing bends that initiated as shear faults, and shears in asphalt roadbeds were done using surveying and GPS. Subsurface faults in developed areas of the unincorporated Seal Cove and Moss Beach areas were mapped by consolidating numerous trench-aided geologic consultant reports and additional faults were mapped in the undeveloped area of Pillar Point Bluff using manual magnetic anomaly scans.

Stress shears in asphalt roadbeds were mapped where they exhibited Riedel R-shears indicative of right-lateral movement. These shears were located and photographed, although many have since been removed or covered by the efficient San Mateo County road department. Offset road marker lines on West Point Road and stress features along the edges of the roadbed and on a service road, here referred to as “coordinated pairs of arcuate extension cracks”, were used to locate and orient the fault on the south end of Pillar Point Bluff. These are part of preliminary indications of possible aseismic creep, as reported in Appendix C, that is yet to be confirmed. The projection of an alignment of these two features to the northwest intersected the headscarp of a large landslide area in the middle of the bluffs. Following that path precipitated the discovery, made with John Caskey, of the faults which were subsequently exposed along that headscarp.

In the absence of well-constrained typical piercing points use was made of the change in dip angle along the restraining bend to estimate horizontal fault offset over a defined time frame, namely the time since the abandonment of the wavecut platform. The Purisima wave-cut platform west of the faults reported here, plotted to the southwest of FWWF in Figure 7, currently dips landward (NE) whereas when formed it would have dipped seaward (SW). The change in bedrock angle that this represents is then related to the measured change in bedrock angle along the restraining bend to calculate an offset. As an improvement to the precision of the dip measurements, the offshore folded structure, which is extensively quantified by the bathymetry data of Bretz et al, (2014), was also used to calculate the dependence of fold angle on distance into the restraint, and that combined with the measured change in slope of the wave-cut platform since it was abandoned was used to estimate the tectonic offset in that time. This process is detailed in Appendix D. It is found to provide precise, well constrained results that are used to calculate a lateral offset since the wavecut platform was abandoned. Dating the sediments above the wavecut platform using both CRN techniques with Be^{10} and IRLS, with the lab work primarily done by Kimberly Blisniuk, Alianora Walker and coworkers, which together gave consistent results, then provide an accurate date of abandonment of the wavecut platform and hence a slip rate.

Results:

Mapping:

Figure 4 summarizes the current strike-slip fault mapping for this on-land section of the SGF-E. Tracing from southeast to northwest, this eastern strand of the SGF-E crosses Half Moon Bay along about a 333^o azimuth, bends through about a 13.4 $\pm$ 1.1^o CCW restraining bend, where the Middle Fault, MF, the central component of the Middle Strand, continues along an approximately 319^o azimuth across PPB. Two additional components, the East Wall Fault, EWF, and the West Wall Faults, WWF, are subparallel spurs that form within or near this restraining bend and all three coalesce near the middle of PPB. On the northern end of PPB a western component goes offshore along about 318^o to the northwest while about halfway up Pillar Point Bluff a duplex of releasing faults bends northward to connect the Middle Strand with an eastern path that includes the well-known Fitzgerald Fault, and which then also continues northwest subparallel to the western path. Both northern components eventually turn to about 338^o and continue across the San Francisco Bay entrance as recorded by Ryan et al, 2008, about 12 km north of Seal Cove as their SGF-E branch, Figures 6, 7, and 7a. Figure 7 shows that these two components join at depth. Figure 7a is derived from USGS ofr 2014-1214 and provides a well-delineated view looking south toward PPB of the two fault paths that proceed NW through the offshore folding. The Seal Cove Fault along the eastern scarp of PPB is assigned in Figure 4 as an east-vergent thrust fault as reported by Koehler et al, 2005.

Recent fault exposures, initiated by a landslide along a prominent landslide headscarp near the middle of Pillar Point Bluff, Figure 2, confirm, broaden, and extend the Middle Strand fault originally mapped as a likely fault by Pampeyan, 1981. These faults are further confirmed and mapped by magnetic anomaly scans reported in Appendix F. Details of this exposure are discussed below in the section "Middle Strand Exposure". Figure 4 shows this includes a Middle Fault, MF, a set of faults 30 - 50 m west of that combined here as West Wall Faults, WWF, which approach from the south at a small angle to the MF offshore between Pillar Point and Pillar Point Bluff where it was mapped as concealed by Pampeyan, 1994, although it is traceable in the surf zone at low tide, Figure 8a, and runs about 4 km south, Figure 8. The East Wall Fault, EWF, lies about 40 m east of the MF, runs along the northeastern headwall of the landslide basin exhibits surface disruption both south and north of the landslide basin becomes obscure further south, but appears to align with dip-slip faults identified in trenches near the southern end of PPB by Connelly and Rubin, 2001. Thus, whether EWF is strike-slip or dip-slip is not here established. These two or three sets of faults, WWF and MF and possibly EWF, coalesce in plan view around the north side of the landslide basin, Figures 4 and 10. They appear to represent a classic positive flower structure, Figure 9, as reasonably expected for such a restraining bend.

Evidence for mapping the three faults is also found within the large landslide area in the middle of Pillar Point Bluff. The landslide basin has experienced more recent ground movement than other parts of PPB and it appears to have also retained indications of the faults in its topology. In Figure 10 the MF, the West Wall Faults (the three faults, WWF1, WWF2 and FWWF, discussed in detail below, are combined for this plot), and possibly the East Wall Fault are all projected to intersect within or near this landslide basin. Google Earth elevation profiles through this landslide basin, along the paths indicated in Figure 10, show structure coincident with the projected faults, Figures 11 - 14. In these surface profiles the landslide basin displays a series of 1 – 4 m high bumps that correlate with locations where the Main Fault, the West Wall Faults, and the East Wall Fault are projected to intersect the profiles as shown by the brackets in the figures. In general, there is a steep headwall slope on the right side of the figures that includes a bump part way down the steep section corresponding to the East Wall Fault, then a slope break and another bump at the Main Fault, and a third bump in the flatter region coincident with the projection of the West Wall Faults. The consistency of the correspondences across the basin and the fact they track the converging faults suggests they are not just coincidental. Available lidar mapping through this landslide area with 1m resolution does not clearly show this structure although there is subtle topographic and flora evidence in the photo across the landslide basin in Figure 15. Profile 4 on the PPB surface just south of the landslide basin, Figure 14, shows evidence of the EWF and MF, albeit less pronounced than within the landslide basin, but shows no indication of the WWF suggesting that has not been as recently active and has been eroded smooth. Similar observations can be made in Figure 16, a vertically expanded view of the southern headscarp of this landslide basin where changes in slope are apparent above EWF and MF but not above WWF1. Magnetic anomaly mapping reported in Appendix F identifies structure in this area further confirming the faults. The occurrence of the landslide basin where the three sets of faults coalesce can be reasonably assumed to not be just a coincidence, of course. As the fracturing associated with the faults begins to overlap it likely accelerates the mass wasting forming the basin. The landslide basin is thus exactly where it would be expected to be if it were caused by the faults. Thus, not only the mass wasting along the Distillery Fault, but the landsliding within this basin is here seen as due to tectonic motion along these faults running down the length of Pillar Point Bluff.

North of this landslide basin, a series of aligned consultant fault trends in the Seal Cove highlands and a matching set in the Seal Cove lowlands consistent with lineations reported by Leighton, 1971 and Pampeyan, 1981, plus a series of fault-bounded ridges on the north side of the large landslide area combine to form a set of releasing crossover faults, Figure 4 and Appendix A. The faults in the Seal Cove Lowlands and Highlands are shown separated from each other and from the fault-bounded ridges in Figure 4, however, their alignment and the arrangement of the sets strongly suggest the traces form continuous series of through-going faults that together cross over from the MF to the Fitzgerald Fault. The Distillery Fault, olive green line in Figure 4, previously assumed to comprise cliff-side landsliding (Leighton et al, 1971 and Cotton et al, 1980) follows a series of Riedel shears in roadbeds plus fault scarps, a consultant subsurface fault and one of the Simpson et al, 1997 faults to form one of this series of releasing faults and the Simpson et al, 1997 results indicate this fault likely is responsible for the most recent event. The consultant-reported faults and roadbed shears are detailed in Appendix A and C and Table AI. The contiguous nature of the crossing faults between the Seal Cove Highlands and the “gravity spreading ridges”, the yellow lines to the green lines in Figure 4, is confirmed by magnetic anomaly mapping in Appendix F.

The commercial and residential developed area southeast of Seal Cove where the northwest continuing branch and the northern-most of the releasing duplex faults, locally and here called the Distillery Fault, separate is plagued by frequent ground movement-induced damage. For instance, the county precludes attachment to public sewer lines in some of the area because of this. Numerous Riedel R-shears in roadbeds indicative of right-lateral strike-slip, fault scarps, and subsurface consultant trench-identified faults, mapped in Figure 4 by small blue and magenta features, attest to tectonic activity throughout the area. This mapping strongly suggests tectonic faulting and fracturing provides initiating planes for sea cliff-aided gravity-induced slumping and landsliding likely similar to what previously occurred to produce the large landslide basin.

The three sets of faults from the south, EWF, MF, and WWF, coalesce near the north side of a large landslide basin, Figures 4 and 10. At that point they are projected to cross the releasing faults that connect with the Fitzgerald Fault. These releasing faults include dextral strike-slip motion as recorded by Riedel shears in roadbeds and this shifts the continuation of the MF to the north until it goes offshore through a steep ravine on the south side of Seal Cove (adjacent The Distillery Restaurant). How far it shifts crossing each of the individual releasing faults is uncertain - which is the reason that connecting section is dashed in Figure 4 - but the total northward offset along the crossover shears appears to be roughly 160 m. This is further discussed in the “Fault Sequence” section below.

Figure 17 compares a map of the releasing bend faults to the experimental right-lateral releasing step analogue model of McClay and Dooley, 1995, to suggest that the configurations and aspect ratios are similar for the two situations. Figure 18 is an elevation profile along the length of Pillar Point Bluff that starts on the northern end just west of the Fitzgerald Fault and runs to where the Middle Strand comes ashore on the southern end of PPB, crossing the releasing duplex faults, as indicated by the green dashed line in Figure 17, along the way. Two shallow valleys (roughly 4 – 18 m deep) are seen on the northwestern end in Figure 18, corresponding to the Seal Cove Lowlands and Highlands, with the edges of those valleys roughly corresponding to the releasing duplex faults. The Seal Cove Lowlands are consistent with graben formation due to a releasing bend forming a negative flower structure further supporting the similarity of the processes forming the two fault patterns in Figure 17. In S.I. F the magnetic anomaly scan in Figure F11 also shows an approximately 60 - 80 nT dip in the region of the Seal Cove Lowlands coincident with the expected graben. The Seal Cove Highlands elevation appears to be at least partly due to it having a granitic bedrock throughout much of it as discussed in Appendix E and F and below in the fault sequencing sections.

A shallow graben was also observed in the trench of Simpson et al, 1997. They found two sets of faults in their trench, one set at their 12 to 18 m location and the other at their 34 to 36 m location with a tectonically down-dropped section between those two sets of faults. These two sets of faults are here assigned to two different releasing bend faults, the Distillery Fault and the consultant faults trend 1, respectively, as shown in Figure 19. Their trench happens to be quite close to where these two faults are projected to intersect. It is between these two faults that we find the northern Seal Cove Lowlands graben in Figures 18 and F11.

Figure 19 shows that the current mapping of the Distillery fault (olive green line) aligns in both location and direction with the western-most fault identified by Simpson et al (1997). The MRE of Simpson et al (1997) at their F14.5 location reportedly trends 341° matching the 342° ± 3° trend of our mapping of the Distillery Fault in that location. This suggests the Distillery Fault projects to the Simpson faults at M12-15 and continues to follow the scarp along the Fitzgerald Bluff proceeding northeast to match up with the well-known Fitzgerald sea cliff fault. iPhone Magnetic anomaly profiles across Fitzgerald Bluff in Appendix F, Figures F20 and F24, also support this path of the Distillery Fault (albeit with the caveat that iPhone magnetomers used in that mapping are not established as reliable in identifying faults as the proton magnetometer). While the difference in trends identified by Simpson et al between their MRE and the penultimate fault event at F34.5 is only 15°, and the accuracy of the trend angles is not reported, we take that difference as significant (they specify strike angles to the nearest degree) and find the penultimate Simpson fault event at M34.5, striking 326°, aligns with releasing fault 1, which as previously mentioned is also consistent with lineations of Leighton et al, 1971 and the Pampeyan 1981 map. The two sets of faults, the M12-14 and the M34.5 faults, are projected to merge further north and continue following the scarp to the Fitzgerald fault. It is unlikely the M34.5 fault follows the arcuate loop proposed by Simpson et al, (1997) since it would need to cross consultant fault trends 1 and 2 mapped in Figures 2, 4, and 19. Rather, the faults likely form a releasing duplex bend as suggested in Figure 17.

Figure 20 plots the strike and dip for the Purisima fm bedrock around the shore of Pillar Point Bluff from the Moss Beach Syncline on the north to Pillar Point on the south. The path of the measurements is indicated by the black line in Figure 21 and the data here is primarily of strata near the base of the cliffs that is judged to be intact enough for good measurements. The strike changes direction whenever the path crosses a fault from the current mapping thereby supporting those assignments. For instance, crossing the Fitzgerald Fault produces about a 180^o change in strike, that is, the dip changes from NE to SW. At the extension of the MF that proceeds NW from Seal Cove the strike again switches direction. At the location where the West Wall Faults cross the shoreline there is a more gradual change in strike direction. In the surf zone a rotation of the bedding planes is observed suggesting a rotational component associated with this transition, Figure 8a. Then the strike flips again when the path crosses back across the same fault where it enters Pillar Point. This correspondence of alternating strike directions adds confidence to the current fault assignments while also emphasizing this characteristic behavior.

Also mapped in Figures 2, 4, and 21 are offshore folded layers that are inside of the bathymetry limit. This includes the completion nearshore of an anticline-syncline-anticline folding adjacent the southern end of Pillar Point Bluff and the transition to a uniformly NE dipping structure on the northwestern end west of the offshore extension of MF. The well-documented Moss Beach Syncline lies northeast of the offshore going AP line. A symmetrically positioned anticline that does not breach the sea surface is found south of Pillar Point adjacent the extension of the WWF, Figure 4. Of note is that all three of the folds around Pillar Point plunge toward it, suggesting this is indeed a relatively flat unfolded pillar and accounts for the low dip angles around Pillar Point, typically below 10^o compared to over 15^o for other dips along

PPB shores. This is undoubtedly due to its position just at or before the entry into the restraining bend. The lack of folding and fracturing is in turn why PP remains uneroded.

In summary, three coalescing fault strands on the southern end of PPB have been mapped, a Main or Middle Fault, a West Wall set of faults, and an East Wall Fault. Together these are here referred to as the Middle Strand, at least the first two of which constitutes the eastern component of the right-lateral strike-slip San Gregorio Fault. A continuing set of subparallel strands are mapped northwest of PPB, one a continuation of the Middle Strand NW from Seal Cove and a subparallel one from the Fitzgerald Fault. A series of releasing bend crossover faults connect these two strands on the northern half of PPB. Together these all form a set of flower structures, a positive flower structure along the restraining bend on the southern half of PPB and a negative flower structure in the releasing duplex section, as expected for these types of bends on a strike-slip fault, e.g. Twiss and Moores, 2007, Ch 6. As a result of the above mapping strike-slip faulting can now be traced the length of Pillar Point Bluff and Seal Cove and fit previously identified strike-slip faults without recourse to the prominent eastern scarp of Pillar Point Bluff. What remains uncertain is the connection to and the faulting style of that fault along the prominent eastern scarp of PPB, the Seal Cove Fault. Koehler et al, 2005 found thrust faults in trenches at the base of the scarp, however the extent of any oblique component is unknown. A consultant trench-identified fault on the southern end of PPB (Connelly and Rubin, 2001) included the observation of faint slickensides that were oriented down-dip, Figure A5, and this fault is along the eastern side of the apex and may be aligned with EWF, Figure A4. This dip-slip fault is less than 100 m west of the prominent scarp where SCF is mapped and the relative location suggests the SCF is also likely a dip-slip fault. A strike-slip component along that scarp is not required to explain the strike-slip offset seen in the cliff face at Fitzgerald Marine Reserve or at the Simpson et al, 1997 fault locations, and the scarp has a relatively high degree of sinuosity inconsistent with a strike-slip fault. In S.I. F it is also shown that the asymmetry of the magnetic anomalies across the faults along the prominent eastern scarp are different from those for the here identified strike-slip faults down the center of the bluff and it is argued this suggests they are predominantly dip slip. A reverse fault along this scarp is consistent with the positive flower structure of the restraining bend. A right-lateral strike-slip fault style is confirmed for the Middle Strand as discussed below, however no such evidence has been reported for the Seal Cove Fault.

Stratigraphy:

This section summarizes the general stratigraphy found in the Pillar Point Bluff area although is neither in great depth nor exhaustive.

Within Pillar Point Bluff the late Miocene to late Pliocene Purisima fm, (Powell, 1998) is exposed in the shoreline, the sea cliff, the walls of a large landslide basin, and near the apex of the bluff, (Figure 3, which is from Pampeyan, 1994, and Glenn, 1959). A surface exposure near the apex includes pholad borings in Purisima sandstone indicating it at one time formed the surface of a wave-cut platform. That apex exposure is about 100 m east and 20 m higher in elevation than the Purisima exposed at the Middle Strand fault exposure location, Figure 2. Similar pholad borings were found during excavation in sandstone clasts throughout the interface between the top of the Purisima and the unconformably overlying marine terrace deposits in the fault exposure area. The sea cliff exposures of Purisima and those within the large landslide basin are highly weathered and fractured, shaly and generally not intact enough to identify good strike and dip measurements except in places along the bottom of sea cliffs and the generally intact eroded exposures in the surf zone, Figures 20 and 21. The Purisima around the fault exposures is generally black, shaly, friable, and heavily weathered with poorly defined bedding layers, e.g. Figures 43, 51, 53, and 54. This may partly be due to petroleum intrusion into the fault gouge, which has a strong petroleum odor, plus compression from the restraining bend and attendant extensive folding, faulting, and fracturing in the area.

The marine terrace deposits identified near the fault exposures in Figures 22 and later figures are consistent with a regressive sea sequence with an intertidal sand layer, Qmt-ITs, from 1 to 4 m thick, above the Purisima wave-cut platform within the fault exposure area. In many areas this is overlain by clayey/sandy silt layers, Qmt-cls, about 1 to 2 m thick, probably back-berm deposits (D. Andersen personal communication, 2019), Figures 22, 43, and 52 and in other areas by fine gravel layers, Qmt-fgr, Figure 23 and Qmt-fgr2, Figure 24 and/or by medium gravel layers, Qmt-mgr, Figure 25. The Qmt-fgr2 fine gravel layers are similar to exposures of

Half Moon Bay Terrace deposits east of this locale, such as Figure 27, with sieve analyses in Figure 28 and Table II, that in turn appear to be fan deposits from the eastern foothills. Over much of the exposure a medium gravel layer, Qmt-mgr, Figure 25, is identified either above the back-berm layer or above fine gravel layers and is offset by some of the faults. This layer appears to possibly be fluvial although its frequency south along the HMB coast, where deposits appear to be fan related, suggest it could be another version of fan deposit. Besides the fine gravel layers having smaller median grain sizes, Figure 28 and Table II, the medium gravel shows most of the clasts over 10 mm being sandstone and those sandstone clasts tend to be highly fractured in place, that is they fractured after being deposited.

Figure 28 is a grain size distribution chart for fine and medium (possibly fluvial) gravels near the faults at PPB and compares those to gravel samples from nearby in the HMB terrace. The fine gravel layer abutting the west side of the LAAF faults, fGr, has about half the grain size of the fGr2 gravels on the west wall which are similar to other fine gravels around the Half Moon Bay terrace within about 2 to 7 km of the faults. The medium, possibly fluvial, gravel at PPB is similar to a deposit at Montara State Beach four km north.

Table II: Sieve Analysis for Gravel Layers:

Lat, Deg	Long, Deg	Sample	Median ϕ	Sorting ϕ	Skewness	Kurtosis
37.50897	122.50508	PPB wLAAF fGr	-1.4	1.5	1.8	1.2
37.50875	122.50536	PPB WW fGr 2	-2.9	0.9	4.2	1.0
37.50881	122.50547	PPB FWW fGr 2	-2.2	1.4	2.2	1.1
37.56392	122.51322	HMBT MSB fGr2	-2.2	1.4	2.3	1.0
37.50322	122.47808	HMBT H fGr2	-2.5	1.5	2.3	1.0
37.50325	122.48942	HMBT H fGr2	-2.5	1.1	2.8	1.0
37.50336	122.48911	HMBT HL fGr2	-2.5	1.7	2.2	1.0
37.46539	122.44597	HMBT FB fGr2	-2.3	1.8	2.0	0.8

37.50878	122.50528	PPB wLAAF mGr	-3.5	1.5	2.8	1.0
37.56392	122.51322	HMBT MSB mGr	-3.6	1.5	2.9	1.0

Description: PPB => Samples from near fault exposure on PPB, HMBT=> nearby on Half Moon Bay Terrace. Results are in units of $\phi = -\log_2$ of diameter in mm. MSB => Montara State Beach, H and HL => Pillar Point Harbor, FB => Francis Beach, LAAF => adjacent MF, WW => near west wall faults, FWW => near far west wall faults. [Median ϕ of -1 => 2 mm, -3 => 8 mm. Sorting $\phi > 1$ => poorly sorted, < .5 => well sorted]

The fine gravels in Table II are granule to small pebble sized, sub-angular, and poorly sorted. These gravels appear similar to gravels in the foothills 4 km northeast that are high enough to likely be above any marine terraces which are thus presumed to be fan deposits although sieve analysis was not done on those. Gravel layers up to large cobble size appear further south along the coast but are not included in this data as they don’t appear to be represented on PPB.

The gravel layers are interspersed with ITs-like layers on the far west wall and are generally overlain by other gravel layers and/or soil horizons at the fault exposures. An exception is above the low angle adjacent faults at MF where a uniform homogenous sand layer, Qmt-s, overlays an mGr layer and is below the soil. This is noticeably different from the ITs sand layers and appears to be aeolian, Figure 26.

These strata are mapped in a general view in subsequent figures of the faults, such as Figures 43 and 52. However, T. Ladinsky and A. Powers, 2018, compiled a beautifully detailed wall map of part of the MF wall with several additional subunits identified although without provenance assigned, in Washburn et al, 2018 and also traced many of the MF faults through the Qmt deposits.

Besides the marine sedimentary Purisima formation, Montara granodiorite, Km, also plays a prominent role in the sediments of the area. It outcrops in the vicinity, primarily in the foothills to the east, Pampeyan, 1994. No granitic bedrock is found in the fault exposure area in the large landslide basin nor does it outcrop throughout Pillar Point Bluff. Pampeyan, 1994 indicates it underlies Purisima sandstone over at least part of Pillar Point Bluff but that is here considered uncertain. Leighton et al, 1971, found granite bedrock east of consultant's fault trend 2 but only sandstone west of it. This granite bedrock substantially underlies the Seal Cove Highlands, see Figure 65, and is thought to be the cause for the Highlands being lower in elevation than the Purisima bedrock sections of Pillar Point Bluff, e.g. Figure 18, and the reason the eastern scarp extends about 110 m further east for the Highlands than for the Purisima sections, Figure 64. This is discussed more in the "Faulting Sequence" section.

Pampeyan commented as follows about Montara granite:

> "Basement rock of the La Honda and Pigeon Point blocks is granitic but is so pervasively fractured that sound hand specimens representative of the unit are difficult to obtain. Narrow aplite and pegmatite dikes are common, and in a few places buff-weathering rhyolite dikes as wide as 2 ft are present. The granitic rock of Montara Mountain has been variously called granite (Lawson, 1893, p. 150; Law5on, 1895, p. 8), quartz diorite (Branner and others, 1909; Lawson, 1914, p. 4; Curtis and others, 1958, p. 9; Compton, 1966, p. 285; Ross, 1972, p. 10), granodiorite (Darrow, 1963, p. 9-11), and tonalite (Ross, 1984, figs. 4, 6), the differences largely reflecting the nature of study and the choice of classification scheme. " Pampeyan (1994, report to map I-2390)

Granite, as it will be referred to here, does outcrop along the north shore of Moss Beach indicated by a red marker in the top of Figure 29, and at North Point, the point northeast of the Moss Beach Syncline . The marker is at a granite fault gouge zone surrounded by granodiorite plus highly strained granite and conglomerate with Purisima emplaced within it, Figures E13 and E14. This is further discussed in the Middle Strand Fault Sequence section and Appendix E.

The provenance of the marine terrace sediment is found to vary along Half Moon Bay, as graphed in Figure 30. The medium and coarse gravel layers become less granitic, compared to the sandstone and mudstone component, southward as might be expected further from the presumed source of Montara Mountain Granodiorite. The granitic/sedimentary ratio near the fault exposure at PPB, plotted at 0 distance in Figure 30, is similar to that for HMBT a few km south along the coast.

Along the Pacific coast of Half Moon Bay and south to Ano Nuevo the beach and cliff exposures show a generally similar marine terrace deposit profile above Purisima bedrock of Intertidal sand overlain by multiple layers of likely fan deposits above Purisima but with many of these fan deposits toward the south having much larger clasts than seen at PPB, Figures 31, 32, 33. The Purisima, so prominent along the PPB coast west of the San Gregorio Fault, is below sea level along the northern end of Half Moon Bay, Figure 34, and doesn't rise above sea level until Redondo Beach, 5 km south of PPB. It then rises slowly with less than 1° slope to about Cowell Ranch Beach where it then rises more steeply to 40 m above sea level at Martin's Beach about 15 km south of PPB, Figure 34. There is a fault sub-perpendicular to the trend of the San Gregorio Fault at Cowell Ranch associated with extension in Appendix E and whether that precipitates the steeper rise is not clear.

Half Moon Bay east of the SGF-E was previously noted to constitute a large gentle syncline, Lajoie, 1986, based on terrace strand line warpage and Figures 34 and E7 are consistent with that. Lajoie, 1986 shows a NW directed axis, here it is found more westerly directed, although the small angles make it uncertain. Pillar Point Bluff local uplift on the west side of the SCF is a significant departure from this gentle syncline, Figure 34, in keeping with the restraining bend uplift contribution discussed here. It is argued in S.I. E that the bedrock curve in Figure 34 is consistent with Half Moon Bay being a syncline formed by extension caused by the protrusion of the granite bedrock into the path of the SGF-E. This granite protrusion and its coupling to the western plate is shown to simultaneously be the cause for the restraining bend and subsequent offshore folding at PPB, the compression that causes the Moss Beach Syncline, and the extension producing the Half Moon Bay Syncline.

A more detailed estimated elevation of bedrock, Purisima and Montara Granite where appropriate, along a NW-SE profile at Pillar Point Bluff is plotted in Figure 35, with the data in the Seal Cove Highlands and Lowlands schematically representing the variation as measured by Leighton et al, 1979. Otherwise, the information comes from sea cliff or surface exposures. Of note is the bedrock shows more topological relief in the Seal Cove area, especially short term, than does the marine terrace deposit.

Dating of Sediments:

Dating of the marine terrace deposits was done by Kimberly Blisniuk, Alianora Walker, Dennis Wu and coworkers using cosmogenic nuclide dating with ^{10}Be plus IRSL methods. Samples for ^{10}Be dating were collected along about a 2m depth profile in Qmt at about .3 m vertical intervals on the east side of the Main Fault cliff face exposure as located in Figure 36. The samples were processed at the Lawrence Livermore Laboratory Center for Accelerator

Mass Spectrometry and show a consistent model result over a range of marine terrace deposit layers vertically distributed and thus are considered reliable indicators of the age of the deposits. The ^{10}Be profile model results are summarized in Table III, the terrace deposit age is reported as 44 – 59 kya, a boxcar distribution. **^{10}Be** sample and concentration data for the vertical profile is shown in Table IV and were used with the Cronus model, Marrero et al, 2015.

Five IRSL samples were processed at the UCLA Luminescence Laboratory with results also in Table III. Sample locations are also shown in Figure 36.

Table III: Geochronology data for Marine Terrace Deposits at Pillar Point Bluff

Dating Method	Location Description	Location No.	Date Kya	Type of age
^{10}Be	Qmt Surface of MF (scattered pebbles)		18.8 ± 1.7	mean
^{10}Be	**Qmt Depth E of MF**		**44 - 59**	**mean**
IRSL	**Sand above Tp W side of MF**	**1900**	**47.7 ± 4.1**	**mean**
IRSL	Sand above Gouge/Tp E side MF	1900a	38.1 ± 6.1	minimum
IRSL	**Bot Fine Gr above Sand W side of MF**	**1903**	**50.6 ± 3.4**	**mean**
IRSL	Top Fine Gr above Sand W side of MF	1904	40.3 ± 7.1	minimum
IRSL	Sand above Gr W side of MF	1905	11.4 ± 1.5	minimum
pdf	Wave-cut Platform probability density function results using data in bold above, See Figure D28.		49.7 45.4 – 54.4 41.8 – 57.9	Median 68% Range 95% Range

Table IV: Data for **^{10}Be** vertical profile exposure age dating using Chronus 2.3.

Sample	Lat	Long	Elev	Density	Shielding	Thick	**^{10}Be** Conc	**^{10}Be** unc
SGF-1	37.509	-122.505	51	2.2	1		46697	1159
SGF-2A	37.509	-122.505	51	2.2	1	40	39932	1193
SGF-2B	37.509	-122.505	51	2.2	1		51055	1150
SGF-2C	37.509	-122.505	51	2.2	1		119404	2618
SGF-2D	37.509	-122.505	51	2.2	1	40	168844	3654
SGF-2E	37.509	-122.505	51	2.7	1	2	88058	2315

Data for the two sediment samples, No. 1900 and 1903, collected on the west side of the MF that displayed a fully bleached distribution, indicating they were fully reset by solar radiation, provided mean ages of 47.7 and 50.6 kya with standard deviations of 4.1 and 3.4, respectively. A minimum age model was used for the three other samples because it was reported they appeared to display incomplete bleaching. The minimum ages for these three samples are consistent with the mean ages for the two fully bleached samples so only the mean ages are used here. All the Qmt layers above Tp and below the soil (excepting the one likely aeolian sand layer discussed below) are thus consistently dated to within a span of 43 to 59 kya suggesting a MIS 3 highstand coeval marine terrace deposit. The IRSL results are consistent with the mean ^{10}Be results and together were combined into a probability density function, pdf, as suggested by Zechar and Frankel, 2009, Figure D28, which indicates a median deposition age of 49.7 kya, Table III.

The 95% probability age range of 42 - 58 kya centers the interval at Marine Isotope Stage 3, a sea level high stand, generally considered to have peaked about 30 to 80 m below current mean sea level (Siddal et al, 2008, Figure 38). Using a ^{10}Be and ^{26}Al cosmogenic nuclide inventory method of dating a sequence of marine terraces near Santa Cruz, Perg et al, 2001 found the lowest terrace to be associated with MIS 3. However, those dates were questioned by Muhs et al, 2003, as having been possibly contaminated by overlying alluvium. The results here with both ^{10}Be and IRSL results agreeing suggests contamination is unlikely to be a cause.

Pillar Point Bluff Terrace has not been correlated to the Half Moon Bay Terrace either in this report or previously, nevertheless, the relationships here identified and tectonic processes here proposed do suggest the two may correlate and thus it is considered relevant that previous dating of the HMB Terrace be compared. Stage 5a is the date that had been proposed for the Half Moon Bay terrace by Kennedy et al, 1982 who assigned 80 – 85ka using paleontology of shell beds lying just to the east of Pillar Point Bluff at a depth of 20 m constrained by amino acid racemization data. They found mollusks and other fauna that included at least one extralimital northern species and three to five species that occur today only as far south as Monterey Bay. They assumed the age would be MIS 5 by comparison with other nearby marine terraces and assigned MIS 5a based on the cool water fauna consideration and corresponding cooler temperatures during MIS 5a. The wavecut platform upon which the Half Moon Bay terrace is deposited east of SCF is near or below sea level at this latitude and only rises above sea level several km south, Figure 34, so its correspondence with other nearby raised terraces is uncertain. Amino acid enantiomeric ratio with D/L leucine = 0.41 were reported to provide equivalence with other cool water fauna assigned to 5a. However, this assignment has a large uncertainty and does not appear to be unique, see e.g. Bender, 1974, and a cool water association would also be consistent with MIS 3. The combined IRSL and ^{10}Be data reported here is likely a more reliable and precise indicator of sediment deposition age so a revised interpretation of Kennedy et al, 1982 could be put in agreement with the current results. Direct dating of HMB terrace deposits would be a useful follow on to this study.

Other than the Perg et al, 2001 report previous estimates of marine terraces along the California coast north from Santa Cruz have identified the latest terrace deposition dates to be MIS 5a, Muhs et al, 2003. The uniquely high uplift rate for Pillar Point Bluff due to its being a restraining bend, found to have a vertical rise rate since MIS 3 up to about 2 mm/yr as found in the Slip Rate Section later, could be responsible for preserving a MIS 3 high stand. If PPB does correlate to the Half Moon Bay Terrace then the implied HMB terrace vertical rate would be around 1 ± 0.3 mm/yr, reasonably similar to vertical rates reported elsewhere along the California coast. This is addressed again in the Slip Rate section.

A ^{10}Be surface exposure dating of scattered pebbles collected on the surface gives a mean age around 19 kya. A minimum age from IRSL for a sand layer 1 – 2 m below the surface, SG19-05 in Figure 56, is 11.4 kya. Later dating provided by the UCLA lab using a Central Age (Mean) Model gave a mean value of 23.5 ± 2.3 kya for this sand sample. If the sample had experienced incomplete bleaching as originally stated then this mean age would be too high, so at this point it is considered uncertain if it is a mean age or a maximum age and the mean age as between 11.4 and 23.5 kya, in either case it is roughly consistent with the Last Glacial Maximum, LGM. Either of these ages does not significantly alter the analysis presented here.

While the surface ^{10}Be and near surface IRSL ages might be considered consistent, they are here interpreted as likely representing two different and uncertain processes. Generally larger clasts that can be confidently associated with long undisturbed surface exposure are used to characterize the surface for ^{10}Be dating, but no such clasts are available here. The scattered surface pebbles may have followed any of several processes to get to this surface where surface pebbles are rare. 1) One option is to have been deposited by a fluvial process which would appear to require that the Pillar Point Bluff surface be at the Half Moon Bay Terrace surface elevation at 19 kya in order for the fluvial deposit to reach PPB from its presumed source in the foothills to the east. That is unlikely as it implies the Qmt surface, which presumably would have covered the abandoned wavecut platform at the same elevation on both sides of the Seal Cove Fault, would have needed to remain at about the same elevation for ~ 30 kyr, then over the next 20 kyr the PPB surface would rise about 50 m above the HMB terrace surface at a vertical uplift rate of 2.5 mm/yr, which is an improbable sequence. In addition, if it had been fluvially deposited it is surprising there are so few pebbles remaining. 2) The pebbles could have eroded out of the Purisima that constituted the PPB apex and then distributed across the surface by downhill erosion. However, the pebbles reportedly contained both sandstone and granite original lithologies in which case that is also not likely the only source. 3) The pebbles could have risen to the surface from a lower stratum via a process such as upfreezing, also called frost heaving. This process is a reasonable but unconfirmed possibility. It involves clast upward migration during times of freezing/thawing cycles, as would be expected around the LGM at this latitude (Gozdzik and French, 2004) an event consistent with the 19 kya age. 4) Another variant of option 1, fluvial deposition, is that PPB does not correlate to the HMB terrace and was actually lower than the HMB terrace when Qmt was deposited during MIS 3, subsequently rose to be approximately level with the HMB terrace at 19 ka when the fluvial process deposited the surface pebbles, then continued rising to its current level. In that case, assuming a consistent vertical rate of rise, the PPB terrace would have been deposited at about - 70 m elevation, consistent with the MIS 3 msl estimate, Siddal et al, 2008, and the rate of rise of PPB would be around 2.4 mm/yr, a conceivable, if unlikely, sequence. Two data points that would help clarify this possibility is to date the HMB terrace and date a lithified conglomerate deposit that lies just east of the EWF that appears to be a distinctly fluvial deposit that quickly lithified. Without knowing more about the process by which the pebbles arrived at the surface it is thus difficult to assign a useful tectonic interpretation.

The dating of the Qmt-s deposit to a minimum of 11.4 kya or a maximum or mean of 23.5 kya likely represents a different process. This deposit is a massive, homogenous, well-sorted, fine to medium sand with a unique finite distribution above or adjacent to the west of the LAAF faults, Figure 36. It has many indications of being aeolian, although it doesn’t display crossbedding typical of sand dunes. During the early part of the LAAF fault movements it is reported below that the fault was right-lateral with southwest side moving down. This suggests a large earthquake could create a west-side down wind-sheltered step formed at the surface which could have filled with aeolian sand at 11 – 24 ka, around the LGM when the seashore would have been several km west with dry conditions likely in the vicinity. The location of this deposit fits the positioning for such a vertical offset from a NW plunging slip along one of the LAAFs, Figure 43, producing a scarp with east side up. For instance, a lateral offset of 6 m during the early phase of MF when the fault plunge was about 10^{o} NW, as reported below in Figure 52, would have produced about a 1m vertical offset with east side up similar to the step height observed, Figure 43. (Such a horizontal offset is within the range reported by Simpson et al, 1997.) In that case a settling out of sand in a sheltered location would not likely form a sand dune nor have the boundary wind layer required to produce crossbedding and could have deposited the non-stratified, non-cross-bedded, but well sorted sand.

Thus, while the surface dating of both the scattered pebbles and near-surface sand deposit are interesting subjects in their own right, at this time it isn't warranted to assign a tectonic significance to either without further constraining information except to note that their dates are consistent with their processes depositing them on top of the marine terrace deposit sometime after MIS 3. Nevertheless, the most reasonable processes are included in the proposed most-likely fault sequence in conjunction with Figure 62 below.

Middle Strand Exposures:

The first exposures of the previously unstudied Middle Strand are reported with a location overview in Figure 39 and individual detailed views in the following figures where these Middle Strand components are found to comprise a significant right lateral strike-slip fault with multiple sub-parallel or branching faults. Utilizing an adventitious landslide headscarp aided by manual excavations the faults were traced from the surface Marine Terrace deposits, Qmt, down into the bedrock Purisima fm, Tp, while verifying that in-place strata were exposed. Referencing Figure 39, the detailed figures are shown for the East Wall Fault, EWF, in Figures 40 through 42, Middle or Main Fault, MF, in Figures 43 through 50, West Wall faults WWF2, Figure 51, WWF1, Figures 52 through 54, and Far West Wall Fault and wavecut platform in Figure 55. In a few cases faults are traced up into the soil A-Horizon, Figures 40 and 50, and two are found to exhibit surface disturbance, Figures 41 and 42. Exposures along an approximately 100 m long section of a landslide headwall are traced with vertical sections up to 10 m high. The Middle and West Wall Faults were exposed down to the Purisima layer where fault gouge up to 1.7 m wide is found. The East Wall Fault was not excavated to the Purisima layer. The Far West Wall Fault was not exposed, its characteristics deduced from stratigraphic and magnetic anomaly mapping. Table II lists some of the characteristics, with details discussed in subsequent sections. Figure 9 is a schematic cross-section based on the exposed fault characteristics.

Table II: Fault Exposure Characteristics: Fault locations in Figure 39.

	EWF	MF	WWF2	WWF1	FWWF

Tp Side Higher	NE	NE	Neither	NE	SW
Tp Vert Offset	< 13 m	2 - 3 m	0 m	4.2 m	~1 m
Tp Gouge Width	?	1.3 m	0.1 m	1.7 m	?
Tp Angle Change	?	4	11	22	12
Qmt Side Higher	NE	NE then SW	Neither	NE	SW?
Qmt Vert Offset	?	≤ 1.6 m	0 m	< 2 m	--
Qmt Gouge Width	≤ 3? mm	≤ 30 mm	≤ 5 mm	≤ 20 mm	?
Qmt Litho Offset	Unknown	Large	~None	Medium	Medium
Fault Trend	314° ± 10°	319° ± 3°	324° ± 7°	325° ± 7°	333° ± 15°
Tp Fault dip	SW?	85° ± 7° SW	63° ± 5° NE	50° ± 10° NE	NE
Surface Expression	2-5 cm NE up	Gentle Scarp	--	--	--
Faulting in Soil?	A-Horizon	A-Horizon	None	None	?
Mag Anomaly Height	29 ± 3 nT	30 ± 3	-	5 ± 1	5 ± 1
Mag Anomaly Width	56 m	31	-	25	23
No. Faults in Qmt	≥ 3	≥ 25	8	≥ 15	?

The faults include a fault gouge zone in the Purisima layer composed of a black, moist, plastic clay with sub-horizontal striations (slickensides), Figure 45, which exhibits a strong petroleum odor when first exposed and which after a few day's exposure dries to vertically foliated plates that are subparallel to fault trend. For the MF and WWF1 the gouge zone rises with the rising side of the Purisima so that it becomes the interface between the elevated Tp side and the Qmt on the lower side, Figures 43, 52. For the MF the gouge widens as it rises to compress or offset the non-lithified Qmt deposits and diapirs of extruded gouge intrude Qmt directly above the gouge zone, Figures 22, 43 and 48. On the leading edge of the gouge is a lag of Purisima clasts with prolific pholad borings in them, Figures 46, 47, 53, and 54. These clasts tend not to be altered to the black shale typical of the surrounding Tp in this area, rather remain as lithified tan to gray sandstone or mudrock. The pholad borings on these Purisima clasts confirm they were once at the surface of a wavecut platform.

East Wall Fault:

Because it is visible from a high-use path in the Fitzgerald Marine Reserve the East Wall Fault has received the least excavation and grooming and is thus neither well characterized nor exposed down to Purisima, Figure 40, therefore much of this description is based on surface disruption, a magnetic anomaly scan, and its positioning relative to the other faults and the bluff apex. It exhibits the clearest surface disturbance with cracks exhibiting a sharp vertical offset of about 2-5 cm, NE side up, for at least 15 m south of the headscarp, Figures 41 and 42, and it exhibits the largest magnetic anomaly, Figure F6; thus, the EWF may represent the largest and most recent fault activity although it may be primarily dip-slip. The vertically expanded view of the landslide's southeastern headscarp in Figure 16 indicates this fault is associated with the largest surface topology rise and the magnetic anomaly scan shows the widest peak, Figure F6, features suggesting it is possibly larger and/or more recently active. Since the headwall has not been cleaned off the number of faults in Qmt is unknown, however, there do not appear to be as many faults in Qmt nor a significant lithology change across the faults in Qmt as for other faults suggesting the EWF has not experienced as much strike-slip offset as MF or WWF1. EWF runs along the base of the northeastern headscarp of this large landslide basin, about 170 m from the sea cliff, and is assumed to be responsible for the eastern headscarp, Figure 15, indicating fault motion has been adequate to facilitate that. The apex of Pillar Point Bluff, where Tp is exposed, is about 60 m east of EWF and on the order of 13 m higher than Tp on the west side of the EWF. The magnetic anomaly width is about 56 m. As such it is likely the EWF is at least part of the fault structure bordering the uplifted apex, as suggested in Figure 9, and could be predominantly dip slip with east side up, consistent with the observed surface disturbance, small lithology change across it, and likely being a bordering component of a positive flower structure. Further south the EWF surface expression is poorly defined, however, it appears it may align with a consultant trench-identified fault on the southern section of PPB that exhibited evidence of dip slip (Connelly and Rubin, 2001). The EWF appears to possibly converge with the MF and WWF on the north side of the large landslide basin, however, another currently forming scarp, the eastern most green line in Figures 4 and 10, exhibits up to .4 m of vertical surface offset, NE side up, and may be another northern component of this fault. That scarp is quite sinuous in plan view, Figure 29, suggesting it also may be primarily dip slip in agreement with observations above.

Middle Fault:

The Middle Fault exhibits the largest lithographic change across some of its sub-faults and is believed to have the largest strike-slip offset of the faults. While the vertical offset is less than for WWF1 that appears to be because the sense of the vertical component has changed over its history, as explained in the Fault Behavior in Qmt section below where it is shown the fault transitions from an initial NE side rising to a later SW side rising suggesting the total vertical movement on the MF has been larger than for WWF1.

The black clay gouge exposed below the elevation where Tp encloses both sides of the fault gouge is 1.3 m wide, dips 80° SW ± 10°, is highly viscous and plastic and exhibits a pronounced petroleum odor when freshly exposed. Above where the gouge is constrained on both sides by Tp the gouge zone rises along with the rising side of the Purisima and expands until its width is over several meters. The gouge near the top has a black core with a white or cream-colored gouge surrounding that, Figures 46 and 48. If the black color is from hydrocarbon penetration, as expected, the transition between the black and white clays is surprisingly sharp. Along the top surface of the fault gouge there are two clay diapirs, primarily white clay gouge, that protrude into Qmt locally offsetting the Qmt layers, Figures 43 and 48. The larger one, shown in Figure 48, is .5 m wide and extends .6 m into intertidal sand layers. The fault that reaches prominently into the soil A-horizon, Figures 49 and 50, passes through this diapir and is the same fault that recorded a 0.15 m right lateral offset of the peak of this diapir, Figure 56. The second diapir is about .3 m wide and extends .4 m into Qmt.

Along the southwest side of this gouge zone there occur four oblique faults extending into Qmt initially at about 40 - 75° from horizontal with lateral connecting faults between them which eventually coalesce to one trace and continue at about 45°, Figure 47. These are here referred to as Low Angle Adjacent Faults, LAAF, and are further characterized in the section below titled Fault Behavior in Qmt. The widths of these fault lines in Qmt are from 5 mm up to 3 cm. Curved pressure waves in front of the leading edge of the gouge indicate compression from the gouge protruding into Qmt, item 3 in Figure 47, and these are likely responsible for the small lateral shifts observed along the LAAFs, item 4 in Figure 47. Additional oblique faults occur below this elevation but still above Tp on the lower (western) side.

The coalesced single fault extension of the LAAF faults proceeds another 2 – 3 m into Qmt where it fades then becomes untraceable. Before it disappears, it clearly juxtaposes a coarse sand/fine gravel unit, Qmt-fgr, Figures 23 and 43, on the southwest side against a Qmt-cls clayey-sand layer on the northeast side. The Qmt-fgr appears similar to, although slightly finer than, the predominant deposits on the adjacent Half Moon Bay terrace, Figure 28 and Table II, which appears to be a fan deposit from the Montara granodiorite-derived foothills to the east. This consists of a distinctive dark brown fine gravel of predominantly sub-angular granite with median clast size of -1.4 ϕ (~ 2.6 mm) is poorly sorted with a clayey sand matrix, Table II. That unit does not appear at this locale on the northeast side of the LAAF faults and the Qmt-cls unit does not appear on the southwest side indicating a substantial lithology offset across this fault. Above this Qmt-fgr layer on the southwest side of the fault is another gravel layer, Qmt-mgr, that appears to be fluvial, has median grain size of -3.5 ϕ (~ 11 mm) with the sandstone clasts making up the majority of the larger clasts, with occasional imbrication and corresponds to a similar layer on the northeast side of the fault about 1.6 m higher. That same layer on the northeast side is seen to angle upward starting on the west side of the larger diapir and disappearing into the soil layer indicating it has been pushed up and eroded off, Figure 43. It reappears 1.6 m lower on the southwest side of the LAAF faults. This is consistent with the sequence of fault plunge suggested below in the section on Fault Behavior in Qmt and the process is outlined in Figure 62.

These Qmt units unconformably overlying the Purisima on the southwest side of the Middle Fault have been dated to MIS stage 3 high stand deposit, while a sand layer, Qmt-s, above Qmt-mgr on the southwest side of the fault, Figures 26 and 36, is dated to around the last glacial maximum, Table III.

A rough comparison with Simpson et al, 1997, for offset per event can be made based on this aeolian sand layer. It is suggested in the dating section the Qmt-s deposit formed as a result of a vertical offset with east side up which provided a protected relief step that then filled in with wind-blown sand. The 1-1.2 m high vertical step for this sand suggests a roughly 4 - 9 m horizontal offset using plunge angles from early in the MF sequence in Figure 61. This is similar to the roughly 3 - 11 m horizontal offset reported for the MRE of Simpson et al, 1997.

The difference in dates means it is not the same event, however this does suggest the magnitude of offsets can be similar between the two fault locations and the M7 magnitude estimate made by Simpson et al, 1997 might also apply to this event, although it is also possible this step could result from multiple events. The date of this fault(s) would then be

Compared to the black clay gouge, the adjacent Purisima is a less viscous, more friable black shaly clay, Figures 44, 51, and 54. The clay gouge is distinguished from the Purisima black clay by its response to impact as the gouge is noticeably more plastic and rubbery, the newly exposed gouge color is a darker black with a noticeable sheen and strong petroleum odor. Upon weathering for a few weeks, the exposed gouge dries to foliated plates exhibiting sub-horizontal striations (slickensides), Figure 45, then later disintegrates to a coarse granular clay.

Directly above the Main Fault clay gouge zone there emerge over sixteen smaller faults in Qmt, Figure 56, besides the two clay diapirs. Other than the fault that extends to the soil, and the two faults enclosing the diapirs, none of the components directly above the gouge zone displays a significant lithology change across the faults, nor a vertical offset of strata more than a couple cm. The fault that extends to the soil has a noticeable, but small, change in color and granularity on opposite sides of the fault, has a vertical offset at the soil level of about 9 cm, Figure 50, and near the surface it has a wider dark “organic” zone suggesting a surface crack formed at one time and soil dropped down into the opening. Near either side of this zone were found numerous sandstone clasts more than 1 cm in size (sieved) many of which had pholad borings indicating they had once been at the surface of a wave-cut platform, Figure 57, and few or no such clasts beyond 1 ft from the fault. These clasts are found 3 m above the wave-cut platform indicating the clasts worked their way that far up along the fault zone during the time frame it was active. This zone of pholad exhibiting clasts is .3 m wide and beyond that there are very few sandstone clasts and none with pholad borings, however the zone with clasts is clearly observed to be wider than the visible fault zone width indicating the zone of mixing and/or vertical transport of material was slightly wider than the noticeable fault zone in Qmt. This particular fault has a gouge width of about 3 mm just above the diapir, Figure 56, yet expands to widths of about 5 – 8 cm near the modern surface, Figures 49 and 50, plus appears to have propagated clasts alongside it over a much wider width, Figure 57, suggesting a complex fault behavior and history and that multiple events occurred along the same fault trace that starts as very narrow right above Tp.

West Wall Fault 2:

Twenty-five meters West of the middle fault zone is a smaller fault zone, WWF2, shown in Figure 51. It has a black clay gouge width of 0.1 m, dips about 63^o NE and displays very little vertical offset in either the surface of Tp or Qmt even though it has at least eight fault traces well displayed in Qmt-ITs. Unlike MF and WWF1, which do have significant vertical offsets in Tp and have faults in Qmt trending only in the direction of the lower side, the several faults above WWF2 obliquely trend both east and west as well as sub-vertically into Qmt, Figure 51. This fault in Tp dips more steeply NW than does WWF1, which is 10 m west, implying those two intersect about 20 – 30 m below the top of the Purisima, much shallower than where WWF1 is projected to combine with MF suggesting this fault is a spur of WWF1. Between WWF2 and WWF1 the wavecut platform dips 15^o NE, whereas east of WWF2 the dip sharply changes to 3.5^o NE suggesting WWF2 may be a response to a rotation (folding) of a small block about a sub horizontal axis parallel to the fault rather than or in addition to a lateral offset. As discussed below the usual behavior at these faults is for strike-slip faults above zones where there is no Tp offset is to propagate subvertically into Qmt, whereas at this location they cover a much wider range of angles and directions and some of the more distant faults do not seem to rise from a fault in Tp further suggesting rotation or folding as the origin of WWF2.

West Wall Fault 1:

Following an insightful suggestion from R. McLaughlin, a large fault zone, WWF1, was uncovered 10 m west of WWF2 with a vertical offset in Tp of 4.2 m and smaller vertical offsets along its component faults in Qmt of around 1 m, Figure 52. There is a clear lithology offset of the marine terrace deposit across the fault although somewhat less than that for MF. The gouge width in Tp, below where it is confined by Tp on both sides, is about 1.7 m and the dip is roughly 50^o NE. The gouge in WWF1 also gives off a distinct petroleum odor and is very moist and foliated with smooth oily surfaces when freshly exposed.

This fault has components that extend into Qmt from the rising Tp gouge edge at an oblique angle that gradually bends to a lower angle further from the Tp fault edge, similar to the situation for MF. However, in this case the component faults do not coalesce to one trace as they do for MF. They do display vertical offsets of up to 1 m between gravel layers, where the gravel layers, all labeled Qmt-fgr2, display different colors, although otherwise appear similar, Figures 52 and 24. The approximate 1 m vertical offset suggests a horizontal offset per fault of around 3 - 8 m in agreement with the estimate made for the aeolian layer above MF and also similar in magnitude to the MRE fault of Simpson et al, 1997. These offsets suggest these faults have experienced multiple events with M>7 since MIS 3.

The upper part of the Purisima at the exposure has experienced a landslide obscuring much of the Tp, although the interface between the top of the fault gouge and Qmt is intact and is believed to be in-place at the back wall in Figure 53 and exhibits a few sub-vertical faults into Qmt in this location. The Tp formation along the wall displays a convex curved surface, Figure 53, indicating the layer has been compressed and distorted, consistent with the rotation or folding suggested for WWF2.

The headwall west of WWF1 displays an intertidal sand layer, Qmt-ITs, that is 3 - 4 m thick above Tp, with noticeable mica content in the lower meter, before it reaches a gravel layer, here referred to as Qmt-fgr2, that is similar but not the same as that adjacent MF. The Qmt-fgr2 has a larger median grain size than does Qmt-fgr, -2.9 ϕ (7.5 mm) vs. -1.4 ϕ (2.6 mm), and more angular granitic clasts, suggesting this gravel had a shorter travel path from a granitic source even though it is nominally further from the foothills where this presumably Half Moon Bay Terrace fan deposit should have originated.

The Purisima beneath this headwall has been exposed two places northwest of the fault where it is confirmed that the Tp wavecut platform slopes westward about 6 - 10^o. In the area of these exposures the Tp is a black shaly bedrock that exhibits an oily residue that collects in the excavations suggesting the petroleum must seep not only into the gouge but also into surrounding Purisima layers.

Far West Wall Fault:

The FWWF is implied by a vertical offset and change in Purisima wavecut platform slope directions in Figure 9 and by magnetic anomalies, Figures F6 and F19. The wavecut platform west of WWF1 slopes southwestward about 6^o – 10^o while the platform surface west of the projected FWWF location slopes northeastward about 4.5^o, Figure 55. The fault is beneath heavily vegetated landslide debris and has not been located precisely, so the vertical offset between the two sides of FWWF is uncertain, nominally projected to be 1 m west side down, but that could be within $\underline{+}$ 2 m. A scarp suggests the trend direction. The large change in slope suggests a relatively large fault with significant horizontal offset, possibly similar to or larger than WWF1.

Based on magnetic anomaly mapping in Appendix F, it appears WWF1 is traced southeast past Pillar Point in Figures 4 and 8a. It extends 4 km southeast until it stops among the Purisima folding, Figure 8, suggesting this was a left step spur from the Middle Strand coming across Half Moon Bay. In passing across Whaleman's Cove it exhibits a rotated block that also shows offsets, Figure 8a, due to right lateral drag slip, a second confirmation of right lateral strike slip motion on these faults. This fault also is adjacent to noticeable fault blocks on two sides of Pillar Point, both west of WWF1, one on the northwest face and the other on the south face. Whether the blocks are part of the same one is uncertain although they do not exhibit a consistent cross-section or orientation.

Fault Behavior and Sequencing in Qmt:

Three fault gouge zones in Tp have been exposed and discussed in the previous section, however numerous faults emanate from these Tp gouge zones into Qmt. Certain patterns and characteristics are observed in these Qmt faults and in this section those observations are used to characterize fault development and discuss implications for fault sequencing.

The faults in Purisima, where exposed at MF, WWF1, and WWF2, exhibit a relatively wide and well-defined clay gouge zone ranging from about .1 m for WWF2 to over 1.3 m wide for both MF and WWF1, implying multiple events have occurred in the bedrock that develop ever wider gouge zones. However, as the faults proceed into the overlying marine terrace deposit, Qmt, they form a series of discreet narrower fault lines with visible gouge or fine breccia zones less than 2 cm wide that contain mainly clay and fine sand, e.g. Figures 47 and 56. Many of these faults emanate from along one side of the wide gouge zones in Tp in a vertical series where each extends at an oblique angle into the intertidal sand layers that overlie the Purisima on the lower of the two sides of the fault, Figures 43, 47, and 52. These fault planes provide a means of characterizing the fault movement over time. Results are shown as a sequence of fault plunges on WWF1 and MF in Figure 61 and a sequence of MF fault behavior is outlined in Figure 62 which may be usefully referenced during the explanation below.

The fault planes in Qmt are expected to, on average, conform to the trend and plunge of the fault in Tp. Continuity across the interface and compliance between strata requires any deviations in fault trend or plunge between the bedrock and Qmt to be within a few degrees and any deviation cannot extend very far before needing to be compensated. Significant non-continuities between the two would be evident as distortions or gaps at the interface near the fault zones and none are seen over any of the exposed interfaces. Since the fault planes in Qmt can be at a significant non-vertical angle their attitude (the fault plane orientations) represents the relative movement in both the horizontal and vertical directions. This provides the opportunity to measure a plane attitude that describes fault plunge. The planes so measured for MF and WWF1 are plotted in Figures 58 and 60, respectively, at a distance of about 1 to 2 m from the Tp gouge zone. The apparent slope of the fault plane parallel to fault trend, nominally 319^o for MF and 325^o for WWF1, is the fault plunge, comparable to slickensides in identifying the relative vertical movement of opposing sides in these oblique-slip faults, and these are summarized for the oblique faults in WWF1 and MF in Figure 61. With these NW – SE oriented dextral strike-slip faults a NW plunging plane along the fault trend results in the SW plate moving down relative to the NE plate. These fault plunges in Qmt reasonably represent the behavior in Tp and have an advantage over slickensides in that the latter often only record the latest fault movement since each subsequent movement tends to overwrite prior slickensides. In contrast, these discreet planes represent a series of fault movements that allow the measurement of varying attitudes for each of the faults that can then be combined with a fault sequencing to record a history of fault movement.

Fault motion in the Tp gouge zone is typically subvertical as evidenced by the vertical foliation of the gouge with foliation planes parallel to fault trend. The dip for the MF gouge is 85^{o} SW $\underline{+}$ 7^{o}, and for WWF1 50^{o} $\underline{+}$ 10^{o}, the latter is not strongly vertical but that doesn't significantly change the argument. If the top of the Purisima wavecut platform and the gouge are relatively coplanar, such as would be assumed immediately after it was abandoned at about 50ka, the fault initially proceeds sub vertically into Qmt, as depicted schematically in Figure 62b. With subsequent fault motion (earthquakes or creep) a vertical offset develops due to the fault obliquity as illustrated in Figures 62c and d. The reason there is a vertical series of oblique faults in Qmt is that the motion for these faults that transition into Qmt is confined along the side of the gouge zone that is rising relative to Qmt, Figure 62c. This is essentially by definition otherwise there wouldn't be a vertical offset recorded along that plane plus in the two cases observed this plane appears to be along one edge, the southwestern edge, of the gouge zone. Assuming the sense of the fault remains the same, in the case of Figure 62c that is dextral with southwest side moving down, the two sides of the oblique fault continue to separate vertically after each earthquake and that difference eventually becomes large enough that the new fault proceeds into the Qmt from a new higher location, hence producing a vertical series of faults. This is seen for both MF and WWF1, Figures 43 and 52, respectively, and is schematically depicted in Figure 62c.

The faults that emanate from the side of the gouge proceed into Qmt at an oblique angle from near the upper-middle of the rising gouge wall as outlined in Figure 63. The reason for that relates to the fact that Qmt is weakly consolidated and there is a vertical offset in the bedrock. The force required to move particles is transmitted from the last solid bedrock surface through the sediment and will drop off roughly as the inverse of the distance (to some power near 1) in a plastic-behaving material. The fault line is established where the opposing forces are equal and opposite and where the total differential shear is greater than the internal friction as schematically depicted in Figure 63. This implies it will turn to propagate into Qmt from along the side interfacing to Qmt and it will propagate obliquely such as shown in Figure 62c. This also means it will generally start into Qmt closer to the top half of the exposed gouge than near the Tp on the lower side because of their respective distances from the last fixed surfaces on each side. The sediments overlying Tp, Qmt-ITs, are substantially poorly consolidated sand, but the upper deposits, Qmt-cls and the gravel layers, contain more clay and are noticeably more cohesive so the internal friction coefficient actually increases vertically and may be a reason the fault line tends to bend over as it rises in many cases, even proceeding sub horizontally for some at WWF1 and proceeding along the base of a lithology transition. Eventually the total transmitted differential shear forces will drop to less than the internal friction and the fault line can stop before it reaches the surface, as observed for the majority of these fault lines. Thus, even for strike-slip faults with substantial horizontal offset, it is not necessary for the fault to reach the surface and in these cases it seldom does.

A quick, simple demonstration confirms that fault movement does, in general, project obliquely into loose sediment. Two adjacent, but vertically offset, “bedrock” boards were covered by fine gravel and it was confirmed that a lateral “bedrock” motion involves motion into the sediment projecting obliquely into the sediment above the lower bedrock side just as evidenced in these faults in Figures 43 and 52. So this configuration of oblique faults in Qmt may be considered at least typical and probably indicative of strike-slip motion, or more precisely oblique-slip, in poorly consolidated deposits with a vertical bedrock offset. *{A corollary is that an oblique strike-slip fault orientation in sediment can indicate a fault coming from a bedrock fault with a vertical offset and further indicates which bedrock side is lower without having to expose down to bedrock – a likely useful observation, if further verified at additional fault sites, when doing geotechnical trenching studies. That is, if a strike-slip fault in poorly consolidated sediment is found to be at an angle of about 30 to 60^o then it may be inferred the bedrock below this has a vertical offset and the side below the direction of slope is the lower side.}*

It should be pointed out the form of the force balance equation in Figure 63 predicts a parabolic shape with the fault further from the interface bending vertically up toward the surface in a homogeneous deposit. This is because the equation in Figure 63 is strictly for the case before a fault begins propagating in Qmt. Once a fault starts propagating it reduces the communication of the forces across the fault and the effect is to tend to cause the fault to continue propagating in a straight line. Basically, it replaces a static friction with a much smaller dynamic fraction. This is, of course, typical for all faults, but more pertinent in this case because the force causing faulting is emanating from the bedrock and is poorly transmitted through the unconsolidated layers. In the faults at MF and WWF1 they do not bend upward, rather generally continue at the same angle into the Qmt or actually bend over and become more horizontal. So, Figure 63 is for starting the faulting near the gouge/Qmt interface, but once in Qmt it will continue in nominally a straight line near the angle as initiated.

Of course, if the fault propagates up through the middle of the gouge zone and exits where there is no vertical offset between the two sides then it is expected to propagate sub vertically into Qmt, which is also what is found in these faults. For instance, directly above the gouge zones for both MF and WWF1 there are faults that extend sub vertically into Qmt where the two sides of the fault are nominally at the same elevation in Tp or Tp gouge as seen for MF in Figure 43 and for WWF1 in Figure 53. In other words, the faults at WWF1 and MF behave, not surprisingly, as expected for strike-slip faults.

In contrast, the faults above WWF2, where the two sides of the fault are not vertically offset, project into Qmt at several angles and in both directions, Figure 51. There are little or no vertical offsets or horizontal lithology changes along these WWF2 faults either. This suggests WWF2 is likely a result primarily of folding with very little strike slip, this is supported by the change in dip of the wavecut platform going from about 15^{o} NE between WWF2 and WWF1 to about 3.5^{o} NE east of WWF2, Figures 9 and 51, while there is essentially no vertical offset or lithology change across the fault. This is further evidence WWF2 is likely a fold spur from WWF1 as depicted in Figure 9.

It can further be noted the angle of this wavecut platform on the west side of MF is currently sub horizontal, indicating the 3.5^{o} dip on the east side of WWF2 has been eliminated by the time it gets to MF, likely due to the recent west side rising behavior of MF. The progression of this dip deduced from these behaviors is included in the sequence of Figure 62. Namely, at the abandonment of the wavecut platform, Figure 62a, it would be expected to be sloping seaward about 3^{o}. As MF events proceeded with east side rising this would be expected to reverse and become a gradually increasing landward tilt as shown in Figures 62 c and d. This behavior is in keeping with the high landward tilt seen on the east side of WWF1 which by that time would be well developed. Later, the sense of the oblique motion on MF changes, depicted at Figure 62e, which is likely coincident with the transition to a crossing fault on the northern end of PPB as discussed in the next section. This Tp/Qmt interface tilt angle continues decreasing as the west side rises and eventually becomes sub horizontal as seen currently.

There are several small offsets in the series of LAAF faults on the order of a few mm, seen as item 4 in Figure 47. These arise from compression as the gouge intrudes Qmt on subsequent events deflecting the previous faults slightly due to compression shifting sediment near the gouge interface and less so further away, which in some cases also cause connecting sections between adjacent gouge paths, faults B and D in Figure 47, suggesting part of the fault paths are reactivated and reconnected with others. Effects of compression, and subsequent density variations in the sediment, are also evident as compression arcs in the sand at the interface between the advancing gouge and the Qmt-ITs, seen as item 3 in Figure 47.

Faults for WWF1 also show an oblique angle transmission into Qmt and subsequent faults begin from higher locations along the gouge zone. However, for WWF1 the faults do not coalesce to one fault further from the gouge zone, Figures 52 and 59. This is because the plunge for WWF1, Figure 60, is relatively constant and always dipping the same direction, compared to MF, Figure 58. Figure 61 is a proposed sequence explaining fault progression with each subsequent offsetting earthquake.

The sequence proposed in Figure 61 assumes the lowest faults generally formed earlier in the history of the fault motion and the higher faults later. [The fault labeling for WWF1 is A at the bottom, F the top, but for no good reason MF is the opposite.] In Figure 61 the plunge for WFF1 is relatively constant for all faults and in the range of 4 to 12^o to the NW. the plunge angle for MF starts, similar to that for WWF1, to the northwest about 9 - 14^o for the earlier fault motions then consistently rotates until it is above 10^o to the southeast for the later motions.

The lowest fault, F in Figure 47, is found to bifurcate in the planes along fault trend, labeled F1 and F2 in Figure 58. It is likely F2 was a reactivation of the F fault after the fault plunge reversed and the east side started coming back down relative to the west side and is the reason for the later F2 assignment in Figure 61.

The fault MF-B is noted in Figure 58 to intersect both faults MF-A and MF-C. This crossover fault is likely a continuation of either one or both of these two faults so it is expected that it should follow the same plunge during the same fault movement. Thus, from Figure 58 it appears the trend is likely either along 312^o, if it was coincident with fault C, or 321^o, if it moved with fault A. These azimuths are reasonably close to the overall fault trend of 319^o, so for a short segment can be considered reasonable. It also confirms the plunges may vary slightly from that shown in Figure 61 but is expected to be within a few degrees.

Earlier it was noted that WWF1 appears to have been active prior to MF for a few reasons including the difference in surface topology above the faults, thus the expected sequence in Figure 61 is for the WWF1 faults to first exhibit a consistently NW plunge, lowering the SW side of the WWF1 fault as is currently observed. Then movement shifted to MF and the initial plunge continued to the NW. Eventually MF plunge transitioned to horizontal then to a SE plunge that reversed some of the SW side down offset, eventually causing fault F to be reactivated as noted. There are other faults not listed in this sequence, some lower in the strata along MF that are covered and have not been measured, and there are faults above MF which are subvertical so cannot be similarly oriented, but which are likely later since they continue the SW side up movement of the later events in Figure 61. Even though the NW plunge was only shown for the initial phase of MF, it had been long and large enough to produce the current SW side down configuration for Tp. There is at least one lower fault not measured along this wall, which would have been earlier, and would thus be assumed to have been NW plunging. Recall that the most recent fault on MF appears to be a subvertical fault above the gouge zone that did exhibit a small amount of NE side up in keeping with a continuation of the plunging to the SE. Slickensides observed in the clay gouge diapir above the MF also confirm a SE plunge of ~ 10 – 17^o in agreement with this analysis of recent fault movement. The Qmt-mgr layer also slopes up, Figure 43, indicating a SE plunge of the fault, as it enters the fault zone and disappears, apparently eroded off, as depicted in Figures 62f and g, where it reappears on the west side of the LAAF faults much lower, indicating overall a net SW side down.

This reversed motion of the fault plunge is likely the cause for the concave surface expression seen in the profiles in Figure 14 and 16 for the surface east of the MF. This vertical movement would also have reduced the vertical offset in Purisima so we can assume the maximum vertical displacement, with the currently observed southwest side down, occurred earlier in the fault progression and was likely several meters larger than for WWF1.

As a point to consider, it should also be pointed out that since the southwest side of the fault is gradually tilting to a higher angle as the western plate moves up the restraining bend of PPB, as we discuss below, then the earlier fault paths will also be seeing additional tilts during the later stages of fault motion and one might ask if that contributes to the apparent shifting plunge. However, the tilts in the folding direction are in the dip direction (northeast – southwest) and not significantly in the plunge direction (southeast – northwest) so the interaction between the two can, to at least first order, be considered negligible.

Another observation, the cause for some curiosity, is that the oblique faults in Qmt (and most of the subvertical faults as well) do not extend to a surface. They can, and do, just stop after some propagation distance as indicated by the internal friction term in Figure 63. Their paths have not been obscured nor is there an unconformity. Propagating a force in unconsolidated sediment involves displacement of grains in a plastic deformation which distributes the total displacement along its length, resulting in a scissor motion (a strike-slip earthquake would be equivalent to opening a scissors) with maximum displacement occurring at the sediment/bedrock interface and then decreasing until it goes to zero at some distance from the interface. This is undoubtedly well known but has been here learned again. The effect is not too dissimilar from “pushing a string”. Eventually the forces propagating upwards through the sediment become weaker than the internal friction and movement stops as depicted in Figure 63. For a fault extending into Qmt the net lateral offset on the fault is distributed over the length of the fault trace so it may not reach or even be particularly noticeable at the surface. All of the faults that extend obliquely into Qmt at MF, WWF1, and WWF2 trail off and become untraceable at a distance of about 3 to 8 m from the Tp interface. A simple geometric consideration of the constraining mechanics suggests that for an unconsolidated, uniform, homogeneous sediment the angle of the opening scissors is unlikely to get over about 60^o, (for example, consider shifting from one quasi-stable configuration to another in a stack of spheres), suggesting 1.2 X length of the fault line should be a ballpark estimate of maximum fault offset. This equates to roughly 4 to 10 m offset for most of the MF and WWF1 faults, reasonably consistent with the earlier estimates above. Better modeling of the mechanics of the Qmt sediments might thus better constrain the typical offset per event by measuring the length of the fault line, perhaps a useful future effort.

We may also roughly constrain the number of earthquakes (or “episodes” if we allow the possibility for periods of creep) by counting fault lines in Qmt. It is not known if each trace in Qmt represents just one event, or if one trace can represent multiple events, but it is clear that at least in some cases multiple fault lines coalesce to just one trace, Figure 47, so it is reasonable to assume multiple events can and do share traces. We assume that only one of the narrow sub-parallel fault planes in Qmt is active during any given earthquake (or creep interval) and that the narrowest lines represent one fault movement and wider gouge traces possibly represent more or larger events. For instance, there are six LAAF faults in MF (counting the crossover fault lines), two at the small diapir, at least 16 narrower fault lines above the MF with some wider than others, and one lower than the LAAF faults on the west side of the fault gouge, about 25 total. The LAAF fault traces are wider than the faults above the gouge zone, on the order of about a cm compared to about 1 - 5 mm. Fault width would relate to either the magnitude of the events or number of events activating the same fault lines. If fault width is taken as an indicator of number of events passing through each fault path, and we assume the narrowest paths in Qmt directly above the gouge zone are one event each then the total number of events on MF since the marine terrace was formed would be at least 25 and could be on the order of 60 – 150. There is a possibility one event could produce multiple fault paths but that seems likely to be more than compensated by many more faults reusing the same paths. For the west wall faults there are seven oblique faults included in Figure 60, there are another approximately 5 smaller, lower ones not included, plus 5 - 8 subvertical faults adjacent WWF1, another 7 for WWF2 and an unknown number for FWWF, for a total on the west wall faults around 30 to 150. The EWF is not characterized, and while it may be reasonable to assume a similar number as for the other two we also recognize that EWF may be dip-slip so we do not include its estimated number in our total number of strike-slip events. A total for the Middle Strand on the order of 70 - 300 events might thus be indicated. Based on a 50 ka Qmt age implies a recurrence interval on the order of 700 years (if each line represents only one event) to 200 years (if some fault lines record multiple events) slightly less but in rough agreement with results of Simpson et al (1997) (<1100 years inferred) and Koehler et al (2005) (1037 -2500 years), Table I, and in line with the 400 years for M>6 events suggested by the Working Group on Northern California Earthquake Potential, 1996, (USGS ofr 96-705). The Koehler results relate to larger faults that would record subsidence at the slough and the Simpson estimate also relates to the larger faults that reach near the surface while the magnitude of the events forming the fault lines here observed is not so constrained. These are rough approximations, dependent on the unknown number of events that might recur along the same fault lines but suggest the recurrence interval could be as low as a couple hundred years or lower. A more careful quantification of that interval might be worthwhile for earthquake preparedness.

During excavation a small right lateral strike slip offset of .15 m was noticed directly above the larger diapir, Figure 56. A fault line going directly between the two offset clay peaks and the reconstructed clay figure matches both sides well. Figure 56 is a plan view of part of the floor and part of the wall during excavation showing what would later be recognized as the very top of the larger diapir in Figure 48 with two sides of the very top of a small extrusion right laterally offset by .15 m. This is the one clear data point confirming the right-lateral strike-slip nature of the MF fault with a small offset that goes through the diapir and it is this fault that is traced to the surface shown in Figure 49, thus likely a more recent event for the MF (the EWF appears to have had the most recent events). The .15 m displacement suggests a very small earthquake, or alternatively about 60 years of creep, and by itself is unlikely to have reached the surface where it becomes much wider, plus carry the numerous clasts 4 m up through the adjacent sediment as noted above suggesting even this very narrow fault line must have experienced multiple reactivations. All of this suggests a relatively frequent recurrence, quite likely less than 200 years, which is surprising given the lack of a historic fault being recorded on this section of the SGF-E, perhaps another indicator of possible aseismic creep, or faulting that is becoming locked (see Appendix E for more discussion of the fault becoming locked).

A likely sequence of faults and stratigraphic events through the Middle Fault can now be proposed as schematically depicted in Figure 62 for the MF exposure in the middle of Pillar Point Bluff. Figure 62a is the situation after the wavecut platform is abandoned and covered with marine terrace deposits. Here only the intertidal sand, Qmt-ITs, which grades upward into a clayey sand layer, Qmt-cls, and the gravel layer, Qmt-cGr, are shown above the Purisima with its planarized fault zone. Any other deposits that may have been above this have since been eroded. The wavecut platform would be sloping oceanward about 3^o. Faults at this time would propagate from the gouge subvertically into Qmt, Figure 62b. The oblique fault motion included an east side rising component which eventually produced faults propagating obliquely into Qmt as discussed above and depicted in Figure 62c. Some of the faults were large enough and extended far enough into Qmt to intersect, and offset, the Qmt-mGr layer as shown in Figure 62c. In addition, another layer, Qmt-fGr, that would have been deposited south of this site moved into the current latitude by right lateral transport. Exactly when that layer appeared at this latitude is unknown, it could have been later in the sequence than shown.

At some point one or more of the earthquakes with east side rising produced a large vertical surface step that filled with aeolian sand around the LGM, depicted in Figure 62d. The oblique sense with east side rising continued during this phase and caused a substantial vertical offset, at least 1.6 m more than the current 2-3 m vertical offset. This oblique sense eventually reversed direction and began west side rising resulting in some of the LAAF retracing the vertical offsets and causing them to coalesce, Figure 62e. The fault motion subsequently moved slightly landward, with traces coming from above the fault gouge and was attended by diapirs of gouge protruding into the overlying Qmt as shown in Figure 62f. During these motions, the sense is still with west side rising except now the west side includes some of the section that previously was on the east side of the fault. This produced the vertical ductile deflection of the Qmt-mGr layer as shown in Figure 62f. Eventually more of the upper layers were eroded and overlain by developed soils as shown in Figure 62g which left a gap in the mGr layer between the section above the east side of MF and the down-dropped section of mGr west of the LAAF faults. Subsequent faulting, shifting slightly further eastward, occurred mostly up through the fault gouge exiting subvertically through the top of the gouge with at least one of the faults piercing another gouge diapir and reaching the soil level, still with west side rising, as shown in Figure 62h, the configuration as currently found. Ever since the obliquity changed directions at Figure 62e the slope on the ocean side of the fault was reducing its landward tilt to now become flat.

Middle Strand Fault Sequence:

Besides the sequence of faults within Qmt of the previous section, the sequence of overall fault activity throughout PPB includes several constraints which will be discussed here in conjunction with a proposed overall fault sequence.

An expanded view of the top of the landslide headscarp perpendicular to the long axis of the bluff in Figure 16 shows a noticeable change in slope of the bluff surface above both the EWF and the MF with very little change above the western faults. The profile taken just south of the large landslide headwall shows a similar behavior, Figure 14. In addition, the magnetic anomaly scans in Figure F6 also show larger amplitude and width anomalies above EWF and MF than above WWF. As discussed in SI-F these suggest the EWF and MF movements have occurred more recently than the western faults which, even though the vertical offset of the Purisima is larger for WWF1 than for MF, have noticeably smaller surface expressions. Because two surface cracks in the EWF system, Figures 41 and 42, and one fault in the MF system are traced to the soil layer, Figure 49, and none of the WWF components are traceable to or even near the soil layers, Figure 52, this also suggests the eastern faults were more recently active. Indeed, the expression of the faults in Qmt suggests a relatively consistent trend eastward over time, Figure 61, with the East Wall Fault being most recently active. The WWF likely moved mostly before the deposition of Qmt with only the end of that fault activity occurring after the deposit of the marine terrace sediments. There is a noticeable reduction in thickness of the soil A Horizon from east to west along the southern headscarp of this large landslide basin, Figure 16, that might be considered inconsistent with this timing, however, that is likely related to the surface slopes being steeper toward the coast, Figures 14 and 16, and therefore surface erosion keeping the soil layer on the steeper slopes thinner.

South from PPB two faults are traced in the seabed, extensions of the west wall fault and the middle fault, Figure 8. The MF trace is continuous across Half Moon Bay to where it goes ashore near Tunitas Creek to become one of the Ano Nuevo on-land segments, Bryant and Cluett, 1999, while WWF is traced south only about 4 km, Figure 8, suggesting the MF is the main trace of the Middle Strand and WWF is a stepover spur that reconnects with MF about halfway up PPB. This spur appears to have been active during the early phase after Qmt was deposited in MIS 3, and motion along MF continued after the WWF phase abated.

The granitic bedrock in the Seal Cove Highlands is assumed to be responsible for diverting the SGF-E into a restraining bend and the restraining bend in turn was responsible for the uplift that preserved the MIS 3 wavecut platform. The subsequent compression against this granitic obstruction then caused the visible folding southwest of the fault. At the same time, this granitic obstruction, which originated from the northeast side of the fault, also exerted a force on the eastern plate, here called the Pilarcitos Plate, as explained in Appendix E. This force produced an extensive force on the Pilarcitos Plate southeast of the granitic obstruction and a compressive force north of it which were the causes of the Half Moon Bay Syncline and the Moss Beach Syncline, respectively, as explained in SI-E.

The Fitzgerald Bluff (or Fitzgerald rise) on the NW corner of Fitzgerald Marine Reserve, Figure 2, likely experienced uplift from compression just like Pillar Point Bluff based on a similar structure, so this would likely have occurred when the fault path proceeding NW from Seal Cove was active and applying compression to this uplifting section. In that case the Fitzgerald Bluff would likely have been a continuation of PPB as proposed in Figure 64. This figure shows that when the Fitzgerald Bluff is shifted back about 317 m along the Distillery Fault its eastern scarp aligns with the eastern scarp of the northern end of the PPB, the orange dashed line in Figure 64. Whether the alignment of the Fitzgerald Bluff scarp should be to the Seal Cove Highlands eastern scarp, with its granitic bedrock, or to the scarp determined from the Purisima bedrock section further south as shown by the blue dashed line in Figure 64 is not clear and will be discussed further in the offset estimate section below, but both coincidentally show a similar projected pre-offset location. Note, the west side of this Fitzgerald Bluff would have originally extended further southwest than shown, likely to the black dashed line fault, since it has been a quickly eroding sea cliff, however the protected northeastern scarp will not have changed appreciably.

The motion of the crossover faults, and the Distillery Fault in particular, subsequently created the Seal Cove Lowlands' pull apart basin separating Fitzgerald Bluff from the Seal Cove Highlands and Pillar Point Bluff, Figure 35. Thus, the bluff with its Qmt deposits must have formed first, then the crossover fault separated it from PPB resulting in a halt or slowing of the uplift of Fitzgerald Bluff which now has lower average and peak elevations than PPB. Since the bluff appears to have the same, or similar, wavecut platform, it is assumed the deposits are the same age so all of this must have occurred since MIS 3. In principle, the timing when separation started can be estimated based on the elevation difference between the Fitzgerald Bluff and Pillar Point Bluff, but the uncertainties for MIS 3 msl, the elevations, and the alignment of bluffs is so large that it is felt such an exercise is not productive except to note that the time to produce the elevation difference and the time to shift the Fitzgerald Bluff to its current location can be overlapping based on the range of rise rates and strike-slip rates so this scenario is likely although its timing is uncertain.

There are two estimates possible for the horizontal offset along the Distillery Fault, one from realigning the eastern scarps of the Fitzgerald and Pillar Point Bluffs as suggested above, the other from estimating the distance the NW extension of MF has shifted along the fault, Figure 64. The former is on the order of 317 m, the latter around 160 m, with large uncertainties. These estimates are generally less than the estimated horizontal slip along the MF fault of 326 m since MIS 3 as determined below in Appendix D, Figure D27, so it would be reasonable that there was an early movement along the NW extension which subsequently shifted in a crossover to the Fitzgerald Fault.

The Montara granite and the Purisima bedrock elevations in the Seal Cove Highlands is quite irregular per the findings from borehole drillings in Leighton et al, 1971, yet the Qmt surface shows only minor short term topology relief in the same area suggesting the activity causing bedrock relief must have occurred early enough to allow the Qmt surface to have eroded flat following it, Figure 35. The WWF reasonably aligns with crossover fault 2 of the releasing bend faults suggesting they may have been coeval early, possibly a continuous shear formed in conjunction with the granitic obstruction. The Distillery Fault is recently active judging from Simpson et al, 1997 and modern subsurface motion induced damage. Thus, crossover fault activity appears to have occurred along the eastern strands first, with the western component, principally the Distillery Fault, exhibiting the latest movement.

Thus, a sequence of fault activity along this section of the SGF-E would likely contain the events outlined in Figure 70. The red lines in Figure 70 indicate the more active fault paths, the green lines indicate a path that has become less active. The folding and extension are shown schematically by the gray lines. At some point, likely long before 100 ka, the Montara granite contacts the SGF-E path as depicted in Figure 70a. Initially the fault is likely to deflect around the stronger granitic bedrock and continue to pass through the Purisima fm. As the Km protrusion translates further into the fault path that path eventually switches to a northeasterly path as indicated in Figure 70b. This is the path currently seen trending northwest from Seal Cove which has been found to reconnect at depth to the more easterly path, Ryan et al, 2008. This is the beginning of a restraining bend that causes compression resulting in uplift of PPB, which at the time depicted in Figure 70b includes the Fitzgerald Bluff on its northwestern end. At the same time, on the Pilarcitos Plate extension is starting to occur southeast of the obstruction causing a gentle syncline to form, the beginning of the Half Moon Bay Syncline.

Further compression subsequently causes crossover faults to form that redirect the northwest trending fault motion back over to its prior path north of the granitic obstruction, Figure 70c. The timing for these crossover faults, at least along the Distillery component, appears to be around 20 to 40 ka. Note that this will also change the stress condition south of the crossover fault and is likely the cause for the change in the oblique sense of motion on the MF. As mentioned above in the discussion of Figure 61, MF switches from east side rising to east side falling about halfway through the sequence of faults expressed in the LAAF zone. Exactly how the stress condition changes in the area of the fault exposure south of the crossover faults depends on what happens at depth in the two northern paths. For instance, as seen in the Ryan et al graphs, Figure 7, the western fault has a shallower east dip than does the eastern component, as is needed if the two connect at depth. Thus, as the Pacific Plate moves north it will switch to a less east-dipping fault to the north when the crossover faults are engaged and this would in turn likely change the fault oblique sense south of the granitic obstruction from east side rising to west side rising, just as is confirmed in Figure 61. Thus, the sequence of fault plunge in MF is likely correlated with the timing of the crossover fault formation. Even if the dip at depth is not the cause of the change in the sense of plunge it is nevertheless likely that the change to a crossover fault path is the change that produced such a plunge change.

As motion along the crossover faults proceeds it then translates the northern component of the bluff, the part that becomes the Fitzgerald Bluff, northward, Figure 70d. Both the Fitzgerald Bluff and PPB eventually experience erosion on the west side of the bluffs when the sea level rises back up to an elevation where it comes into contact with the elevated terraces. The granitic obstruction in the SGF-E path causes distortion in the Purisima layer on both sides of the fault as depicted in Figure 70d. The offshore folding continues until it produces the current form seen west of the PPB, and coevally the extension in the Pilarcitos Plate continues until it produces the current Half Moon Bay configuration. After the Fitzgerald Bluff separated from PPB it would no longer be under compression and its uplift would slow or stop and indeed, its current peak elevation is considerably less than for PPB, as expected. The force on the granite protrusion is also likely to cause a fault in the granite on the Pilarcitos Plate as schematically depicted northeast of the obstruction in Figures 70 b, c, and d. This is suggested to align the shoreline granite fault, Figure E13, with the Dennison Creek Fault.

These crossover faults become part of a typical releasing bend duplex along with other faults as shown in more detail in Figure 17, with one of its features being the formation of a graben, the Seal Cove Lowlands. Only the Distillery Fault is included in Figure 70 which appears to be the principal currently active crossover fault. To the north the two faults, the Fitzgerald Fault and the currently less active northwestward extension of the MF, still rejoin at depth and constitute the SGF-E branch in Figure 7. Figure 70 schematically illustrates the development of the principal features of this restraining/releasing duplex section of the SGF-E although it does not include several details such as the subparallel WWF, EWF, and SCF faults to the south, which combine to form a positive flower structure, and the additional crossover faults discussed in the mapping section above, which combine to form a negative flower structure. It does depict the coupling of the offshore folding with the formation of the HMB syncline which is expected due to their similar cause and is further developed in Appendix E.

Offset and Slip Rate Estimates:

There are eight geomorphic features providing possible piercing points or information on horizontal fault offset that will be reviewed here, although few are well constrained. Table IV lists the possibilities and Figures 64 and 65 map locations for five of them. Offset estimate A in Table IV is unusual but is the best constrained and is the only one that includes offsets from all components of the Middle Strand whereas the others, besides being less well constrained, only cover one of the component faults of the Middle Strand. Piercing point A will be discussed in detail below, however, the others will first be briefly reviewed.

Table IV: Offset and slip rate estimates due to several piercing points. Upper value is mean estimate, lower is 68% range where known (±1 sigma where appropriate).

Piercing Point	**Fault Component**	**Offset estimate, meters**	**Time Frame of offset, kya**	**Slip Rate mm/yr**
A. Rotated wavecut platform	**SGF, Eastern strand**	**326** **(264 – 393)**	**49.7** **(45.4 – 54.4)**	**6.5** **(5.2 – 8.0)**
B. San Vicente Creek offset (path 1, Fig 65)	Fitzgerald Fault	>~ 200 > (180 – 300)	< 54 < (45 – 54)	> 3.3
C. Fitzgerald Bluff offset along Distillery Fault (Fig 64)	Distillery Fault	224 (134 – 346)	< 54	> 2.5
D. Fitzgerald Fault with slickensides (path 2, Fig 65)	Fitzgerald Fault	57 (30 – 125)	< 54	> 0.6

E. Gouge diapir (Fig 56)	MF of Middle Strand	.15 ± .02	-	-
F. Granite bedrock (path 3, Fig 65)	Seal Cove Fault	TBD	-	-
G. Granite bedrock (path 4, Fig 65)	Releasing Fault 2	- (340 -1000)	> 59	< 17
H. Offset S. of PP offshore	WWF	(150 – 460)	-	-

Piercing point B is a tectonically induced San Vicente Creek offset at the northern end of Fitzgerald Bluff. The Fitzgerald Fault exposure is just east of where the creek enters the sea and from the geometry of the fault path and the San Vicente Creek it is apparent the creek, approaching from the east, was deflected to the northwest by the offsetting fault and rising bluff, path 1 in Figure 65. The Fitzgerald Bluff rise is assumed to begin coeval with abandonment of the PPB wavecut platform, namely 50 ka. However, the timing for the start of the crossover faults is uncertain, and likely later than the abandonment of the wavecut platform. In that case the minimum offset of 200 m (180 – 300) over a maximum of 54 kyrs produces a minimum slip rate around 3.3 mm/yr. However, the current creek path enters the sea at about a 25° angle to the fault and adjacent a northwest facing seacliff such that any northern limit to the westerly continuation of the creek path is lost to erosion in the tidal zone and is thereby unable to provide an upper limit and even the minimum offset is not particularly reliable since there is no local stream curvature suggesting the onset of a westerly bend through a rising bluff.

Piercing point C is the motion along the Distillery Fault causing the shift of the Fitzgerald Bluff shown in Figure 64 which would have occurred after the Qmt deposits were uplifted and after the Distillery Fault became active. The Fitzgerald Bluff appears to have been an extension of Pillar Point Bluff in which case its northeastern scarp is assumed to have formed when PPB formed and is assumed to have been reasonably aligned with it as indicated by the orange dashed line in Figure 64. It would then have shifted northwestward along the Distillery Fault, shown by the red arrow in Figure 64, producing the Seal Cove Lowlands graben as it went. This piercing point at least provides both a minimum and a maximum offset. Besides the measurement uncertainty for piercing point C there is also a configuration uncertainty. The orange line in Figure 64 aligns with the northeastern scarp of the Seal Cove Highlands that is likely underlain by granitic bedrock, as discussed in the sedimentology section. All indications are that Fitzgerald Bluff is underlain by Purisima as is all of PPB southeast of the Seal Cove Highlands. The granite bedrock appears likely responsible for the lower elevation rise of the Highlands as well as the eastern scarp extending about 110 m further northeast than the Purisima bedrock section just south of it, Figure 64. Thus, an argument can be made that the location of the Fitzgerald Bluff scarp should be aligned with an extrapolation of the Purisima bedrock section south of the granitic section. This is depicted in figure 64 where the orange dashed line aligns with the granitic bedrock section and the blue dashed line aligns with the Purisima section. Coincidentally, both nominally extrapolate to similar points along the Distillery Fault, but the uncertainty from the Purisima extrapolation is larger, Figure 67.

Another effect of this same fault movement is included in Figure 64 as the offset of the extension of the MF fault NW from Seal Cove. Once the Distillery Fault became active it would also have translated that fault northward as shown in Figure 64, from the black dashed line to the black dotted line. The black dashed line is an extrapolation of the MF mapping through PPB and contains a large uncertainty although the current path, the black dotted line, is well known, Figure 69. This offset is measured as 160 ± 50 m. Combining the two estimates of offset in a pdf, Figure 67, then produces a median of 224 m. As a point of interest, this estimated median is about 70% of the 326 m measured for the entire Middle Strand using piercing point A, suggesting most of the movement along the northern end of PPB has gone through the Distillery Fault since MIS 3. However, the timing of motion along the Distillery Fault is not established. It was earlier assumed the NW extension of MF was active when the bluff was formed with the Distillery Fault motion occurring later, however the most that can be assured is that motion of the bluff recorded along the Distillery Fault occurred after 54 ka since it has the abandoned wavecut platform and Qmt on top of it and even that would best be dated to confirm. It is also possible the offset of the MF extension fault and the Fitzgerald Bluff were not exactly coeval, but that uncertainty can be considered to be part of the offset distribution in

Figure 68. That's not formally exact but considering the uncertainties and that the result is not being used here anyway, it is reasonably illustrative.

The Fitzgerald Fault sea cliff exposure, piercing point D and Figure 5, must have passed through the San Vicente creek along path 2 in Figure 65, where it would have been eroded down to creek elevation and then subsequently regained about 10 m of elevation with reported slickensides of ~10° SE (Wiley, 1983) resulting in its current west side up vertical offset allowing a rough estimate of how far it has risen since crossing through the creek. A 10m vertical rise implies a horizontal offset of about 57 m. Besides an estimated uncertainty of ± 5° in the slickensides, both the Half Moon Bay Terrace and the bluff to the west have been rising since the wavecut platform abandonment so that provides an uncertainty to the elevation gain since the fault passed under the San Vicente Creek. The sediments above the Purisima on this fault exposure have not been separately dated so we currently assume they were deposited after the wavecut platform was abandoned but could have been significantly later. Thus, the offset and slip rate for this path provides only a minimum and it only covers the Fitzgerald Fault component of the SGF-E.

A fifteen cm offset encountered during excavation on top of the clay gouge diapir in the main fault, discussed above in regard to Figure 56 and constituting piercing point E, clearly indicated the Middle Strand was primarily right-lateral strike-slip, but doesn't allow an estimate of the time of occurrence other than it likely occurred before the MRE determined by Simpson et al, 1997 if it resulted from an earthquake. If it was caused by creep, a possibility considering its very small offset, the time frame is unconstrained. There are several small faults (greater than 16 with less than 1cm wide gouge in Qmt at MF and relatively small or no vertical offset) similar to this one that were exposed above the main fault gouge, Figure 56, and while it is believed these have been among the more recent faults to have occurred there is no constraining timeline for that sequence.

A wedge of Montara granodiorite that underlies a small section of Pillar Point Bluff, Figure 65, (Leighton et al, 1971), has the potential to provide offset estimates as piercing point F that could prove instructive. It abuts one of the releasing faults and extends to at least the Seal Cove Fault providing the unique possibility to inform about both the releasing fault and the

Seal Cove Fault. It currently opposes Purisima sandstone along at least 340 m of one of the releasing faults (path 4, Figure 65, which is also coincident with one of the Leighton lineations) while exhibiting minor geomorphic surface expression, suggesting very little recent activity, although it is well delineated by consultant faults in Qmt indicating it has responded to tectonic motion since MIS 3. It is unclear how far it extends into Pillar Point Bluff, nor is it known if it stops at the SCF or proceeds out onto HMB terrace. There is an upper limit of about 1km offset along the releasing fault because there is exposure of Purisima on both sides of this fault in the large landslide area. The time frame when it was actively causing the granite offset is unconstrained, although it most likely occurred much earlier than 59 kya but less than the age of the Purisima of about 2Ma. It provides only an upper limit for slip rate, and that is very large. Its main contribution is to suggest it could provide key information about the SCF and this releasing bend fault if it were better constrained, such as by gravity or magnetic measurements. Appendix F contains magnetic anomaly scans that offer support for the granite extending onto Half Moon Bay Terrace and connecting to the granite outcrop along the northwestern shore of Moss Beach but is not yet definitive. [It does suggest that this releasing fault may have been a significant strike-slip fault at one time. Intriguingly, this fault is reasonably aligned to the southwest with the West Wall Faults that, as mentioned previously, were earlier active faults of the Middle Strand and northward it extrapolates to the western edge of the granite outcrop along the shore.]

Piercing point H is along the WWF strand that extends south of Pillar Point, Figure 8. It is not very precise, covers a wide possible offset range, and there is no timing constraint. It does suggest that the west wall faults may have experienced up to about 460 m total offset in the process of forming a 1.7 m wide gouge zone at WWF1 and an unknown amount at FWWF.

One more offset estimate that was checked but not included in Table IV is mentioned here for completeness and can be noted in Figure 30. The ratio of granitic to sedimentary clasts in the gravels is a strong function of its distance south along the coast so a difference in provenance of the gravels on two sides of the fault could be expected to show a corresponding difference depending on how far they have offset since being deposited. Over 200 clasts were measured at each site along the coast, and about twice that at the fault sites. Interestingly, the value suggests they both are similar to others several km south, but some of that difference is likely due to PPB being further from the foothills where granitic fan deposits would originate. That distance is difficult to define plus a regression of the residuals from Figure 30 on that distance from the foothills shows a rough dependence but with much more scatter than seen in Figure 30. Perhaps of more relevance is that the difference in ratio of granitic clasts between the two sides of MF is .025 and that difference corresponds to about 230 m of offset using the coefficient for the fit to the other data in Figure 30. This is tantalizing close to what is found below. However, while the slope is relatively steep, the difference in ratios is still too small and the uncertainty too large to offer a statistical significance and so is not taken here as a realistic measure.

The primary offset estimate is obtained from tilting of the bedrock west of the SGF-E as the Pacific plate moves through the restraining bend. The marine terrace deposits making up the top layer of Pillar Point Bluff sit unconformably on a Purisima fm wavecut platform. That wave-cut platform exposed along the landslide headscarp where the faults discussed in this report are also exposed, Figure 39, is currently tilted landward several degrees, Figure 55, whereas it would have tilted oceanward when the wave-cut platform was abandoned. The Qmt layers above the Purisima in Figure 55, and throughout the exposure area, also show a similar landward tilt indicating the Purisima and all the layers above have undergone a similar tilt. Simpson et al, 1997 noted a similar eastward (landward) tilt of alluvial sediments, which they interpreted as an indication of a pre-unconformity (Holocene dated pond deposit on Qmt) tectonic activity. In their case the Holocene deposits occurred after most of the tilting had already occurred. In our case we note that tilting has actually been occurring ever since the wavecut platform has been abandoned (and, of course, likely before that). In fact, we currently measure the top of the Purisima to be tilted 4.5° ± 0.5° landward, and when we measure current Purisima wavecut platforms in the area we find, as shown in Figure 66, that they slope on the average 3.1 ± 1.2° seaward implying the wavecut platform has rotated 7.6° ± 1.3° since it was abandoned. Thus, as the Pacific plate was moving northwestward along this restraining bend the wavecut platform, along the west side of the fault, has been rotating landward. If there was a way of measuring how much it rotates for a given offset along the fault, that would then provide a way of quantifying how far it has slipped since the wavecut platform was abandoned. When we look at the dip of the bedrock along the shore on the west side of PPB we see that it does indeed record a change in dip as the bedrock has moved into the restraining bend and that is graphed in Figure 68. This shows a change in dip angle as a function of distance along the fault of -.0231 Deg/m, which implies that the 7.6^o rotation occurred over a nominal distance of 326 m, as indicated in Table IV, Row A. This estimate of offset is then combined with the dating of the Qmt deposits to provide the probability density function for the slip rate shown in Figure 69 and listed in Table IV.

Above it was stated this method of measuring the slip rate is the best constrained yet Figure 68 does not look very well constrained. Dip measurements of in-situ bedrock is not particularly precise and the length over which the measurements are made is only a couple hundred meters because it can only cover from the location adjacent where the faults are exposed southeast to where the WWF goes offshore and changes the tectonic configuration represented by the bedrock along shore. Thus, slope coefficients of about -0.01 to -0.1 could reasonably fit the data shown in Figure 68 which would imply uncertainties of around an order of magnitude. That was significantly improved upon by using much more data to estimate the slope dependence on distance along the fault than is possible with a short length of isolated dip measurements. Appendix D explains how all the data contained in the folded structure offshore adjacent this section of the fault is used to calculate a more precise coefficient and the result of that is -0.0231 $\underline{+}$ 0.0023, Table DI. Basically, the folding follows a clear pattern with the slope of the bedrock increasing along the fault as the plate moves up the restraining bend and the entire folded pattern is obtained from bathymetry data in USGS 2014-1214 and used in Appendix D to extrapolate the slope along the fault with much more precision than is possible from Figure 68.

Using the rotation of the wavecut platform is a non-conventional method of determining tectonic offset and will thus be subject to skepticism. Nevertheless, the method in Appendix D not only is reasonable, but the results are internally consistent and include data that provide independent verification and, perhaps most germane, it is the best constrained piercing point in the area and all other results in Table IV are consistent with it.

Appendix D presents the details of how the bathymetry is used to quantify the folding structure to give a more precise dependence of Purisima bedding angle on distance into the restraint. It uses bathymetry data from USGS report ofr 2014-1214 (Bretz et al, 2014) digitized along lines perpendicular to an azimuth of 319°, the trend of the MF Fault, and determines slopes of the exposed tilted resistant layers which are then used to reproduce the uneroded folded structure. That model calculates the structure from the measured slopes of all the layers on the three sections of folding covered by the bathymetry data, namely the SW sloping side of the furthest offshore anticline, the NE sloping side of the anticline to syncline transition, and the SW sloping side of the syncline to nearshore anticline transition, and along fault trend covers about 1 km of the restraining bend from the southern entry into the bend up to where the faults are exposed in the landslide headscarp and before the crossover faults begin. Besides the measured slopes of the exposed tilted layers several physical features are used to constrain the fit of the model to the exposed folded structure, those being the shortening it needs to accommodate, the known elevations of certain exposed layers as identified in Figure D8, and the plunge of the fold axes. The model then reproduces the fold surfaces as shown in Figure D9 that are then extrapolated to the NW sloping side of the near-shore anticline which is not covered by the bathymetry data. There is some complication in needing to account for erosion which causes the measured erosional surfaces to deviate from actual bedding surfaces, and the constraints mentioned above are used to compensate that as explained in Appendix D. The result is a plot of bedding angle versus distance into the restraining bend such as is plotted in Figure D17. The coefficient of a linear fit to that data provides the desired slope change per distance offset and is shown in Figure 68 to also reasonably fit the raw dip measurements. This coefficient, in degrees rotation per km of lateral offset, is then divided into the change in wavecut platform rotation, Figures 66 and 55, to obtain the offset since the wavecut platform was abandoned. The constraints mentioned above provide multiple ways to optimize the model fit resulting in four different model results which are combined in a probability density function, Figure D27.

A measure of the change in wavecut platform slope is required to translate the coefficient above to a lateral offset. The abandoned wavecut platform is currently tilting landward 4.5° ± 0.5, Figure 55. This is along a trend of 230° ± 12°, nominally perpendicular to the Middle Strand. Wavecut platforms are reported to typically slope from 1 to 4° seaward, Johnson et al, 2018. However, we take as a better local indicator the modern wavecut platform in this area with a Purisima bedrock and a sampling of those is shown in Figure 66 to give an average angle of 3.1° with a standard deviation of 1.2°. Together these produce an angle change of 7.6 ± 1.3 °.

The coefficients from the model and the change in angle both entail probability distributions which are then combined, as outlined by Zechar and Frankel, 2009, to produce an offset probability density function, Figure D27. The resulting offset since the wavecut platform was abandoned as summarized in the table in Figure D27 results in a median offset of 326 m with a 68.27% (nominally ± 1 sigma) range of 264 to 393 m and a 95.45% range of 205 to 466 m.

The probability density function, pdf, for the offset in Figure D27 is combined with the pdf for the age of the abandonment of the wavecut platform as discussed above and plotted in Figure D28, as outlined by Zechar and Frankel, 2009, to produce the slip rate pdf and cumulative probability distributions shown in Figure 69. The distribution shows a median slip rate of 6.5 mm/yr with a 68.27% range of 5.2 to 8.0 mm/yr and a 95.45% range of 4.0 to 9.7 mm/yr. These values are within range of previous estimates for the Seal Cove Fault, but now include better constraints for the age and the offset and represents motion along a more accurate assignment of faults along this section of the eastern strand of the San Gregorio Fault.

The digitization for the model was along lines perpendicular to the MF, which trends along an azimuth of 319°. There are components that appear both east and west of the Main Middle Strand, MF, in Figure 2, namely the WWF and EWF. The results above are for the total distribution across all these strands since the model calculation is for the east side of anticline 2 without consideration of how many faults take up the offset. The angle of the restraining bend and the shortening calculation depend on the fault path used and the shortening is one constraint on the compensation factor. For that we continue to use the Middle Strand since it is the most prominent, represents an average middle path, and can be traced south across Half Moon Bay. The traces for the other two do not extend as far so even if the local fault angle is slightly different the effective angle for the overall restraining bend from the south is that for the MF. However, if the EWF does not include strike-slip, which is unlikely but possible as discussed previously, then the model may underestimate the contribution of the WWF because that movement would be along a smaller restraining bend and thus not cause as much fold angle change with the result the total slip rate on the Middle Strand would be larger, roughly nearer the upper range of the values calculated here.

A vertical slip rate estimate is also possible. With 50 kya (45 – 54) as the wave-cut platform abandonment date the vertical slip rate depends on the starting elevation when the wavecut platform was abandoned at MIS 3. Unfortunately, that is not well constrained, Figure 38, and Siddall et al, 2008 estimate it around -30 to -80 m relative to modern sea level. The apex at Pillar Point Bluff is about 55 m but the average along the peak ridge is around 50 m giving an estimated vertical slip rate around 2 mm/yr ± 0.4, higher than normal along the Santa Cruz coast, see for instance, Perg et al, 2001, but consistent with this being a restraining bend with its attendant accelerated vertical rise in this positive flower structure. If HMB terrace was coincident with PPB when the wavecut platform was abandoned the differential rise of PPB relative to HMB terrace is about 1.2 mm/yr.

As a final check on the folding model the shortening is calculated for the remaining northern section of the restraining bend and is plotted in Figure D30 where it is aligned with a map of the restraining bend. On the northern end the fault bifurcates with a releasing bend duplex of the Middle Strand to the Fitzgerald Fault. The shortening calculated from the folding model is extended north, although with less averaging of adjacent lines thereby giving more scattering. The shortening peaks at the same place along the restraint where the releasing bend begins, then decreases going to the northwest and flattens, Figure D30, exactly as expected since the distance needed to be shortened is reduced. Indeed, the shortening required after the releasing duplex bend is roughly half what it would be if there had not been a bend, in reasonable agreement with the reduction in shortening found in Figure D30. On the northern end the measured shortening again decreases as the fault begins bending northward, as expected, although another factor is the deviation of the baseline from the fault line in Figure D30a. The exact amount the shortening is reduced depends on how much of the fault movement has switched from the western branch to the eastern branch and when it started. A more precise calculation of the shortening, in fact, might help constrain that. In any case, this qualitative and semi-quantitative correlation between the folding model and the fault geometry is another confirmation that the folding is primarily a result of this restraint. This folding structure, laid out so clearly with the aid of sea erosion, has thus provided this unique opportunity to quantify the structural response to this restraining bend.

Conclusions and Discussion:

The Middle Strand of the San Gregorio Fault along the on-land section from Pillar Point to Moss Beach has been mapped and found to include both a restraining bend and a releasing bend with the releasing bend section connecting this Middle Strand with the fault identified in the sea cliff at Fitzgerald Marine Reserve while passing through the Holocene faults identified by Simpson et al, 1997. An exposure of several branches of the fault was aided by a landslide headscarp that allowed detailed characterization over an area 100 m wide and up to 10 m high. This includes observations that verify it is a right-lateral northwest-southeast striking strike-slip fault with measurable oblique movement that has sequenced through a history of plunge angles where earlier slip with east side rising was followed by a period of west side rising coincident with a progression of fault activity from west to east. The fault exposures are traced in both a marine sedimentary bedrock Purisima formation, Tp, with a wave-cut platform cut into it and exhibiting gouge zones up to 1.7 m wide, and also into an unconformably overlying marine terrace deposit, Qmt, with fault displacement traced to the surface in some cases. Multiple fault paths have been active since MIS 3 with five major components exposed at the headscarp near the center of Pillar Point Bluff, which could have originated during either earthquakes or aseismic creep intervals or some combination of the two. Horizontal offsets for some events are estimated to be about 3 – 10 m suggesting multiple large events (M>7) have occurred since MIS 3 and the earthquake recurrence interval for all events is estimated to be in the range of about 200 to 650 years. The faults propagate through a restraining bend forming a positive flower structure along the southern section of PPB and transitions to a releasing section on the northern part of PPB that exhibits a negative flower structure crossing over to the Fitzgerald Fault producing the Seal Cove Lowlands graben in the process. The faults were further observed and characterized by magnetic anomaly scans that suggests the faults east of the apex may be predominantly dip slip compared to the strike slip faults west of the apex. The conclusion is that Pillar Point Bluff and the Seal Cove area of Moss Beach are perforated by tectonic fault strands and most of the ground movement evident in the Seal Cove area of Moss Beach appears to be initiated along and influenced by these tectonic strike-slip faults. Proceeding northwest from this on-land section are two subparallel strands separated by about 0.6 km where their path is then consistent with that described by Ryan et al, 2008. Whether there is a strike-slip component to the previously identified thrust faulting of the Seal Cove Fault along the prominent eastern scarp of Pillar Point Bluff is not established, available evidence, including magnetic profiles, suggests it is primarily dip-slip.

Dating of the unconformably overlying marine terrace deposit using both CRN and IRSL found a date of 50ka (68% probability range 45 – 54 ka, 95% range 42 – 58 ka) indicating a Marine Isotope Stage 3 high stand abandonment of the wavecut platform. The best constrained lateral offset was obtained by making use of the offshore folding visible in the Purisima formation to calculate a dependence of bedrock slope angle on distance into the restraining bend and combining that with the observed rotation of the wavecut platform since it was abandoned to calculate an offset of 326 m (68% probability range of 264 – 393 m) since the wave-cut platform was abandoned. The offset and age distributions are combined to calculate a probability density function of slip rate with a median of 6.5 mm/yr (68% range of 5.2 – 8.0, and 95% range of 4.0 – 9.7) since MIS 3. These are within with prior estimate ranges but are here based on well constrained offsets and sediment ages and relate to reinterpreted fault paths. The vertical rate of rise of PPB since MIS 3 is on the order of 2 mm/yr ± 0.4.

The geologic interpretation of the Pillar Point Bluff section of the San Gregorio Fault, based on the mapping and modeling in this report, is that the restraining bend, which is responsible for the existence of Pillar Point Bluff, is a response to a granitic bedrock obstruction, presumably Montara granodiorite, that causes the SGF-E to bend counterclockwise about 13.4^o (12.3 – 14.5) with the marine sedimentary Purisima formation riding on the plate on the southwest side of the fault moving to the northwest continuing to shorten until it gets past the granitic obstruction which occurs beneath the eastern section of the Seal Cove Highlands. The Leighton et al, 1971 borehole results are indications of this granitic bedrock. Several sub-parallel strands, collectively the Middle Strand, of the fault approach from the south of the Seal Cove Highlands and bifurcate going northwest with one strand proceeding as an offshore continuation of the Middle Strand and another right bending around the granitic obstruction to the Fitzgerald Fault. In the area where it steps over there are at least three components with the southeastern-most path being adjacent and along the granite obstruction. The Seal Cove Lowlands, referred to as a “wind gap” by Simpson et al, 1997, likely originated as a pull-apart basin resulting from the crossover right-lateral strike-slip Distillery Fault. Whether it has also served as a drainage pathway is not here determined.

A Montara Mountain granite intrusion into the SGF-E path appears to have caused the restraining bend and is also responsible for an extensional force east of the fault that has produced the Half Moon Bay Syncline while simultaneously constraining the eastern plate north of the obstruction to form the Moss Beach Syncline.

This SGF-E fault has shown very little recent earthquake activity although that does not mean this fault is without risk. The currently most active releasing bend strand appears to be the Distillery Fault which is the most northwestern of the releasing faults and it passes through the Simpson et al, 1997 MRE fault. There is a possibility that it is aseismically creeping at around 1.6 – 3.7 mm/yr as measured by Holocene offsets at a Tree Line on Fitzgerald Marine Reserve and on the West Point Road, thereby also suggesting the active path is the Middle Strand to the Distillery Fault crossing over to the Fitzgerald Fault and then continuing north, but creeping has not been confirmed by alignment array measurement. Yearly changes are observed along the Distillery Fault path and the gravity spreading ridges. Roadbed shears that show up regularly generally indicate right lateral motion. A small landslide in 2017 uncovered the MF gouge in the headwall of the large landslide basin. Offset on West Point Road has apparently occurred during the last 20 years. And yet, the mapping in this report suggests this fault may becoming locked. The recurrence interval since MIS 3 is best estimated around 200 years, yet no measurable earthquakes have been recorded along this section of the SGF-E in recorded time and no events greater than 3 have been recorded by the USGS. So, there is uncertainty; is this fault locked, is it creeping? These may appear incompatible, although conceivably it could be a very high stress fault that is partially locked, but with stress building high enough to induce creep. The deflection around the granitic obstruction may have produced a high impedance, highly damped point slowing down the movement around it (in comparison with an overdamped electrical circuit or a highly damped plunger analog). One that slowly releases stress rather than suddenly breaks into an earthquake, perhaps controlled by the strength of the granite protrusion. This would seem to carry with it the risk of a sudden failure releasing a lot of built-up stress. Such a possibility appears to be worth monitoring for signs of instability. Monitoring the West Point Road alignment array, geodetic velocity measurements, perhaps adding additional geodetic measurement points, and stress modeling the fault configuration may all be worthwhile follow-up actions.

Acknowledgements:

The author greatly appreciates San Jose State University Geology Department allowing him to be a volunteer researcher, the interactions with all the faculty and staff have been helpful and an immense pleasure. In particular, Professor Kim Blisniuk has been a remarkable advisor throughout this project and has graciously allowed and encouraged the author to be a part of her research group. This project started as a paper in her Active Tectonics class. Professor Dave Andersen has also been particularly helpful and a valued mentor. Numerous students in Professor Blisniuk's classes helped with excavations and sample collections at the research site as part of class field trips and I wish to thank them but hesitate to name them all in the likely case I forget some. Alianora Walker, along with Kim, was responsible for the lab work on the Be10 dating samples and Kim did the CRN age modeling and also obtained the IRSL data. Dennis Woo, a high school intern for Kim, was particularly helpful in collecting the digital data from the USGS bathymetry data set and was an enjoyable field assistant, and I appreciate Ryan Missel's help who is also advancing the project.

The staff of the Fitzgerald Marine Reserve and San Mateo County Parks Department have been very generous in allowing access and field work on this beautiful Reserve and I particularly appreciate the interest, help and assistance of Ranger Robert Cala and resource manager Ramona Arechiga. The cooperation of Tim Iverson of the Vandenberg Air Force Station at Pillar Point is much appreciated.

The generous assistance and expert consultation of Jean DeMouthe (since deceased), the San Mateo County Geotechnical Officer and the keeper of the reports at the time of most of the consultant report data collection and Chris Vandrey, county surveyor, is gratefully acknowledged and much appreciated. It was Jean who told me that no one, particularly the USGS, was interested in the San Gregorio Fault. I think she was trying to keep me from wasting my time, but little realized it had quite the opposite effect. To me it suggested I would not interfere with anyone, could take my time, spend a lot of it in the field – a beautiful site – and no one would bother me, just what I was looking for as a retired person working on something totally outside my career field. But I also learned she was not quite right. Bob McLaughlin, in the process of retiring from the USGS (apparently not a binary step) lived in the area, sniffed

out what I was up to and with his generous guidance and organizing field trips, making connections with other geologists, well-aimed criticisms, and spot-on suggestions was a tremendously beneficial influence. One of those connections was Tyler Ladinsky of CGS who, along with Aaron Powers, made an expertly detailed map of part of the fault exposure wall. Several people have been to the site and provided valuable input including John Caskey whose SFSU group is also responsible for the alignment array at PPB and who graciously agreed to add another branch. In addition, Carol Prentice, Belle Philibosian, Dave Andersen, Emmanuel Gabet, Richard Stanley, Andre Sarna-Wojcicki, Sherry Liu, James Conrad, Sam Johnson along with many of his group whose bathymetry mapping has been so key in this report, and Nate Brown who provided direction on IRSL sample collection; Elizabeth Miller and Roland Burgmann provided additional valuable input. Despite all the expert input it is stressed that all errors, omissions, misinterpretations and silly things said in this report are solely the responsibility of the author and it certainly is not implied that any of the people acknowledged endorses any of the results or conclusions of this report. It has been a pleasure carrying this project this far, I recognize all the prior work it builds on, particularly the solid work of Earl Pampeyan, and the Simpson, Koehler, and Leighton groups. My main hope is the information provided here, with its numerous limitations, serves as a useful bridge to additional future work.

Appendix A:
Geotechnical Mapping Compilation

This is a summary of data derived from consultant's geotechnical reports for the unincorporated Seal Cove area of Moss Beach, California, Table AI and Figure A1. The reports are available from the Planning Department of San Mateo County, although are not accessible on-line.

Table AI: Trenching-identified faults by commercial geo-consultants. APN is San Mateo County Assessor's parcel number.

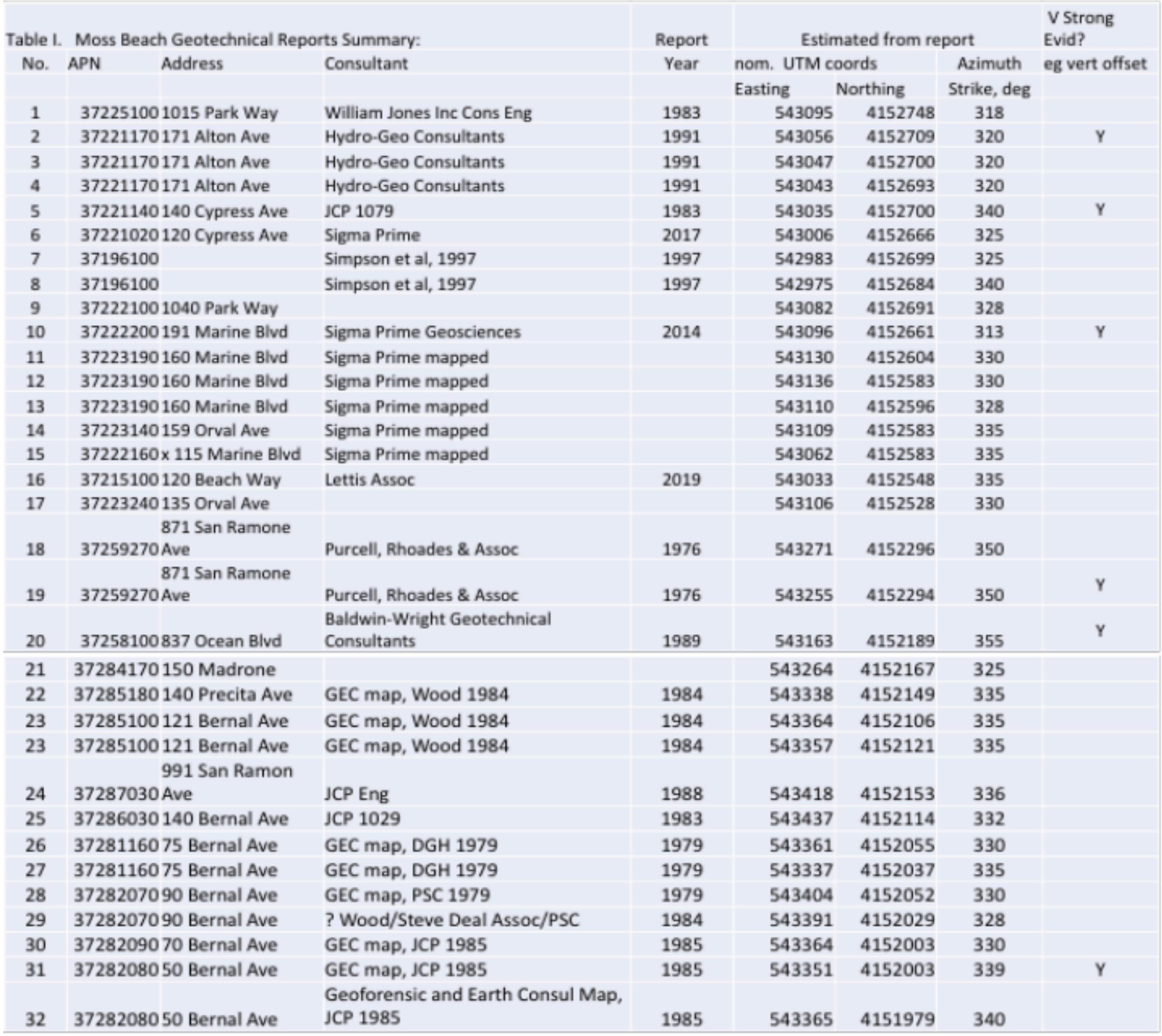

Table I. Moss Beach Geotechnical Reports Summary:

				Report	Estimated from report			V Strong Evid?
No.	APN	Address	Consultant	Year	nom. UTM coords		Azimuth	eg vert offset
					Easting	Northing	Strike, deg	
1	37225100	1015 Park Way	William Jones Inc Cons Eng	1983	543095	4152748	318	
2	37221170	171 Alton Ave	Hydro-Geo Consultants	1991	543056	4152709	320	Y
3	37221170	171 Alton Ave	Hydro-Geo Consultants	1991	543047	4152700	320	
4	37221170	171 Alton Ave	Hydro-Geo Consultants	1991	543043	4152693	320	
5	37221140	140 Cypress Ave	JCP 1079	1983	543035	4152700	340	Y
6	37221020	120 Cypress Ave	Sigma Prime	2017	543006	4152666	325	
7	37196100		Simpson et al, 1997	1997	542983	4152699	325	
8	37196100		Simpson et al, 1997	1997	542975	4152684	340	
9	37222100	1040 Park Way			543082	4152691	328	
10	37222200	191 Marine Blvd	Sigma Prime Geosciences	2014	543096	4152661	313	Y
11	37223190	160 Marine Blvd	Sigma Prime mapped		543130	4152604	330	
12	37223190	160 Marine Blvd	Sigma Prime mapped		543136	4152583	330	
13	37223190	160 Marine Blvd	Sigma Prime mapped		543110	4152596	328	
14	37223140	159 Orval Ave	Sigma Prime mapped		543109	4152583	335	
15	37222160	x 115 Marine Blvd	Sigma Prime mapped		543062	4152583	335	
16	37215100	120 Beach Way	Lettis Assoc	2019	543033	4152548	335	
17	37223240	135 Orval Ave			543106	4152528	330	
18	37259270	871 San Ramone Ave	Purcell, Rhoades & Assoc	1976	543271	4152296	350	
19	37259270	871 San Ramone Ave	Purcell, Rhoades & Assoc	1976	543255	4152294	350	Y
20	37258100	837 Ocean Blvd	Baldwin-Wright Geotechnical Consultants	1989	543163	4152189	355	Y
21	37284170	150 Madrone			543264	4152167	325	
22	37285180	140 Precita Ave	GEC map, Wood 1984	1984	543338	4152149	335	
23	37285100	121 Bernal Ave	GEC map, Wood 1984	1984	543364	4152106	335	
23	37285100	121 Bernal Ave	GEC map, Wood 1984	1984	543357	4152121	335	
24	37287030	991 San Ramon Ave	JCP Eng	1988	543418	4152153	336	
25	37286030	140 Bernal Ave	JCP 1029	1983	543437	4152114	332	
26	37281160	75 Bernal Ave	GEC map, DGH 1979	1979	543361	4152055	330	
27	37281160	75 Bernal Ave	GEC map, DGH 1979	1979	543337	4152037	335	
28	37282070	90 Bernal Ave	GEC map, PSC 1979	1979	543404	4152052	330	
29	37282070	90 Bernal Ave	? Wood/Steve Deal Assoc/PSC	1984	543391	4152029	328	
30	37282090	70 Bernal Ave	GEC map, JCP 1985	1985	543364	4152003	330	
31	37282080	50 Bernal Ave	GEC map, JCP 1985	1985	543351	4152003	339	Y
32	37282080	50 Bernal Ave	Geoforensic and Earth Consul Map, JCP 1985	1985	543365	4151979	340	

33	47311070	PPB	Connelly and Rubin	2001	544245	4150971	310	Y (BR Slick)
34	47311070	PPB	Connelly and Rubin	2001	544274	4150991	317	Y (BR)
35	47311070	PPB	Connelly and Rubin	2001	544293	4150932	323	
36	47311070	PPB	Connelly and Rubin	2001	544315	4150948	315	
9a	37225070	1035 Park Wy	Connelly and Rubin	2021	543115	4152730	302	Y

Also included is mapping of other features including stress shears in roadbeds, complementary pairs of arcuate extension cracks (explained in Appendix C), and faults identified by other investigators; Simpson et al, 1997, Koehler et al, 2005, Leighton and Associates, 1971, Cotton and Associates, 1981, Pampeyan, 1991.

A large portion of Moss Beach is within a short distance of the Seal Cove Fault, part of the Alquist-Priola special fault zones designated by California Geological Survey, 2018, to require geological investigations for habitable construction.

All faults identified in consultant reports found during the review are included, although it is noted that some of these identifications have been questioned by other consultants and several have been the subject of disputes, and not all consultant reports were found. Two sources, Sigma Prime and GEC (Geoforensics and Earth Consultants), provided maps of faults they had compiled and are indicated in the table. It is also acknowledged that precise location of faults is not always readily accomplished from the reports and in several cases the locations derived from the trench map is adjusted to account for the actual house location. That is, it is assumed that following a geotechnical study for a particular lot the subsequent house (excluding the garage) on that lot was positioned in conformance with the required 10ft exclusion distance and if my reading of the trench map did not result in that margin then I assumed the actual siting of the house was accurately done to the real location of the fault and was thus a better location guide. A house positioned at an odd angle relative to the lot or with a corner cut off is a certain sign it was aligned to fault constraints. No adjustment was made if the projection of a fault goes under a neighboring house, a common occurrence. While it is believed most faults are located within about 3 meters of the trench-identified location, in some cases the location was adjusted up to 10 meters. Figures A2, A3, A4 and A5 are expansions of the mapping for more detailed identification with fault numbers added corresponding to the sequence number in Table AI.

Few of the consultant-reported faults exhibit significant lithology changes or strata offsets across the faults and only that of Connelly and Rubin at the south end of PPB included an exposed Purisima bedrock. The requirement to be recorded as a fault is that they exhibit a noticeable fracture or fault trace that extends to the bottom of the trench which is typically 6 to 10 feet deep. All reported faults are included in this mapping while those few with stronger evidence, such as a noticeable lithology change, vertical strata offset, or wide soil-filled cracks, are so noted in the last column of Table AI. The fault 33 in Figure A4 is from the consulting report of Connelly and Rubin, 2001. It is exposed in two trenches dug into Purisima bedrock and included the observation of "faint slickensides oriented down dip" in one of the exposures, Figure A5, indicating this fault, which may align with the East Wall Fault as extrapolated in Figure A4, is primarily dip slip. This fault is roughly 100 m west of the SCF mapped by Pampeyan, 1991.

It is noted that for the exposed faults described in this report if trenches had only been dug 6 to 10 feet into the marine terrace deposit, Qmt, several of the faults would not have been exposed, or noticed as minor cracks and many would not show obvious lithology offsets even though some of those faults are here traced to the Purisima where they show clear faulting with fault gouge zones over a meter wide with significant vertical offsets. There is often reported skepticism for the findings of the geotechnical reports partly because the requirement for calling features a fault appears overly inclusive. However, one lesson of this report appears to be contrary to that. That is, fault evidence in Qmt, as often reported in consultant reports, likely is an indicator of faulting in the underlying bedrock but does not necessarily fully reflect the degree of faulting in the bedrock, and the absence of faulting in upper levels of Qmt likely cannot conclude there is an absence of faulting in bedrock.

The consultant faults generally align in a few linear groupings delineated by the yellow lines in Figure A1. It is of interest to compare these trends with an earlier map by Leighton et al, 1971, where they mapped "lineations" from aerial photographs. These are the gray lines in Figure A1 and are similar (perhaps the same) as those mapped by Pampeyan, 1991. The two eastern Leighton lineations reasonably follow the trends of consultant-identified faults in the Seal Cove highlands. The western-most of the Leighton lineations does not match any consultant faults here recorded. However, few trenching studies have been done in the western section of the Seal Cove Highlands since that area apparently is far enough from the A-P line not to require such. Rather, only a few soil studies were done in that area. Thus, the lack of consultant-identified faults cannot be taken to imply there are not faults there. There is some coincidence between the Leighton western lineation and roadbed shears but not enough to conclude there is a correlation. The relationship between the Leighton lineations and the consultant-identified faults in the Seal Cove lowlands is not as clear. The eastern-most lineation was not extended beyond its intersection with the AP line and the center lineation deviates most from the consultant fault trend in an area that is topologically saddle shaped and following the lineation in that area may not have been obvious. It is also noted that the Seal Cove Lowlands have substantially lower bedrock per the Leighton report - none was detected in borings down to about 10 to 15’ elevations – so the finding that faults may not have reached the upper 6’ or they may deviate more from a straight path than in the Seal Cove Highlands is not surprising. The lower bedrock is likely the result of the Lowlands being a pull-apart basin as discussed in the report. Slumping within the pull-apart basin may be responsible for some of the reported faults in the Lowlands.

Some of the gravity spreading ridges, the green lines on the north side of the large landslide area in Figure A1 and south of the developed area, likely also align with the consultant fault trends. The two longest ridges appear to align with the two best-defined consultant fault trends. Extending both sets of lines the 100 meters that separate them results in close matches in both location and direction. The two long ridges are also the highest and most pronounced ridges, up to 2 m high and 10 m wide, and are traceable the furthest toward the developed area. Only the uphill-facing scarp is plotted for each spreading ridge, but there is also a corresponding subparallel downhill-facing scarp for each of the ridges. The width of the ridge is roughly the width of the plot line. Leighton did not extend his lineations past the designated development area, Bernal Avenue being the last street developed, so we don’t have the benefit of his lineation interpretation in the intervening area, and no trenching has been done in this area either. Currently, the heavy undergrowth prevents a confident surface topology mapping in this area absent a high definition lidar map, but the alignment of trends strongly suggests a continuation of the faults connecting the gravity spreading ridges to the consultant fault trends. Similarly, the alignment of the two consultant fault trends in the lowlands with those in the highlands suggests they may also be connected thereby forming multiple fault paths from the large landslide area, where the Middle Strand has been exposed, across to the AP fault line and on to the Fitzgerald Fault exposed at the shoreline.

The additional gravity spreading ridges could only be mapped over shorter distances and they are smaller in height and are without clear fault extensions in the developed area. The term “gravity spreading ridge” was used when first mapping these ridges, however, while the term is descriptive and continues to be used and they may look similar to such structures, also called Sackungen (Varnes et al, 1989), it is now felt that term may imply an origin not consistent with the current understanding of these faults. These ridges now appear, by their location and orientation, to be tectonic in origin and not just due to gravitational forces.

In summary, the fault trends, lineations, spreading ridges and shears throughout Moss Beach and Pillar Point Bluff indicate the area is generally perforated by faults, nevertheless particular trends are apparent and are instructive as discussed throughout this report.

Appendix B:

Simple Demonstration of Folding at a Restraining Bend

When a strike-slip fault encounters a restraining bend, as it does for the San Gregorio Fault at Pillar Point, there is a need to accommodate the constraint by shortening one or both plates. A demonstration of this was set up to get a general idea of what that shortening might entail. This was just meant to aid the author's visualization of the expected folding, but since the result was reproducible and surprisingly reminiscent of the actual folding observed at Pillar Point it is included here for interest. It can be pointed out this is really an issue of topology; rock mechanics are secondary. The strata at PPB are folded, the rock mechanics obviously allow that, the question addressed here is how might folding progress at a restraining bend. Numerical modeling might be useful but would not be definitive due to so many parameters that inevitably change during folding and would likely never be adequately quantified. Instead, it was decided to just try a simple demonstration using materials available. It was not an exhaustive experiment but shows what can occur at a restraining bend.

A rug was pushed against a wall at a small angle and the resulting deformation of the rug was observed. This experiment does not duplicate the situation found offshore of Pillar Point Bluff. There are numerous differences in setup, material parameters, and process and no effort to achieve a correct scaling. However, it was mainly intended to see the type of folding structure that might be observed, and the arrangement was roughly like that at Pillar Point.

First, when the flexible media is pushed against the wall at a very small angle, essentially grazing angle, the folding is a simple single linear anticline-type structure (or syncline if the initial edge curves up rather than down which depends on the details of that interface). The entire side of the flexible media starts folding simultaneously. This is common experience and is not shown here. This is what might be expected when a straight section of fault slowly starts transitioning to a restraining bend and in the case at PPB represents what likely caused the long northern section of the offshore folding where a single long tilted formation is found.

Second, folding at higher restraining angles was investigated. Figure B1 shows the general arrangement of the setup, the rug was placed against a restraining wall, a contact/pushing plate was emplaced which covered a small area of the rug and a force was applied to that contact surface to push the rug in the direction indicated by the wood stake. This angle was about 15^{o} to the restraining wall. Figures B2 to B4 show a sequence of photos of the progress throughout the demonstration. Figures B5 and B6 show a sequence of a second recorded run of the experiment where the rug was turned over and the location of the contact surface was changed. Both orientations were repeated numerous times.

Several observations are possible:

- Two “anticlines”, i.e. ridges, were formed in both experimental runs (plus in all of many other runs not recorded) in front of the pushing surface.
- The anticline fold axes were at angles counterclockwise to the restraining wall.
- The fold axis of the anticline closest to the restraint was at a smaller angle, essentially sub-parallel, to the restraint than the one furthest away.
- The anticline closest to the restraint was smaller in amplitude (height and width of the fold) in both runs of the experiment (plus in all the other runs not recorded).
- In all cases the folds were plunging toward the upper right in the figures. That is, roughly toward the contact surface.
- In the first run the fold axis furthest from the restraint was curved, going from one at a higher angle to the restraint to one at a smaller angle as it got further from the restraint, i.e. it had a concave fold axis toward the restraint. Another way to look at this is that it tended to “curve around” the anticline/syncline structure closer to the restraint.
- In the second run, where the pushing point was further from the loose end, the anticline fold axis furthest from the restraint was nearly straight and at a higher angle to the restraint.

All these observations find similarities to the folds observed at Pillar Point. A table of numerical values also shows rough agreement in trends if not in absolute values. Despite all the differences that can be enumerated between the experiment and the layout at Pillar Point, it is nevertheless informative that the topology seen offshore of Pillar Point can be representative of a low angle restraining bend for a right lateral movement with a detachment fault. Initially the folding is a straight fold when the restraining angle is very small as expected along the northern section of the offshore folding, then as the restraining angle increases the folding transitions to the “double anticline” folding as seen in the southern end of the structure. This simple demonstration is considered further support for the proposal that the folds off-shore of Pillar Point Bluff were formed in-situ in response to that restraint.

Table BI: Comparison of fold parameters between demonstration and actual.

	Offshore Fold axes angle wrt fault at Pillar Point	Demonstration
Near-fault Anticline	20° ±	0-5°
Far Anticline Near Pillar Point	50°	19-40°
Far Anticline Furthest Offshore	15°	9-40°
Anticline south of Pillar Point	5°	0-5°

Appendix C:
Aseismic Creep Evidence

The occurrence of stress features, such as Riedel shears, Figures C1 to C6, graben subsidence, Figure C7, offset road lines, Figure C8 to C10, offset tree line, Figure C11, and coordinated pairs of arcuate extension cracks, Figures C12 to C14 in modern roadbeds, during which time no earthquakes have been recorded in the vicinity, suggests aseismic creep as their possible cause. The data reported in this Appendix is suggestive, although confirmation of aseismic creep by alignment array measurements (as stipulated by Galehouse and Lienkaemper (2003)) has not yet been accomplished.

Riedel Shears:

Riedel shears seen in asphalt roadbeds in several locations throughout the Seal Cove area are shown in Figures C1 to C6. These shears are consistent with right-lateral fault movement, i.e. they are a series of left-stepping en echelon subparallel cracks and the trend of the line of cracks are roughly 15^o clockwise from the proposed fault paths, Davis et al, 2000. The shear locations are mapped in Figures 2 and A1 – A3. They generally encompass and delineate the Distillery Fault. It is possible the movement recorded by these shears is not necessarily tectonic creep directly, rather it may involve movement that is activated along tectonic faults such as by releasing built-up stress or by gravity aided processes along a tectonic fault.

The San Mateo County Road Department is inconveniently efficient and has replaced or patched most of these roadbeds since these pictures were taken. The age of the roadbeds is difficult to assess since many had been previously patched and had re-sheared. However, according to verbal communication with the SMC Road Department and the example drawing referenced, Los Banos Avenue Road Drawing, 1991, the roads in this area were paved initially in about the early 1990's, so they would have been less than 30 years old at the time of the photos, a few are much less, on the order of a few years, judging from appearance of patched pavement.

The deflected road lines in Figures C8 and C9 are seen to be a few meters outside (west) of the span of an alignment array (SF-07 of Galehouse and Lienkaemper (2003) and designated SGWP at the current data website; funnel.sfsu.edu) that has been monitoring the expected fault path along the eastern scarp of the bluffs since 1980, Figure C9. Indeed, the extrapolation of these features appears to cross the reference line of that creep array (the IS to OS line) at a low angle of about 5^o. During that time "no creep" was reported (measurement below a threshold of 1 mm/yr), however, it is interesting to note that the average trend of the existing creep data over 38 years indicates a net trend of about -0.2 mm/yr, where the sign implies it was net left-lateral. If the identified offset road lines on West Point Road plus the stress features on the service road do represent the path of the Middle Strand fault and if that path cuts the reference line for this creep array at a 5^o angle, then the - 0.2 result would translate to roughly + 2 mm/yr of actual right-lateral creep. The array has recently been modified to now include another ES point to span the section encompassing the offset road lines (thanks to J. Caskey, 2017, personal communication) so in a few years creep monitoring data should quantify any creep along this strand. The observed offset of the three road lines averaged about 47 mm (30 – 63), Figure C10, since the lines were laid down in 2000, 17 ± 1 years prior to the measurements implying a possible creep rate of roughly 2.7 ± 1.0 mm/yr, reasonably consistent with that interpreted from the creep array data. Ironically, even though this data suggests creep and following the trend of these features, which themselves would require creep to have occurred to be real, is responsible for the later uncovering of the Middle Strand faults, such aseismic creep still needs to be considered tentative until confirmed by new alignment array results.

Coordinated Pairs of Arcuate Extension Cracks:

Coordinated pairs of arcuate extension cracks, CPs, are features the author observed in a few places in the Seal Cove and Pillar Point area and thinking they might result from creep he looked for and found similar features on the Hayward Fault near downtown Hayward where that fault is known to creep. These features have not been found to be reported elsewhere, although the literature search has admittedly not been exhaustive. Given the frequency with which they are found along the creeping Hayward Fault they most likely have been previously noted with apologies due for not referencing such. They are stress cracks in asphalt roadbeds that straddle the fault as illustrated in Figure C12, with pairs symmetrically placed on either side of the roadbed. These are explained by observing that the stress applied to the cohesive asphalt roadbed by a fault transmitted through the roadbed sublayer will apply a slight tensile force near the fault which is uncompensated (that is without an opposing force from the surrounding asphalt) only near the edge of the asphalt sheet. Since they have not been seen elsewhere reported they are here tentatively assigned. Particularly for asphalt, which, like most materials, is strong in compression, weaker in shear, and very weak in tension, a relatively small extensional component will cause failure before a much larger shear component because of the difference in strengths. In the case of Riedel R shears, which form in the body of the roadbed away from the edges, this usually occurs along a roughly 15 deg angle to the direction of the applied shear. However, in the configuration of Figure C12, of a rectangular plate with a shear force applied to the short axis, the outside edges of the plate will undergo a net tensile force closer to perpendicular to the force as shown by the cracks forming on each side of the roadbed and slightly straddling the fault. A competing failure is at the shear force in the horizontal plane between the asphalt and its sublayer, however, judging from the results recorded in Table CI it appears in the roadbed case an engineered sublayer forms a strong enough bond to result in the asphalt being the weaker component along this Hayward Fault section. These extension cracks probably require a certain range of both plate physical strengths and thicknesses and the coupling strength between the plate and the underlying bed and the strengths in that underlying bed. Pairs of arcuate cracks, one on either side of the plate, may not always form in roadbeds. A single crack can form for a variety of reasons, thus cracks subparallel to the roadbed edges is not uncommon. But if a pair of arcuate cracks is found symmetrically placed as in Figure C12 they greatly increase the probability that they straddle a creeping fault which is the objective of their mapping in this report.

In the case of the Hayward Fault the fault location is easily located by nearby linear offsets. Thus, it serves as a test for confirming and characterizing the CPs as described above. Observations from the Hayward Fault are summarized in Table CI. Eleven examples of arcuate extension cracks were recorded on September 29, 2016 along this segment of the Hayward Fault that show a range of crack lengths and widths with seven of those being coordinated pairs of cracks. Arcuate cracks may typically be disregarded, they can appear as general roadbed damage as seen in Figures C13 and C14, however, it is noted that most of the cracks along asphalt is commonly subparallel to the bed edges, having arcuate cracks straddling the fault and oriented and arcing as shown in Figure C12 is found to be relatively uncommon and coincident with known faults in the Hayward fault section. Unfortunately, just as in Moss Beach, the road department is quite efficient in repairing and covering over these cracks. No CP's were observed on high use, high visibility streets that appeared to be recently recovered. However, parking lots and neighborhood streets are more neglected and thus yield useful data for Table CI. For characterization purposes data was recorded even if there was an extension crack on only one side of the asphalt beds as long as it was appropriately located relative to the fault. A general observation is that in most cases where it was reasonable to expect a CP there was at least one extension crack. Recently repaired or new roads or where constraints prevented displacement of the asphalt did not record them. But CPs were found on most free edges of asphalt roadbeds that were, from appearances, more than a few years old and were crossed by the creeping Hayward Fault.

On Pillar Point Bluff there are two main locations where CPs were identified plus a couple other tentative locations. Figure C15 shows the location on the West Point Road where offset road lines also were observed, and Figure C16 shows CPs on the curved section of the Service Road along which the OS alignment array point is located. The latter is important (and the main reason for researching these features) because it served as the second location of the Middle Strand which, along with the offset road lines, was used to extrapolate a trend line, azimuth of $319^o \underline{+} 2^o$, that intersected the headwall of the large landslide area where a (apparently confirmatory) Middle Strand fault exposure was subsequently identified. The service road markings include a couple light roadbed shears that are coincident with the purported fault location but are oriented at about -15^o rather than the $+15^o$ expected for R-shears on a right lateral strike-slip fault. This roadbed has a center joint, (although not easily seen in Figure C16a), that is oriented such that it could possibly relieve the shear that would otherwise cause synthetic R-shears and antithetic R'-shears and it may be only synthetic P-shears, that are here formed. That is a stretch, I know.

Three other possible CPs are located within the Seal Cove area, Figures A1 through A3, although none was identified confidently enough to use for mapping a fault. One fits the Consultant Fault Trend 2 on Los Banos Avenue, one fits the Consultant Fault Trend Line 3 on Bernal, which itself is the least confidently mapped of the trend lines, the other is between the Leighton lineation 1 and the Consultant Fault Trend Line 1.

Table CI: Hayward Fault creeping section data on Coordinated Pairs of Arcuate Extension Cracks in Sept, 2016. Refer to Figure C12 for definition of parameters. Lo is the stepped-off distance east from Mission Blvd sidewalk, except for locations near Prospect (*) where the distance is from Prospect.

Location in Hayward Ca:	Distance from Ref	Horizontal Fault	NW Crack Length	NW Width	SE Crack Length	SE Width
Parameter	L_o	L_1, Offset	L_{NW}	W_{NW}	L_{SE}	W_{SE}
Units	~ ft.	Inches	ft.	Inches	ft.	Inches
Pkg Lot btw **A**&**B** St	75	6	18	52	10	27

A St Pkg Lot SE corner	90	10			15	12
Alley N of **A** St	108		18	19	10	12
El Taquito Pkg Lot	81					
Apt Bldg Pkg Lot N of **A**	102	3			11	36
Simon Str 2nd Trace	270	12	16	12 - 24	16	12 - 24
Sunset Blvd –from Prospect*	84		7	18	3	10
Rose St/Prospect corner *	0		12	21	7	22
Grove		6	14	-		
Pkg Lot btw **B**&**C** st	81		8	36	10	50
Eden Loan Pkg Lot	75	6	12	36	9	18
Fletcher Lane ylw line		15	36	?		
Avg		**7.2**	**12.4**	**26.8**	**10.1**	**22.8**
Sigma		**3.3**	**4.6**	**12.7**	**3.9**	**13.1**
Range		**3 - 12**	**6 - 36**	**12 - 52**	**3 - 16**	**10 - 50**
For comparison:						
Pillar Point - West Point Rd		*2.6*	*10 - 36*	*16 - 30*	*26*	*24*

Tree Line Offsets:

Earlier measurements searching for possible creep had been carried out before the Middle Strand was exposed. These focused on several potential small offsets found throughout the Seal Cove area. Among them were two tree lines in Fitzgerald Marine Reserve that were measured and found to exhibit possible offsets where the SCF was expected to cross them. The Cypress trees had been planted in straight lines about 1915 by a German immigrant farmer/mining engineer, Mr. Wienke, who was developing a vacation resort, (Conradson and Welch, 1990). Tree lines are not readily accepted as accurate indicators of tectonic movement unless the offsets are large enough to easily overcome potential inaccuracies. While I took great care, (in particular, did not use the large mature lobed trees which grow asymmetrically, rather only those small stunted, usually dead, symmetric ones less than 1 ft in diameter that were assumed to still accurately represent their original planting location) the measured offsets were on the order of the uncertainties so are not presented here. The exception is the Wienke Long Tree Line, Figure C11. The displacement on this tree line did align with one of the proposed releasing faults, namely the Distillery Fault extension that also aligns with the Simpson MRE fault path. The line of trees runs over a fault scarp at an angle of about 35° to the scarp and the offset along the trees occurs near the base of the scarp. The measured offset of 100 - 130 mm, at an angle of 35° to the scarp over 103 years results in an implied creep rate of 2.0 ± 0.4 mm/yr. Whether this nominal agreement with the road line offset implied creep rate of 2.7 ± 1.0 mm/yr on the other end of the on-land portion of the fault, is just coincidental is unknown. Lots of room for skepticism exists so the creep array measurement is needed. However, if confirmed, it would further suggest that the actively creeping fault that goes down the center of the bluff may also cross over via the Distillery Fault. Of further interest is that the Simpson et al (1997) and Koehler et al (2005) results combined, Table I, imply a fault offset of roughly 4 m every 1450 years, or about 2.8 mm/yr, about half the rate determined in this report, but suggesting much of the fault movement could be associated with aseismic creep (if creep is confirmed).

Appendix D:
Folding Model

As the Pacific plate moves NW along the PPB restraining bend folding is produced southwest of the restraining bend resulting in a tilting of the Purisima bedrock adjacent the SGF-E fault which is observed by noting the tilt in the wavecut platform that has been rotated landward since it was abandoned during MIS 3, Figure 55. That tilting increases as a function of distance along the restraining bend which is also reflected in the change of bedrock dip as seen in Figure 55a. However, the dependence in Figure 55a is not very precise because the small dip change, with relatively large uncertainty, is only over a relatively short distance. In this S.I. a better constrained and more precise measurement of that angle change is made using a much larger data base consisting of all the data from the folded structure southwest of the fault.

The extensive offshore folded structure, Figure 2, is due to shortening in the Purisima formation by the constraint of the restraining bend. As the Pacific plate moves northwestward along the restraint the increasing shortening needs to be accommodated, in this case by an increase in the fold angles. Measuring the change in fold angle over a given length of time, in this case it is the time since a wave-cut platform was abandoned, can then be used to relate how far the fault moved in that length of time. Dating the sediments covering the wave-cut platform then establishes a slip rate. A change in fold angle is recorded by the wave-cut platform etched into the Purisima formation. When the wave-cut platform was formed it would have tilted ocean-ward by a few degrees, but if the wave-cut platform oceanward of the fault now tilts land-ward, as it currently does, then we can estimate the rotation angle of the bedrock since the wave-cut platform was abandoned. That angle change, along with the dependence of angle on distance into the restraining bend allows us to calculate the distance the plate moved during that angle change. The model presented in this Appendix provides a means of determining that dependence of angle on distance.

[Sidebar: A concern often noted about using the offshore folding to quantify movement along the restraining bend is whether it can be established that the folding really did occur at its current location, or whether some component of it occurred elsewhere and moved into this location. Several lines of evidence combine to indicate the offshore folding represents the effect of the restraining bend and substantially only this restraining bend. First, the prominent folding visibly occurs along the restraining bend, extending symmetrically short distances from both ends of the restraining bend, Figure 2. That is, the prominent folding occurs where it should and only where it should to accommodate the restraint. Second, the folding is visible. Erosion of the overlying strata was accomplished by sea wave action and yet it retains clear indication of structure that has not yet been eroded or covered by sediment. If it had occurred some other place it would have moved here significant distances and with the typical wave erosion rates on the order of .1mm/yr and a similar continental shelf sand deposition rate it would have been eroded flat and/or been covered. For example, the only other likely place for its formation is off the Ano Nuevo peninsula, 30 to 50 km southeast. If it had occurred there and transported here, much of the time undersea and in the intertidal zone, it would have taken on the order of 6 Myr to reach its present location (longer than the age of the Purisima) and been eroded flat and/or

covered by sand on the order of hundreds of meters thick. Third, along the southern end of Pillar Point Bluff the folding exhibits an anticline/syncline/anticline sequence that is exactly indicative of this restraint. This is supported by the results of a simple demonstration outlined in the Supplementary Information B where the folding pattern generated by pushing a flexible layer against a restraint at the angle of 15^o produces a folding pattern similar to that observed offshore of the southern end of Pillar Point Bluff. The similarities include that there are always two "anticline" folds with the one nearest the restraint being close to parallel to the restraint and the further anticline being at a higher angle and its fold axis typically curved the same as seen offshore, the further away anticline is higher in magnitude than the nearer one, and the slope (dip) angle on both anticlines increase with distance into the restraining bend. That is, the folding is laid out just like it should be for occurring at this restraining bend. Figure B4 shows one example of this demonstration.

The results in this section also support this folding model in that the shortening calculated from the folded structure, as described for Figures D7 and D18, show that the amount of shortening linearly increases with distance into the bend as expected. Perhaps most clearly, correlation between shortening and distance along the restraining bend in this area in Figures D7 and D18 shows an excellent fit over its full length with an R^2 of .92 to .96, the interpretation being that over 90% of the variation in shortening is determined by the distance along the fault. If the folding at this location were imprinted on prior folding then it should be reflected in those plots and also in the plan view, Figures 2 and D1. None of these shows any indication of overprinting, thus it is concluded the displayed folding is not significantly overprinting an earlier fold structure. Finally, in Figure D17 it is shown that the measured onshore dip in the Purisima beneath the wavecut platform increases with distance into the restraint along the southern stretch of Pillar Point Bluff as expected by this process and in good agreement with the model results. Indeed, if the model is too unusual a step for acceptance, then these measured dips versus distance shown in Figure D17 could be used. Why isn't that just used, it might be asked, rather than add the complication of the model? That data is more scattered than the model data, not as extensive, and it is not as reliable an indicator since it includes individual outcrop results which represent local disturbances such as buried fractures, *rotations, and local volume changes, yet it yields a similar dependence of angle on distance which is the objective of this model. If only that shore-measured data had been presented it is doubtful it would have garnered any confidence. This model is more precise and instructive, it uses the full set of data available and more tightly constrains the results as seen by comparing the tight distribution for the model to the scattered measured data points in Figure D17. So, an option exists: unusual, accurate and complete, or traditional and uncertain. End of sidebar*]

The topography of the offshore folded structure was obtained from the USGS bathymetry data in report ofr 2014-1214 (Bretz et al, 2014). Eight hundred lines over a length of 8 km, each separated by 10m, are digitized with elevations collected every 2m along the lines perpendicular to the mapped Middle Strand from the bathymetry data, Figure D1. (Many thanks to Mr. Dennis Woo, a high school intern for Kim Blisniuk at the time, for doing this digitization). The lines will be identified in this section by their distance from the arbitrary starting location on the north end at UTM coordinates 541160 E, 4154378 N with the baseline running along an azimuth of 139°. Pillar Point Bluff is transected between distances 1900 to 5200 m and the Middle Strand fault exposure described in Section 3 occurs at about 3800 m. The region of interest for this modeling is from about 3800 to 5000 m, the lead-in to the fault exposure region from the beginning of the restraining bend and where the offshore folding is of the form depicted in Figure D2. Figure D2 is a schematic view of the structure found offshore of Pillar Point Bluff, before erosion, that is intended as a simple conceptualization and visualization aid and does not precisely represent the actual folding structure. The offshore folding pattern is two anticlines with a syncline between them all of which grow in amplitude as the plate moves further into the restraint. Of particular interest here is that the slope of the NE facing side of the anticline on the right increases from south to north. The bedrock on both sides of the Middle Strand was at one time eroded into a wavecut platform, the angle of that wavecut platform was set when the wavecut platform was abandoned and would have sloped ocean-ward a few degrees (this is as distinguished from the dip of the strata). Subsequently, the bedrock on the SW side of the Middle Strand continued to rotate clockwise as it translated further into the restraining bend until the paleo wave-cut platform on that side of the fault eventually sloped land-ward. That change in angle depends on the distance moved. It is that dependence of angle on distance translated that is calculated by the model presented here.

Simple geometry is used to reconstruct the folded layers before erosion as shown for one individual digitized line in Figures D3 and D4. The blue line in Figure D3 is the bathymetry data and the structure seen is due to resistant layers remaining exposed after the intervening erodible layers have been removed by ocean-current and wave-induced erosion. The slope on the up-facing side is related to the dip of the bedrock strata, although it is not the same as will be discussed with regard to Figure D4. The slope of the bedrock strata bedding layer is depicted by the gray lines in Figure D3. The slope of each layer above the exposed strata is assumed to be the same as for the exposed layer. These are then added in sequence to the layer above it as depicted in Figure D3, resulting in a surface that represents the folded, uneroded surface of the top strata. The overall structure in Figure D1 is used to identify which side of the individual anticline and syncline folds represents the up-facing side. For instance, in Figure D3 where the anticline fold axis is crossed the sides of the exposed bumps used to calculate the layer slopes are accordingly switched.

The slope is determined over a length of 4 m (3 digitized points). To identify the location of separate strata segments, such as in Figures D3 and D4, a local minimum is used as the demarcation between segments. Then the maximum slope within the previous segment, between two consecutive minima, is assigned as the slope of that layer. Whether the largest positive or negative slope is used is determined by where in the sequence of folds it occurs. That is, whether the strata are rising or falling going west to east. The lines along which the slopes change direction is shown as the blue lines in Figure D1. (They are mostly the same as the fold axes, although the southern end of the anticline line deviates slightly, where it bends southward, because the line where the slope changes along a transect deviates from the apex line.) The sloped line across each segment is then added to that from the previous segment to form the reconstructed surface as shown in Figure D3.

Reconstructed profiles across this area are shown in Figure D5 where each line is an average of five profiles. The data doesn’t extend all the way to the second anticline axis (anticline 2) nor does it include the east side of that anticline which is our region of interest.

Since the surfaces are relatively linear the short sections of rise available between the syncline bottom and the anticline 2 axis are used to represent the slope over the full length of rise. Then the average slopes of each section of fold are used to extrapolate the slope on the falling side of anticline 2 by assuming a constant ratio as:

D1 Rise 1 / Rise 2 = Fall 1 / Fall 2

Or equivalently:

D1a Rise 1 / Fall 1 = Rise 2 / Fall 2

Where Rise 1 and 2 represent the average slopes of the rising sides of anticline 1 and 2, “rise” implying ascending from left to right in the figure and Fall 1 and 2 are the falling sides of the same. Examples of the measured slopes and the projected slopes determined by equation D1 is included in Figure D15 below. The implications of these extrapolations are shown for one of the reconstructed profiles as dashed lines in Figure D5. The location of the anticline 2 axis is available in Figure 2 from the blue structure-mapped lines which outline the anticline 2. Hence, the full folded structure is derived from the bathymetry data available with the locations of the anticline 2 axis from Google Earth plus other visual-based databases. This is the method of estimating the slope on the eastern side of the second anticline which is the location of interest here because it is the surface that abuts the faults in PPB. (It should be noted that even if the topography data for that eastern side of the second anticline were available it would not be useful since as the surface nears and enters the surf zone the slopes of all the exposed bedrock approaches that of a wavecut platform which is an ocean-ward tilt of about 3^o thus it would not provide any information on the tilt of the bedrock bedding layers.)

An important consideration is that the up-facing surfaces in Figures D3 and D4 are actually erosional planes and not bedding planes. While they are surfaces in the resistant strata the discrimination between erodible and resistant is not perfect resulting in the erosional surface being tilted relative to the bedding plane as illustrated in Figure D4. Several factors influence this; as the tilted layers are eroded vertically the upper parts of the up-facing section is exposed to erosive forces longer than the lower parts and the wave and current flux will be greater on the upper sections (as long as the strata is not overturned, which it is not in this case). In all instances the exposed surface should exhibit an erosional slope lower than the bedding plane. This is supported in Figure D6 where the slopes measured both offshore from the bathymetry data and onshore from in-situ dip measurements upsection along a line perpendicular to the fault. The offshore apparent dips, calculated from the surface slopes obtained from the bathymetry data, are significantly lower than the upsection onshore measured dips. Note these onshore dips are not at the fault, where the dip does increase, but still far enough away to represent a substantially steady state slope. These data in Figure D6 are from the more northern section of the structure where the offshore structure is a simple tilted surface and can be traced upsection to a corresponding location onshore that remains on the same side of the fault, striking in the same direction, and the simple tilting observed is expected to result in a relatively consistent set of dip angles, but as seen the onshore dips are all much higher than the offshore slopes along roughly the same transect. The same difference in amplitude of slope angles persists in the southern section where the offshore folding is more complex. Similar results, that is offshore angles much lower than onshore angles, were reported by E. Miller and students, (E. Miller, 2017 personal communication with Kim Blisniuk). This strongly suggests the offshore slopes are not true dips, rather have been eroded so as to display surface angles lower than the bedding plane angle. It is necessary to compensate for this erosion effect in order to get an accurate bedding angle across all parts of the folded structure.

There are multiple ways to estimate the compensation factor, CF, in Figure D4. One is to use the data in Figure D6, although that has a large uncertainty and represents only one of the several situations encountered. Another is to individually measure in-situ strikes and dips along all, or a large number, of the folded layers, a daunting task considering they are under sea depths up to 40 m in a relatively treacherous area of the sea and the elderly author is no longer a qualified scuba diver. The method employed here is to use criteria imposed by the expected shortening and the layer exposures observed by the bathymetry data to constrain the CFs.

It is noted that the folding starts along the red line in Figure D8. Southwest of that the strata are uplifted but are not significantly folded. The first obviously folded layer is labeled “layer 8” in Figures D1 and D8. This layer is seen to be overlain by other layers, labeled 1 to 7 in Figure D1, in the syncline portion of the structure. Those layers are not exposed as folded layers southwest of the layer 8 structure so when we calculate the structure starting from the red line in Figure D8 we will be reconstructing layer 8. However, layer 8 does not remain exposed all the way to the northern limit of the area of interest shown so in that case the reconstructed surface will reproduce a layer lower in the strata and that also will be taken into account below.

The first constraint to consider is the expected shortening. The angle of the restraint on the south end of Pillar Point Bluff is the appropriate restraining angle for the region of interest. Various measurements of this included the fault mapping south from PPB from the USGS mapping, alignment of the visible ocean bottom scarp, Figure 14 in Johnson et al 2018, and the trend along the Middle Strand using various locations mapped in this report found:

trend south from the PPB:	333.0^{o}	std dev	0.7
Middle Strand trend:	319.6^{o}	std dev	0.9
Thus, restraining bend angle:	$13.4^{o} \pm 1.1$		

This is obtained by fitting the model shortening to the theoretical shortening expected based on the 13.4^{o} restraining bend angle as follows:

D2 $\quad$ Expected Shortening $\simeq$ d x 2 $\sin(13.4^{o}/2)$

Where d is the distance along the fault into the restraining bend. As shown in Figure D7 a good fit is obtained across the full length from 3800 to 4900 m when using, in this case, two CFs of 2.1 and 1.3 as will be discussed below. The model shortening is the surface length over the reconstructed surface minus the horizontal distance from the start of the folding to the fault. The surface length is simply the sum of segment lengths, L_i:

D3 $\quad$ $L_i = \Delta x_i / \cos(\theta_i)$

Where Δx_i is the length of the segment and

D4 $\quad$ $\theta_i = \tan^{-1} (CF * s_i)$

with s_i the measured maximum slope of the segment and CF the compensation factor. Note that s_i is the slope and not the angle, i.e. the tan (slope angle).

This neglects effects from flexural slip, buckling, rotation, or volume changes, but with the relatively small fold angles and keeping within the same style of folding (that is, in this section where we traverse the same anticline-syncline-anticline structure) these appear to be relatively small and consistent along fold lines. The shortening in Figure D7 appears to go to zero around 5000 so that is made the starting point for the bend which fits well the mapping of the intersection of the Middle Strand with the SGF-E approaching from the south along an azimuth of about 333°.

A second constraint is from noting that layer 8 in Figures D1 and D8 is traceable through most of the folded structure. Thus, besides knowing the elevation of layer 8 where the folding calculation starts, the red triangles just to the right of the red line in Figure D8, the elevation of layer 8 is also known along the entire exposed expression of it including the segment where it is exposed between the furthest offshore anticline apex, here called anticline 1, and the syncline apex and again between the syncline apex and the near-shore anticline 2 apex. Thus, we can compare the reconstructed layer 8 folded structure from any model to the known elevations at the locations where it is exposed and labeled in Figure D8. In Figure D9 the black circles are the elevations from the bathymetry data, the red triangles in Figure D8, at points where the profile lines cross the locations of the exposed layer 8. The red diamonds in Figure D9 are elevations at those same locations from the model using two CFs of 2.1 and 1.3. Along the west side of the anticline 1 the measured and model results are set equal as reference starting points. Then the deviation of the model points from the actual elevations along the two sides of the syncline in Figure D9 represent the degree of disagreement between model and actual at those locations. That deviation is somewhat easier to decipher in Figure D10 where the elevation differences are compared in cross-section looking NE toward the fault with the same data as in Figure D9.

South of about 4250 m the location of the layer 8 exposures along the east side of the syncline, the orange triangles in Figure D8, are no longer covered by the bathymetry data. However, the exposure is visible at low tide near the surface of the ocean and in other visual databases, such as GPS Toolbox and Google Earth, and Google Earth is used to measure the locations and elevations along those profile plots. Since the average slope for the profiles in this section is determined by the model the profiles can then be extrapolated to the location where the exposure occurs as shown in Figure D8 and the results are included as orange triangles in Figure D10. There is somewhat more uncertainty in these extrapolated results, mainly due to uncertainties in determining locations, but they provide an additional check of the accuracy of the model and are used to constrain the compensation factors.

A third constraint is the plunge of the fold axes. From the pattern of the anticline and syncline structures in Figures 2 and D1 the fold axes of both the anticline and the syncline exhibit classic shapes indicating they plunge toward the SE. (It is acknowledged that they actually plunge to the SE relative to the erosional plane of the seafloor, which itself slopes seaward and slightly NW. However, the northwestward slope, typically less than 1^o, is minor relative to fold axes plunges on the order of 10^o and doesn't significantly alter the argument.) Another check on the model results is thus a comparison of the trend of the peaks and valleys in the reconstructed fold axes to the expected plunge direction and amplitude.

A separate measure of that plunge is included in Figures D11 and D12 which are plots of the axis profiles obtained by digitizing the elevation profiles in Google Earth along the anticline 1 and syncline axes - which are not along straight lines rather follow the implied peak axes as shown by the axes in Figure D1 - and reconstructing the layer 8 surface similarly to what is done for the transects perpendicular to the fault except the CF is set to 1 due to the axes being nominally perpendicular to the wave erosion direction. Figure D11 shows the anticline 1 axis plunges about 11^o SE and in Figure D12 the syncline plunges about 13^o SE. For comparison, using the same CFs as reported in Figures D9 and D10, the anticline peaks for layer 8 shown in Figure D13 shows the anticline peaks plunging 11^o SE, in agreement with Figure D11, but the syncline valleys in Figure D13 are plunging at a small angle to the NW.

It should be noted that the profiles along lines below about 4100 m do not represent layer 8. In Figures D1 and D8 it is seen that in the northern end of the western area of interest where the calculation of the profile begins the trace of layer 8 gets less distinct then disappears below the sand deposits going north. In that region the layer being profiled by the modeling then becomes one of the lower layers and that causes both the anticline peaks and the syncline valleys reported in Figure D13 to represent layers lower in the strata column for lines below about 4100 m. This is in agreement with the plots in Figure D10 and in Figure D13 where below 4100 m both the anticline and syncline peaks decrease.

The model profiles shown in Figure D9 tend to have slopes that are relatively constant over the length of each rise and fall region. The average slopes tend to increase for each segment from the south to the north resulting in the amplitude of folds also increasing from south to north. Figure D15 shows three representative sets of slopes across profiles for the north end, line 3800, the central region, line 4300, and the south end, line 4700, and illustrates the method of using the ratio of rise 2/rise 1 to equal the ratio of fall 2/fall 1 to project the slope on the east side of anticline 2. The ratio of slopes, rise 2 / rise 1 and fall 1 / rise 1, tend to increase from south to north as shown in Figure D16. This suggests the slope on the east side of anticline 2 will also follow a similar pattern which is why the ratio of slopes in equation D1 is used to project the anticline 2 slope. The projected slopes result in a surprisingly tight dependence on distance, Figure D17.

Figure D17 is the objective of the modeling, the dependence of bedrock slope on distance along the restraining bend on the east side of anticline 2. It means that for each km of translation along the Middle Strand Fault the bedrock bedding plane rotates 20.8^{o} clockwise. These are referred to as slopes rather than dips because they are along the direction of the profile lines, perpendicular to the fault not necessarily along dip, however, since the strike along shore in this region, as seen in Figure 23, is generally within 25^{o} of the fault trend the dip and apparent dip generally differ by less than 3^{o}.

The calculated slopes in Figure D17 follow a trend with distance consistent with the trend of the measured dips also included in Figure D17, within about 11% in this case, and actually have a significantly tighter distribution than the measured on-shore dips which is reasonable since the model results are based on averages over the length of a given segment of the folds and over multiple lines while the individual measured dips include local variations possibly due to local fracturing and faulting. The correlation between the measurements and model and the well-defined trend of model results provide confidence in the projected slopes and more broadly in the dependence of bedrock slope on distance and with the cause of that dependence being folding due to the restraining bend. Such confidence would certainly not attend the measured results alone.

Slope Compensation

An important part of the modeling is the bedrock slope compensation factor depicted in Figure D4, the ratio of the bedrock slope to the measured erosional slopes. It is unlikely the same compensation factor applies to all erosional surfaces for several reasons. For instance, the shoreward-dipping surfaces will experience a different eroding current than seaward-dipping surfaces, physical characteristic variations between layers result in different erosional rates resulting in variations in the resistant/erodible erosion ratio, strike-parallel and strike-perpendicular surface exposures to the eroding current also will likely experience different resistant/erodible layer contrasts all producing different compensation factors. In addition, the depth of the sediment partially covering eroded surfaces also results in different measured slopes. A consequence of this is that while a single CF applied to all erosion surfaces can produce an excellent fit to the expected shortening curve over its full length, see for instance Figure D18 for the case of a single CF = 1.65, nevertheless, the layer 8 elevation, Figure D19, and the folding axes plunge, Figure D20, from that model are not in good agreement with actual results indicating the reproduced uneroded surface of layer 8 is not accurately depicted with the single CF. Absent comprehensive in-situ strike and dip measurements a more precise modeling of the folding, and thereby of the compensation factors, is desirable. Several geomechanical modeling software packages are available, such as the MOVE suite from Petroleum Experts, all with advantages and limitations and long learning curves, nevertheless, it was decided the quickest path to a quantitative, site-specific model producing the functional dependence needed for the current purpose was the multi-constraint geometric analysis employed here.

A typical goal of a reliable and useful model is to use the fewest number of independent variables that reasonably represent the results. As such, it is noted the direction and energy of wave and current incidence is significantly different for surfaces dipping oceanward and those dipping shoreward so representing those two directions with different CFs is reasonable. After exploring a wide range of parameters, the CF combination of 2.1 and 1.3 for oceanward and landward dipping surfaces, respectively, improved significantly upon the single CF model by producing an overall reasonably good fit to most parameters and are reported above in Figures

D7, D9, D10, and D13 for shortening and layer 8 elevation and plunge. For instance, while comparison of Figure D7 to Figure D18 shows shortening can be well fit for the two cases, Figure D19 shows elevations of layer 8 below actual values and much lower than the two CF model in Figure D10 and much lower than the actual values, and Figure D20 has even more plunge of the syncline axis in the wrong direction than does Figure D13. Some of the measures of model results for different CFs are compared in Table D1.

Issues of optimizing CFs for three constraints; layer 8 elevations along both the west and east sides of the syncline as well as the shortening, are illustrated in Figure D21. These are results for just one of the transect lines, 4320, where bathymetry data is available covering the layer 8 exposure location on both sides of the syncline. Selecting one of the CFs the other CF can then be adjusted to perfectly match a given criteria and the set of CFs for matching a given criteria are plotted in Figure D21. For instance, the gray line and triangles outline where the shortening curve is fit and indicate a second order curved line such that as CF1 is increased the corresponding CF2 decreases. To fit layer 8 elevation on the west side of the syncline the orange lines labeled L8-2 indicate that as CF1 is increased CF2 also needs to increase. Where the orange line and the gray line cross both the shortening and the west side layer 8 elevation would be met. However, the blue line labeled L8-3 matches the layer 8 elevation on the east side of the syncline and it does not pass through the intersection of the other two lines and, in fact, does not cross the L8-2 line within a realistic range of CFs. A reasonable compromise is to use a point midway between the two intersecting points that also lies on the shortening curve, the black triangle in Figure D21.

The physical interpretation of the optimization process is that as a CF is increased, the calculated slopes on the corresponding side of the fold increase. So, as CF1 is increased it steepens the ocean facing side of the fold, and CF2 controls steepness on the shore facing sides. To match a given shortening it makes sense that as one side of the fold is steepened, the other side needs to decrease to maintain the same total shortening. That is what is shown by the gray line in Figure D21. For fitting layer 8 elevation on the west side of the syncline there are two fold segments determining it. As the west facing side of anticline 1 is steepened, by increasing CF1, then the anticline peak is raised and the slope on the east side of anticline 1, controlled by CF2, also has to steepen to get back down to the required layer 8 elevation. Layer 8 elevation on the east side of the syncline has similar considerations, but with additional oceanward and shoreward facing segments which provide a separate constraint on the steepness of the two sides, so it follows a separate optimization path. As Figure D21 illustrates, it is unlikely to satisfy all three constraints with just the two parameters on a single transect, and each transect will also introduce separate optimization parameters. Considering this, the results provided by just the two constant CFs, 2.1 and 1.3, shown in Figures D7 through D10 provide a reasonably good fit using a minimum of parameters.

The fourth constraint, the plunge of the two fold axes, involves the evolution of the peaks over a range of transect lines. The anticline peak is dependent on the slope of just west facing surfaces, amplified by CF1. The rise of the first anticline alone is used to determine CF1 if the plunge of the anticline 1 axis alone is used as a constraint. In this case a CF1 of 2.1 gives an anticline 1 axis plunge of 11^o SE, matching the separately measured anticline axis profile, Figure D11. The Plunge of the syncline is then determined by the slopes measured amplified by CF2, but that same CF2 also needs to be adjusted to fit the layer 8 elevations on both sides of the syncline. One issue encountered is that the measured slopes do not produce a syncline axis plunging to the SE with any CF2 above 1 and a CF below 1 is considered not realistic. A SE plunging syncline axis is obtained if the CF1 is raised high enough to produce a very strongly plunging axis and then CF2 lowered enough to avoid counteracting this plunge so much as to make it plunge NW. For instance, the set of CF1 = 2.6 and CF2 = 0.6, does produce a 6^o SE plunging syncline axis, but the anticline plunge is quite high, 13^o SE, the layer 8 elevations on either side of the syncline are all much too high, and a CF below 1 is not realistic.

At least part of the problem with the syncline plunge direction is likely related to the syncline exposure seen in Figure D1 or D8 becoming shallower as it approaches Pillar Point with the surface exposures being relatively high, nearer the surf zone, so they are not yet well delineated by long term erosion. That is, the erodible and resistant layers have not yet been well discriminated and the slopes not well defined. This is seen in the bathymetry data in Figure D1. This could explain the lack of a syncline plunge to the SE. In any case, it suggests the syncline plunge may not be well described and should not be a priority constraint. This would also contribute to the shortening calculations, where the shortening calculations could be up to an estimated 5-10% higher at the far southern end, and the layer 8 elevations on the east side of the syncline in the extrapolated southern section, where the calculated elevations would also likely be somewhat lower. This difference is relatively minor and does not significantly alter the model.

An alternative optimization strategy is to use a separate set of CFs for each transect. That is, each line could go through the same process shown in Figure D21 for the line at 4320 m where the shortening is exactly fit and with a compromise for the specific elevations on the two sides of the syncline. When that is done the set of optimized CFs for each profile is shown in Figure D22. The correction factor for ocean facing slopes, CF1, is in the range of 1.9 to 2.4 and tends to decrease slightly going south along the restraining bend, whereas that for the landward facing slopes, CF2, increases in the range of about 1 to slightly over 1.5. The results summary shown in Figure D23 show layer 8 elevations closer to the actual values, as expected since they are now individually optimized, and the axes both plunge to the SE, the anticline axis about 9^{o} but the syncline axis less than 3^{o}. The bedrock slopes on the east side of anticline 2 in Figure D23 show a similar trend to the two CF result, Figure D17, but with a slightly lower trend of angle versus distance, 0.019 deg/m. The similarity of the coefficient to the two CF result suggests the model is relatively robust, nevertheless, there appears little justification for using a separate set of parameters for each line, other than it tightens the distribution, and so the two constant CF result appears more reliable and preferable at this point.

One last comparison is made with the case of using no CFs. Although that is considered an unrealistic case it is included here for completeness. In this case the CFs in the model are set equal to 1, no amplification of slopes. In Figure D24 the calculated shortening values are less than half that needed to fit the expected shortening. The calculated layer 8 elevations are all less than measured by up to and over 100 m, Figure 6. The anticline axis plunge, Figure D26, is too low and the syncline axis plunges even more in the wrong direction than for the case of two CFs, Figure D13. Besides being essentially physically impossible it also produces unrealistic results and is not used.

Table DI summarizes the results of this Appendix and Figure D27 shows the probability density function, PDF, for slip rate as proposed by Zechar and Frankel, 2009. The PDF is derived from a density function of offset and age density functions in Figure D27b and D27c, respectively, that were derived by combining four folding model profiles as shown in Table DI and the three age results where a mean was calculated in Table III of this report. The two CF model is in general the most reliable result, this is highlighted in Table DI, but the other CF schemes are included for comparison and to give an idea of the possible range of coefficients for less likely cases. The 1 CF and the 2 CFs and the preferred options in Table DI give a range for the slope coefficient of 20.5 to 25.9 deg/km, an average of 23.1 and standard deviation of 2.3.

Table DI: Folding model results, preferred models in bold.

Model	CF1	CF2	Shortening Deviation	L8 Elev AC1-SC	L8 Elev SC-AC2	AC Plunge	SC Plunge	Slope Coeff
Type			m/pt	m/pt	m/pt	Deg, Dir	Deg, Dir	Deg/km
1 CF	**1.65**	**1.65**	**1.6**	**35**	**36**	**9 SE**	**12 NW**	**25.9**
2 CFs[1]	**2.15**	**1.5**	**1.9**	**16**	**16**	**11 SE**	**8 NW**	**23.8**
2 CFs[2]	**1.97**	**1.36**	**1.6**	**14**	**14**	**11 SE**	**7 NW**	**22.2**
Var CFs[3]	**Var**	**Var**	**0**	**5**	**7**	**9 SE**	**2 SE**	**20.5**
2 CFs[4]	2.6	0.6	3.1	41	78	13 SE	6 SE	10.1
No CF	1	1	9.2	23	24	6 SE	7 NW	17.2
Alt Meas						11 SE	13 SE	21.5
Average of preferred models								23.1 ± 2.3

[1] 2CFs optimized with 14.5° restraining bend.

[2] 2CFs optimized with 12.3° restraining bend

[3] CFs optimized for each transect individually

[4] 2CFs chosen mainly to obtain a SE plunging syncline axis

The modeling results in SI-D address the segment of the fault from the beginning of the restraining bend on the south end to where the fault begins crossing over to the Fitzgerald

Fault. This point is coincidentally near where the Middle Strand has been exposed and conveniently where the slope of the wavecut platform is discernable in a cliff face, Figure D1. North of this segment the Middle Strand bifurcates with one strand continuing northwestward along about the same azimuth and the other bending eastward along a releasing series of faults to the Fitzgerald Fault. Both strands eventually proceed sub-parallel northward offshore. Figures D30 a and b show the shortening calculated as discussed in Appendix D over the length of the digitized bathymetry data and aligns it with points along the Middle Strand fault mapped in this report. The shortening plot in Figure D30b includes model results for the individual lines plus a trend line that captures the major features. The trend follows a pattern explainable by the results of Appendix D and the mapping presented in this report. Starting on the southeastern end and proceeding northwestward (right to left in Figure D30); at around 5000 meters the western plate, moving NW, enters the restraining bend and proceeds along the bend until about 3800 meters. This is the section described well by the model presented in Appendix D where shortening continuously increases as the plate moves into the restraining bend. Between 3800 and 2600 meters the fault bifurcates with a releasing bend duplex crossing over to an eastern fault path (the previously identified Seal Cove Fault). The shortening declines in this segment by almost half since less shortening is required west of the Middle Strand to accommodate the fault north of the releasing duplex. How much it declines depends on factors not quantified here, such as when the restraining bend was formed, when the releasing cross over started, and the amount of shortening taken up between the two strands. However, since the distance between the two strands is about half of the distance to the projection of the non-restrained path a reduction by half is reasonable. It is also noted that this segment is where the offshore folding transitions from the anticline-syncline-anticline structure on the south end to a simple tilting. By about 2600 meters the cross over is complete and the two faults proceed sub-parallel to the northwest. Over the segment where the two strands of the fault proceed in parallel the shortening is nominally constant.

On the northern end the shortening declines coincident with where the projected fault begins bending northward and where also the baseline for the digitized data base deviates from the Middle Strand extension. Thus, the full curve in Figure D30 is reasonably explainable by the geometry of the faulting. This further supports both the mapping of the releasing bend faults and the model used to calculate the shortening.

Now we can make use of the observation that the abandoned wavecut platform is currently tilting landward 4.5° ± 0.5, Figure 55. This is along a trend of 230° ± 12°, nominally perpendicular to the Middle Strand. When the wavecut platform was abandoned it would have sloped seaward. After it was abandoned, and since we know it is a dextral strike-slip fault, the strata on the west side of the Middle Strand has moved northwestward, further into the restraining bend, and according to our result in Figure D17 the strata, including the wavecut platform, would have rotated clockwise, going through horizontal and eventually tilting landward just as we now see it. How far it has rotated depends on the wavecut angle at the time of abandonment which we cannot directly measure. Wavecut platforms are reported to typically slope from 1 to 4° seaward, Johnson et al, 2018. However, we take as better local indicators the modern wavecut platforms in this area with a Purisima bedrock and a sampling of those is shown in Figure 67 to give an average angle of 3.1° with a standard deviation of 1.2°, Figure 67. The net wavecut platform rotation would thus be expected to be 4.5 – (-3.1) = 7.6° (6.4 – 8.8 after adding distribution standard deviations in quadrature). To calculate the distance moved since the wavecut platform was abandoned, the probability distribution functions of the coefficients obtained by several results of the model were combined as proposed by Zechar and Frankel, 2009 as shown in Figure D27. The result is a median of 326 m with a 68.27% probability range of 264 – 393 m and a 95.45% probability range of 205 – 466 m. In the preceding section the Purisima wavecut platform was dated to have been abandoned 49.7 kya (45.4 – 54.4), Figure D28. The probability density function for the slip rate is then determined as proposed by Zechar and Frankel, 2009 and shown in Figure D29. The resulting horizontal slip rate for the Middle Strand then is determined to have a median of 6.5 mm/yr with 68.27% and 95.45% ranges of 5.2 – 8.0 and 4.0 – 9.7, respectively.

There are strands that appear both east and west of the Main Middle Strand, MF, in Figure 4, namely the WWF and EWF. The results above are for the total distribution across all these strands since the model calculation is for the east side of anticline 2 without consideration of how many faults take up the offset. The angle of the restraining bend and the shortening calculation do depend on the fault path used and the shortening determines the compensation factor and for that we continue to use the Middle Strand since it is the average middle path, is the most prominent, and can be traced south across Half Moon Bay. The traces for the other two do not extend as far so even if the local fault angle is slightly different the effective angle for the overall restraining bend from the south is that for the MF.

Appendix E:
Half Moon Bay

Mapping from this report is here used to offer insight into the formation of the Half Moon Bay Syncline as well as the Moss Beach Syncline. One finding, based on Leighton et al, 1971, in this report is that granitic bedrock underlies and is responsible for the Seal Cove Highlands. It was also pointed out that the Consultant's Faults Trend 2, which coincides with one of the Leighton lineations, borders this granite bedrock and can be extrapolated to a granite outcrop on the north shore of Moss Beach, as shown in Figure E3. Support for that bedrock mapping from magnetic anomaly mapping is discussed in Appendix F. In this Appendix the granite bedrock is presumed to extend from the Highlands bedrock to the granite exposure along shore bordered by the blue line in Figure E3, a distance of about 1 km.

The Half Moon Bay Syncline is a gentle westward plunging syncline in Purisima along the Pacific Coast east of the SGF-E (Lajoie, 1986). Surface expression of this syncline extends from the northwest end of the Half Moon Bay Airport about 17 km southeast to approximately Purisima Creek, Figure E7. The Half Moon Bay Terrace surface slopes about 0.3° on the northwest side and about 0.5° on the southeast side. The Purisima surface follows a similar pattern, blue circles in Figure E7, and the bottom of the syncline is below sea level, forming Half Moon Bay, which accentuates topology that might otherwise be almost indistinguishable.

The granite bedrock underlying Seal Cove Highlands has been pointed out in this report to be the progenitor of Pillar Point Bluff by deflecting the Middle Strand into a restraining bend that then produced the offshore folding west of the SGF-E as well as the uplift of PPB as outlined in Figure 70. In this Appendix it is proposed this also is responsible for the formation of the gentle syncline that forms Half Moon Bay as well as Moss Beach Syncline.

The SGF is the western-most component of the San Andreas Fault System, SAF. Figure E1, (copied from the USGS report 037-046 by Ryan et al), gives a view of this and shows that wedges of Permanente (primarily limestone, LaRue et al, 1989) and Salinian (primarily granite, Wakabayashi and Moores, 1988) Terranes are interspersed between SAF and SGF.

Figure E2, also from Ryan et al, shows the geodetic plate velocities relative to a stable central North American plate across the SF Bay region. The Pacific Plate has the largest NW directed velocity, about 44 mm/yr, which is then subsequently reduced crossing each of the several right-lateral strike-slip faults in the region, presumably reduced between successive slices of plate by partitioning and friction across each fault. The Holocene geodetic velocity difference across the SGF-E fault is on the order of 4 mm/yr. This is within range but on the low end of the 6.5 mm/yr average (4.0 – 9.7) since MIS 3 geologically measured here. The combination of Figures E1 and E2 indicates there is a slice of plate west of the San Andreas Fault and east of the San Gregorio Fault, which will here be referred as the Pilarcitos plate, that contains Salinian Terrane (Montara Granodiorite in this case) and that slice is being funneled into a narrower width between faults as it moves north. Exactly how the fault moves, or the terrane slivers respond as they move NW at different rates is not certain. Nevertheless, it is reasonable that the Salinian Terrane would eventually be forced into contact with the Pacific plate west of the SGF-E. This appears to be what has happened at PPB.

By all measures the strength of granite is greater than that of the sandstone or mudstone typical of the Purisima fm; for instance, unconfined compressive strength, rigidity, and shear strength are typically 2 to 20 times larger. As the granitic protrusion pushes into the SGF-E path this path continually adjusts, typically by faults deflecting into the Pacific Plate around the granite in the Pilarcitos Plate and faulting the Purisima. That response produces the mapping and timing of faults outlined in this report. However, the effect is not confined to the west side of the SGF-E, it also must have effects on the east side.

The map of granite bedrock is important in interpreting the geology east of the SGF-E. While most maps show the Montara granodiorite underlying the foothills east of Half Moon Bay

Terrace, Pampeyan 1991, as shown in Figure 3, they are not certain on what bedrock underlies the terrace deposits in this region. Kennedy et al, 1985, found Purisima in their borehole near PPB, and that site is assumed to be near the Koehler et al, 2005 trench sites based on logistics, Figure 4, but the exact location of that sample is not known. The mapping in this report finds Purisima (or similar marine sedimentary rocks) along the HMB coast from PPB south to Ano Nuevo. However, adjacent the NE side of the Moss Beach Syncline the exposed bedrock in the shoreline changes to granite at North Point and remains such to Montara Beach, about 2 km, Figures E3 and E15. Leighton et al, (1971) identified granite bedrock underlying part of Seal Cove Highlands, Figures 65 and E3. It is not certain where or even whether granite exists between the two pink outlined areas in Figure E3. Pampeyan, 1994, shows Km below a thin layer of Tp on PPB and then a much thicker Tp without Km below it west of the sea cliff with Km underlying HMBT east of the fault. However, we know from Kennedy et al, 1985, that Tp underlies at least some of HMBT and certainly further south along the coast Tp visibly underlies HMBT throughout, so we should not assume Km underlies Qmt in the HMBT adjacent PPB. An older gravity map, Figure E9 copied from Pampeyan, 1994, shows an elevated, but steeply decreasing, gravity at PPB with a possible bulge of slightly higher gravity near the northern end of PPB, suggesting granite from Montara Mountain may extend to this region and extend slightly further into the northern end, but the map is not detailed enough for adequate resolution of the granite.

Two creeks within this area, the San Vicente and an apparently unnamed creek that empties at the Moss Beach Syncline, referred to here as MBS Creek, have deep riverbeds cut into Qmt and were searched for bedrock. Massive granite, presumed to be bedrock, has been confirmed about 1 m down in MBS Creek near the sea outlet as shown in Figure E3. This is about 300 m from the beach where granite outcrops, how much further south granite extends is unknown. Otherwise, bedrock has not been found in the creeks within the top meter of sediment. The sediment in these creeks is substantially granitic in origin. [f.i. of 52 clasts from MBS creek adjacent the church on California Ave in the size range of 5 to 30 mm 46 were clearly crystalline/granitic, 3 appeared to be sedimentary rock, the other 3 were uncertain. Of the 46 granitic clasts about 1/4 appear to be typical of the granite exposed along the Moss Beach coast as judged by the color and biotite content.] That is not strong evidence of a local granite bedrock since these are only a km or two from the foothills where the sediment source is mainly Montara granite. Nevertheless, for current purposes, it is here presumed that granite bedrock underlies Qmt as schematically illustrated in Figure E4. The west limit is coincident with Consultant's Faults Trend 2 and its extension to the western exposure of granite on the Moss Beach shoreline. The southern limit within PPB is assumed to be the scarp defining the southern edge of the Seal Cove Highlands, which approximately parallels the Pillar Point Bluff trail in the Fitzgerald Marine Reserve on the north end of Pillar Point Bluff. The eastern limit goes to the foothills (and, of course, well beyond) but limited to being northwest of a line in the HMB terrace shown by the yellow markers in Figure E3. Appendix F, following, includes magnetic anomaly scans that find a slowly decreasing amplitude on either side of the projected transition points in both Seal Cove Highlands, Figure F10, and along Airport St, Figure F14, that are in reasonable agreement with the assignments in Figure E3 thereby supporting, although not confirming, this proposed granitic outline.

The limit crossing HMB Terrace just north of the airport is suggested by the NW-SE profiles across the Half Moon Bay Terrace in the vicinity of the Half Moon Bay Airport, Figure E5. This profile shows a smooth rise from the Half Moon Bay shore to about 3 km NW and then levels off, except for the San Vicente river drainage, before reaching the sea cliff. The airport has certainly been graded, but such disturbance is expected to be inconsequential on this scale. The slope of this Qmt surface from the shore north of less than 1^o fits well the Purisima bedrock slope estimated in this region, Figure 34. Near the northern end of the Half Moon Bay Airport the profile has a slope break and becomes subhorizontal north of that, suggesting a bedrock structure change at this latitude as the most likely cause for such a slope break. This slope break is here taken as a change from Purisima to Montara Granodiorite as suggested in Figures E4 and E5 and supported in Appendix F.

It was pointed out in the Stratigraphy Section and seen in Figure E10 the elevation in the Seal Cove Highlands is lower than in the bluff south of that, but higher than in the Seal Cove Lowlands which is proposed to be a pull-apart graben. Also, the location of the prominent eastern scarp in the Highlands extends about 110 m further east and the scarp dip is reduced about 9^o from the Purisima bedrock section adjacent to the south. Combined with the Leighton et al, 1971 findings, these all suggest that the Seal Cove Highlands result from a granitic bedrock versus the Purisima bedrock for the remaining bluff sections north and south. The location where the slope across HMB terrace flattens is adjacent this Highlands section as shown by the yellow markers on the map in Figure E3. Proposed here is that Montara granodiorite bedrock likely underlies this region and the two known Km regions are connected something as shown in Figures E4 and E6, although at depth they may have much more substantial connection. The shading in Figure E6 stops at the foothills, but granitic bedrock is understood to continue into and underlie all of the foothills in this area.

Figure E6 shows a Montara granodiorite, Km, spur extending from the foothills to Pillar Point Bluff with a point of it protruding into the Seal Cove Highlands of PPB. It is this granitic protrusion that appears to have caused the SGF-E branch to deflect into a restraining bend. As a restraining bend it restricts motion on both sides of the fault plus the granitic block on the northeast side becomes a separate obstruction in the Pilarcitos plate since it becomes partially coupled to the Pacific plate. Fault gouge and breccia in the granite outcrop observed at the red marker near the top of Figure E3 and pictured in Figure E13, combined with a layered intrusion layer in a seam a few meters east of that gouge, Figure E14, indicates faulting oriented about 316^o $\underline{+}$ 10, dipping about 50^o SW. About 130 m west of this location is North Point, a point adjacent the MBS in Figure 2, which consists of a cove bordered by sandstone one the west and granite on the east as shown in Figure E15. The erodibility within the cove suggests a fault contact although some locations display a depositional contact (May et al, 1976). Between North Point and the granite fault near Vallemar Bluffs are a series of granite, sandstone and conglomerate subvertical layers that display an enigmatic interface suggesting a complex contact history.

The Middle Strand fault has been shown to divert around the protrusion in the Highlands, as mapped in this report, yet the granitic spur must still absorb some of the NW-directed force of the Pacific Plate as depicted in Figure E6. This additional force on a localized component of the Pilarcitos plate applies an extensive force on the Pilarcitos plate southeast of this location and a compressive force northwest of it.

The extensive force on the bedrock SE of this location is then consistent with the formation of the gentle syncline across Half Moon Bay as depicted in Figure E6 and profiled in Figure E7. The granitic bedrock anchors the northern end of the syncline in Figure E7. The southern end is between two gravity lows, but adjacent a gravity high, which coincidentally coincides roughly with the Purisima type locale, Figure E9. It is also near a normal fault at Cowell Ranch that is sub-perpendicular to the SGF-E, Figure E11, which appears to be an extension fault resulting from this configuration. This SE dipping bedrock near Cowell Ranch, (note marker in Figure E7) displays thin layers of erodible marine sedimentary rock lying in the surf zone yet remains exposed and angular indicating its relatively recent formation. It lies near the southern limit of the HMB Syncline. The profile in Figure E7 represents the Qmt surface. However, the Purisima elevation profile in Figure E7, blue circles, suggests the Purisima profile is substantially sub-parallel to the Qmt surface above sea level and corresponds to Tp where the profile goes below sea level.

The Moss Beach Syncline is now seen as formed in the wedge between the western edge of the granite and the Fitzgerald Fault as arranged in Figures E3 and depicted in Figure E8. The Purisima remnant, riding southeast on the Pilarcitos plate, is squeezed into the wedge between the fault and the granitic bedrock wall producing a triaxial compression resulting in orthogonal shear plane failures oriented as shown in Figure E8. This is a welcome finding since this Moss Beach Syncline previously didn't appear to be in the right place because the Fitzgerald Fault does not constitute a restraining bend at this location. So, it wasn't understood by the author why the tightly folded syncline formed there. Now it is clear. It is not the Fitzgerald fault alone that is causing it. The Purisima appears detached from whatever bedrock is below it, so it continues to be pushed SE into the wedge by the plate north of it as shown in Figure E8. The eastern arm of the MBS parallels the granitic wall around 333^o, and the western arm parallels the Fitzgerald Fault both exactly as would be expected from these constraints. This Purisima remnant has not needed to move very far relative to the granite wall during its compression to form the MBS. To get the folding required I estimate has taken on the order of 20m of relative offset which at the slip rate found in this report would take about $3X10^3$ years if the granite wall suddenly locked to the Pacific Plate. The wall likely has slowed but not stopped relative to the Pacific Plate, so the actual time of formation is probably longer than that.

Now an enigmatic set of faults within the Fitzgerald fault zone identified by Lohr et al, 2009 that were not parallel the main fault are also explained as shown in Figure E8 which is based on their Figure 4. They found sinistral faults oriented at about 265° azimuths intersecting dextral faults oriented near 0°. These are now consistent with a triaxial compression formed by the Purisima plate moving SE along about 130° between the granite wall at about 333° and the Fitzgerald Fault and causing shortening along about 312°. One of their hypothesized origins for these faults, was that “the faults formed under a different stress field than the main fault”, Lohr er al, 2009. They rejected that explanation in favor of one involving a complex rotation of the plate during separate faulting episodes. It is now evident it is indeed likely a result of a different stress field than the main fault. The pattern of fractures in bedrock from uniaxial compression, let alone triaxial compression, is not readily predicted, see e.g. Chakraborty et al, 2019, so it is not surprising that the sense of fault offsets appears somewhat different from what might be expected from the compression arrangement in Figure E8, nevertheless It is consistent with an expected orthogonal set of shear faults symmetric about 312°.

If the coupling of the granite protrusion with the Pacific Plate applies compression northwest of the contact, then there may be further evidence of compression north of the MBS. Ryan et al, 2008, show that there is an extension caused graben along the SGF on the north side of the Golden Gate entrance called the San Andreas Graben, however the stress situation just north of where the SGF-E exits land at Moss Beach was not clear from that report. Certainly, the MBS folding is caused by compression so there is compression on the southern end. A review of the near-shore topology using Google Earth profiles indicates there are indications of compression folds northwest from MBS, Figure E12, where lobate folding is suggested in the profile. No similar profiles are found along the near-shore further north from Montara Beach to Ocean Beach nor south from the Marin headlands and Bolinas area. The northern profiles indicate only smooth drop off across the near-shore extending to the deeper entrance trench. This suggests that compression is being absorbed along the MBS section of the plate, but not along the northern section. This is as would be expected if that section of the

Pilarcitos Plate had previously been under extension that recently shifted to compression at the southern end. Immediately after switching from an extension to a compression regime across the plate between MBS and Marin headlands the first thing to happen is to start compressive folding at the southern end, where the obstruction is, and then that compressive folding gradually moves north as the previous extension is taken up, first to a neutral state and then to a compressive state that moves northward. Thus, there does appear to be a transition from compression near Moss Beach to tension near the Marin Highlands and it appears this transition has recently started on the southern end of this plate section but has not yet reached the northern end. This then suggests the onset of the compression that caused MBS is relatively recent, approximately the last 3 to 8 K years. Recent folding of MBS is also apparent due to the angularity of the faulted and folded strata without much erosional smoothing of the wavecut platform in the surf zone. (Coincidentally, the epicenter of the 1906 SAF earthquake is in the region where Pilarcitos Plate extension is here suggested to be transitioning to compression although any connection is beyond the scope of this investigation.)

As is now proposed the Montara granite block, having become wedged between the two plates, acts as an obstruction deforming the Purisima formation within both the Pacific and Pilarcitos plates. This obstruction likely also contributes to at least some of the gradual reduction in slip rates on the SGF recorded by Clark (1997) from 25 mm/yr in the Miocene to 16 mm/yr in the Pliocene and 6 mm/yr in the Holocene with a possible further decrease to the current geodetic rate difference across the fault of about 4 mm/yr. As the Pilarcitos plate continues to the NW (relative to the North American Plate) this granitic obstruction likely gradually pushes further into the Pacific plate increasing the frictional force which continuously reduces the differential plate motions, tending toward locking the two plates. Whether additional friction points have formed along the SGF-E is not clear, but it is likely this granitic obstruction has significantly altered the behavior of the SGF-E. How strongly this granite protrusion is coupled to the western plate is not known and is worth further investigation. It is pointed out in this report the Distillery Fault (which would be subparallel to any motion transferred to the granite fault) appears to have a slip rate that is a large fraction of that determined for the Middle Strand south of the granitic obstruction suggesting very little motion is currently transferred to the granite fault.

Another perspective, referencing the geodetic vectors in Figure E2, is that, depending on the amount of coupling between the granitic protrusion and the Pacific plate, the Pilarcitos plate sliver is more likely speeding up and approaching the Pacific plate speed. Hence the slip rate across the SAF might be expected to be speeding up as the SGF-E (as well as the Pilarcitos fault) is slowing down, particularly north of Crystal Springs Reservoir. It is reported that motion along the Pilarcitos fault has ceased since about 3 Ma (McLaughlin et al, 2007) which may also have resulted from the Montara Granite being squeezed between the San Gregorio and Pilarcitos Faults and forcing a tighter coupling with both adjacent plates across those faults.

The mechanics of the granitic protrusion presents a constraint on the granite configuration since a simple configuration as shown in Figure E4 could produce a substantial torque on the granitic spur tending to rotate it clockwise with a shear force tending to break off that spur and, depending on the center of rotation, that is, the fulcrum location, it could be projected to compress the eastern plate to the SE, the opposite of that observed. However, depending on the granitic configuration at depth and any faults within the granite bedrock, the fulcrum is more likely east toward Montara Mountain resulting in the applied stress forces as depicted in Figure E6 to produce the results observed. The gravity map of Figure E9 suggests the fulcrum likely is within the foothills or further east toward Montara Mountain.

One other comparison is made in Table EI of the area being folded times the fold height for the two sides of the fault, essentially a deformation volume. Generally, it is not practical to assign any conservation across the fault, such as energy or deformation, because the amount of energy absorbed by the subsurface plates on opposite sides of the fault is not known. Nevertheless, the area times fold height (a measure of surface deformation volume) gives a rough measure of change in potential energy that should be somewhat equivalent on the two sides if the deformation is confined to a relatively uniform, similar type rock, a thin layer that is deformed mainly by horizontal forces. In the present case, the deformation is indeed mainly of a relatively deformable Purisima layer near the surface on both sides of the SGF-E. Using rough measures of areas and surface elevation change (using the results of the model in Appendix D) the deformation volume on the west and east sides of the fault is about 3.1 km^3 and 2.3 km^3, respectively, reasonably similar given the roughness of the estimate, Table E I. The point being this appears consistent with a single mechanism causing the deformation on both sides. It can also be separately noted this is one more confirmation that the offshore folding to the west occurred at its current location and did not move there from elsewhere.

Table E I: Vertical Deformation Volumes estimated for each side of SGF-E.

Region	Area, km^2	Ave Elev Chg, km	Volume, km^3
Offshore Fold, SW Total	13.6	.23	**3.1**
Half Moon Bay Syncline	45	.05	2.3
Moss Beach Syncline	.12	.1	.02
NE Total			**2.3**

The conclusion drawn here is that a Montara granodiorite protrusion intersects the SGF-E fault path causing not only the restraining bend and attendant folding visible in offshore strata west of the SGF-E fault, but simultaneously produces extension on the Pilarcitos plate SE of the impact point resulting in extension causing the syncline that underlies Half Moon Bay as well as compression north of the impact point resulting in the Moss Beach Syncline. This conclusion relies on a granitic connection from the granitic bedrock in the Seal Cove Highlands to the Montara Mountain Granite underlying the foothills to the east and exposed along the Moss Beach shoreline. Support for such a granitic bedrock connection has been found in magnetic surveys reported in the next section, Appendix F, although additional confirmation would be helpful in this conclusion.

Appendix F:
Magnetic Survey

A preliminary magnetic survey of parts of Pillar Point Bluff and surrounding area was undertaken, and the findings are reported in this SI. This survey is informative but might best be used as an indication of what can be expected from a more complete mapping. The principal objective was to see if magnetic mapping could be used to outline the granitic bedrock region of PPB and the adjacent Half Moon Bay Terrace, with a secondary objective of characterizing and tracing faults. It was found that the magnetic contrast between the Purisima sandstone and Montara Granite is small and while some supportive information is obtained, it is not yet considered conclusive in defining the extent of the granite bedrock. However, faults were readily observed and characterized by the survey.

The survey uses a Geometrics 857 portable proton magnetometer with a Garmin GPS unit. This measures only the maximum or total field, no vector components. Figure F1 lays out the scan paths identified by Line numbers referenced in this Appendix and Figure F2 is a Google Earth map placing the scans in relation to previous mapped features and also locates noted anomalies. Figure F3 is expanded to more clearly correlate fault mapping from the magnetic survey with earlier mapping. Only one magnetometer was rented so a reference (base station) was obtained by returning to a fixed location throughout the day to record the diurnal variation. This is shown in Figures F4 and F5 where it is seen that diurnal variation is reasonably consistent and in agreement with other typical results so one equation is used to correct the amplitudes as a function of time of day. Since most of the data presented here is of line scans which were generally accomplished within an hour the diurnal effect is not a significant factor in the interpretation. The location chosen for the reference unfortunately had a higher amplitude and gradient than most of the typical scan regions but was nevertheless adequate for the purpose.

The Geometrics 857 magnetometer uses an 8 ft staff placed vertically on the ground with the magnetometer sensor on top and the sensor roughly oriented to maximize the signal amplitude. A measurement is made by an electronics unit strapped to the body (terrible ergonomics) and data is recorded if it doesn’t show an error. An error typically indicates the local gradient is too large, a frequent occurrence near strong magnetic anthropic features. A scan involves making a measurement about every meter in a relatively straight line. A straight line through the heavily vegetated eastern scarp was impossible, much bushwhacking was required, and foot paths were followed where convenient, hence the circuitous paths in Figure F1. Of course, all magnetic materials, to be safe all metals, were removed from my person during the walking scan. The 8-foot aluminum staff for carrying the sensor plus the battery, GPS unit, and electronics unit do not appear to significantly affect measurements. The repeatability for the reference measurements typically had a sigma of around 2-3 nT.

The density and uniformity of the scans is not adequate to obtain a well-defined 2-D aeromagnetic anomaly map that may be familiar to readers. That requires a comprehensive survey with at least 10-100X the number of scans and a separate continuous reference for correction. The equipment for that would ideally be a low-altitude heavy-duty drone to carry an aerial survey magnetometer such as the Geometrics Mag Arrow, and that procedure would be complicated by residential development and the policy forbidding drones in San Mateo County Parks. For precise mapping such a survey is required and as such the current data is useful for indicating what is possible but by itself is not complete. An advantage of this ground level survey is the better resolution of short-term variations which is necessary when looking at faults. A high-altitude aeromagnetic survey, such as provided by the airplane derived USGS magnetic anomaly survey plot in Figure E8, lacks adequate resolution. It is useful for large scale bedrock changes but inadequate for fault mapping or precise bedrock boundaries. A comprehensive walking survey of the area with a continuously monitoring sensor is possible and is the next step up from the manual point-by-point measurements reported here, but the walking time and bushwhacking requirement is daunting and best accomplished by younger legs. A serious limitation of ground level surveys is the influence of anthropic features. Besides buildings, all utilities, underground pipes, metal posts, nails in wooden posts, some of the roadbed materials, any non-natural disturbance can produce confounding anomalies. Figure F23 shows scans from a typical metal signpost indicating the field is measurable within about 5 m of the object although, of course, each object would be somewhat different. Despite much effort to deal with this problem it seriously limited the use of magnetic surveys in developed areas. A map of the underground utilities in San Mateo County will help verify some of the structure but was unfortunately not available due to Covid protocols at the county offices and may be updated later. Most underground features, while usually readily apparent in the data scan, introduce complicating magnetic structure and removing their effect from the data may not be assured. The Fitzgerald Reserve maintains a largely pristine environment that produces useable data, with some exceptions.

The Garmin GPS is typically within ± 5 m or better but with 1 m distances between points it sometimes results in scans incorrectly appearing to reverse course for short distances. In some cases where this effect confuses the resulting plot the GPS coordinates are corrected to fit the known path. At times when the battery neared a low level, such as on scans 105, 109 and end of 108, the GPS became significantly inaccurate and is corrected to the known path where possible. GPS coordinates were translated using standard methods to lengths along the MF fault, about a 319° azimuth, and perpendicular to that for convenient plotting. For instance, the distance perpendicular to the fault is determined using

$$D_{perp} = [(Lo_i - Lo_1)*C1]^2 + [(La_i - La_1)*C2]^2]*[\sin(\theta + \tan^{-1}\{(Lo_i - Lo_1)*C1/(Lai - La1)*C2\}]$$

Where Lo_i and La_i are the measured longitude and latitude in fractional degrees,

C1 = 88885.572, and C2 = 110435.987 are coefficients to convert longitude and latitude to UTM meters in this region,

Lo_1 and La_1 are longitude and latitude of a reference location along the MF fault line,

θ is the azimuth of the MF fault. The distance along the fault length is a similar equation with the sin replaced by cos.

The question of what geologic structure exactly is being measured by the magnetic anomaly map is not always certain. The magnetometer manual by S. Breiner, 1999, offers a review of the magnetometer interpretation issues. Most materials have a magnetic susceptibility, which can go from around .3 cgs units for magnetite to less than 10^{-6} for some sedimentary rocks. The earth's magnetic field induces a field proportional to the volume of a material and its susceptibility that then adds or subtracts to the earth's magnetic field and with sensitive enough instruments and a large enough change this induces a measurable magnetic anomaly, a small change in the background field amplitude as seen in Figure F6 and subsequent figures. It is only a change in the background, always due to an induced dipole although if the dipole is long enough it often looks locally like a monopole, that is sensed. Both magnetically induced (including paramagnetic, diamagnetic and ferrimagnetic) and ferromagnetic materials will alter the earth's local magnetic susceptibility. Sometimes in geology it is claimed the magnetic anomaly is a measure of ferromagnetic materials, primarily magnetite, but that is clearly not always the case, especially in the more subtle variations observed here. Most materials have a small paramagnetic component that changes with density, stress, water and mainly mineral content etc. so it is difficult to predict how something like a fault will affect the local magnetic field or even whether an anomaly will be positive or negative. Generally, a deviation from geologic uniformity does appear to produce a measurable anomaly large enough to be sensed by the better magnetometers (and even cell phone magnetometers as discussed at the end of this appendix) which are then assigned to expected geologic features based on location and shape of the anomaly (e.g. Breiner, 1999 and Lopez-Loera et al, 2010). The shape of the anomaly combined with the ambient field orientation contains information about the magnetic shape and distance of the feature which is useful in the analysis. Lopez-Loera et al, 2010 modeled volcanic bedrock shapes based on anomaly maps although in their case they incurred much more magnetic bedrock with thicknesses on the order of kilometers to obtain anomaly amplitudes slightly larger than those found here with much larger widths, whereas in the present case we assume relatively low susceptibility changes closer to the surface are producing the current lower amplitude and narrower changes.

It should be pointed out that this characterization with low ambient fields and very low magnetic amplitude changes is inherently a "low field" measurement, it uses only the change in the earth's magnetic field due to local fluctuations in the low-field magnetic susceptibility. It does not involve "high field" measurements that measure changes to hysteresis curves of magnetic minerals that can be used to characterize changes in rock mineralization or anisotropy due to faulting (e.g. Yang et.al., 2020). Those require rock samples measured in a laboratory magnetometer and generally look at strongly magnetic minerals, often iron-bearing.

Fault Mapping Using Magnetic Anomaly:

The results reported here confirm that faults in PPB can be seen by magnetic mapping and their agreement with the previous mapping is demonstrated. Figure F3 includes locations of several anomalies that coincide with prior mapping. In several cases they are found to add constraints and new interpretation to some of the faulting.

A scan that crosses known faults is first discussed to establish that faults are identifiable. Scan Line 108, Figure F6, crosses PPB about 10 -20 m south of the headscarp where faults are exposed, Figure F2. In the present case the faults trend primarily NW-SE and the earth's field is oriented about 13.5° NE with an inclination of about 62°, so a vertically offset fault would be expected to have an induced positive anomaly on the SW side of the fault and possibly a small negative anomaly on the NE side of the fault as depicted in Figure F9c. This is seen, such as in Figure F6 where the MF and EWF positive anomalies are displaced to the SW of their respective faults about 10 m. The MF anomaly location is nominally at zero distance (recorded about 10 m to the SW) from the MF fault reference, whereas the EWF anomaly is about 42 m to the NE of MF, about the same as measured on the ground between the faults. They display magnetic anomalies about 25 - 35 nT (1 nanotesla, also called 1 gamma, = 10^{-5} gauss, the earth's magnetic field is .47 gauss or 47,000 nT) in amplitude with the full width of the EWF anomaly, ~45 m, being larger than that for MF, ~25 m. WWF1 and FWWF are distinguishable, with widths similar to that for MF, but with much lower amplitude, less than 8 nT.

The width of the EWF anomaly in Figure F6 and its possible continuation beyond the apex suggests that fault zone involves much of the region between the location where the fault is nominally mapped and the bluff apex, as schematically illustrated in Figure 9. The distance between the peaks in EWF and MF matches that recorded by on the ground mapping. The distance between MF and WWF1 is also as measured for the faults, although the FWWF structure appears about 10-20 m further west than expected. This suggests FWWF trends more westward than previously thought and the fault seen offshore west of PPB which crosses Pillar Point and further traced southwest is likely from WWF1 and not FWWF or a combination of the two. The good agreement between the magnetic anomaly structure and the mapped faults indicates that this method is useful for detailing the fault structure within PPB and possibly for fault mapping in general.

Shapes of magnetic scans above geologic features depend on the geologic structure and its orientation relative to the orientation of the earth's magnetic field (e.g. Figure F9b copied from Breiner, 1999). Simplified interpretations from Breiner, 1999, suggest anomaly widths are approximately 1 to 3 times the depth to the feature causing the anomaly. This suggests the source of the MF anomaly is about 8 - 25 meters below the sensor, which is 2.5 m above the ground surface. The fault profile from the mapping section indicates the top of the Tp is about 4.5 m below the surface on the east side of the fault and about 7 m below the surface on the west side. The offset in Purisima thus occurs between about 7 and 9.5 m below the sensor in reasonable agreement with the low-end estimate of depth to the source of the anomaly. This suggests the vertical offset in Purisima is the most likely source of the anomaly as illustrated in Figure F9c as would be reasonably expected.

A separate measurement of the magnetic field adjacent the exposed offset MF layer was made using an iPhone magnetometer. The anomaly (field above background) to the right of the offset shown in Figure F9c is about 600 nT. As discussed below the iPhone generally produces anomaly amplitudes about 7X that of the proton magnetometer, so it is here estimated the proton magnetometer would have found about a 90 nT magnetic moment due to the bedrock offset implying a magnetic susceptibility for the Purisima layer of around 10^{-4} cgs units. This is on the high end for sedimentary and shale rocks, (10^{-6} to 10^{-4} per Breiner, 1999), however higher values have been reported for shales with low temperature metamorphosed petroleum content (Cisowski and Fuller, 1987). Petroleum is found in and near the Purisima gouge zone in the present case.

The anomaly amplitude for WWF1 in Figure F6 is smaller than for MF even though its vertical offset is larger. This is likely due to the inclined Purisima between WWF2 and WWF1 as shown in Figure F9d. In that case there is an effective dipole due to this ramp. The induced magnetic field then also includes a demagnetization factor which reduces the net induced field plus the drop off with distance perpendicular to a dipole is closer to r^{-3} compared to a r^{-2} drop off from a monopole, these two effects combining for the smaller WWF1 anomaly amplitude.

The geometry details for FWWF are not exposed, however the lower anomaly amplitude for that fault suggests it has a relatively small vertical offset which agrees with the approximately 1 m offset previously deduced from the visible Tp surface geometry, Table II.

The larger amplitude and broader signature for EWF then indicates the depth to the EWF magnetic anomaly source is about 12 m below the surface, also in rough agreement with the profile suggested in Figure 9. Plus, the anomaly profile for the EWF in Figure F6 suggests a more complex, possibly multi-step, fault profile between the EWF and the apex.

East of the bluff apex, but west of the prominent eastern SCF scarp, a smaller scarp with exposed Purisima is noted in the field and is here clearly observed magnetically, labeled "NE Side of Apex Fault" in Figure F6 or "AF" in Figure F19. This region is also seen to have several faults corresponding not only to the exposed scarp as seen in Scan Lines 108 and 107, Figures F6 and F7, but at least two other faults. The prominent eastern scarp, the Seal Cove Fault, is recorded primarily at the top of the scarp in Scan Lines 108, 107, and 106b, Figures F6, F7, and F8, respectively. The low broad peak in Figure F6 between 170 and 300 m locations, possibly to 400 m, suggests a possible broad or deep source as anticipated from the Seal Cove Fault , although that is not duplicated in Figure F7, a sub-parallel scan about .5 km further north.

MF and WWF1 are known to be and FWWF is assumed to be strike-slip with subvertical gouge zones and the slightly lower slope on their western sides in Figure F6 results from the earth's magnetic field intersecting them at about 55° in the horizontal plane from its long axis, hence inducing a small horizontal magnetic component from the unbalanced bedrock offset as depicted in Figure F9c. On the other hand, faults east of the apex have a noticeably lower slope on their eastern side than on their western side as quantified in Figure F9a. A dip-slip fault likely has a more non-vertical component as depicted by the left drawing in Figure F9b. This introduces a larger distance between the peak and valley magnetic amplitudes on the eastern side of the faults which in turn produces a wider asymmetric shape, higher peaked on the southwest side with a longer lower angle slope on the northeastern side, and this is reflected in Figure F9a. This suggests the faults east of the apex may be primarily dip slip faults which supports the assignment of the Seal Cove Fault as a dip-sip fault in Figure 4. The EWF slope ratio is between the two sets and its fault characteristic is not certain from this plot. It has a slope ratio lower than the known strike-slip faults, but on the high end of the likely dip-slip faults. It is plotted with the strike-slip faults in Figure F9a, but as discussed in the report and in Appendix A it is possibly primarily a dip-slip fault. As noted in Figures F7 and F8 as well as F6 there are additional faults between the apex and the eastern scarp. These apparently dip-slip faults are all mapped as just SCF in Figure 4 as the others appear smaller and perhaps more dispersed throughout this uplifted zone. A more complete, higher-density, set of scans, as mentioned previously, would more clearly produce a 2-D trace of these multiple faults throughout the bluffs.

The larger magnetic anomalies along the prominent eastern scarp occur near the top of the scarp with little structure seen near the bottom further suggesting dip slip faulting. There is a large magnetic anomaly in the flat region of Half Moon Bay Terrace between the scarp and Airport St., but that is here associated with an underground anthropic feature (likely pipeline) apparent from maps and in the field. Koehler et al, 2005, found thrust faults in a trench near the bottom of the scarp and while some small suggestion of those is distinguishable in Figures F6, F7, and F8 they do not appear as prominent as at the top of the scarp.

Scan Lines 107, 106b, and 106a, Figures F7, F8, and F10, together map out connections from the faults initially termed “spreading ridges” on the north side of the large landslide basin in Figure 4 to the crossover faults that coincide with the Leighton Lineations, Figure F3. Thus, we can now confidently identify these as continuous through-going faults connected from the region where the WWF, MF, and possibly the EWF converge within the landslide basin over to the crossover faults and continue to where they combine northward to exit offshore at the Fitzgerald Fault, Figure 4, forming a right-stepping crossover of a right lateral strike-slip fault as discussed in the report.

Figure F11 is a composite of all scans plotted as a function of the projected distance along the length of the MF fault. It shows a general drop in magnetic level in the Seal Cove Lowlands area. While many features contribute to this the general pattern suggests this may be due to a pull-apart graben produced by the crossover faults as discussed in the report.

Additional magnetic mapping in both PPB and Fitzgerald Bluff is discussed in conjunction with a review of cell phone magnetometers below. Since those results are not as reliable as these from the 857 magnetometer they are not included in this section.

Bedrock Mapping using Magnetic Anomalies:

A principal objective of this magnetic anomaly mapping was to delineate the bedrock changes in the vicinity of the Seal Cove Highlands and out onto the Half Moon Bay Terrace. As a first check on the discrimination ability of this method Figure F12 compares scans from three areas, Lines 107 and 108 are from PPB where the bedrock is clearly Purisima and 110c is on a marine terrace believed to be underlain by Montara Mountain Granodiorite, Pampeyan, 1991. Figure F12 includes sections of the scans where little structure is seen indicating these are likely uniform sections of marine terraces. The relative terrace sediment thickness is not known but is likely roughly similar. The amplitudes of all three scans are around 47,650 nT indicating there is very little magnetic amplitude contrast between a Purisima sandstone and a Montara granite bedrock. This is reasonable since above a uniform magnetic plate far from any structure there is little contribution from the ends of the magnetic moment. However, it confirms we cannot use a change in base level as an indicator of bedrock differences.

A second check on the effect of a granitic bedrock is Scan Line 110a, Figure F13, which is along the Vallemar Bluffs which overlie granite and along the adjacent seashore where granite is exposed. Again, the amplitude in the uniform regions is around 47,650 nT further supporting that level as the measure of a uniform bedrock, in this case with the granite fairly shallow at around 3 m below the surface. The conclusion is that there is very little difference in magnetic background above a Montara granite or a Purisima sandstone uniform bedrock.

[Unrelated to the geology, but of interest in the interpretation is that in the Line 110a scan in Figure F13 there is a large negative anomaly around 640 m. The two large V-shaped drops can be used in locating the source of this anomaly using an expected $1/r^2$ dependence on distance from the magnetic source. This projects the magnetic source to the back-patio area of the residence at 193 Reef Point Rd. This residence has more construction features, such as steps and wall, embedded in the granitic scarp exposed at the beach than is apparent at the neighboring residences. This suggests there is a magnetic source included in the back-yard construction of that residence, possibly rebar in the concrete. The anomaly is negative due to these scans being north of the structure, so they record the north pole or "negative" component of the induced field, Figure F9b, further confirming the source is in that direction.]

In the Line 110a scan in Figure F13 there are also positive anomalies in both scans around the 690 m location in-line with a prominent fault gouge zone in granite as seen in Figure E13 suggesting this granitic fault also exhibits a magnetic anomaly signature.

Lack of a bedrock magnetic contrast doesn't preclude structure in the transition zone between the two bedrocks. Indeed, such an interface, if it exists, implies a likely fault structure and that may be observable similar to what is seen in the fault mapping above. In particular, a wide magnetic anomaly transition zone would be expected to occur due to an expected uniform deep narrow fault if that fault zone has any magnetic signature, such as in the middle drawing in Figure 9b. Such a wide linear transition is in fact seen above all the zones where a sandstone / granite interface is proposed in S.I. E. For instance, scan Line 106a, Figure F10, shows a relatively wide linear transition zone which bottoms at about the location where Leighton et al, 1971, shows a bedrock transition to occur, Figure F3. The Leighton cores were taken along Bernal Ave and the scan in Figure F10 is subparallel and about 100 m southeast of that at a similar elevation so is likely to also contain such a transition. Scan Line 102, Figure F14, also scans across a region that is hypothesized to contain a SS to granite transition. It contains several features of anthropic origins (signposts etc. along Airport St), nevertheless it includes a slow linear drop in the region where the slope break occurs and where a SS transition to Gr is proposed in S.I. E. Thus, 102 and 106a scans both show similar relationships to the proposed bedrock transition zones with estimated depths on the order of several hundred meters as might be expected for a deep uniform bedrock transition. However, it is recognized that the scan shapes and the correspondence of the two scans to expected bedrock transitions may not be strongly compelling to other investigators suggesting that even though such a Purisima / granite transition at both locations is possible, even likely, it should not be here concluded based on these magnetic anomaly scans alone. Scan Line 101, Figure F15, traverses

Bernal Ave and follows precisely the path of the Leighton et al coring unfortunately it is heavily affected by anthropic features making interpretation inconclusive.

In conclusion, while all the available scans and fault mapping are consistent with a SS/Gr transition as mapped in S.I. E, confirmation along the 1 km between the Moss Beach shoreline granite exposure and the granite bedrock in the Seal Cove Highlands is still not considered definitive. On the other hand, there is no evidence to suggest that Purisima sandstone exists on both sides of the fault in this central 1 km region and granite is known to border sandstone on the two ends of this region.

Magnetic Survey Summary:

- Previously identified faults are clearly identified by the magnetic anomaly scans and substantially agree with other mapping.
- The width of the anomalies indicates the origin of the fault anomalies is likely the vertical offset of Purisima between the two sides of the faults.
- The fault bounded ridges on the north side of the large landslide basin (formerly called gravity spreading ridges) are confirmed to transition to the crossover faults mapped throughout the Seal Cove Highlands and Lowlands.
- The MF and EWF are magnetically the most prominent faults. This is in agreement with topographic analyses and the MF fault anomaly amplitude appears consistent with measurements of the magnetic moment caused by the offset in Purisima.
- The comparatively small magnetic anomaly amplitudes for the west wall faults appear to be explainable by their detailed configuration.
- The fault along the prominent eastern scarp (SCF) is magnetically most pronounced along the top of the scarp.
- Anthropic structures seriously disrupt magnetic scans and make interpretation within developed areas difficult and unreliable.
- Additional faulting is recorded between the PPB apex and the prominent eastern scarp with faults east of the apex having an asymmetric sawtooth shape that is here associated with dip-slip faulting as opposed to an opposite asymmetry found for the faults west of the apex that are known to be strike-slip.

- The fault in granite bedrock near Vallemar Bluffs is also recorded in magnetic profiles.

- The magnetic profiles support the granitic bedrock map proposed in S.I. E although may still not be considered definitive.

- A more complete magnetic mapping or detailed gravity mapping could be helpful in both the fault mapping and the bedrock mapping.

- The small magnetic contrast between a Purisima and a Montara granite bedrock limits interpretation of bedrock mapping, and anthropic features in the developed area of Seal Cove limits magnetic profile interpretation in that region.

Cell Phone Magnetometers:

Mobile phone magnetometers were initially evaluated out of curiosity and to try to avoid renting and carrying a better, heavier one. While certainly not as good as the proton magnetometer used above, they are found to be almost adequate for magnetic mapping of some faults. Because of their convenience and potential usefulness and for informational purposes the evaluation for a couple of iPhones is reviewed here. It is surprising cell phone scans haven't become part of a standard initial survey of most fault areas and with future improvements it is anticipated they may become commonly used.

The typical Hall effect sensor plus sensing circuit noise level, essentially the short-term stability, can be as low as about 200 nT for an iPhone 8, although an older iPhone 5 exhibited on the order of 2000 nT. Judging from the significant improvement noted over the years in the compass operation in a series of iPhones it is clear progress has been made in magnetometer accuracy and stability. An Apple engineer told me the sensors are essentially the same and are not particularly sensitive, but the signal processing is quite advanced and provides most of the precision. Odenwald, 2021, compared smartphones for detecting magnetic storms and found an iPhone to have a better detectability than other models. However, the analysis implied the result was from sensor differences rather than the signal handling software. The upside potential is that cell phone usability for fault mapping may improve with future upgrades.

In the scans done here an iPhone 8+ was found to discern larger anomalies and appears already useful for initial surveys of an area where faults are suspected, and apps are available to record GPS coordinates simultaneously with the magnetic vector amplitudes (plus several other sensors, if desired). Besides the noise level, the other key detractor is the stability over longer times, such as an hour, which can add another 500 nT or more of slow variation that is not a diurnal variation and cannot be removed by a reference. This is likely a result of thermal drift and it is found that allowing at least an hour for the cell phone to thermally equilibrate was helpful in reducing drift. By comparison the Geometrics 857, the lower end of advanced magnetometers, has longer term stability on the order of better than 3 nT which is less than the diurnal variation of around 30 nT. As a result, short term local variations less than one nT are identifiable by the better magnetometers and longer-term variations on the order of 10 nT can be reliably distinguished. One potential advantage of the cell phones' Hall effect sensors is that they provide vector amplitudes compared to just the total magnetic field from the proton precession magnetometer used above. However, in order for the vector values to be useful the cell phone needs to be oriented very well. The changes in magnetic inclination at a fault are much smaller than the accuracy with which a cell phone can typically be oriented in the field. The declination cannot be obtained from cell phone data alone and is programmed in. Another difference, not yet here understood, is that anomaly amplitudes for the same geologic features were in all cases larger for the cell phone than for the scalar magnetometer. This may relate to the vector vs scalar nature of the respective measurements, but theoretically the total amplitudes are expected to correlate. The cell phones were also typically about 1 m closer to the anomaly sources but that is estimated to be a relatively small factor.

Figures F17 and F19 compare a couple of scans where both iPhone 8 and the Geometrics 857 magnetometer were run. The paths are not exactly the same and in Figure F17 the horizontal scale is just the data sequence so the plots are not aligned horizontally, and this cell phone data is unsmoothed, nevertheless some of the main structure can be correlated. In Figure F19 three scans similar to the 857 scan path across the main fault zones show good agreement for the MF and EWF signatures and the fault east of the apex, AF. Surprisingly, the amplitude of the anomalies is larger for the iPhone (note the 857 data is expanded 7X in Figure

F19 to better compare) and the FWWF and WWF1 particularly appear much larger, although much noisier also than the 857. The raw noise level of the iPhone in Figure F17 is over 20 times higher than for the magnetometer although it can be greatly improved with smoothing of the data as in Figure F19. The larger range and different direction of background variation for the iPhone in Figure F17 is due to its longer-term instability. Thus, while scan 106a was seen to show a long sloping region in Figure F10 that is tentatively assigned above as an indication of bedrock change, the sloping region over the same region for the iPhone 8 in Figure F17 cannot be relied on to make any claims. However, the prominent short-term features observed on the iPhone may be useful for an initial fault survey.

Several cell phone applications are available to record sensor data with drawbacks and advantages of each and three for iPhones will be discussed here. The Physics Toolbox app appears to be perhaps the most popular sensor app (Odenwald, 2021), but I don't consider it useful for fault mapping. It provides files of only one sensor set at a time and records magnetometer data to only the nearest 1000 nT which is a major limitation. It does provide the best real-time display which is useful for monitoring when setting up or making a quick scan, but the output sensitivity limitation prevents it from being useable for actual fault mapping.

The Sensor Log app is my preferred app even though it can be confusing to use. It provides multiple sensor outputs simultaneously. (Cell phone gravity measurements are available but not surprisingly are not nearly precise enough to be geologically useful.) It also can record cell phone attitude and motion so theoretically it might be used to correct the magnitudes of all three axes of the magnetometer to get an estimate of inclination, but I didn't do that because it would be very complex and probably uses the magnetic field to determine at least one of the orientation angles so the calculation would probably end up being circular. Sensor Log provides three "raw" magnetometer axes where the raw designation means there is a large self-field that requires calibration to remove. Alternatively, the "heading (CLLocation)" was found to be the preferred mode since it uses an internal calibration but is slower. The raw values can be read faster, up to 100 Hz, but require a subsequent calibration by accurately rotating the cell phone about each of the three axes in a uniform magnetic field. When rotated about all three axes multiple times a reasonably consistent offset plus a small magnitude correction achieves the same magnitude change on all axes when pointing in the same direction. A 180^o rotation with the sensor at the same location should result in equal + and – values along the other two axes and any deviation from that equality implies a constant internal field. The internal field is quite large. For instance, for my iPhone 8+ it was 65.99 μT (microtesla) for the X-axis, 60.36 for Y and -434.41 for Z. After applying these offsets, the net field magnitude is around 50 μT, implying the internal Z-field is almost 10 times higher than the earth's field. The total amplitude is slightly larger than that measured by the proton precession-based magnetometer of around 47.6 μT, which is very close to that expected at this location, but the difference is small enough to be neglected. It is likely this internal field drifts due to thermal or other changes of the cell phone which in turn could account for the observed longer term drift in amplitude, nevertheless, it is remarkable that cell phones do as well as they do when considering the magnitude of the internal field. The Sensor Log data can be recorded in a csv file that is then emailed to oneself and subsequently loaded into Excel for analysis.

The EXA Sensor app records one table of multiple sensors' data at one location but does not record continuous scans. I found this useful at the starting or stopping locations of a scan or to compare basic values of many sensors at several single sites.

When making a walking scan it is preferable to hold the cell phone level and steadily pointing about 45^o to the direction of magnetic north as it was noticed that going through a 0 to 360^o transition can produce an anomalous amplitude spike. Inevitably there is a modulated signal imposed on all components due to the motion of the person carrying the phone, but the total calculated field (square root of the sum of squares of all components) is surprisingly steady when the phone is carefully held this way. Using a glove to hold the phone may reduce thermal changes due to transfer of body temperature. The GPS coordinates from the iPhone are path following (differential) which makes them much more precise than the Garmin GPS unit used with the proton magnetometer. This avoids most "backtracking" found with the Garmin (such as the jumble of data near the 80 m location of the 857 data in Figure F19). Recording rates up to 50 Hz for the calibrated magnetometer data with the Sensor Log app are possible, which provides plenty of data for smoothing to reduce noise, but the drawback of the high rates is the excessive amount of data that slows computer response when using Excel or other data handling programs. A rate of 10 Hz is a good compromise. The GPS can only record at a 1 Hz rate, but I can provide extrapolation between GPS points in Excel if needed.

Example plots of iPhone 8 magnetometer scans are included in Figures F 17 through F22. Known faults are readily observed. For instance, the MF, EWF, WWF1 and FWWF are all readily apparent in Figures F18 and F19 and are compared with the proton magnetometer scan showing a similar result for the principal faults. A surprising effect is that the anomaly amplitude is larger for the cell phones than for the proton magnetometer so the anomalies for the 857 have been increased by a factor of 7 to better compare in Figure F19. This may be related to the vector measurement for the cell phone versus the scalar measurement for the proton magnetometer even though it is the total magnitude compared in both cases. The faults are better distinguished with the 857 plus the level drifting makes longer term variations unreliable and the higher noise makes faults less convincing for the cell phone. Perhaps more problematically, the cell phone plots show additional structure in Figure F19 that is unlikely actual faults so multiple scans, at least, are needed to verify faults.

Figures F20 and F21 show cell phone scans crossing Fitzgerald Bluff starting near the Simpson trench and continuing over to where Crossover Fault 2 would be expected. Also located in Figures F20 and F21 are where the expected Distillery Fault and Crossover Fault 2 cross the profiles. There is some agreement with structure in the profiles, these are also plotted as red markers with black dots in Figure F24. Included in Figure F21 are faults that are found to project from the crossover fault 2 line toward the granite defined border along the Moss Beach shoreline. This suggests the crossover fault 2, which in the Seal Cove Highlands has been found to be the fault between granite and sandstone bedrocks, Leighton et al, 1971, likely extends to the granite/sandstone transition identifiable along the shoreline and thus supports that granite likely lies to the east of this fault along its entire length. However, it is unlikely the plots in Figures F20 and F21 would confidently locate those faults without motivated identification. In addition, there is a small empty lot at the end of the Arbor Lane cul-de-sac that lies above where a granite to Purisima transition is anticipated. In Figure F22 there is structure in the profile where this transition is projected plus a possible decreasing amplitude going toward the granite direction similar to that found in Figures F10 and F14. Again, it adds support in helping locate faults that are otherwise identified even though by themselves the plots in Figures F20, F21 and F22 would not provide confidence in locating the Distillery and Crossover 2 Faults and the Purisima to Granite transition. It should be pointed out that the various levels of apparent noise of the iPhone scans in Figures F17 to F22 is due to different parameters (raw vs calibrated), data frequency and smoothing used.

In the presence of anthropic features there is almost always some magnetic response. Figure F23 shows the signal contribution from a 2-3" heavy magnetic metal (presumably an iron alloy) 4' high post at various distances from the post. The scan is transverse to the post and the distance recorded is the closest to the post and shows the amplitude depending on about the -1.7 power of the distance, reasonably close to the expected -2. This suggests a distance of at least 5 meters is required to reduce the effect to being below 30 nT.

The fault locations suggested by cell phone magnetometer scans are included as red markers with a black dot in the Fitzgerald Bluff area in Figure F24 and reasonably match the previously mapped Distillery Fault and the extension of Crossover Fault 2. However, without reasons to look for those faults at those locations they would probably not be obvious from Figures F20 through F22. Nevertheless, in areas where faults are anticipated a cell phone scan can provide additional confirmation and this capability is likely to improve.

In summary it appears that cell phone magnetometers may be useful for initial surveys to identify possible fault locations or support fault maps located by other data, but by themselves cannot yet confidently produce fault maps. In contrast, the better magnetometers can generally identify faults with confidence, although anthropic features remain confounding issues for all magnetic scans.

Only the iPhone 5 and 8+ were evaluated here and any other cell phone would need to be separately considered. However, the possibility of providing a convenient inexpensive means of tentatively locating faults could be a boon for university and even high school geological field trips. One concern is that the iPhone improvements made so far may now be considered adequate for consumer navigation purposes by the manufacturers and result in a loss of commercial incentive for further improvements. I have encouraged Apple engineers to continue improvements, another factor of three to five in sensitivity would likely enable this application, but I encourage additional input as I believe government geologists and university professors would be more persuasive to incentivize a continued improvement in these magnetometers.

References:

Alquist-Priolo fault maps from maps.conservation.ca.gov ; Montara Mountain and Half Moon Bay Quadrangles, 1982

Andersen, D. W., Sarna-Wojcicki, A. M., and Sedlock, R. L., 2001, San Andreas Fault and Coastal Geology from Half Moon Bay to Fort Funston: Crustal Motion, Climate Change, and Human Activity: Fieldtrip 4 in Geology and Natural History of the San Francisco Bay Area, A Field-Trip Guidebook: Stoffer, P. W. and Gordon, L. C. eds, USGS Bull 2188, p 87 – 103.

Anderson, R.S., 1994, Evolution of the Santa Cruz Mountains, California, through tectonic growth and geomorphic decay: Journal of Geophysical Research, v. 99, p. 20161–20179,

Bedrossian, T. L., 1979, Fault Evaluation Report FER-03, Calif Div of Mines and Geology.

Bender, M. L., 1974, Reliability of amino acid racemisation dating and paleotemperature analysis on bones, Nature, 252, p. 378 – 379.

Bradley, W.C., and Griggs, G.B., 1976, Form, genesis, and deformation of central California wave-cut platforms: Geological Society of America Bulletin, v. 87, p. 433

Breiner, S., 1999, Applications Manual for Portable Magnetometer, Geometrics, www.geometrics.com, pp 58.

Bretz, C. K., Kvitek, R. G., Dartnell, P., and Phillips, E. L., 2014, Colored Shaded Relief Bathymetry, Offshore of Half Moon Bay Map Area, California, USGS ofr 2014-1214, 10 sheets.

Bruns, T. R. Cooper, A.K., Carlson, P.R., McCulloch, D.S., 2002. Structure of the submerged San Andreas and San Gregorio fault zones in the Gulf of the Farallones as inferred from high-resolution seismic-reflection data. In: Parsons, T. (Ed.), Crustal Structure of the Coastal and Marine San Francisco Bay region, California. USGS Professional Paper, pp. 77-117. 1658.

Bryant, W. E., and Cluett, S. E., San Gregorio Fault Zone, San Gregorio section (Class A) No. 60a, 1999, USGS Earthquakes Hazards Program Database Search http://earthquakes.usgs.gov/hazards/qfaults, accessed 3/29/2016.

California Geological Survey, 2018, Earthquake Fault Zones: Special Publication 42, 83 pg.

Burgmann, R., Segall, P., Lisowski, M., Svarc, J., 1997, Postseismic strain following the 1989 Loma Prieta earthquake from GPS and leveling measurements, Jour. Of Geophysical Research, v 102, pp 4933 – 3955

Burgmann, R., Hilley, G. E., Ferretti, A., and Novali, F., 2006, Resolving vertical tectonics in the San Francisco Bay Area from permanent scatterer InSAR and GPS analysis, Geology, 34, p 221-224.

Clark, J.C., 1997, Neotectonics of the San Gregorio Fault Zone: Age dating controls on offset history and slip rates: USGS Final Technical Report 30 p.

Cisowski, S. M., Fuller, M., 1987, The generation of magnetic anomalies by combustion metamorphism of sedimentary rock, and its significance to hydrocarbon exploration, GSA Bulletin, 99, p 21-29.

Conradson, D. R. and Welch, V. B., eds, 1990, "The Natural History of the Fitzgerald Marine Reserve" pub by Friends of Fitzgerald Marine Life Refuge, Moss Beach, California.

Cotton, W. and Associates, 1980, Geologic Analysis of The Seal Cove Area, Technical Report to Planning Director, County of San Mateo, 22 p.

Connelly, S. F., and Rubin, R., 2001, Fault Investigation, CEG report project 0103, 34 p.

Cummings, J. C., Touring, R. M., and Brabb, E. E., 1962, Geology of the Northern Santa Cruz Mountains, California, in Gas and Oil in Northern California – Part II, California Division of Mines and Geology Bull. 181, pg 179 – 220.

Davis, G. H., Bump, A. P. Garcia, P. E., Ahlgren, S. G., 2000, Conjugate Riedel deformation band shear zones, J. Struct. Geol. 22, pg 169-190.

DeLong, S. B., George, E., Hilley, G. E., Prentice, C. S., Crosby, C. J., and Yokelson, I. N., 2017, Geomorphology, denudation rates, and stream channel profiles reveal patterns of mountain building adjacent to the San Andreas fault in northern California, USA , v 129, pg 732 – 749.

Dickinson W.R., Ducea, M., Rosenberg, L.I., Greene, H.G., Graham, S.A., Clark, J.C., Weber, G.E., Kidder, S., Ernst, W.G., Brabb, E.E., 2005, Net dextral slip, Neogene San Gregorio-Hosgri fault zone, coastal California: Geologic evidence and tectonic implications, GSA Special Paper 391, pp 44.

Edwards, B.D., Phillips, E.L., Dartnell, P., Greene, H.G., Bretz, C.K., Kvitek, R.G., Hartwell, S.R., Johnson, S.Y., Cochrane, G.R., Dieter, B.E., Sliter, R.W., Ross, S.L., Golden, N.E., Watt, J.T., Chin, J.L., Erdey, M.D., Krigsman, L.M., Manson, M.W., and Endris, C.A. (S.A. Cochran and B.D. Edwards, eds.), 2014, California State Waters Map Series—Offshore of Pacifica, California: U.S. Geological Survey Open-File Report 2014–1260, pamphlet 38 p., 10 sheets, scale 1:24,000, *https://dx.doi.org/10.3133/ofr20141260*.

Ernst, W. G., Martens, U. C., McLaughlin, R. J., Clark, J. C., Moore, D. E., 2011, Zircon U-Pb age of the Pescadero felsite: A Late Cretaceous igneous event in the forearc, west-central California Coast Ranges, GSA Bulletin, v 123, pp 1497 – 1512.

Galehouse, J. S., and Lienkaemper, J. J., 2003, Inferences Drawn from Two Decades of Alinement Array Measurements of Creep on Faults in the San Francisco Bay Region, Bull. Seismological Soc. Am., v 93, p 2415-2433.

Glen, W., 1959, Pliocene and Lower Pleistocene of the western part of the San Francisco Peninsula, University of California Publications in Geological Sciences, v 36, no. 2, p 147 – 198.

Grove, K., and Caskey, S. J., 2005, Theodolite and total station measurements of creep rates on San Francisco Bay Region faults, USGS Final Technical /Report, award number 03HQGR0080, and online data at http://funnel.sfsu.edu/creep/

Gudmundsdottir, M. H., Blisniuk, K., Ebert, Y., Levine, N. M., Rood, D. H., Wilson, A., and Hilley, G. E., 2013, Restraining bend tectonics in the Santa Cruz Mountains, California, imaged using ^{10}Be concentrations in river sands, Geology, v 41, pg 843 – 846.

Hanson, K. L, and Lettis, W. R., 1994, Estimated Pleistocene slip rate for the San Simeon fault zone, south-central coastal California, *in* Alterman, I. B., McMullen, R. B., Cluff, L. S., and Slemmons, D. B., eds., Seismotectonics of the Central Caifornia Coast Ranges: Boulder, Colorado, GSA Special Paper 292, p 133 – 150.

Janssen, C., Wirth, R., Wenk, H. R., Morales, L., Naumann, R., Kienast, M., Song, S. R., and Dresen, G., 2014, Faulting processes in active faults – Evidences from TCDP and SAFOD drill core samples, Journal of Structural Geology, v 65, pg 100 – 116.

Johnson, S. Y., Watt, J. T., Hartwell, S. R., and Kluesner, J. W., 2018, Neotechtonics of the Big Sur Bend, San Gregorio-Hosgri Fault System, Central California, Tectonics, v 37, pg 1930 – 1954.

Koehler, R. D., Witter, R. C., Simpson, G. D., Hemphill-Haley, E., Lettis, W. R., 2005, Paleosseismic Investigation of the Northern San Gregorio Fault, Half Moon Bay, California, USGS NEHRP Final Technical Report, Grant Number 04HQGR0045.

Kennedy, G.L., Lajoie, K.R., Blunt, D.J., and Mathieson, S. A., 1982, The Half Moon Bay Terrace, San Mateo County, California and the Age of its Pleistocene Invertebrate Faunas, Western Society of Malacologists, Annual Report, v.14, p. 11-12

Kirk, R. M., 1977, Rates and forms of erosion on intertidal platforms and Kaikoura Peninsula, South Island, New Zealand, New Zealand Journal of Geology and Geophysics, 20:3, 571-613, DOI: 10.1080/00288306.1977.10427603.

Knudsen, R.D., Witter, R.C., Garrison-Laney, C.E., Baldwin, J.N., and Carver, G.A., 2002, Past Earthquake-Induced Rapid Subsidence along the Northern San Andreas Fault: A

Paleoseismological Method for Investigating Strike-Slip Faults, Bulletin of the Seismological Society of America, V 92, No. 7, pp. 2612-2636.

Keller, E. A., Pinter, N., 2002, Active Tectonics: Earthquakes, Uplift and Landscapes. 2nd ed. New Jersey, Prentice Hall (338 pp).

Kopp, R. E., Simons, F. J., Mitrovica, J. X., Maloof, A. C., Oppenheimer, M., 2013, A Probabilistic assessment of Sea Level Variations Within the last Interglacial Stage, Geophysical Journal Internation, 193, pg 711-716.

LaJoie, K. R., Weber, G. E., Mathieson, S., and Wallace, J., 1979, Quarternary tectonics of coastal Santa Cruz and San Mateo Counties, California, as indicated by deformed marine terraces and alluvial deposits, in Weber, G. E, LaJoie, K. R., and Grigg, G. B. editors, Coastal tectonics and coastal geologic hazards in Santa Cruz and San Mateo Counties, California: Field Trip Guide, Cordilleran Section of the Geological Society of America, 75th Annual Meeting, p. 61-80.

LaJoie, K.R., 1986, Coastal tectonics, in R. Wallace ed, Active tectonics: Studies in Geophysics Research Forum Washington, National Academy Press, p. 95-124

Larue, D. K., Barnes, I., Sedlock, R. L., 1989, Subduction and accretion of the permanente terrane near San Francisco, California, Tectonics, 8, pg 221.

Leighton, F. B., and Associates, 1971, Final Engineering Geologic Report of the Seal Cove – Moss Beach Area, County of San Mateo, San Mateo County Geologist's Report

Leinkaemper, J. J., McFarland, F. S., Simpson, R. W., and Caskey, S. J., 2014, Using Surface Creep Rate to Infer Fraction Locked for Sections of the San Andreas Fault System in Northern California from Alignment Array and GPS Data, Bull Seismological Society of America, **104**, pg 1-21.

Lohr, M., Yamagata, T., and Moore, J. C., 2009, Structural fabrics and hydrocarbon content of the San Gregorio Fault Zone, Moss Beach, California, AAPG Pacific Section, pg 21 – 34.

Lopez-Loera, H., Urutia-Fucugauchi, J., Alva-Valdivia, L., 2010, Magnetic characteristics of fracture zones and constraints on the subsurface structure of the Colima Volcanic Complex, western Mexico, Geosphere, V. 6, p. 35 – 46.

Los Banos Avenue road drawing; San Mateo County Public Works Department Drawing No. 88112-02, Feb. 1991.

Marrero, S. M., Phillips, F. M., Borchers, B., Lifton, N., Aumer, R., Balco, G., 2015, Cosmogenic Nuclide Systematics and the CRONUScalc Program, Quarternary Geochronology, 92 pg.

Martinson, D. G., Pisias, N. G., Hays, J. D., Imbrie, J. D., Moore, T. C., Shackelton, N. J., (1987), Age dating and isotopic analyses of sediment core RC11-120, PANGAEA, https://doi.org/10.1594/PANGAEA.726602 as plotted and reported in https://www.e-education.psu.edu/earth107/node/1496 .

McClay, K., and Dooley, T., 1995, Analogue models of pull-apart basins, Geology, v 23, p 711 – 714.

McClay, K., and Bonora, M., 2001, Analog models of restraining stepovers in strike-slip fault systems, American Association of Petroleum Geologists Bulletin, v 85, p 233 – 260.

McLaughlin, R. J., Powell, C. L., McDougall-Reid, K., Jachens, R. C., 2007, Cessartion of Slip on the Pilarcitos Fault and Initiation of the San Francisco Peninsula Segment of the (Modern) San Andreas Fault, California, AGU, Fall Meeting 2007, T43A-1089.

May, D. J., Keller, C. K., and Newberry, R. J., 1976, The General and Structural Geology of a Portion of Moss Beach, San Mateo County, California, unpublished student report for Geol 110, Structural Geology, Stanford University 19 pages.

Muhs, D. R., Prentice, C., Merritts, D. J., 2003, Marine terraces, sea level history and Quaternary tectonics of the San Andreas fault on the coast of California: in Easterbrook, D., ed., Quarternary Geology of the United States, INQUA 2003 Field Guide Volume, Desert Research Institute, Reno, NV. P 1-18.

Muhs, D.R., Kennedy, G.L., and Rockwell, T.K., 1994, Uranium-series ages of marine terrace corals from the Pacific coast of North America and implications for last-interglacial sea level history: Quaternary Research, V. 42, p 72-87.

Nelson, A.R., Shennan, I., and Long, A.J., 1996, Identifying coseismic subsidence in tidal-wetland stratigraphic sequences at the Cascadia subduction zone of western North America, Journal of Geophysical Research, 101, No. B3, pp. 6115-6135.

Noller, J. S., Simpson, G. D., Thompson, S. C., Lettis, W. R., Hylkema, M. G., 1995, Geoarchaeologic and Paleoseismic Investigations of the San Gregorio Fault, Seal Cove, California, USGS ofr 95-210, p 600 – 601.

Odenwald, S. F., 2021, Can Smartphones Detect Geomagnetic Storms? AGU, **doi.org/10.1029/2020SW002669**

Page, R.A., Stauffer, P.H., and Hendley, J. W., 1999, Understanding Hazards in the San Francisco Bay Region, USGS Fact Sheet 155-99

Pampeyan, E. B., 1981, Geologic Map of Montara Mountain Quadrangle, San Mateo County, California: USGS Open-file Report 81-451, 14 p.

Pampeyan, E.H., 1994, Geologic map of the Montara Mountain and San Mateo 7 1/2-minute quadrangles, San Mateo County, California: U.S. Geological Survey IMAP 2390

Perg, L. A., Anderson, R. S., Finkel, R. C., 2001, Use of a new ^{10}Be and ^{26}Al inventory method to date marine terraces, Santa Cruz, California, USA, Geology, v 29, pg 879-882.

Powell, C. L., 1998, The Purisima Formation and Related Rocks (Upper Miocene – Pliocene), Greater San Francisco Bay Area, Central California, Review of literature and USGS collection (now housed at the Museum of Paleontology, University of California, Berkeley), USGS ofr 98-594, 101 pages.

Ryan, H. F., Parsons, T., Sliter, R. W., 2008, Vertical tectonic deformation associated with the San Andreas fault zone offshore of San Francisco, California, Tectonophysics, doi:10.1016/ j.tecto.2008.06.011.

Siddall, M., Rohling, E. J., Thompson, W. G., Waelbroeck, C., 2008, Marine Isotope Stage 3 Sea Level Fluctuations: Data Synthesis and New Outlook, Reviews of Geophysics, v46, 29 pgs.

Simpson, G. D., S. C. Thompson, S. Noller, and W. R. Lettis, 1997, The northern San Gregorio Fault zone; evidence for the timing of late Holocene earthquakes near Seal Cove, California: Seismological Society of America Bulletin, v 87, p 1158-1170.

Solum, J. G., and van der Pluijm, B. A., 2009, Quantification of fabrics in clay gouge from Carboneras fault, Spain and implications for fault behavior, Tectonophysics 475, pg 554 – 562.

Tsimi, C., Ganas, A., 2015, Using ASTER global DEM to derive empirical relationships among facet slope, facet height, and slip rates along active normal faults, Geomorphology 234, p 171 – 181.

Varnes, D.J., Radbruch-Hall, D.H., Savage, W.Z., 1989, Topographic and Structural Conditions in Areas of Gravitational Spreading of Ridges in the Western United States, USGS PP 1496, pgs 27.

Vrolijk, P., van der Pluijm, B. A., 1991, Clay Gouge, Journal of Structural Geology, v 21, pg 1039 – 1048.

Wakabayashi, J., and Moores, E. M., 1988, Evidence for the collision of the Salinian block with the Franciscan Subduction Zone, California, Geology, 96, p 245-253.

Washburn, H., Blisniuk, K., Ladinsky, T., Powers, A., 2018, Geomorphic and Paleoseismic Study of Pillar Point Bluff Along the Seal Cove Fault, Northern California, AEG/IAEG San Francisco, poster and Field Guide.

Weber, G. E. and Lajoie, K. R., 1980, Map of Quaternary faulting along the San Gregorio fault zone, San Mateo and Santa Cruz Counties, California: USGS Open-file Report 80-907.

G. E. Weber and J. M. Nolan, 1995, Determination of Late Pleistocene - Holocene Slip Rates Along San Gregorio Fault Zone, San Mateo County, Ca, USGS Report, Award no. 1434-93-G-2336, p 805-807

Working Group on Northern California Earthquake Potential, 1996, Database of Potential Sources for Earthquakes larger than Magnitude 6 in Northern California, USGS ofr 96-705, 40 pp.

Weber, G.E., 1990, Late Pleistocene slip rates on the San Gregorio fault zone at Point Ano Nuevo, San Mateo County, California, in Garrison, R.E., Greene, H.G., Hicks, K.R., Weber, G.E., and Wright, T.L., eds., Geology and tectonics of the central California coast region, San Francisco to Monterey: Pacific Section, American Association of Petroleum Geologists, Book GB67, p. 193-203.

Weber, G.E., and Allwardt, A.O., 2001, The Geology from Santa Cruz to Point Ano Nuevo – The San Gregorio Fault Zone and Pleistocene Marine Terraces, in Geology and History of the San Francisco Bay Area: A 2001 NAGT Field-Trip Guidebook. pp 32.

Weber, G.E., and Lajoie, K.R., 1980, Map of Quaternary faulting along the San Gregorio Fault zone, San Mateo and Santa Cruz counties, California: U.S. Geological Survey Circular 1053, 51 pp.

Weber, G. E., and Cotton, W. R., 1981, Geologic Investigation of Recurrence Intervals and Recency of Faulting along the San Gregorio Fault Zone, San Mateo County, California, U.S.G.S. open file report 81-263, 99 p.

Weber, G. E., and others, and Proskurowski, G., 2005, The San Andreas and San Gregorio Fault Systems in San Mateo County, usgs pubs Field Trips, 1127, Chapter 8.

Wiley, T. J., 1983, Pliocene shallow-water sediment gravity flows at Moss Beach, San Mateo County, California, unpublished Stanford thesis, 57 p.

Wiley and Moore, 1983, Pliocene shallow-water sediment gravity flows at Moss Beach, San Mateo County, California in SEPM Pacific Section, Cenozoic Marine Sedimentation, Pacific Margin, USA, p. 29-43

Yang, T., Chou, Y., Ferre, E., Dekkers, M., Chen, J., Yeh, E., Tanikawa, W., 2020, Faulting Processes Unveiled by Magnetic Properties of Fault Rocks, Reviews of Geophysics, v58.

Zechar, J. D., and Frankel, K. L., 2009, Incorporating and reporting uncertainties in fault slip rates, J. Geophys. Res., 114, B12407, doi: 10.1029/2009JB006325.

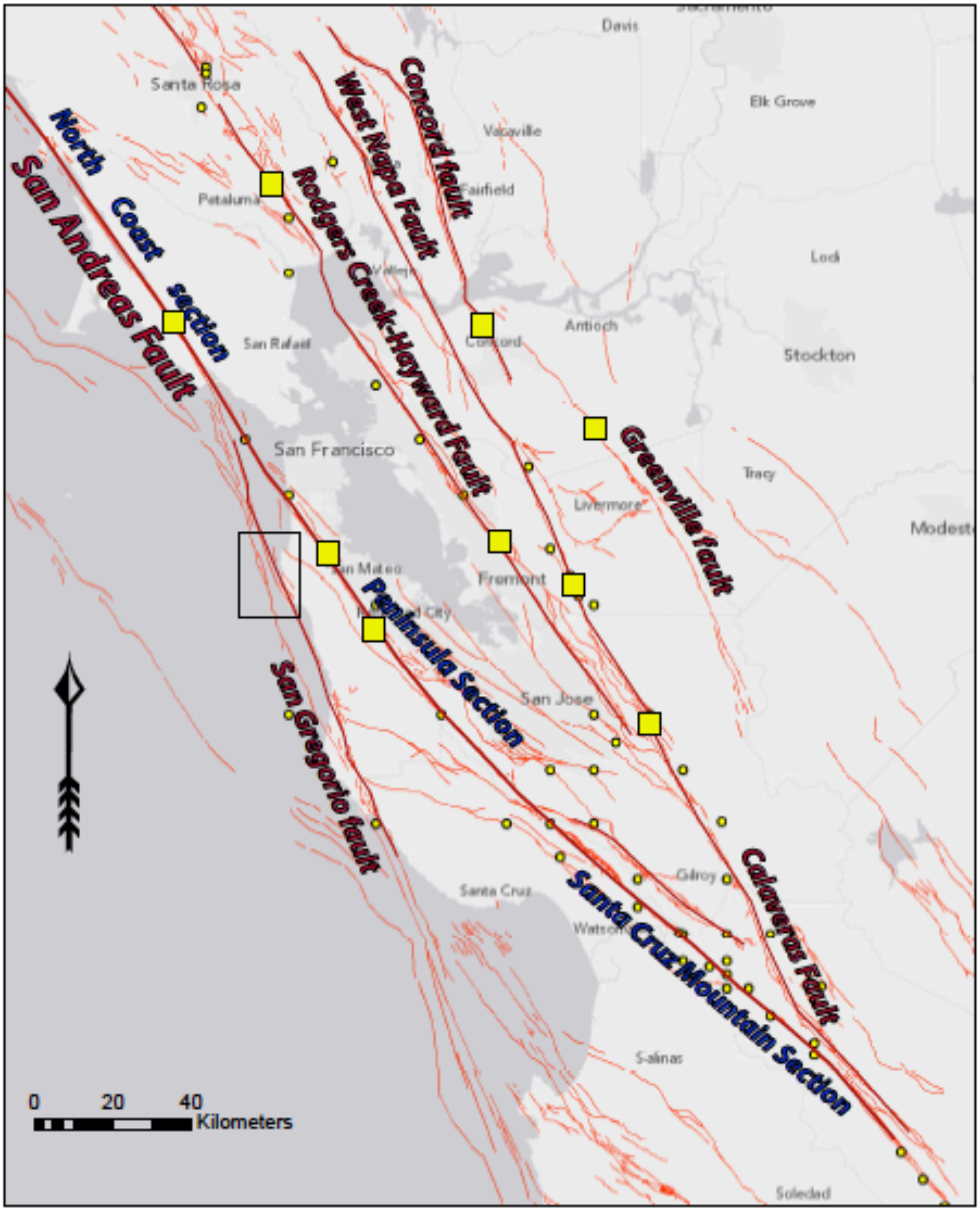

Figure 1: Overview of San Andreas Fault System in San Francisco Bay area with black rectangle indicating region on San Gregorio Fault that is investigated in this study.

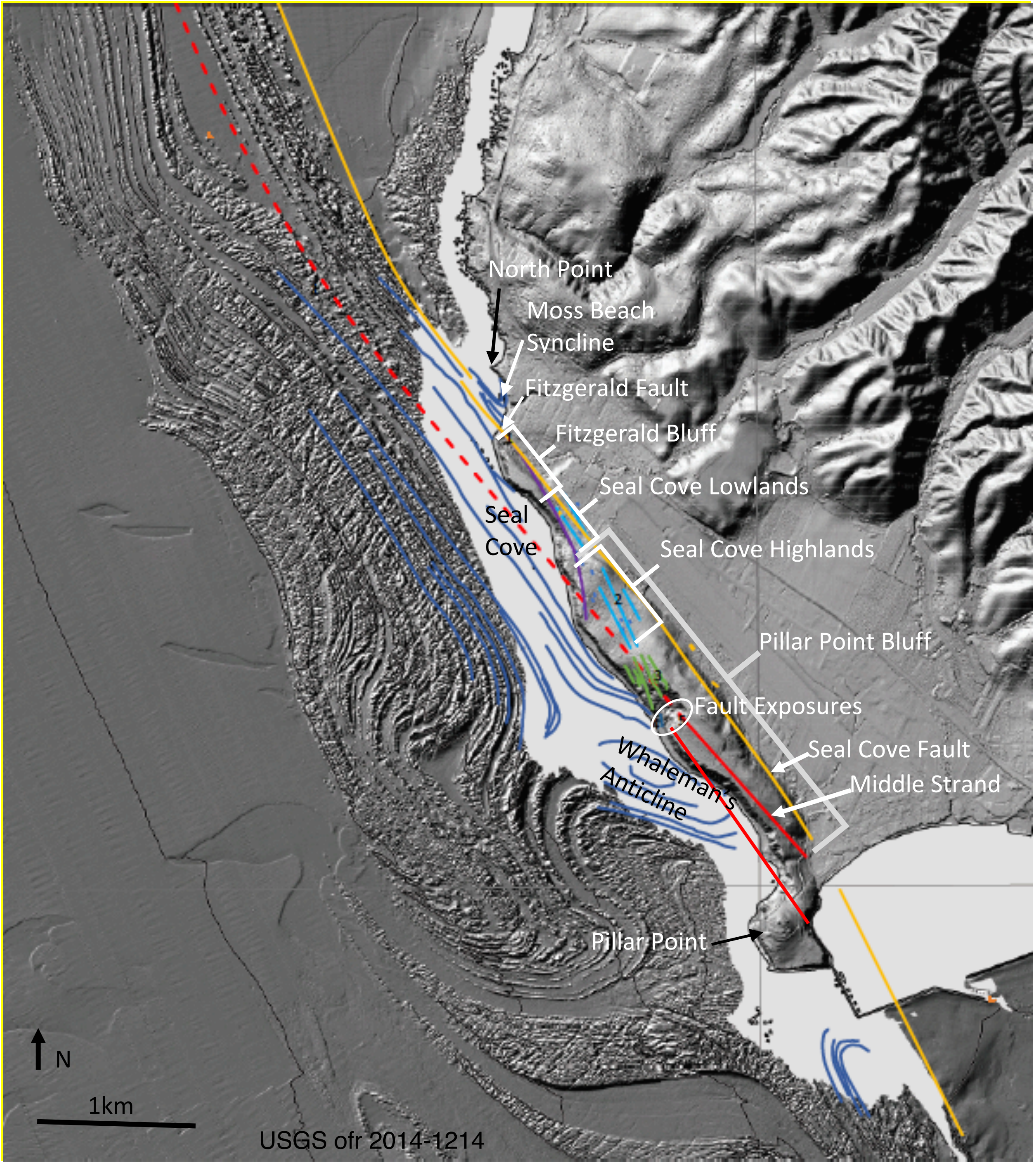

Figure 2: Bathymetry map offshore of Pillar Point Bluff and lidar of on-land area, Bretz et al, 2014, with identification used in this report and near shore folds and on-land faults added. The Seal Cove Fault, in orange, follows the current Alquist-Priolo mapping part of which is disputed in this report, see Figure 4.

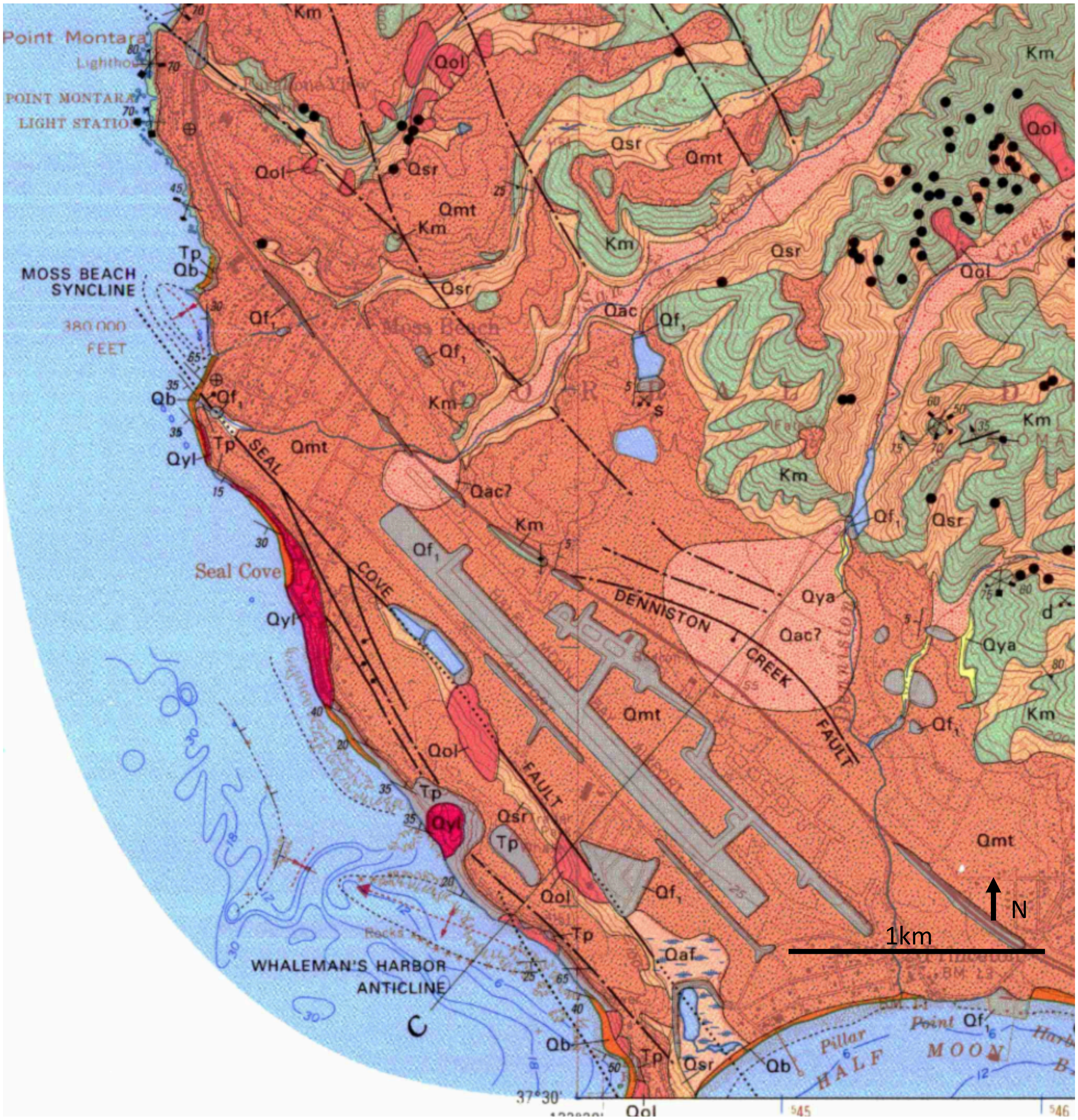

Figure 3: Section of Pampeyan, 1994 geologic map of Montara Mountain Quadrangle.

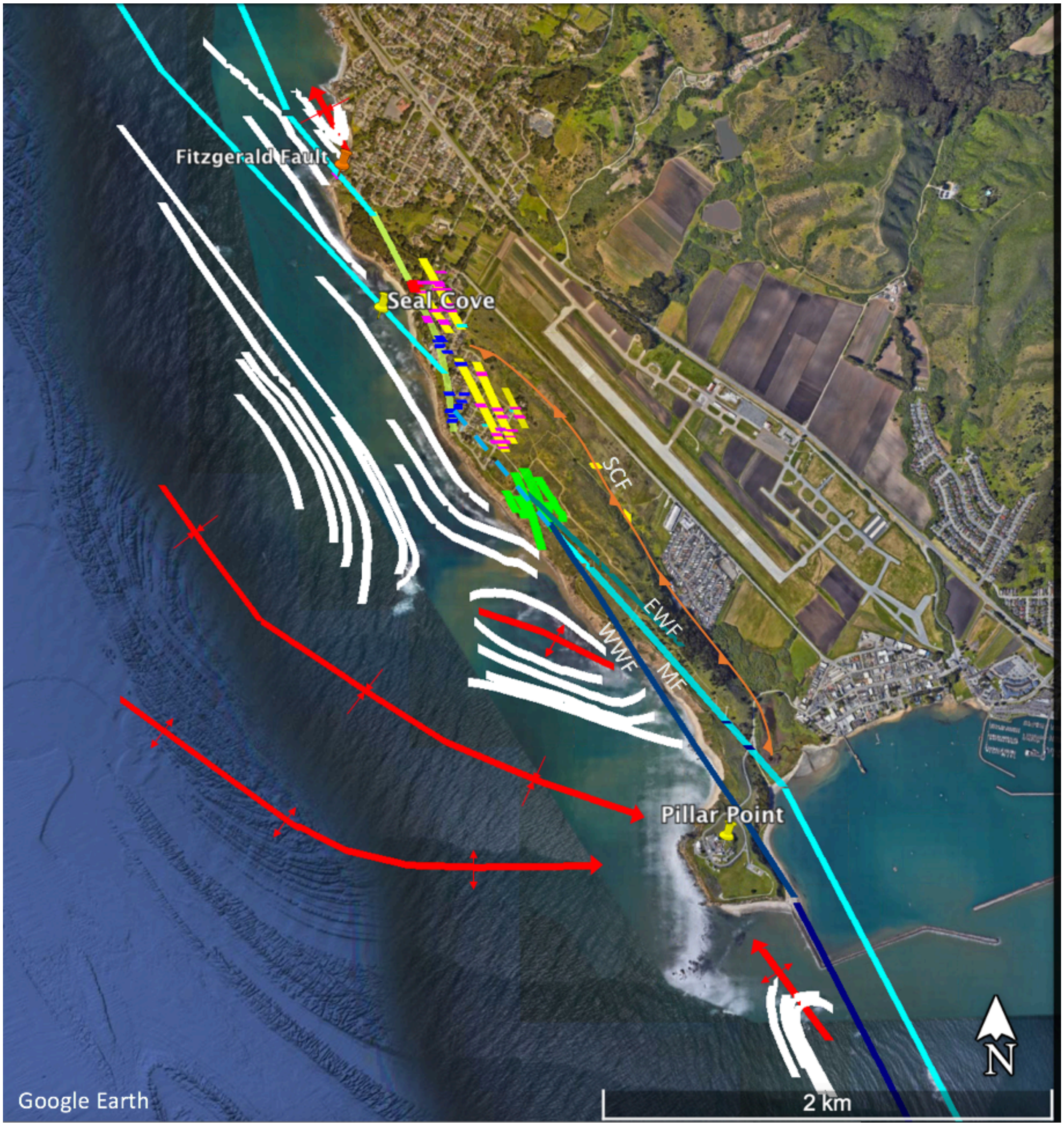

Figure 4: New mapping of faults along Pillar Point Bluff. South to north: The Middle Strand, in cyan, enters from the south, goes through a restraining bend, one component continues NW from Seal Cove, another crosses over (yellow and green lines) to the Fitzgerald Fault, the two sub-parallel strands continue north-northwest. Small magenta marks are consultant trench-identified faults, blue marks are surface shears, short red lines are faults of Simpson et al, 1997, yellow lines are alignments of consultant faults, green lines are fault ridges, light green line is alignment of surface shears, scarps and faults. Orange line is Seal Cove Fault interpreted as a thrust fault. Red lines are fold axes of offshore anticlines and synclines, white lines are eroded offshore folded strata too shallow to be recorded by bathymetry.

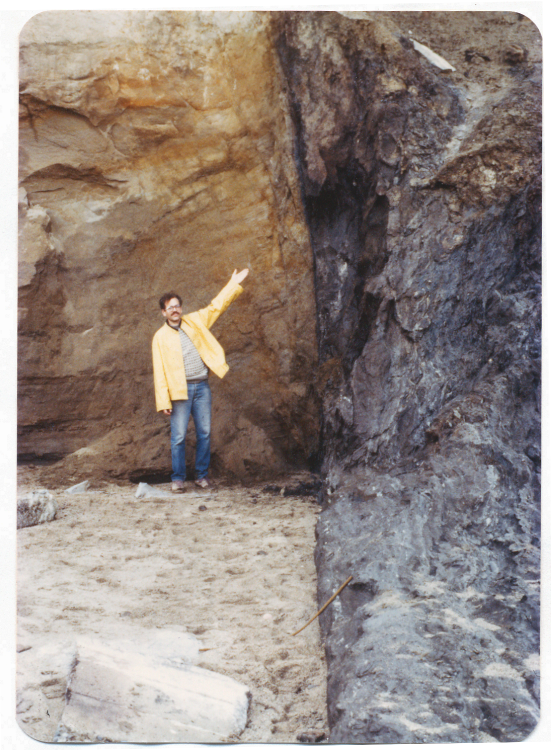

Figure 5: Fitzgerald Fault exposure. T. Wiley Photo 1984, looking SE. Marine terrace deposit on left against Purisima mudrock on right, slickensides plunge reported as 10^o SE. Notice thin line of black (clay?) gouge between the two, then a larger width of variable blackness Purisima, and west of this a few meters the Purisima is grey and brown. The elevation on cliff at this location is about 11m and view is about 7m vertically in this photo. No Purisima is seen on east side here, but it is exposed in the surf zone (including the Moss Beach Syncline). This exposure is currently covered by rip rap.

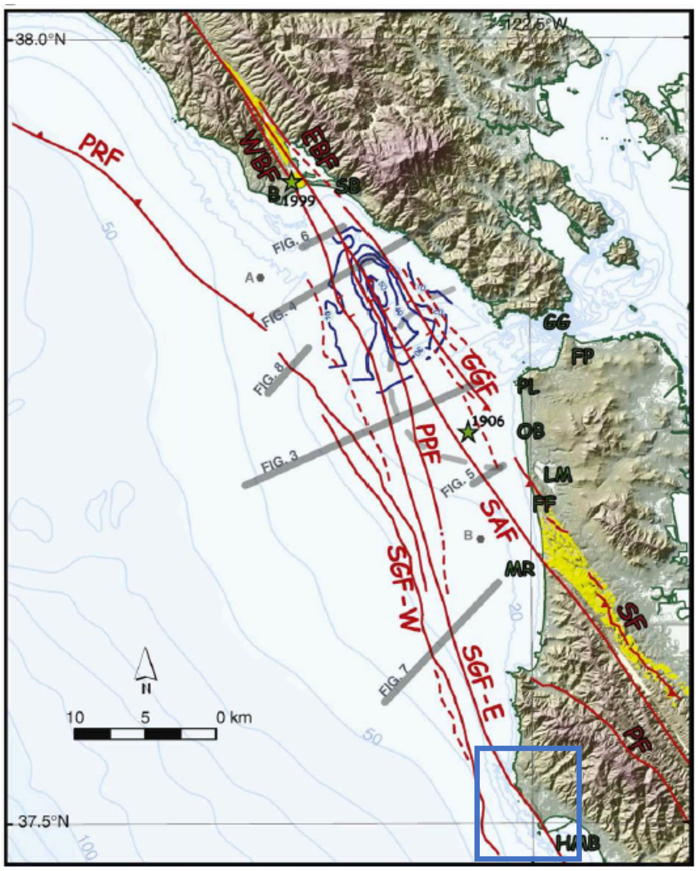

Figure 6: Figure 1B of Ryan et al, 2008. Their mapping of SGF and other faults in the offshore area northwest of current region of interest (blue square). SGF-E is their San Gregorio Fault eastern strand and is the strand being investigated here. SGF-W is their western strand and correlates to the offshore Frijoles strand, not studied here.

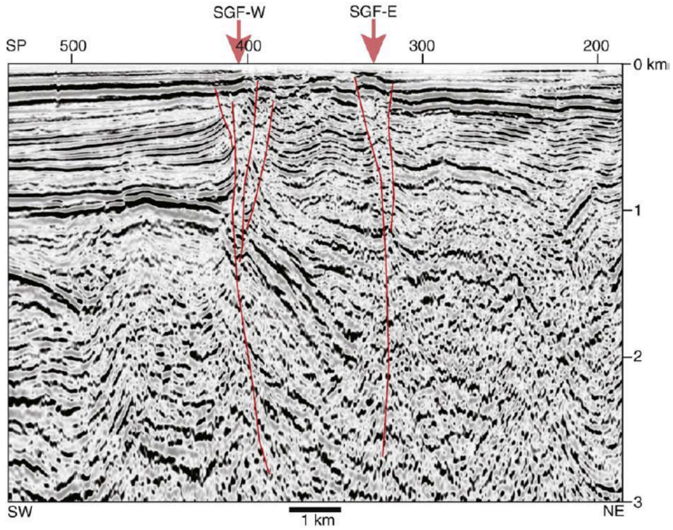

Figure 7. This is the "Fig. 7" referenced in Figure 6. A migrated and depth converted MCS profile which shows the SGF-E fault has two branches that converge at depth. This location is about 12 km northwest of Seal Cove.

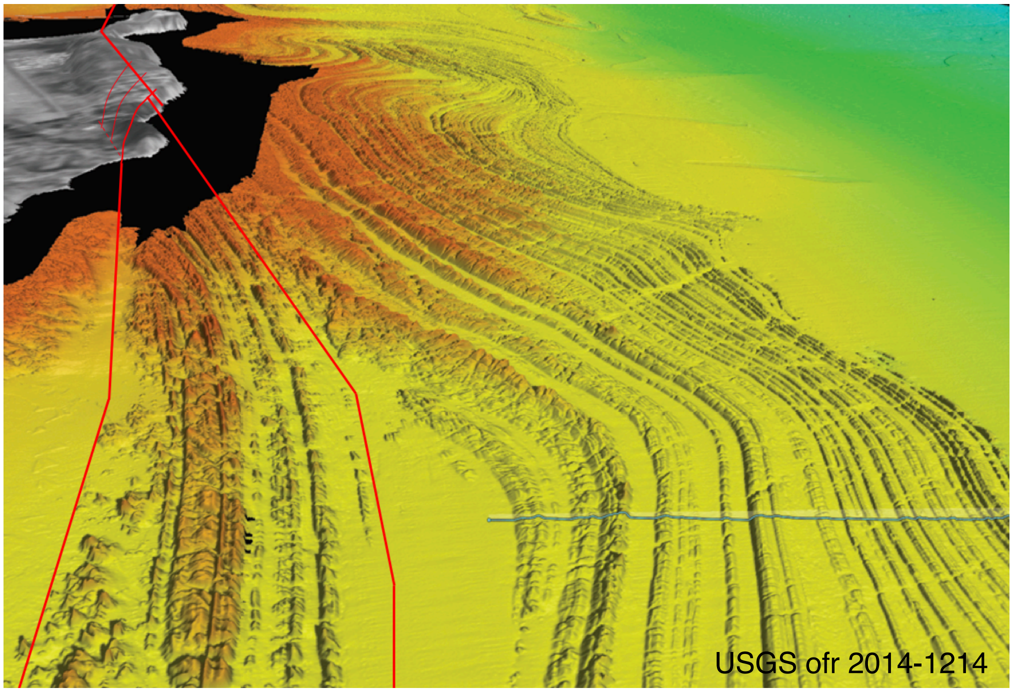

Figure 7a: Two northwest proceeding fault paths in red. View looking south modified from USGS ofr 2014-1214.

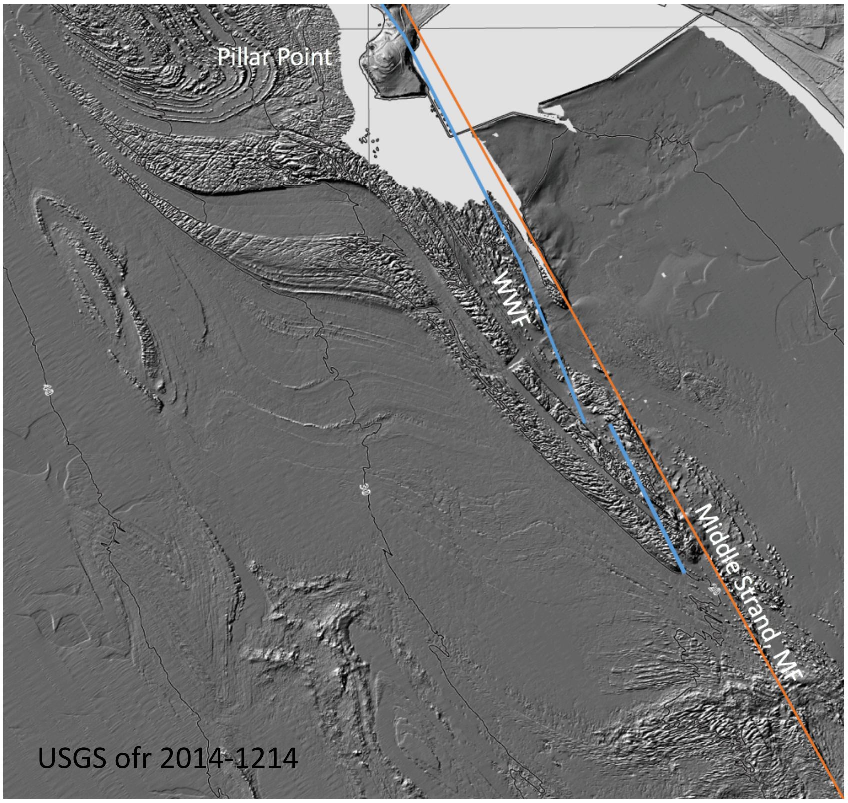

Figure 8: Southeastern extension of West Wall Faults, light blue lines, past Pillar Point subparallel to the San Gregorio Eastern Strand, orange line, here referred to as the Middle Strand that crosses Half Moon Bay.

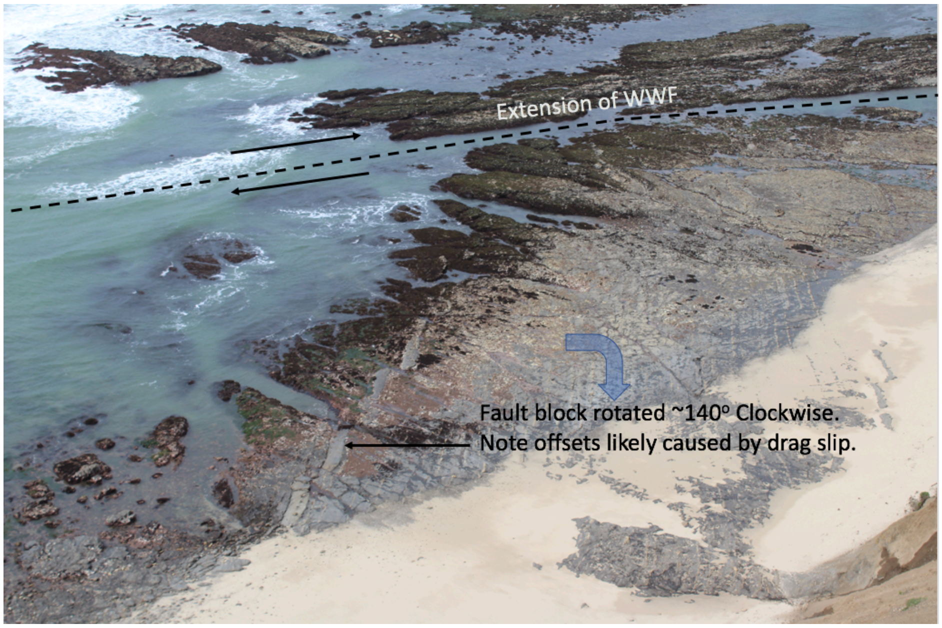
Extension of WWF
Fault block rotated ~140° Clockwise.
Note offsets likely caused by drag slip.

Figure 8a: West Wall Fault looking west crossing Whaleman's Harbor between Pillar Point and Pillar Point Bluff. Note rotated block in foreground.

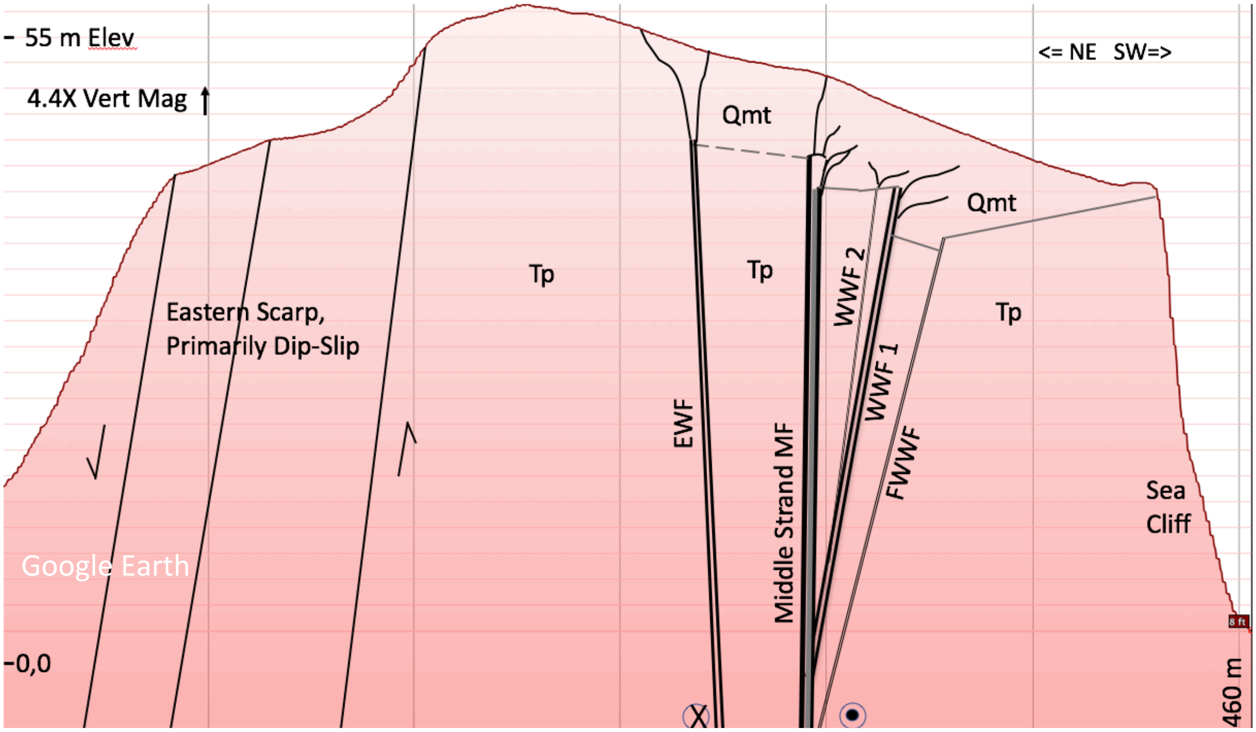

Figure 9: Cross-section of the Middle Strand of the San Gregorio Fault at Pillar Point Bluff near the latitude of the investigated fault exposures along an azimuth of 229°. Faults in Qmt are schematic, many more not shown. Two faults, as shown, have been traced to the surface.

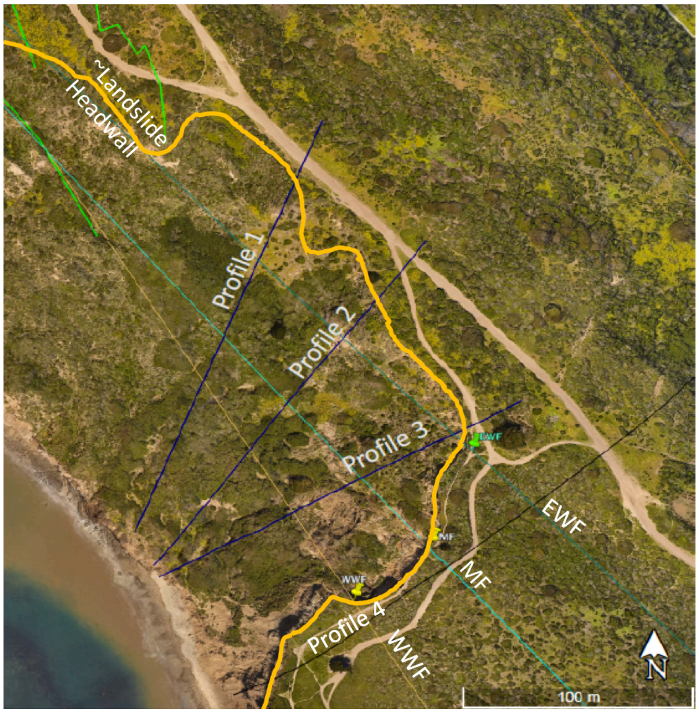

Figure 10. The large landslide area in Pillar Point Bluff showing the locations of profiles in Figures 11 – 14 below and the projected traces for faults EWF, MF, and WWF.

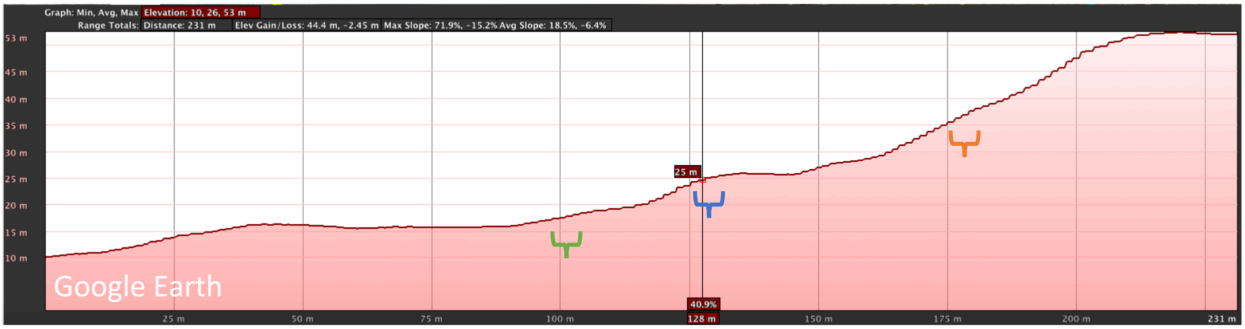

Figure 11. Google Earth elevation Profile 1 through Large Landslide area, from 543609 E, 4151452 N, heading 22°. In this and following figures the Blue bracket = Main Fault projected intersection with profile. Green bracket > West Wall Fault. Orange bracket > East Wall Fault.

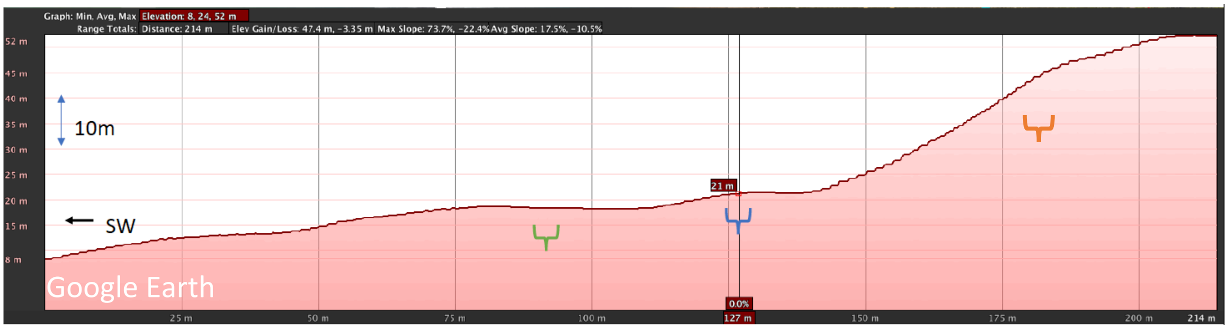

Figure 12. Profile 2 through large landslide area, from 543618 E, 4151433 N, heading 35.5°.

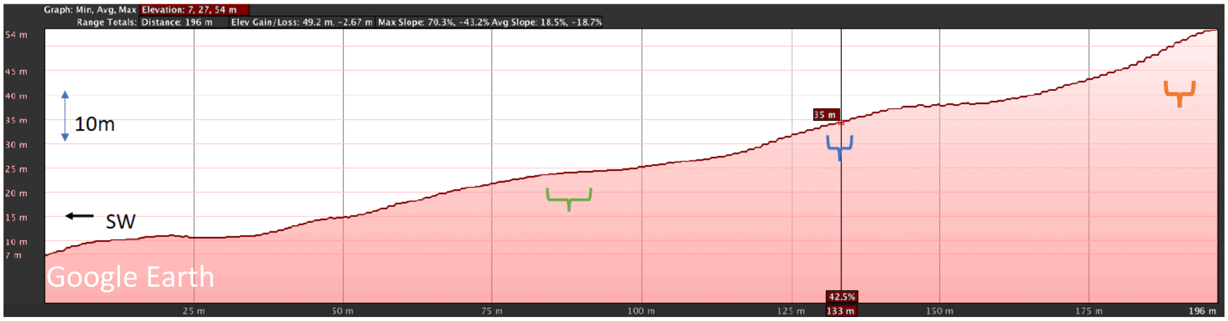

Figure 13. Profile 3 through large landslide area, from 543620 E, 4151426 N, heading 58°.

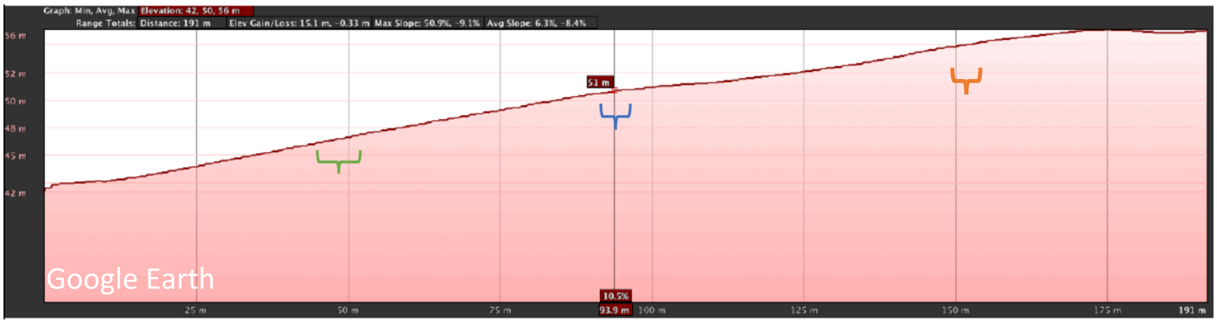

Figure 14. Profile 4 across surface of Pillar Point Bluff just south of Landslide Basin shows indications of MF and EWF, but not WWF.

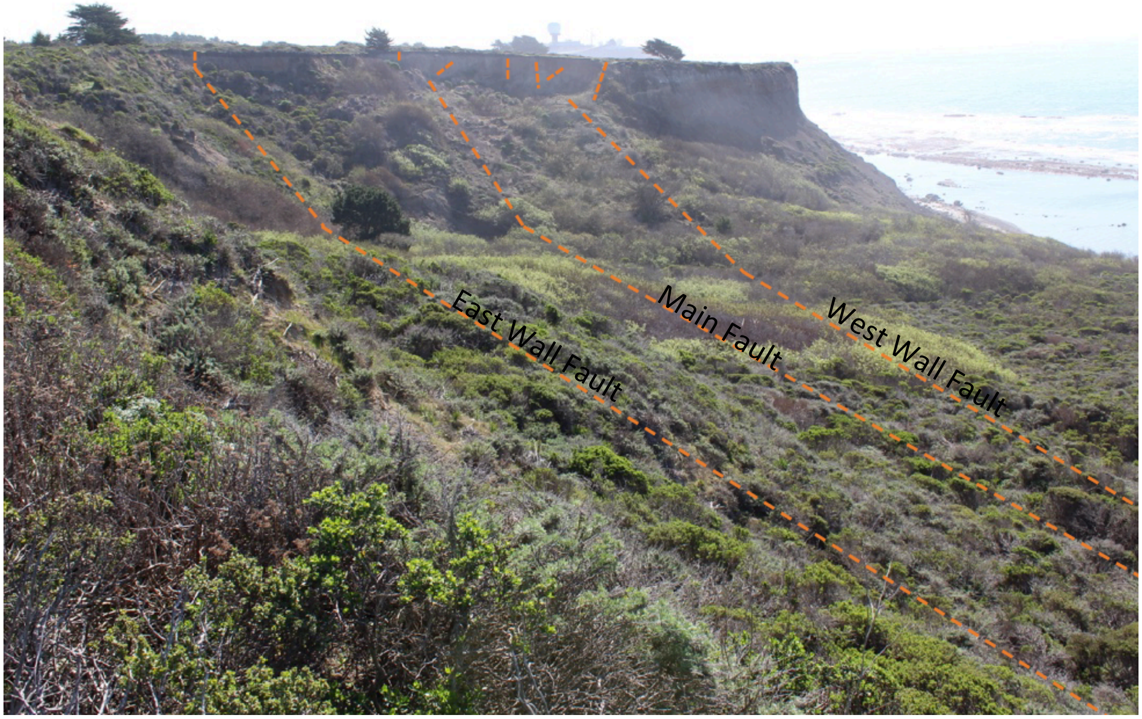

Figure 15. Photo looking south across large landslide area showing approximate projected paths of East Wall Fault, Main Fault and West Wall Faults.

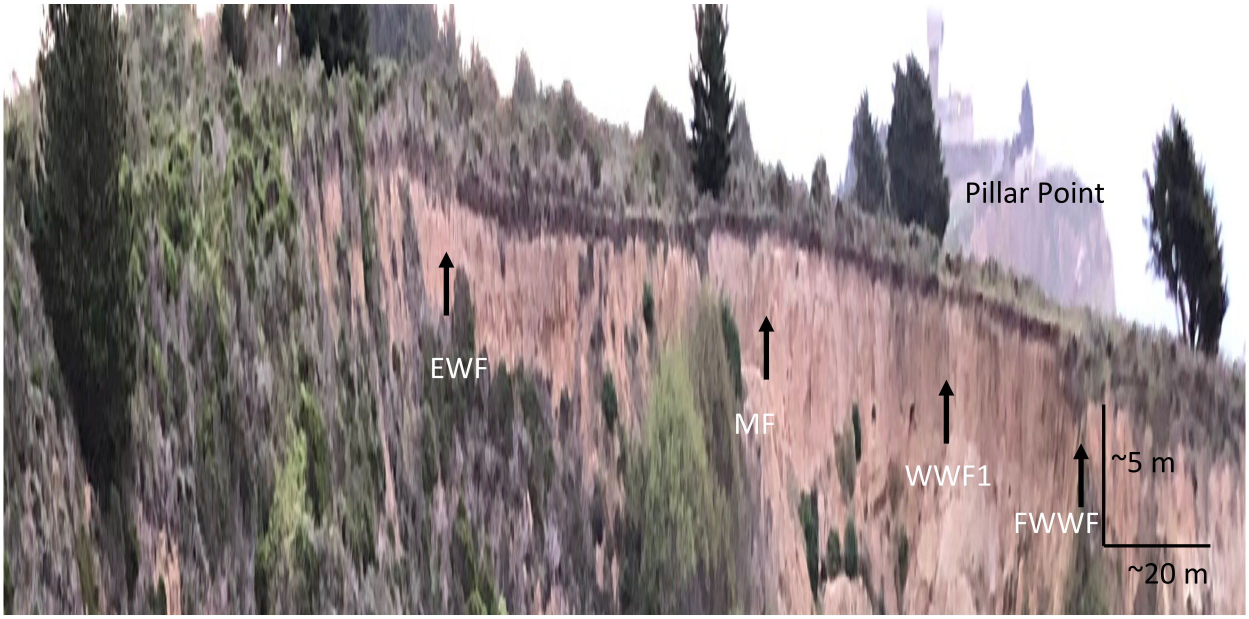

Figure 16: Vertically expanded photo (~6X) of landslide headwall looking south illustrating location and topology of faults and soil horizon thickness variation. Elevation of the camera is approximately at the elevation of the surface above the MF headwall.

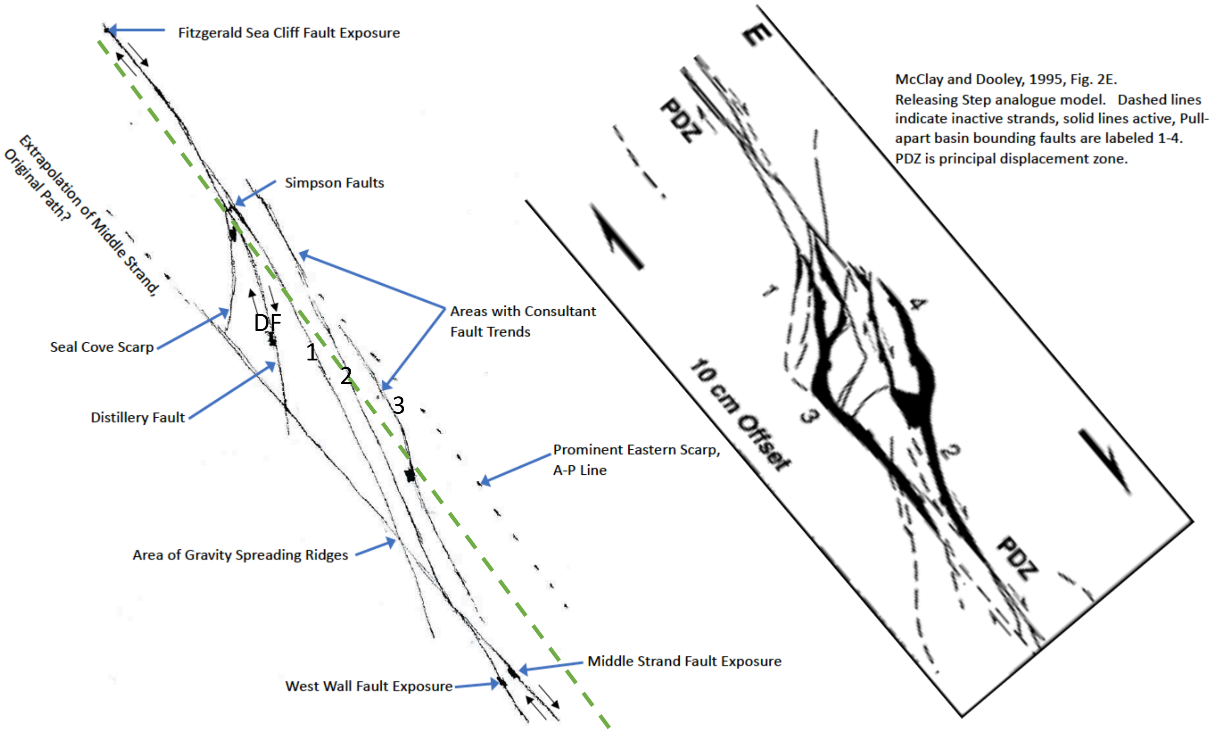
Fitzgerald Sea Cliff Fault Exposure
Extrapolation of Middle Strand, Original Path?
Simpson Faults
Areas with Consultant Fault Trends
Seal Cove Scarp
DF
1
2
3
Distillery Fault
Prominent Eastern Scarp, A-P Line
Area of Gravity Spreading Ridges
Middle Strand Fault Exposure
West Wall Fault Exposure
E
PDZ
1
4
3
2
PDZ
10 cm Offset

McClay and Dooley, 1995, Fig. 2E. Releasing Step analogue model. Dashed lines indicate inactive strands, solid lines active, Pull-apart basin bounding faults are labeled 1-4. PDZ is principal displacement zone.

Figure 17. Comparing the releasing fault mapping at PPB with the McClay and Dooley, 1995 experimental analogue model of a releasing right lateral fault. The green dashed line is the location of the profile shown in Figure 18, its termination at southern end of PPB is not shown.

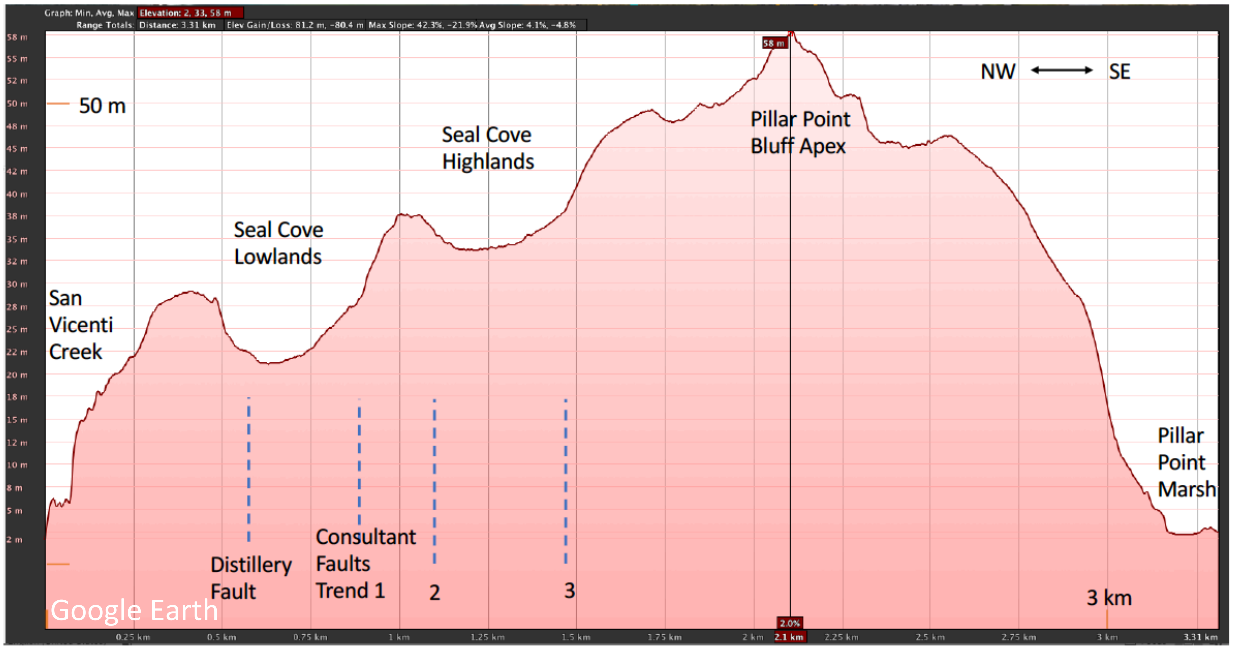

Figure 18. Google Earth elevation profile along the length of Pillar Point Bluff following the path of the dashed green line in Figure 17. Dashed blue lines are where the profile crosses the Distillery Fault, and consultant fault trends 1, 2, and 3 as shown in Figure 17.

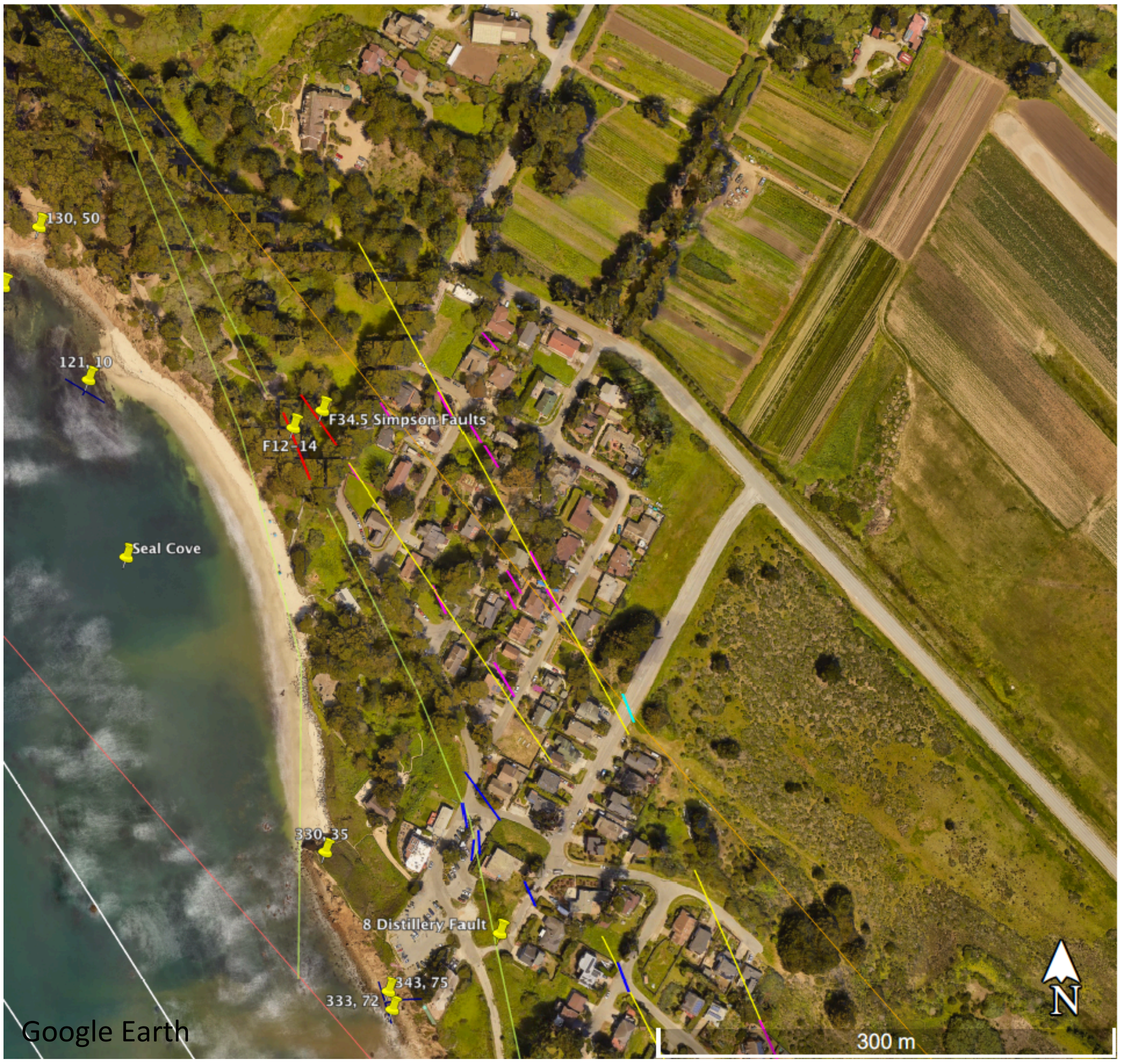

Figure 19. Google Earth image of Seal Cove showing the Distillery fault and its alignment with the western faults identified by Simpson et al (1997). The eastern Simpson fault aligns well with the consultant-identified faults that make up another of the proposed releasing faults.

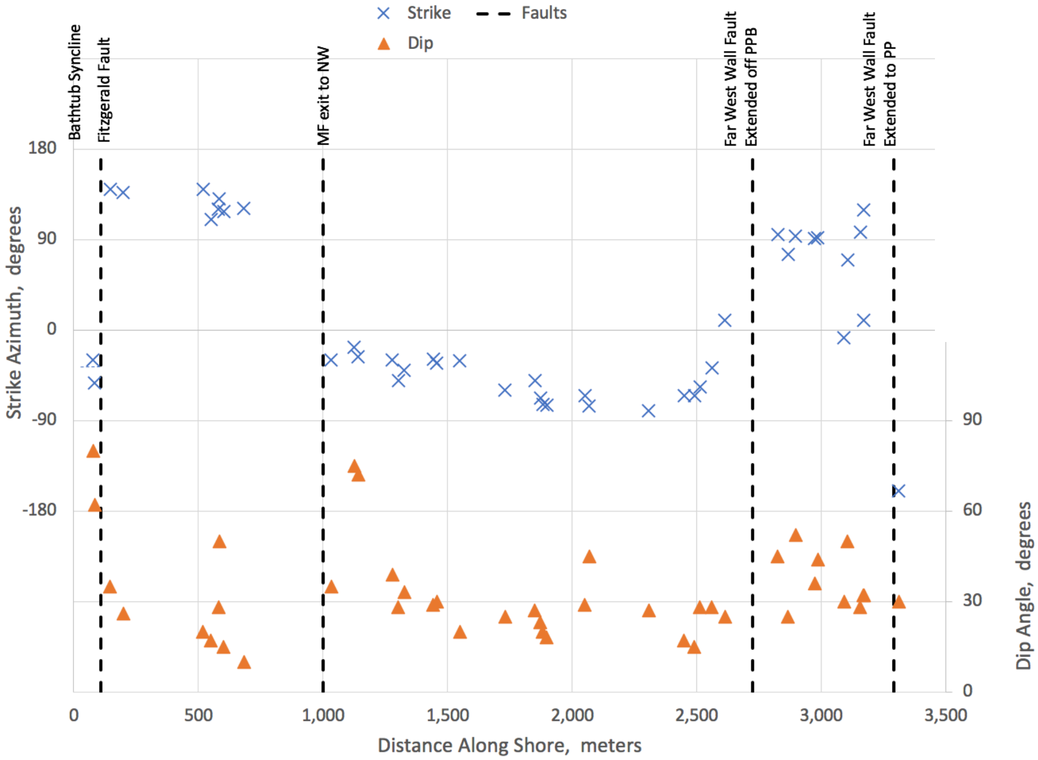

Figure 20: Strike (using right hand rule) and dip of Purisima along shoreline of Pillar Point Bluff, along path in Figure 21, starting on the N at the Fitzgerald Fault and ending at Pillar Point. Dashed vertical lines show where faults from the current mapping cross the shoreline.

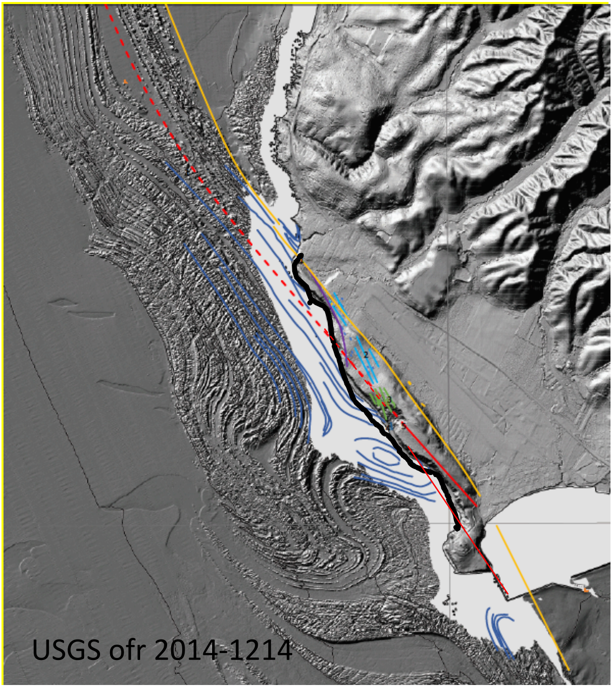

Figure 21: Path of the strike and dip plot in Figure 20, black line, including the mapped faults in red with releasing faults in green and light blue, previously assigned A-P fault line in orange.

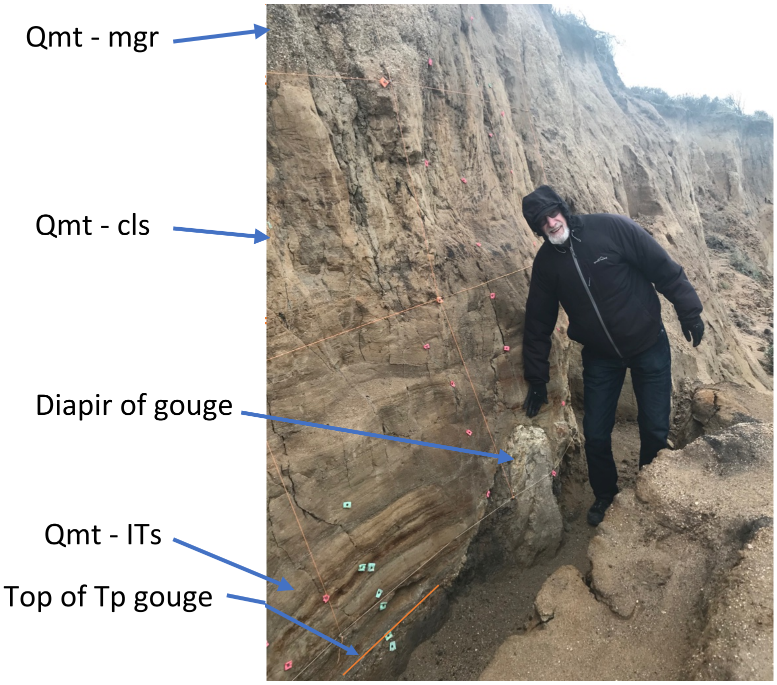

Figure 22: Strata above MF gouge includes Qmt-ITs (marine terrace deposit of intertidal sand), Qmt-cls (clayey sand, likely a back-berm deposit), Qmt-mgr (medium gravel deposit). Pointing to a clay gouge diapir extruded from fault gouge in Purisima at bottom of trench into Qmt vertically offsetting Qmt strata by the height of the diapir. See Figure 47 for detailed view.

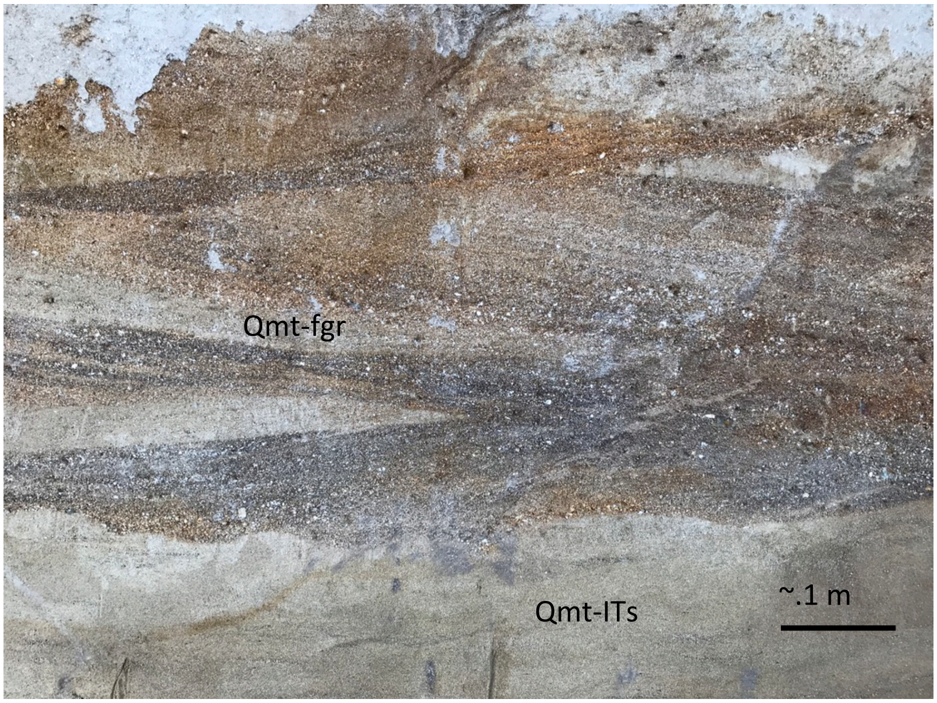

Figure 23: Qmt-fgr displaying small angle crossbedding above Qmt-ITs on landslide headwall between MF and WWF2.

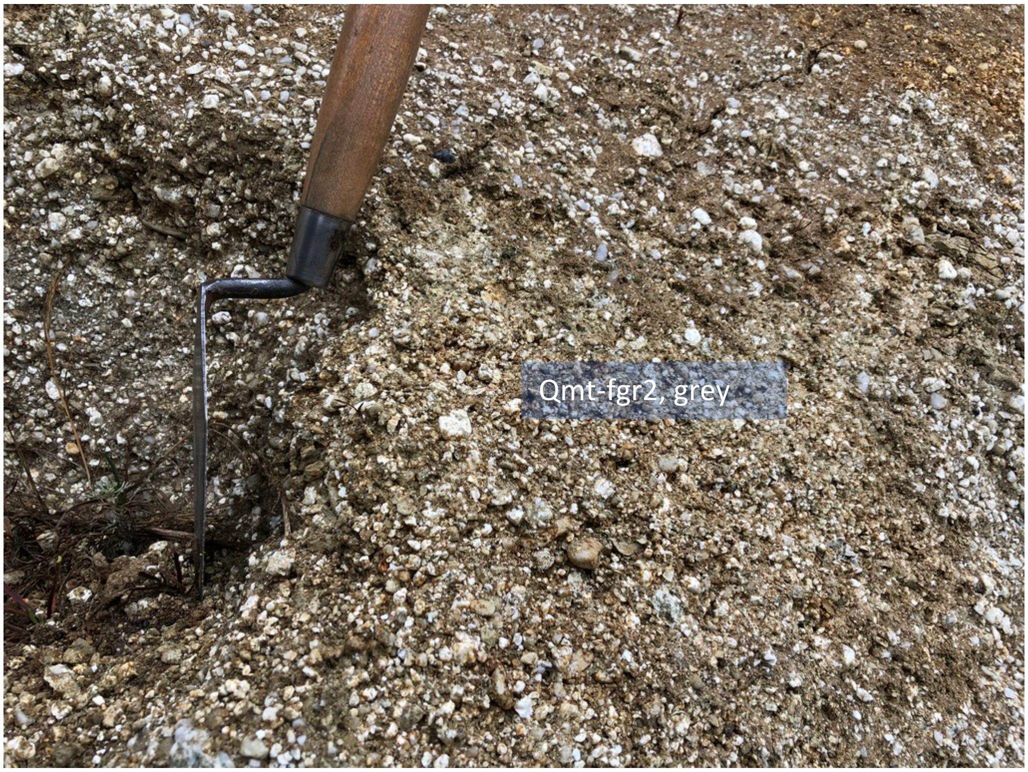

Figure 24: Qmt-fgr2 on west side of WWF1. Trowel is .25 m long.

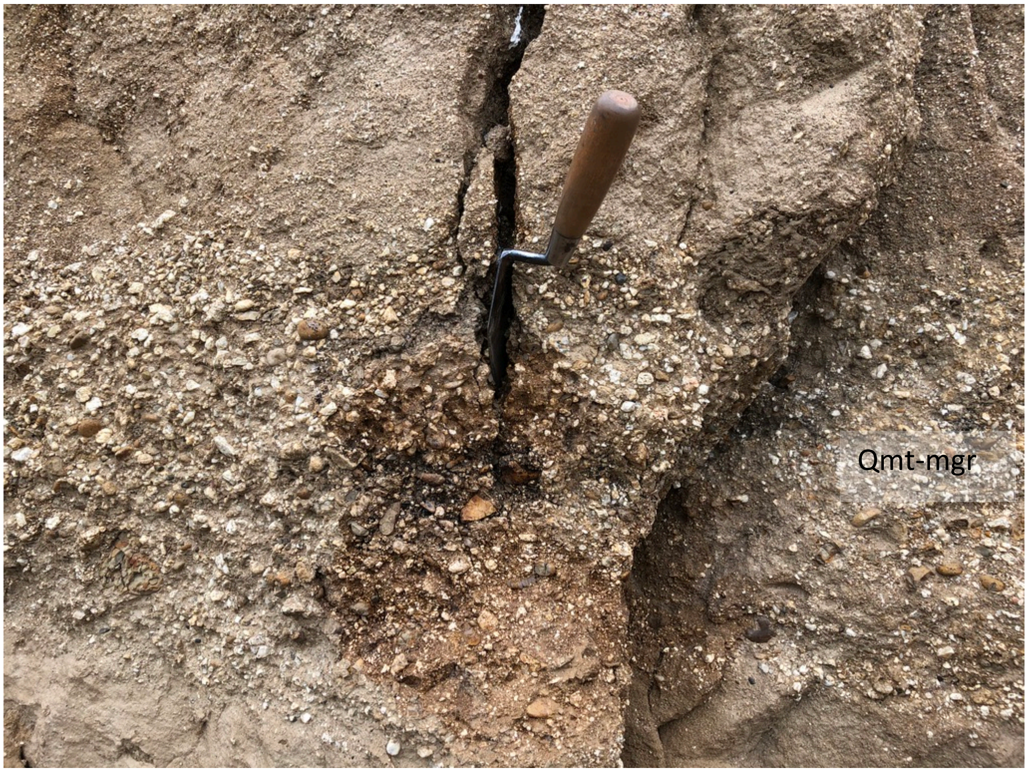

Figure 25: Qmt-mgr on wall between MF and WWF. Trowel is .25 m long.

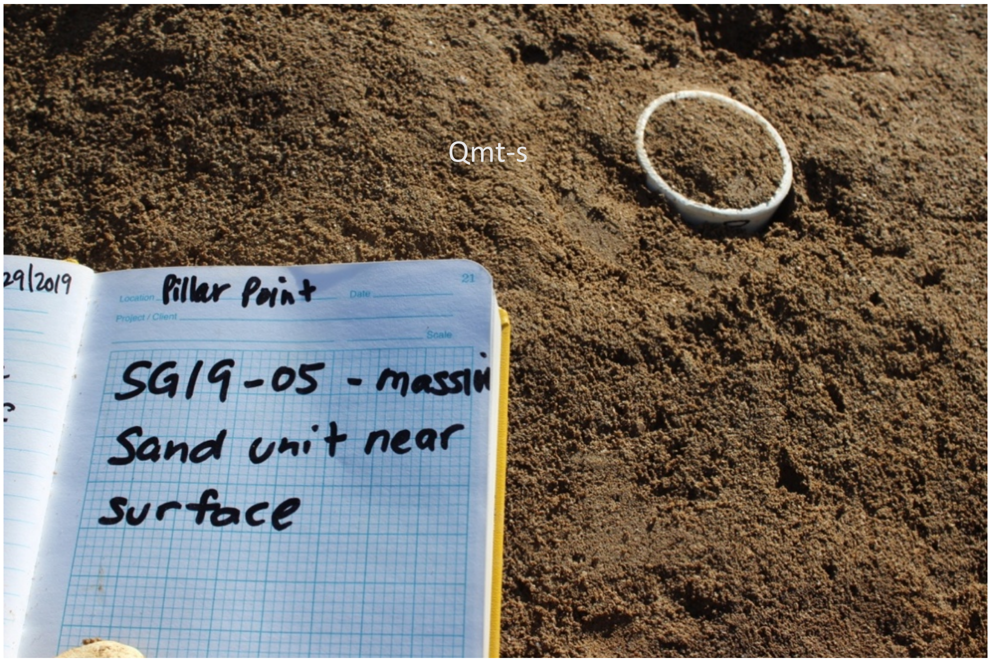

Figure 26: Homogenous well-sorted sand layer near surface, Qmt-s, probably aeolian. Dating sample location SG19-05. Notebook is .12 m wide.

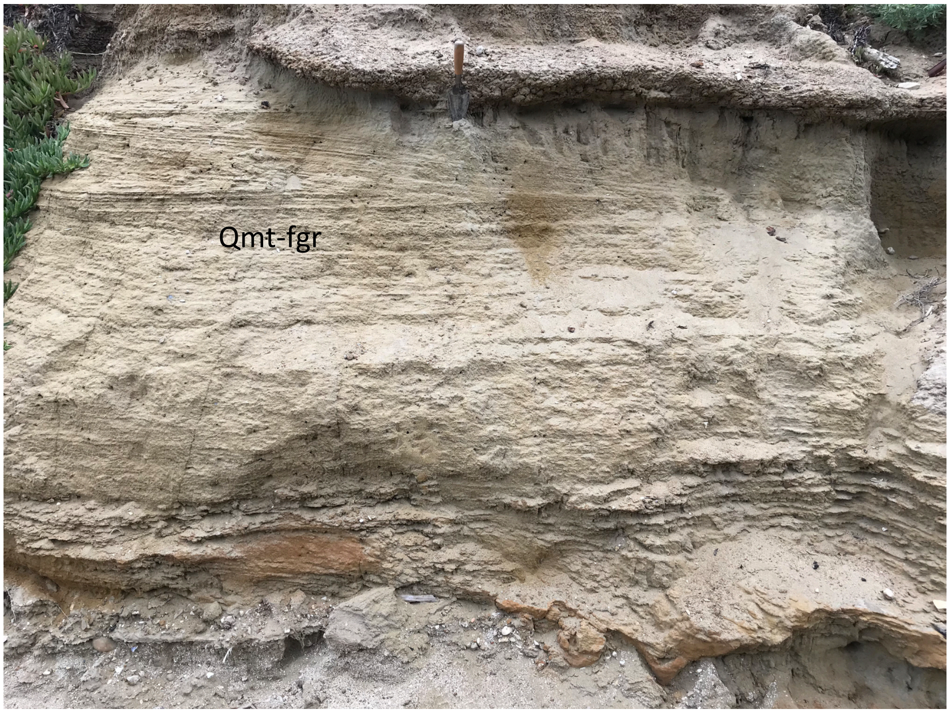

Figure 27: Cliff along Frenchman's Creek outlet at Miramar beach, Half Moon Bay about 3 km south of PPB. Intertidal sand at bottom, mostly covered by colluvium, with fine gravel layers above that compare with those in Figure 24 in appearance, lithology, and grain size and with low angle crossbedding similar to that in Figure 23. Trowel is .25 m long.

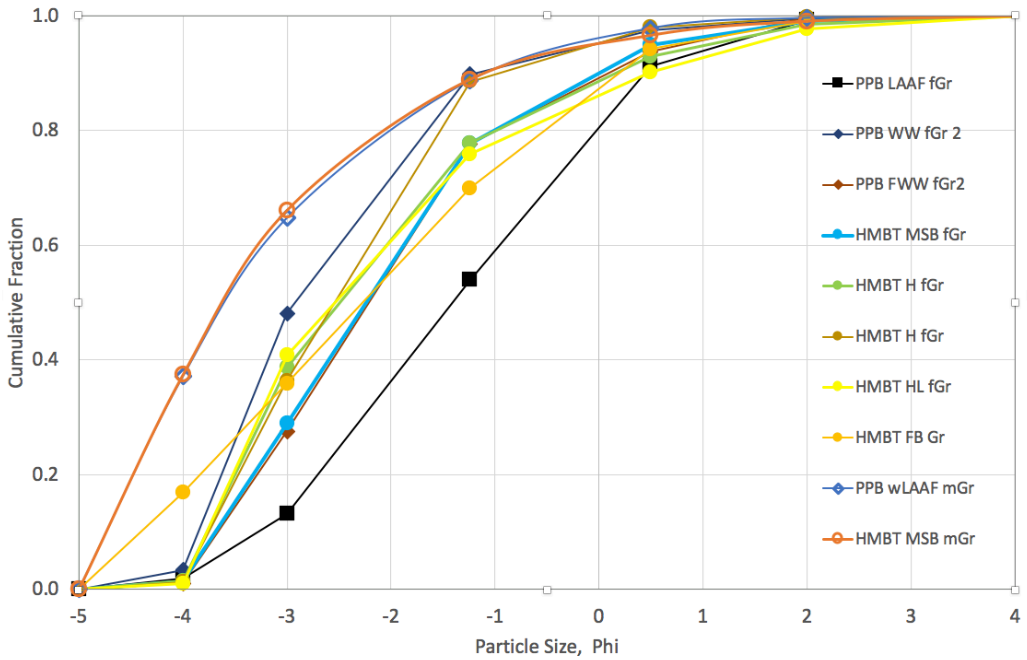

Figure 28: Grain size distribution for fine, fGr, and medium, mGr, gravels at PPB and HMBT. MSB is Montara State Beach, H and HL are around Pillar Point Harbor, FB is Francis Beach, LAAF is adjacent MF, WW and FWW are adjacent the west wall faults.

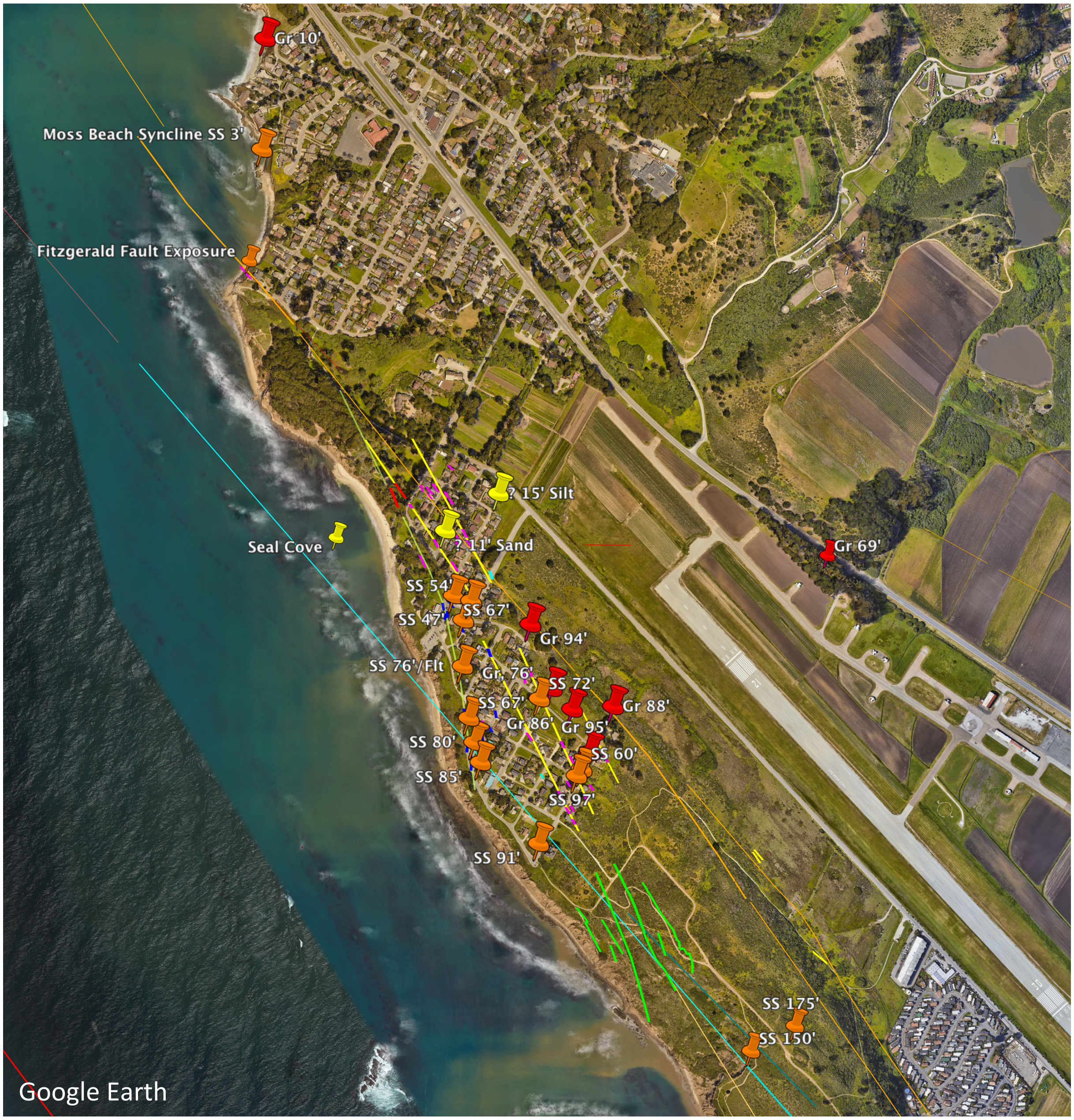

Figure 29: Bedrock map derived from borings in Leighton et al, 1971. Orange markers with SS indicate Purisima fm found at depth, Red markers with Gr for Montara granodiorite, numbers are bedrock elevations in ft. Yellow markers in Seal Cove lowlands indicate they were unable to find bedrock down to about 11 to 15 ft. of elevation. Granitic Bedrock in nearby terrain is also indicated, plus all of the PPB shoreline exposes Purisima.

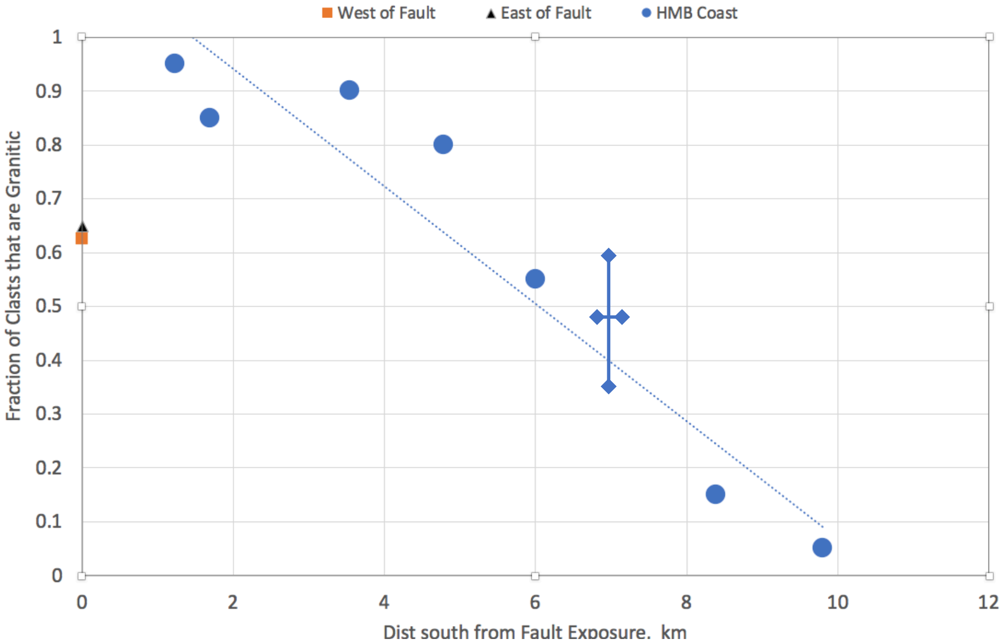

Figure 30: Fraction of clasts of granitic origin (vs sedimentary) larger than .5 cm in Qmt gravel deposits along HMB coast and at the fault exposure. Error bars represent typical uncertainty along the coast, at the fault they are much smaller due to larger sample sizes.

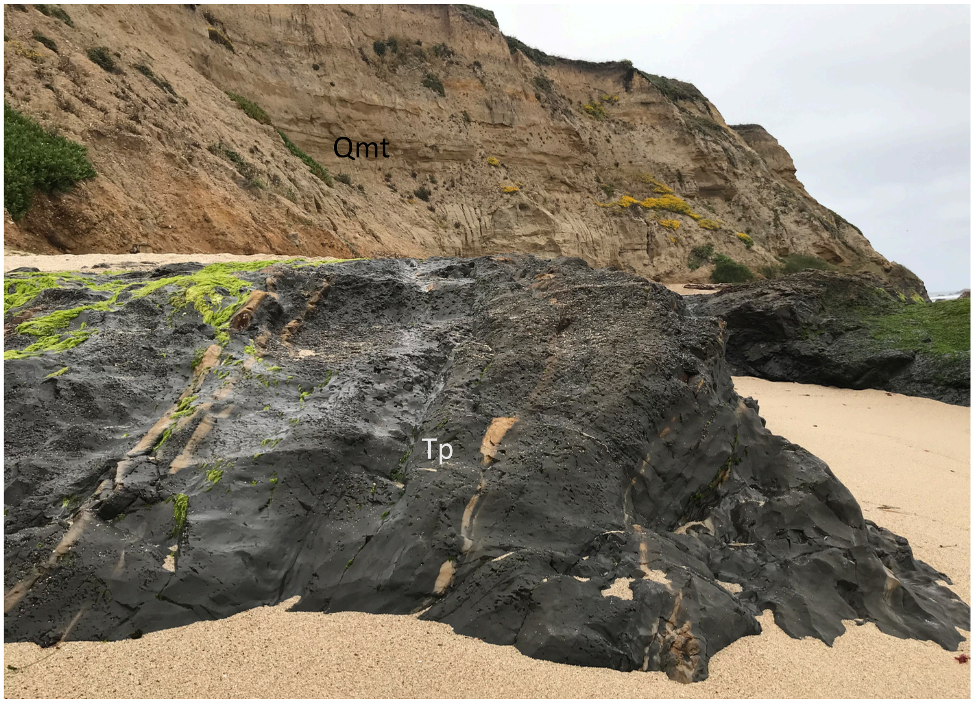

Figure 31: Redondo Beach 5 km south of PPB showing first appearance of Purisima south of PPB in foreground and marine terrace deposits with interleaved layers of sand and fine and medium gravels on cliff face.

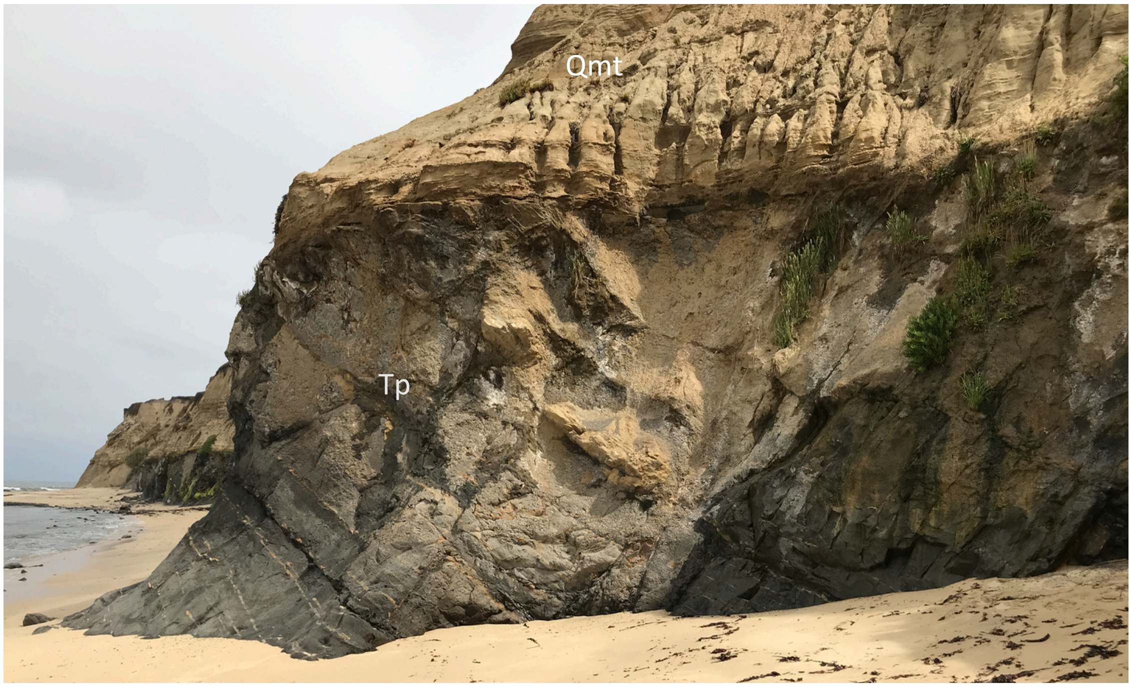

Figure 32: Miramontes Point 8 km south of PPB. Purisima reaches 3-5 m above beach with interleaved layers of sand and fine and medium gravels.

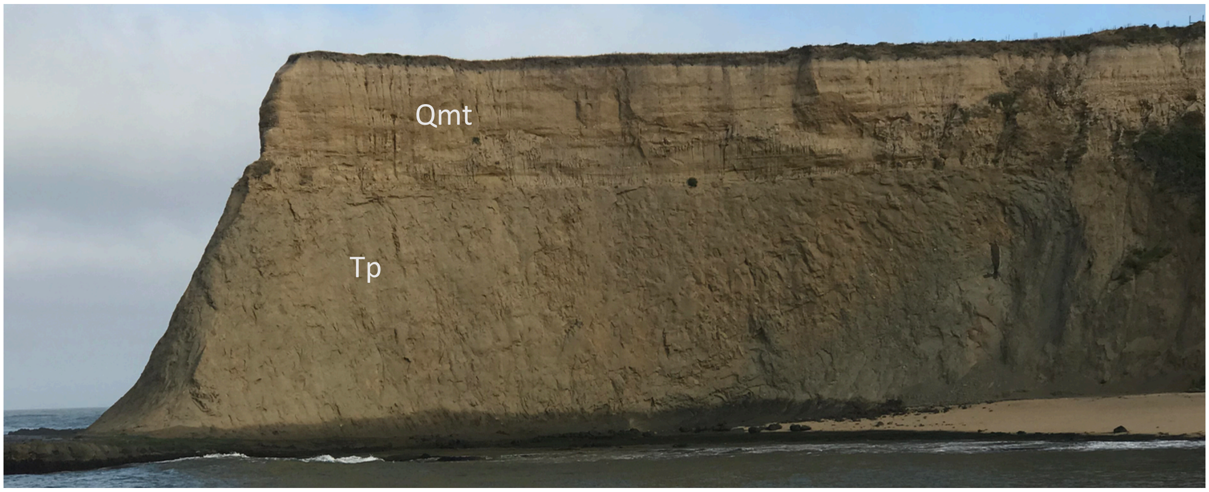

Figure 33: Martin's Beach 15 km south of PPB. Purisima, about 40 m above sea level, is overlain by marine terrace deposits, interleaved layers of sand, and fine to coarse gravel.

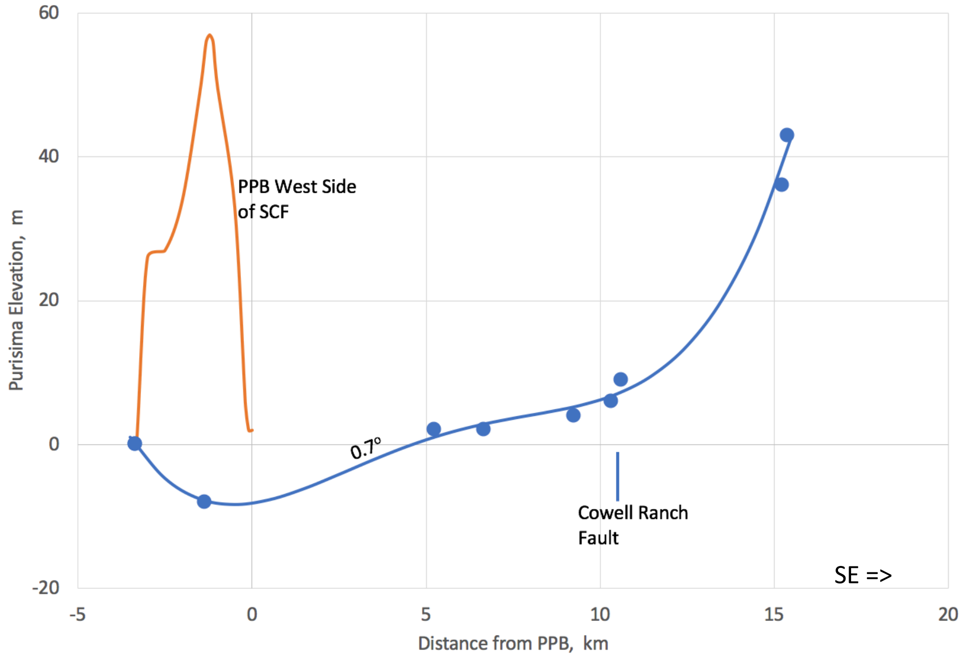

Figure 34: Purisima surface elevation on east side of SGF along coast of Half Moon Bay from north end of PPB to 16 km south, blue circles. For comparison, the orange line is approximate profile of PPB, west of SCF. Note the elevation of -8 m at -1.3 km is from the drilling depth to the wavecut platform in Kennedy et al, 1982, and both the horizontal location and elevation have significant uncertainty.

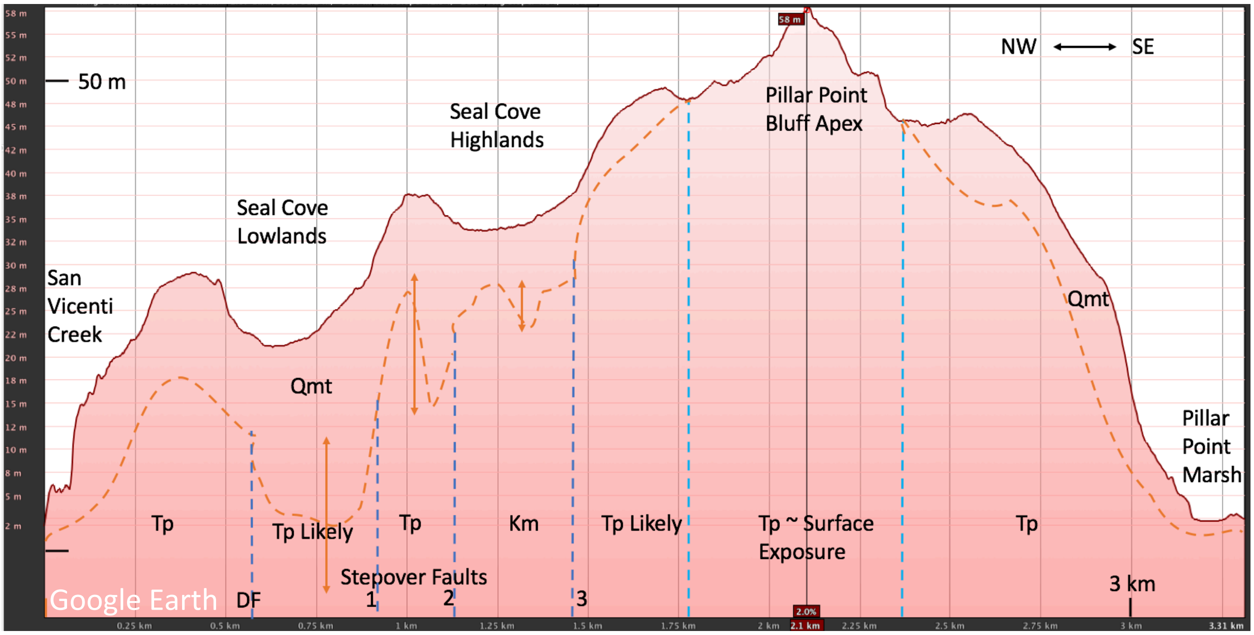

Figure 35: Bedrock along Profile in Figure 18. Dashed orange line is separation between bedrock and Qmt is estimated from cliff exposures and in Seal Cove area measured by Leighton et al, 1979, with uncertainty range arrows. Km = Montara Granodiorite, Tp = Purisima fm., Qmt = Marine Terrace Deposit. Relief of bedrock in Highlands is schematic.

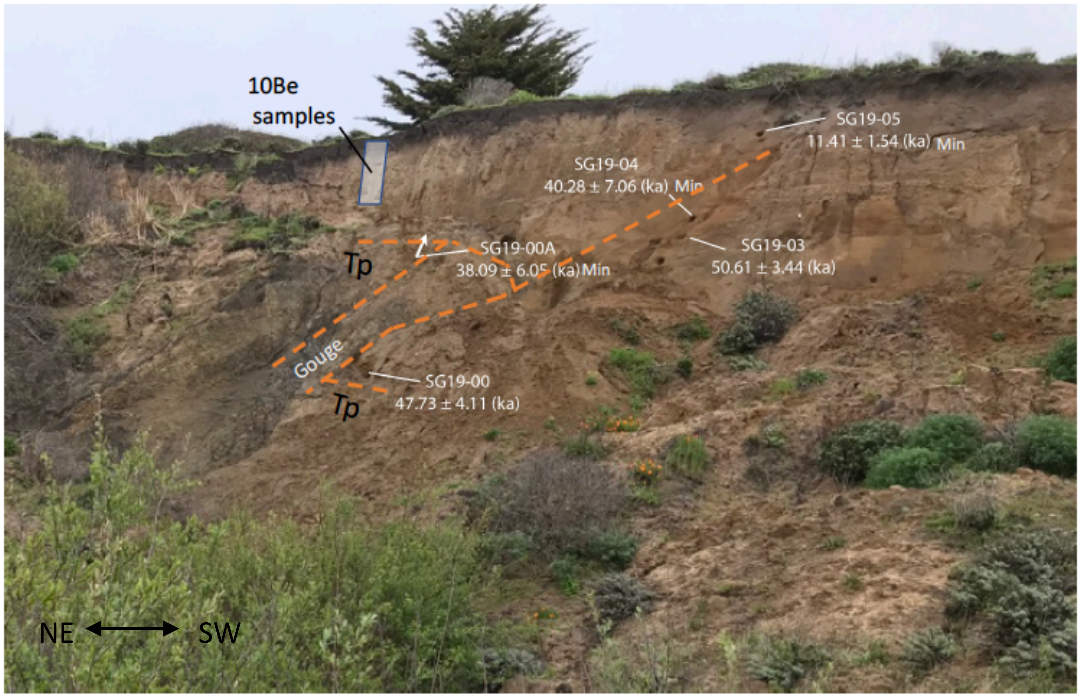

Figure 36: Locations of samples used for dating sediment layers. "Gouge" refers to the main fault gouge. Cosmogenic samples were taken from a vertical section labeled "10Be samples" plus a sample of pebbles collected on the surface. Locations labeled SG19-xx were IRSL sample sites.

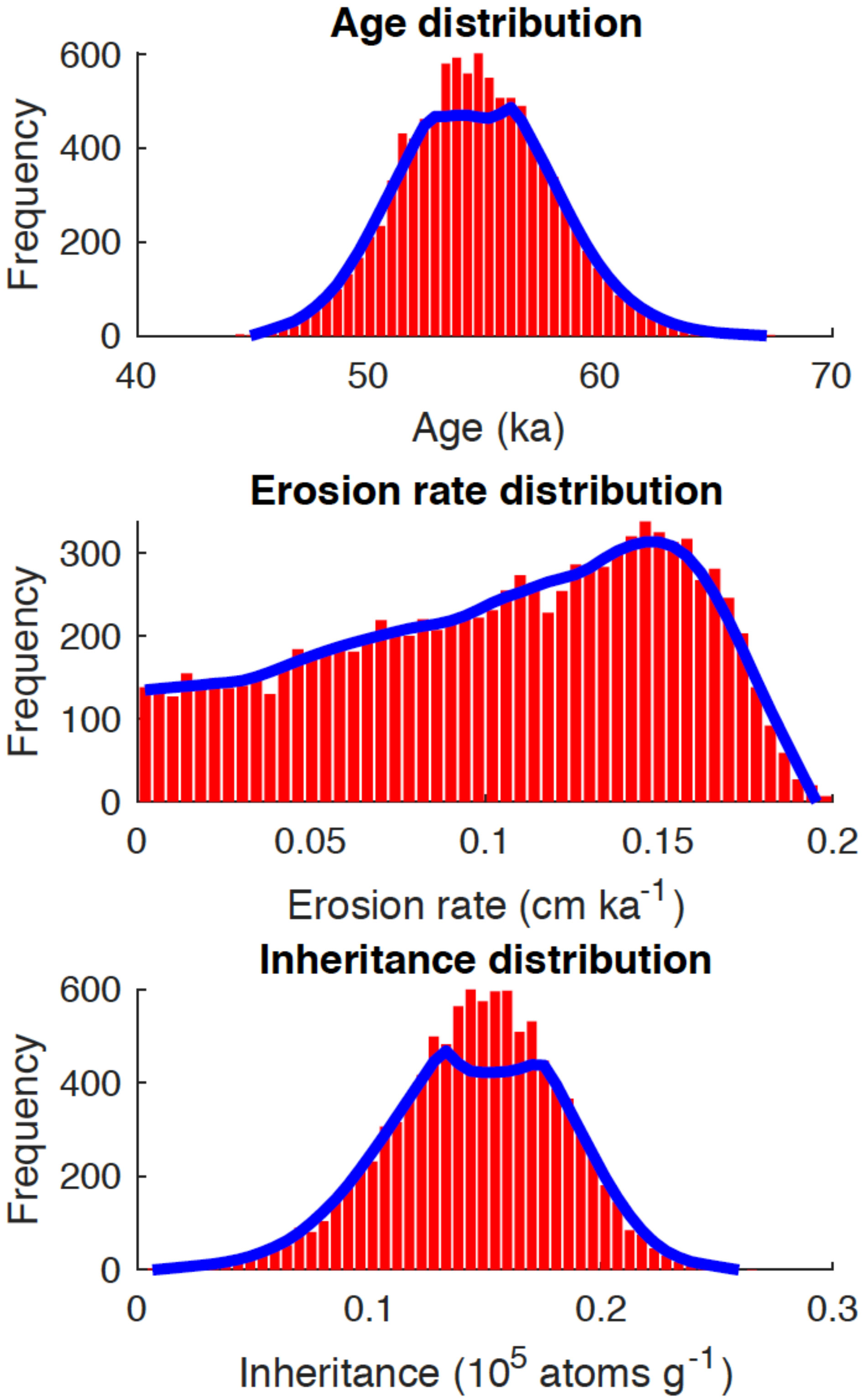

Figure 37: Age distribution, erosion rate, and inheritance from cosmogenic 10Be dating of sediments above Tp by K. Blisniuk, A. Walker, and coworkers, 2020. Modeling provides a mean age min and max of 44 and 59 ka, respectively. A surface age from a sampling of pebbles on Pillar Point Bluff surface is 18.8 ± 1.7 ka.

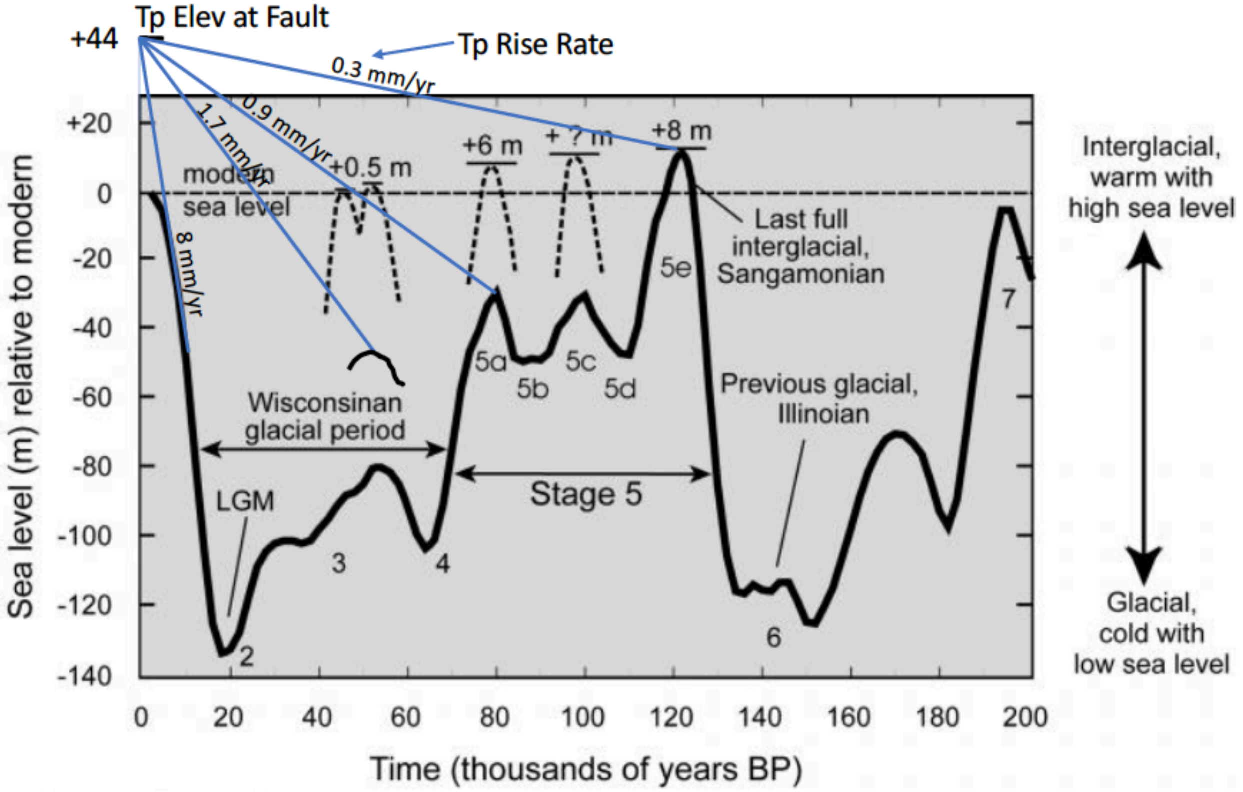

Figure 38: Global Sea Level during the Late Quaternary from Martinson et al, 1987, with superimposed vertical rise rates for the Purisima wavecut platform depending on when it was formed and abandoned. Stage 3 sea level is taken as the middle of the range reported in Siddall et al, 2008.

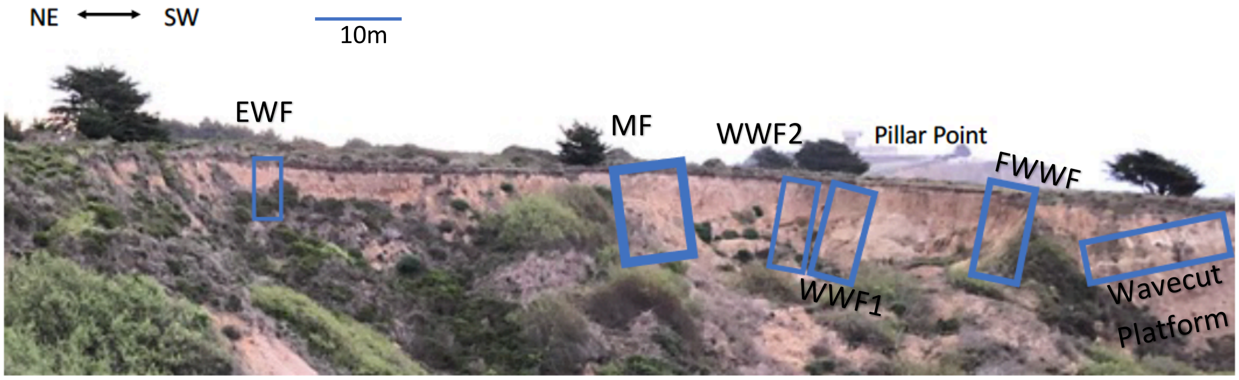

Figure 39: Landslide headscarp exposure in middle of Pillar Point Bluff outlining fault locations. EWF – East wall fault, MF – Middle fault, WWF2 and WWF1 – West wall faults 2 and 1, FWWF – Far west wall fault. A landward tilted wavecut platform is shown west of all faults. The sea cliff is just off the photo on the right.

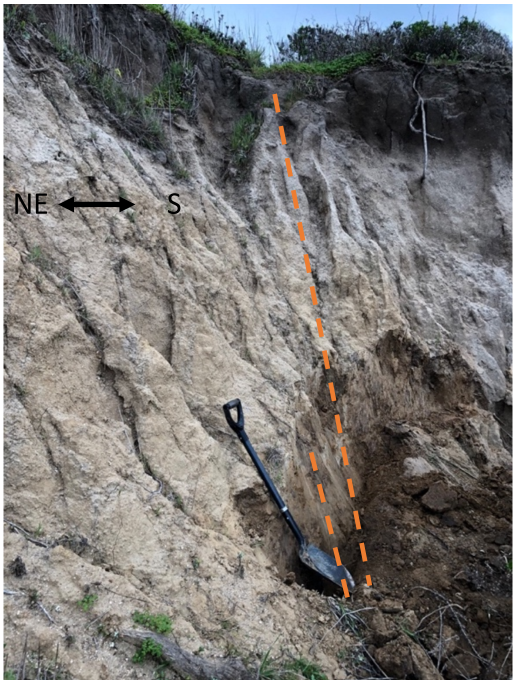

Figure 40: East Wall Fault, headscarp view, fault schematically indicated in orange in Qmt. It is not well exposed due to its location.

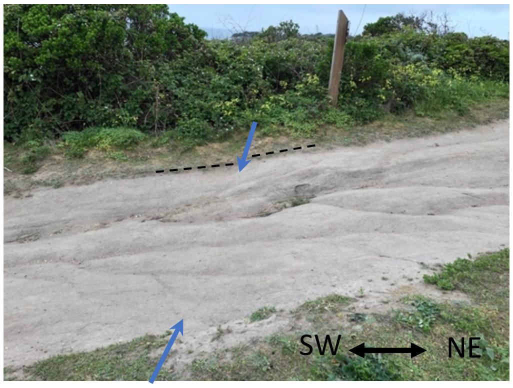

Figure 41: Surface expression of EWF between blue arrows with about 2 cm vertical offset, northeast side up.

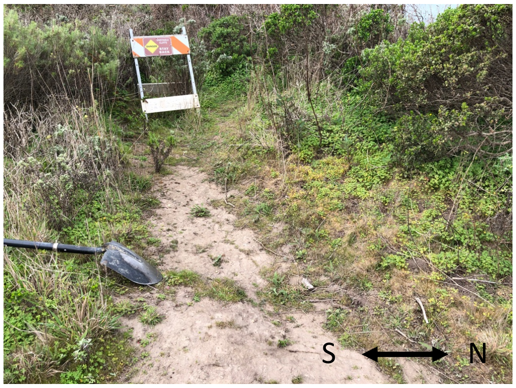

Figure 42: Surface expression of EWF across path, aligned with shovel, about 4 m SE of wall in Figure 40 and 10 m NW of Figure 41 but on a different fault path.

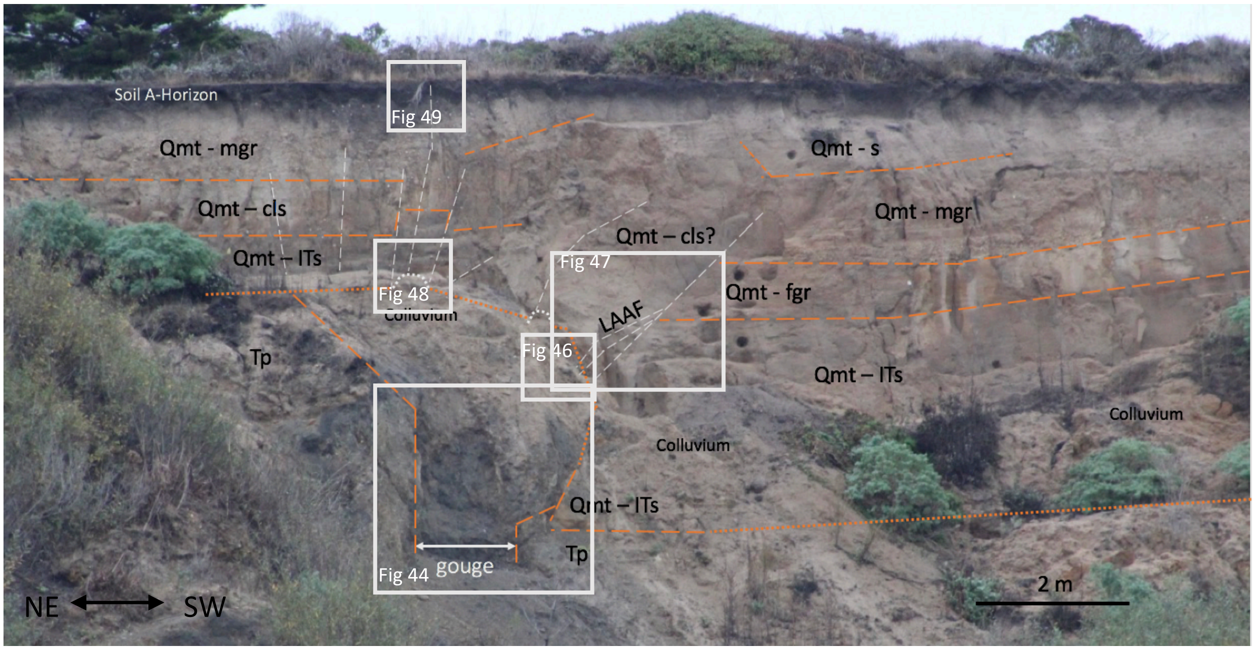

Figure 43: MF main features including low angle adjacent faults, LAAF, in Qmt. Tp – Purisima fm, Qmt – marine terrace deposits, ITs – intertidal sand, fgr – fine gravel, mgr – medium gravel, cls – clayey sand, s – sand. ∩ – clay diapir extruded from gouge into Qmt, dotted where hidden. Orange dashed line – approximate stratigraphic interface, dotted where hidden. White dashed lines – approximate fault locations in Qmt, only a few are shown.

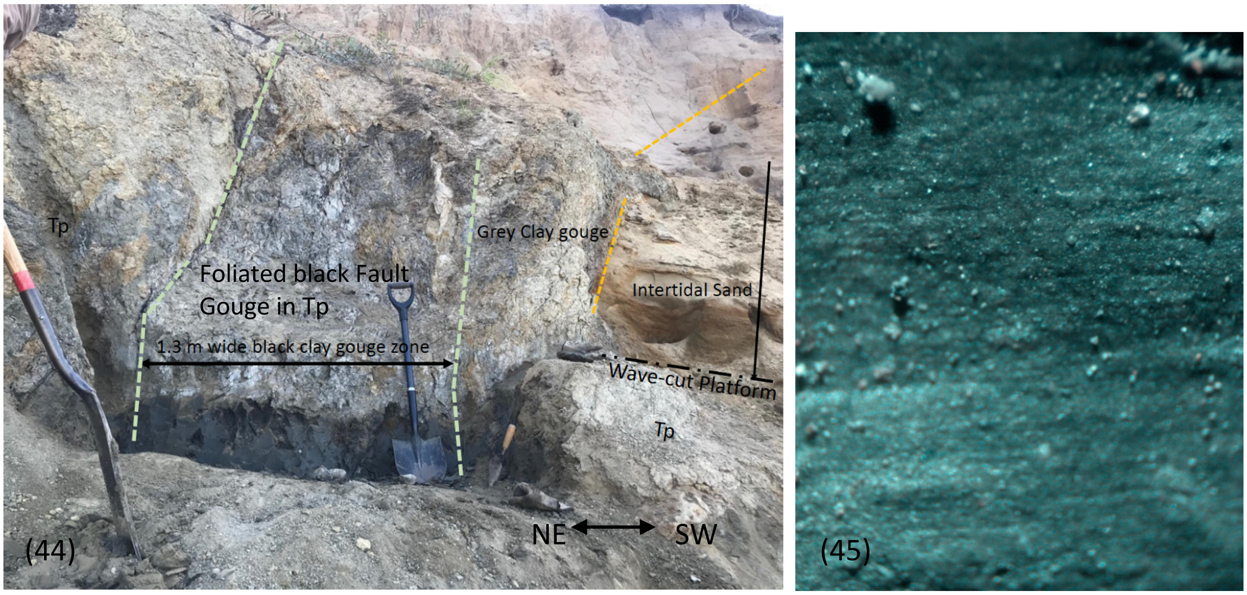

Figure 44: Lower part of MF looking SE, foliated fault gouge in Purisima adjacent intertidal sand above Purisima (obscured) and the wavecut platform. Vertical offset of Purisima is about 3m, east side up. 45) Striations in the foliated fault gouge, width ~ 4 mm, with the horizontal axis in photo approximately horizontally oriented.

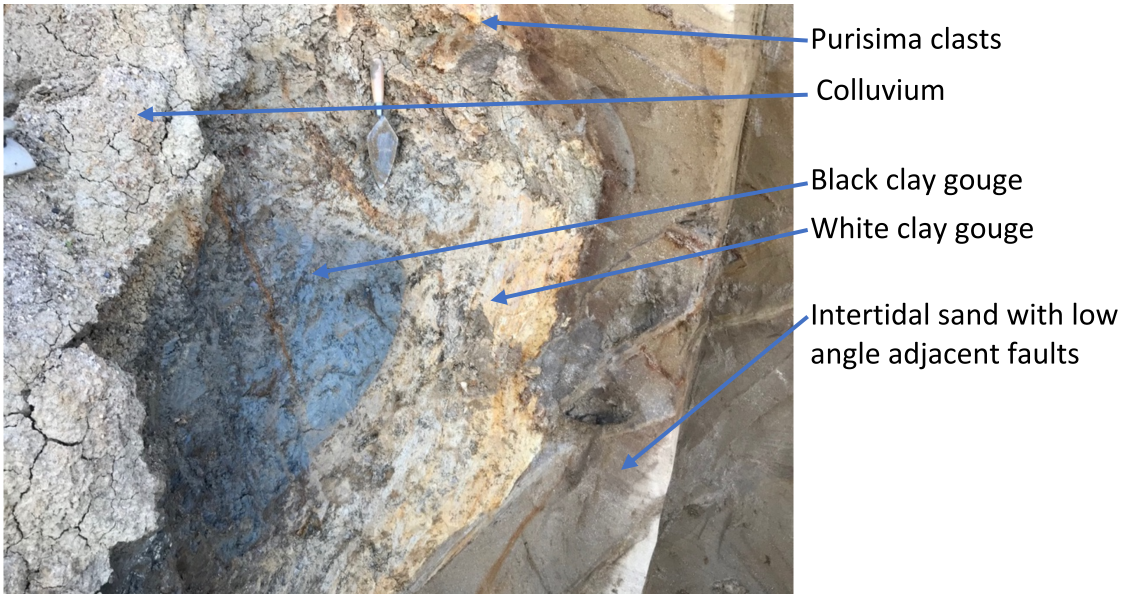

Figure 46: MF exposure looking SE, top west corner of Tp gouge intruding into Qmt, showing black clay gouge surrounded by white clay gouge with a lag of Purisima clasts with abundant pholad borings on leading edge of gouge interfacing to intertidal sand. Low Angle Adjacent Faults detailed in Figure 47. Trowel is 0.25m long.

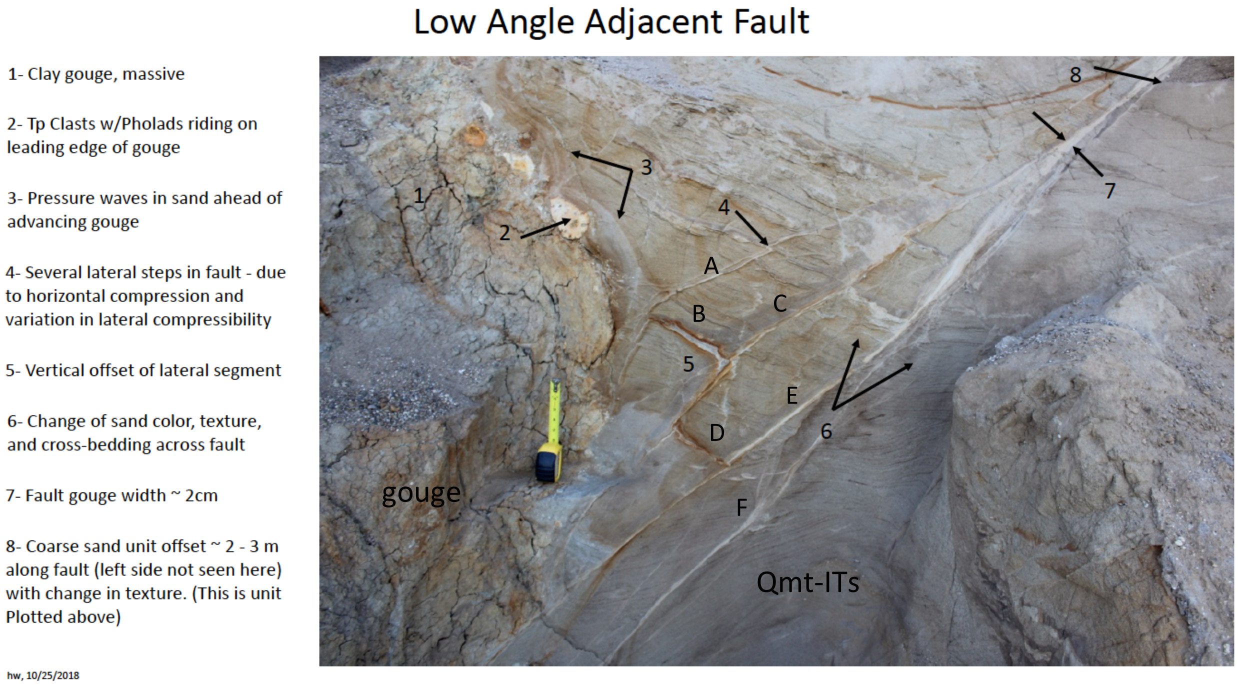

1- Clay gouge, massive

2- Tp Clasts w/Pholads riding on leading edge of gouge

3- Pressure waves in sand ahead of advancing gouge

4- Several lateral steps in fault - due to horizontal compression and variation in lateral compressibility

5- Vertical offset of lateral segment

6- Change of sand color, texture, and cross-bedding across fault

7- Fault gouge width ~ 2cm

8- Coarse sand unit offset ~ 2 - 3 m along fault (left side not seen here) with change in texture. (This is unit Plotted above)

hw, 10/25/2018

Figure 47. View of faults in Qmt that emanate from the Tp gouge zone.

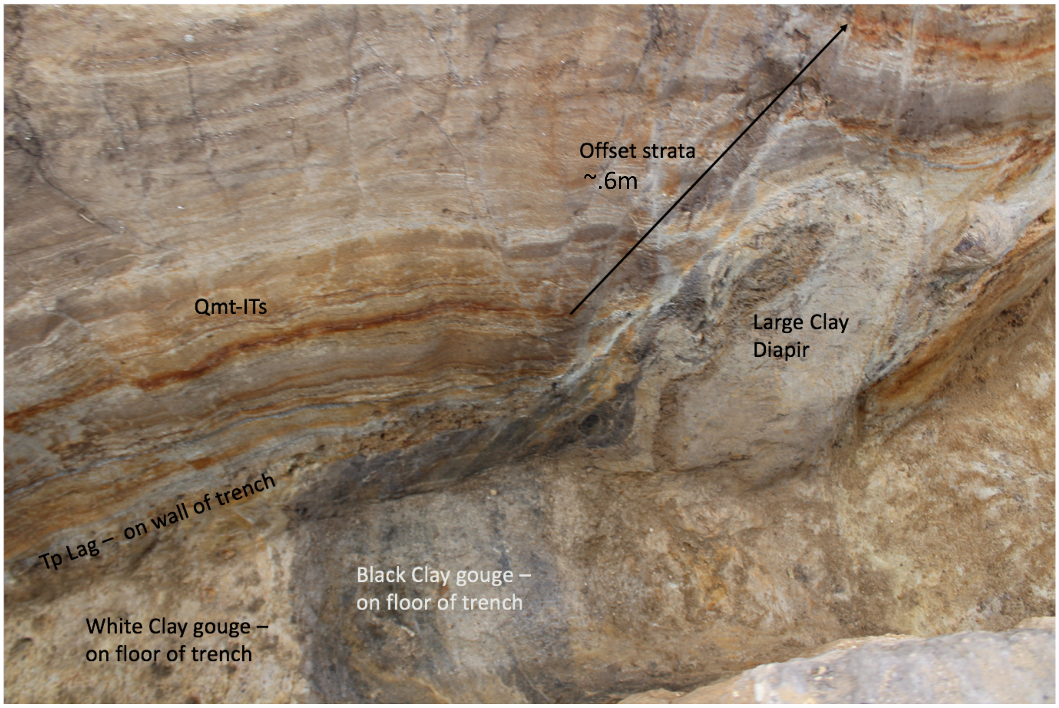

Figure 48: Closer look at diapir in Figure 22 and the floor of the trench above MF showing sections of black and white clay gouge. Strata vertical offset is equal to height of diapir.

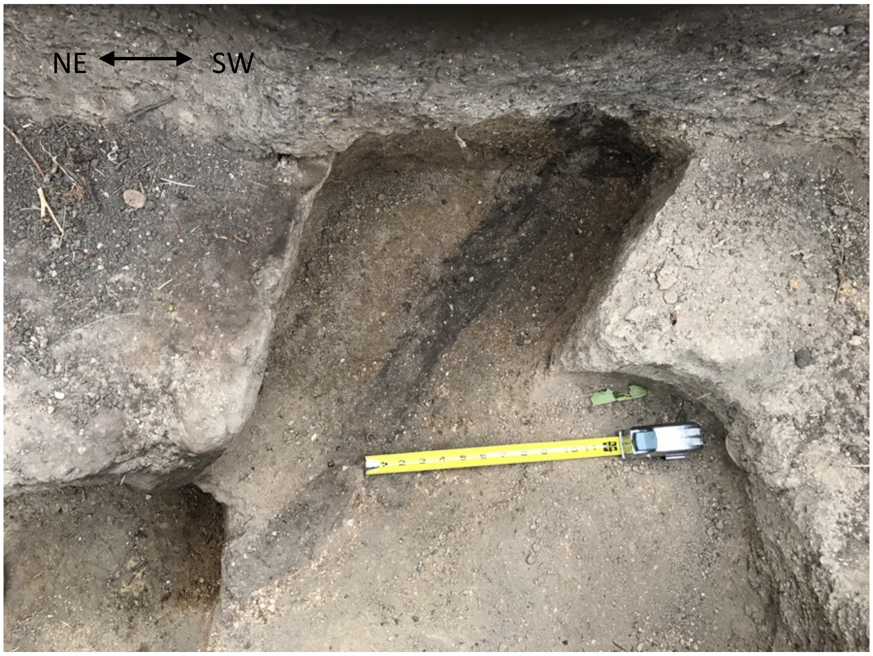

Figure 49: Plan view of trench dug on bluff surface 1 m south of MF wall exposure. Fault line on floor is shown about .5 m below surface, .2 m below soil. Dark trace appears to be organic soil settled into fault crack. This fault passes through large diapir in Figure 48.

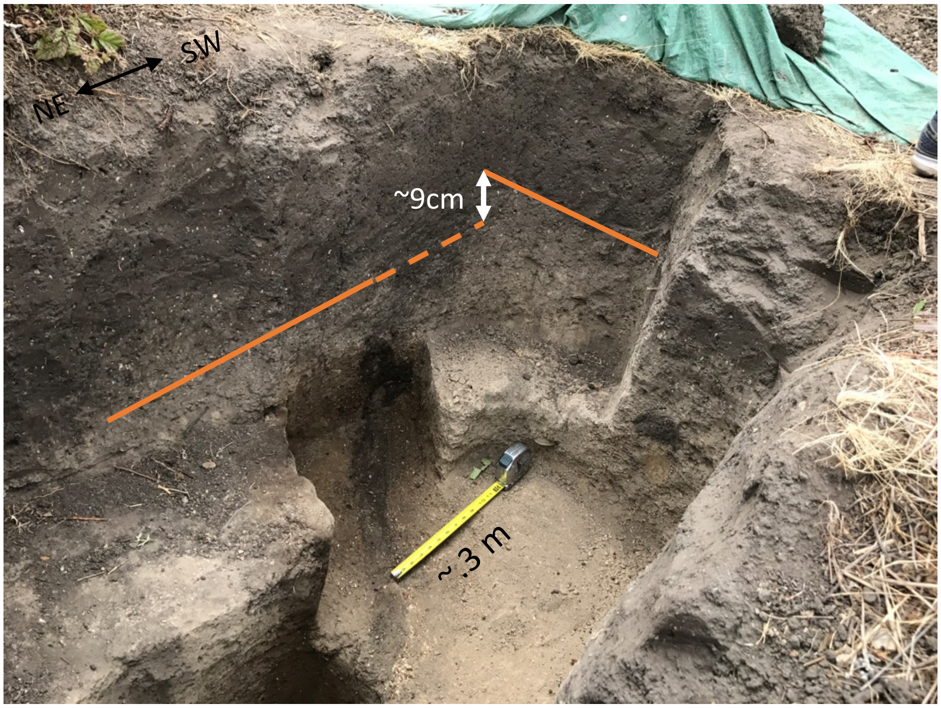

Figure 50: Lower angle perspective of trench exposure in Figure 49. Vertical offset across fault below soil level is ~ 9 cm, SW side up. Fault strike in Qmt is 325° ± 8°, dip is subvertical.

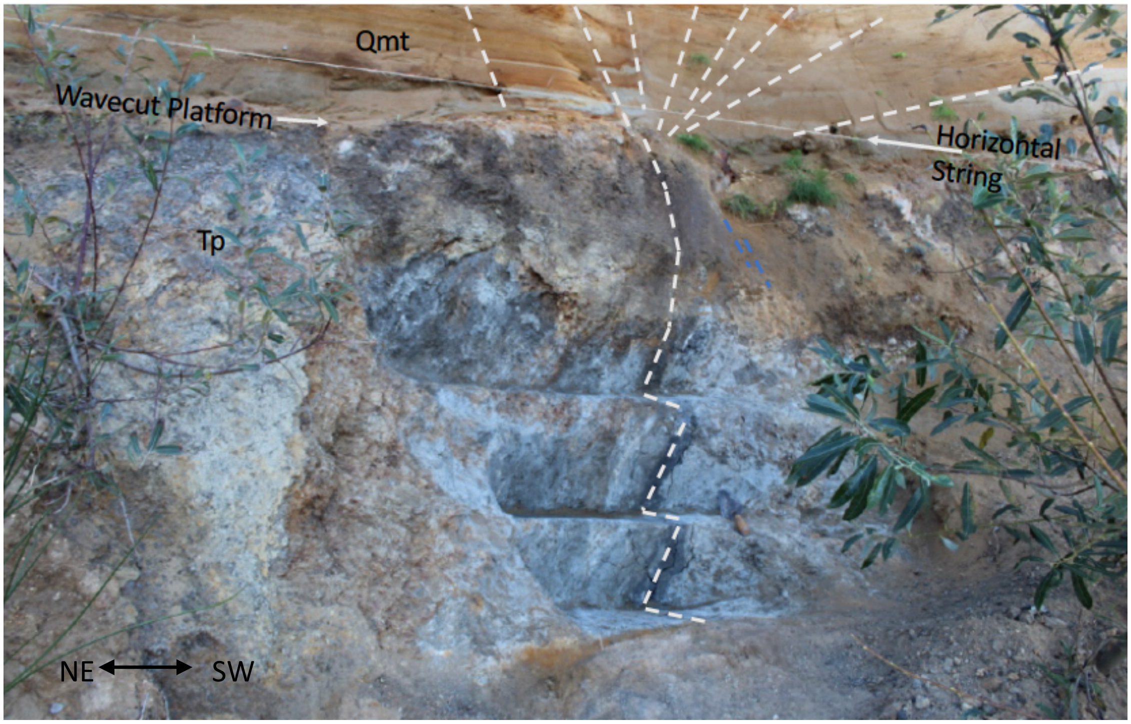

Figure 51: WWF2, Fault, white dashed lines, in Purisima, Tp, and extending into marine terrace, Qmt-ITs. Black clay gouge .1 m wide along fault line (excavation tiered). Fault strike/dip 340°/ 60° E. Horizontal string for orientation, note the wavecut platform tilts NE (landward) 3-4° on the east side of WWF2, but 15° NE west of WWF2.

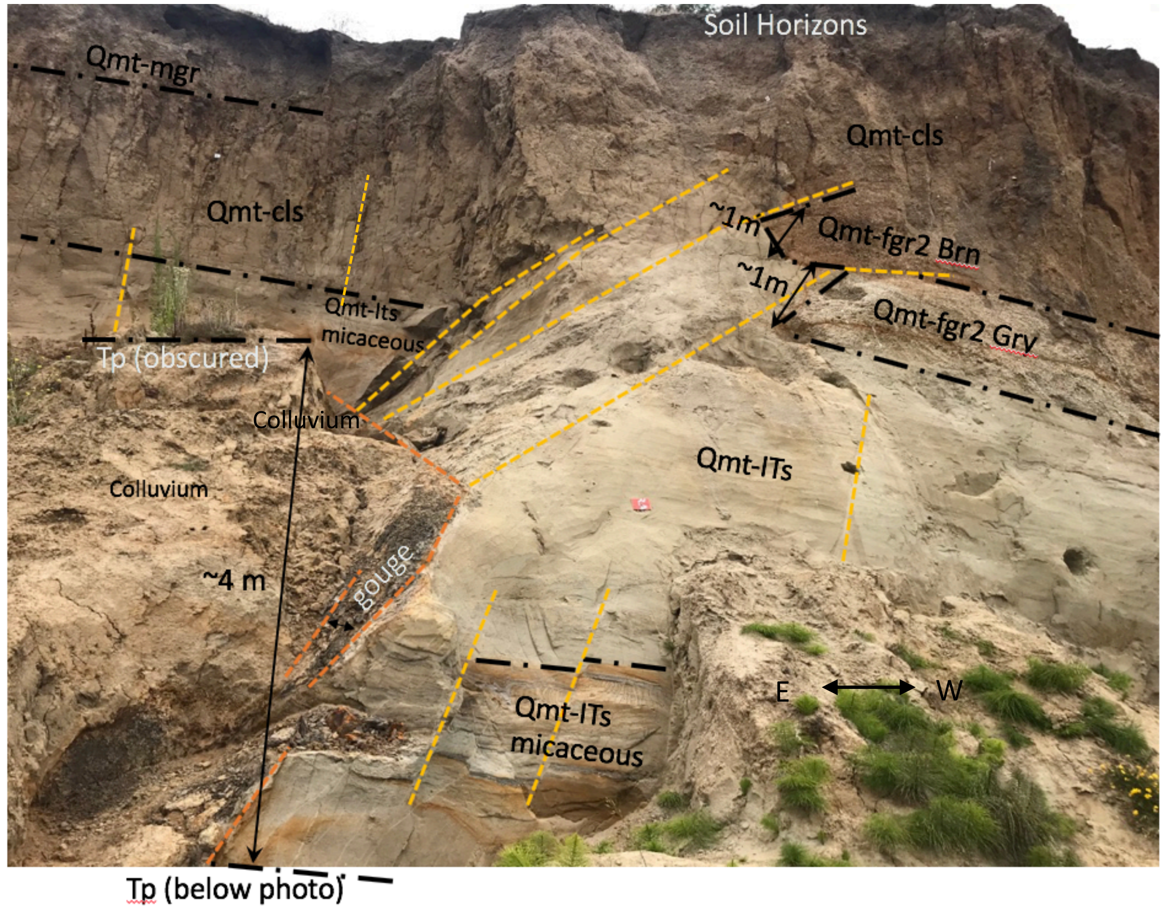

Figure 52: WWF1 looking SW. Yellow fault lines in Qmt, orange lines roughly outline fault gouge in Tp. Fault step in Tp is ~ 4 m high. Obscured Tp area shown in Figure 53, gouge and Tp below photo shown in Figure 54.

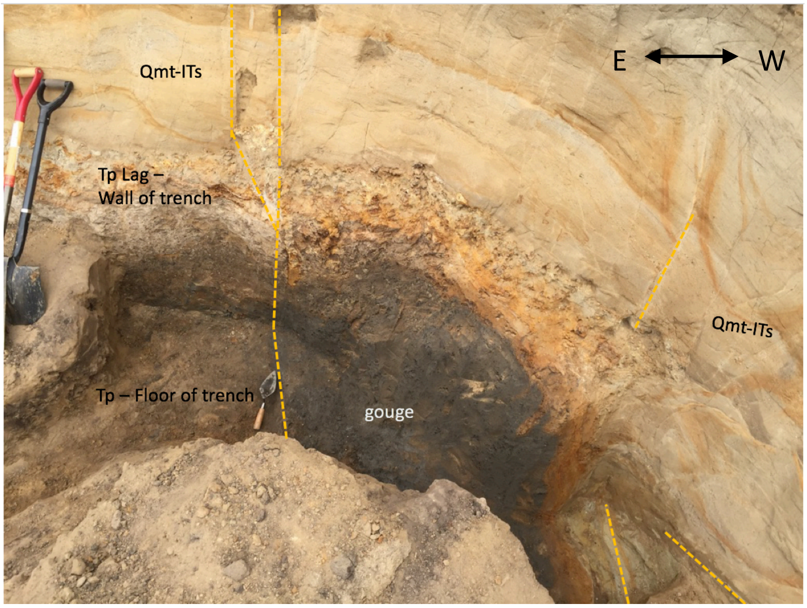

Figure 53: WWF1, top of Tp (the "obscured" part of Figure 52) showing black clay gouge with faults along both sides of it.

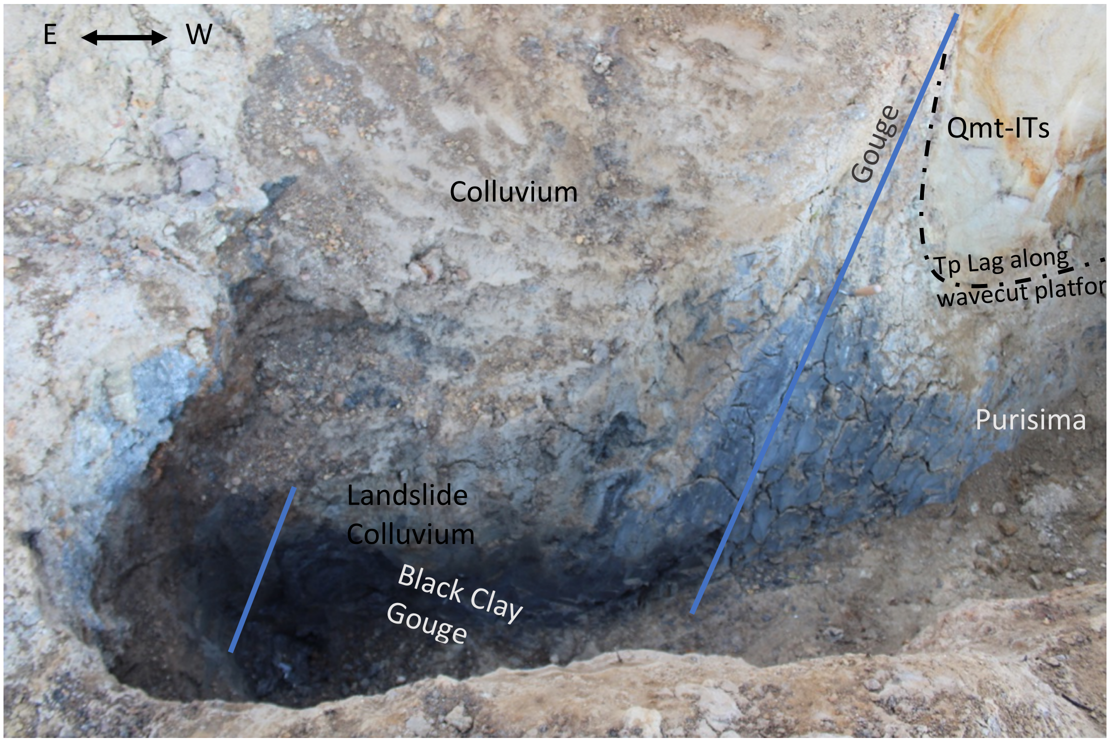

Figure 54: WWF1 view below Figure 52 of gouge in Tp between blue lines. Gouge width is 1.7m wide below the fault triple intersection point (black dot-dash line).

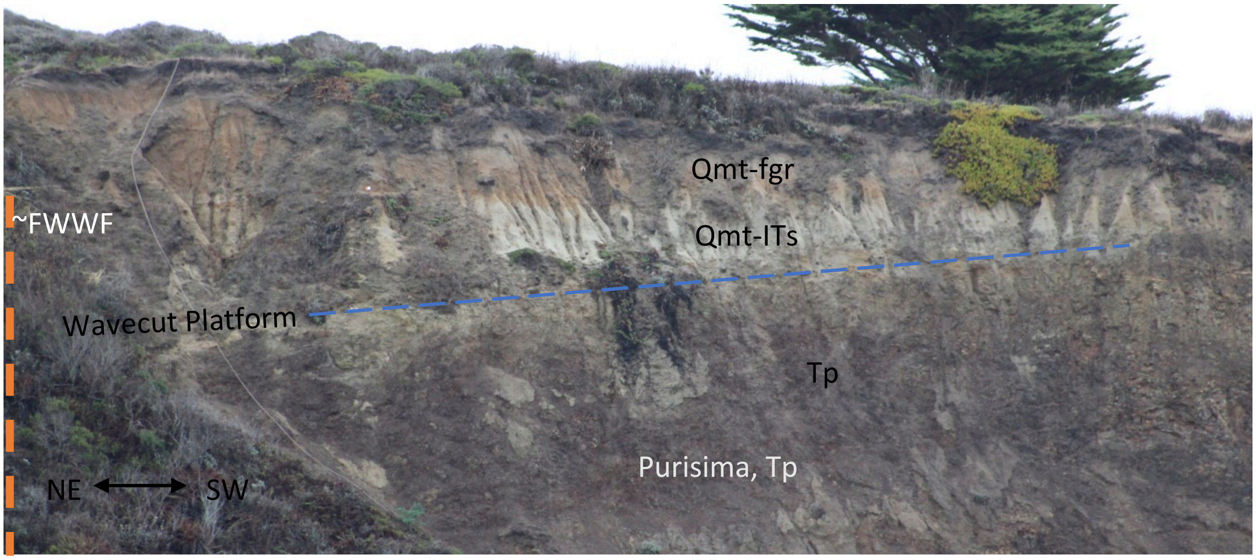

Figure 55: Wavecut platform exposure on landslide scarp west of all faults, blue dashed line, the top of the greenish-grey layer. The current slope is 4.5° ± 0.5 NE, landward. Orange dashed line is approximate location of FWWF.

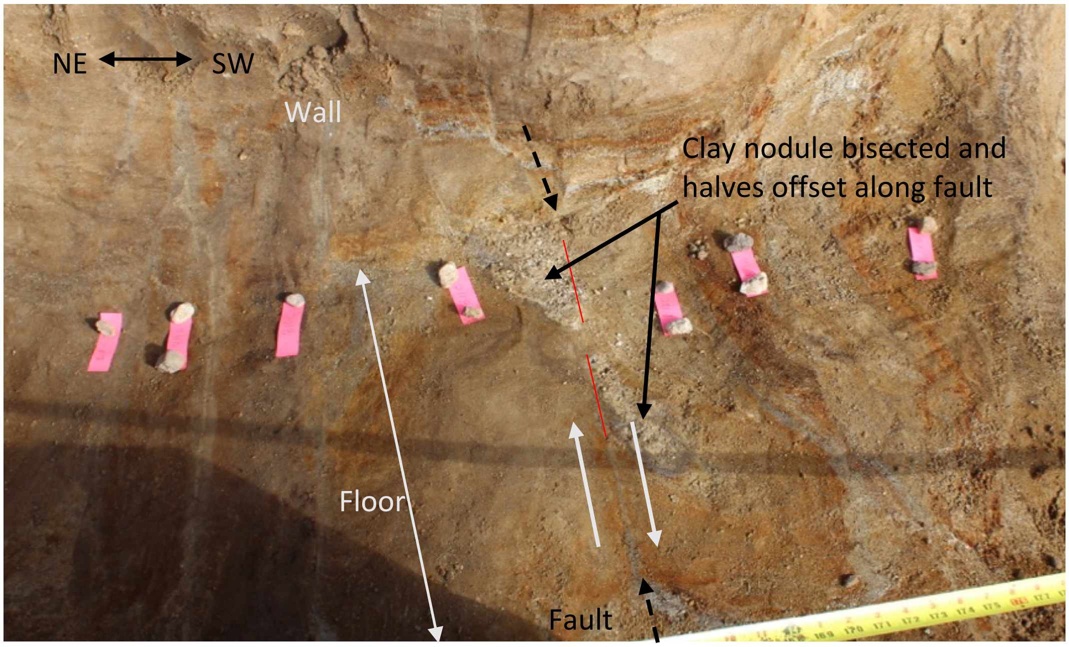

Figure 56: Floor of trench in Qmt along Middle Strand main fault, just above large diapir (later exposed below this floor, Figure 48). Clay peak of diapir is cut by fault and offset 6 inches right-laterally. Red lines are equal length and orientation – representing matching surfaces. Notice several other faults visible in floor labelled by pink sheets with many more off-photo.

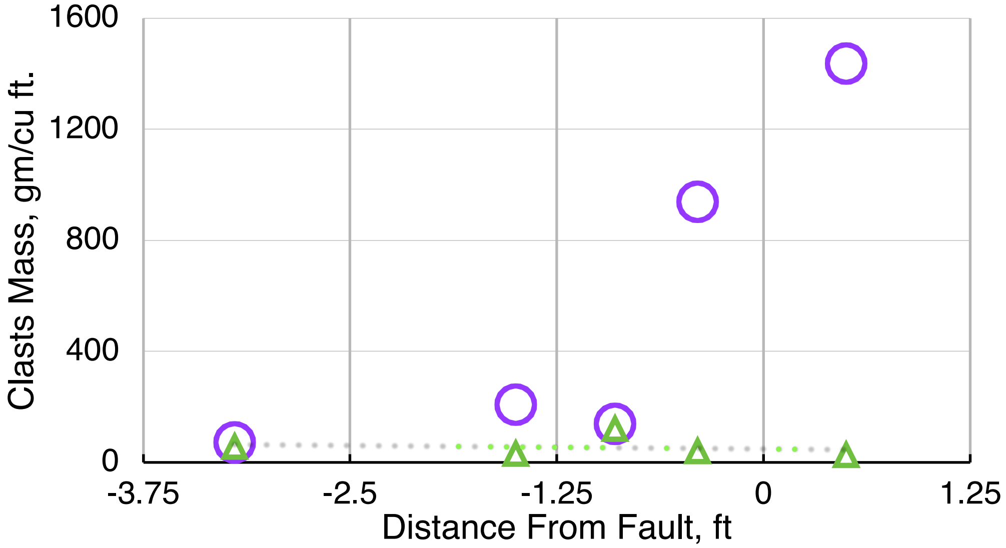

Figure 57. Mass of SS clasts > 1.5cm with pholad borings versus distance from the fault in the Upper trench above the large diapir in the Main Fault in Figure 35. Green triangles were from the soil layer, Violet circles from Qmt between 1' and 2' below surface, below A horizon.

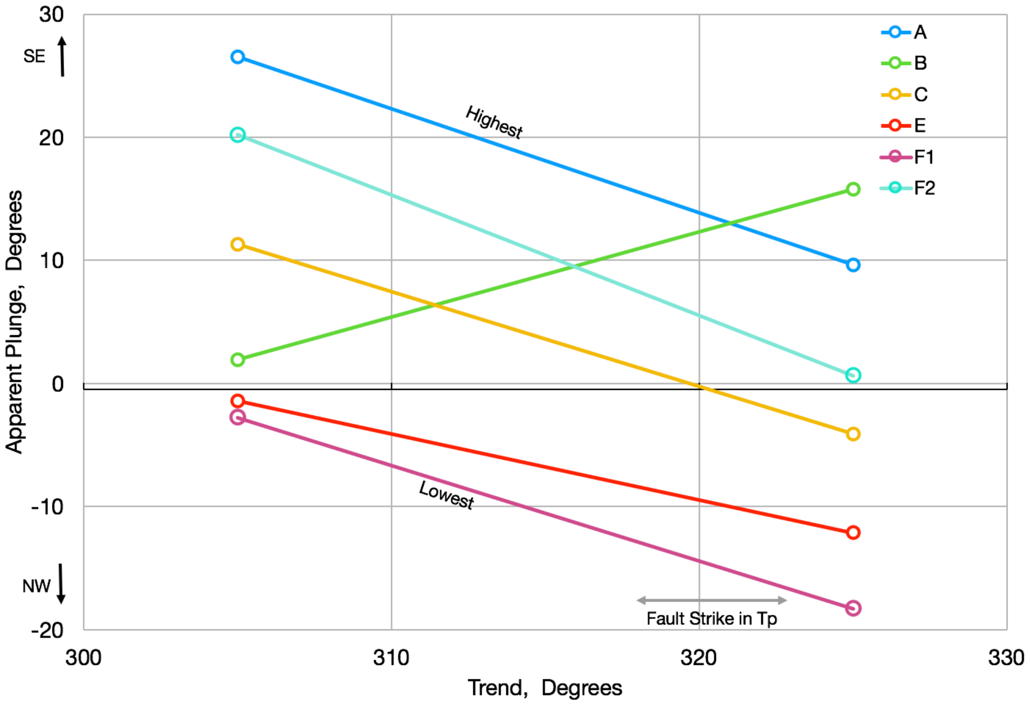

Figure 58. Apparent plunge of faults on MF from Figure 47 as a function of trend direction. At the fault trend, around 320°, they go from plunging to the NW for faults E and F (believed to be the earliest of these faults) to the SE for fault A (later). The lowest fault, F, bifurcates suggesting it was reactivated with F2 being a later path.

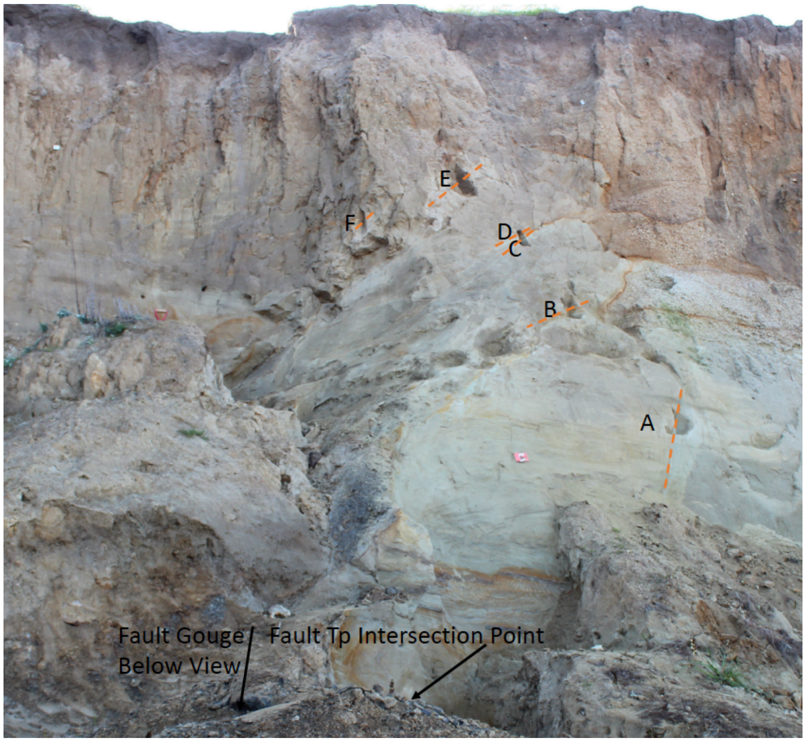

Figure 59. Location of WWF1 faults in Qmt used for fault plunge measurements.

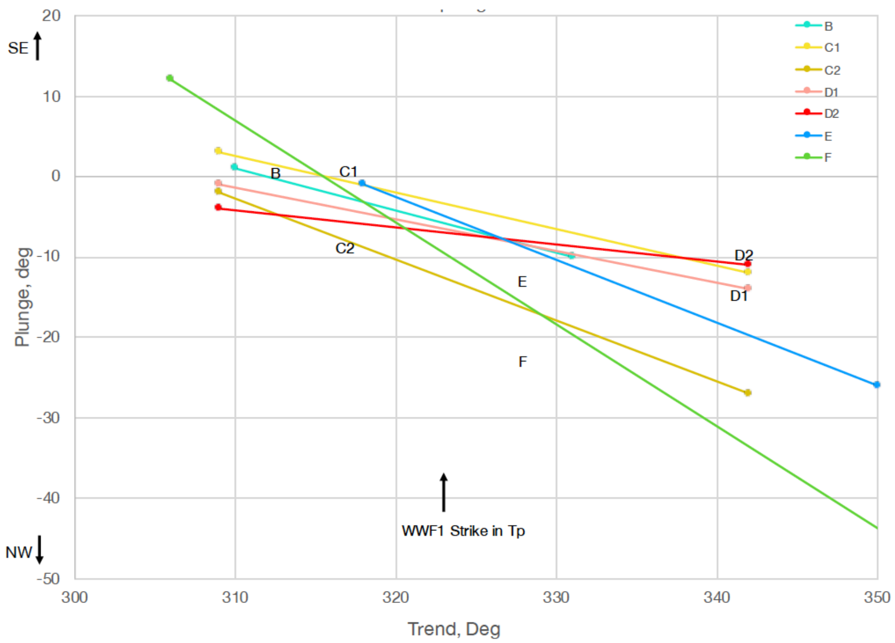

Figure 60. WWF1 Fault attitudes in Qmt. Location of faults shown in Figure 59.

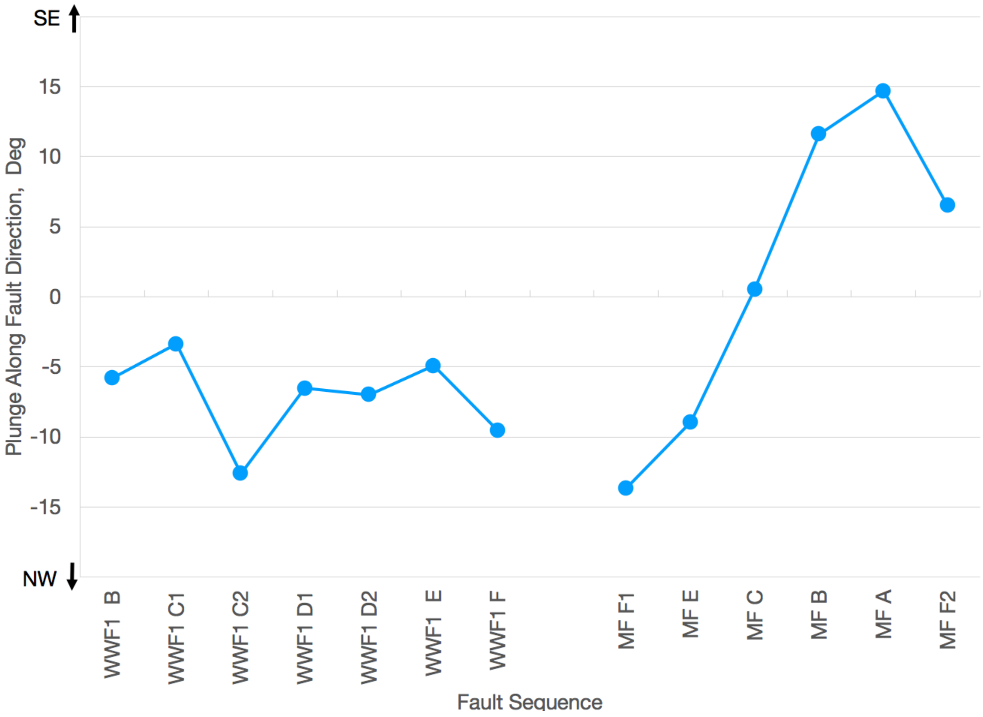

Figure 61. Plunge for proposed sequence of faults in Qmt. WWF1 likely occurred first with a relatively constant plunge. MF plunge changes direction through the sequence. There are other faults not included in this sequence, particularly early in MF.

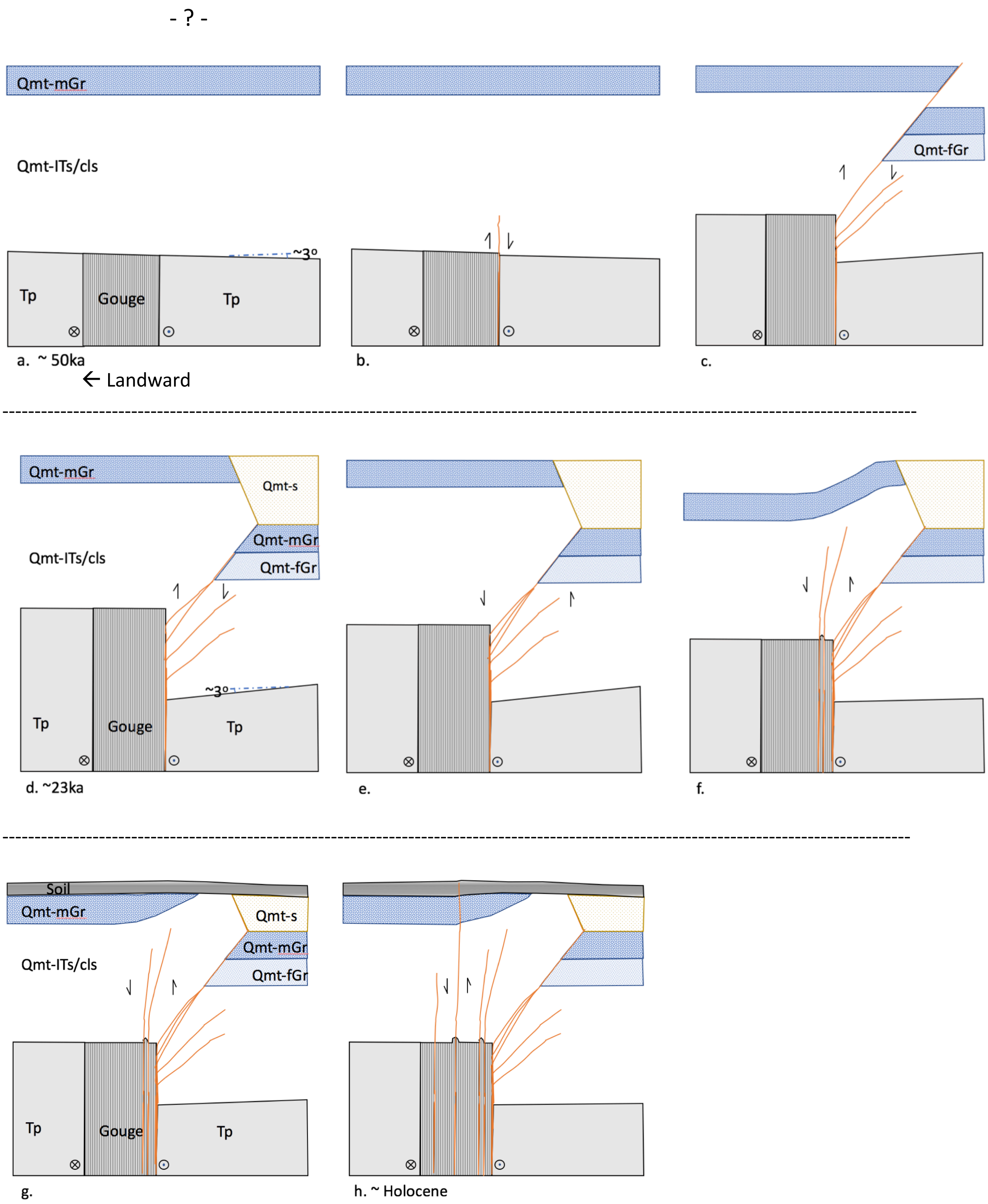

Figure 62 a-h: Fault and stratigraphic sequencing schematic for Middle Fault. Tp is Purisima fm bedrock. Gouge is fault gouge in bedrock. Qmt-ITs/cls is marine deposited intertidal sand above Tp grading into clayey sand. Qmt-mGr is medium gravel deposit, Qmt-fGr is fine gravel deposit. Fault sequencing explanation in text.

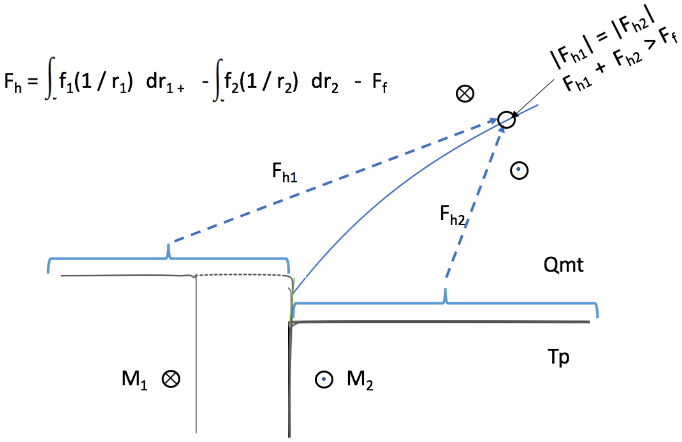

Figure 63: Horizontal movement along a fault in Qmt is determined by the net of opposing forces from bedrock solid surfaces moving in opposite directions and transmitted through poorly consolidated Qmt deposits reduced by internal friction. The force from the moving bedrock plates is a function of the inverse distance integrated along the fixed boundary surfaces and is equal and opposite at the fault line, and induces fault shearing as long as the total differential stress is greater than the internal static friction.

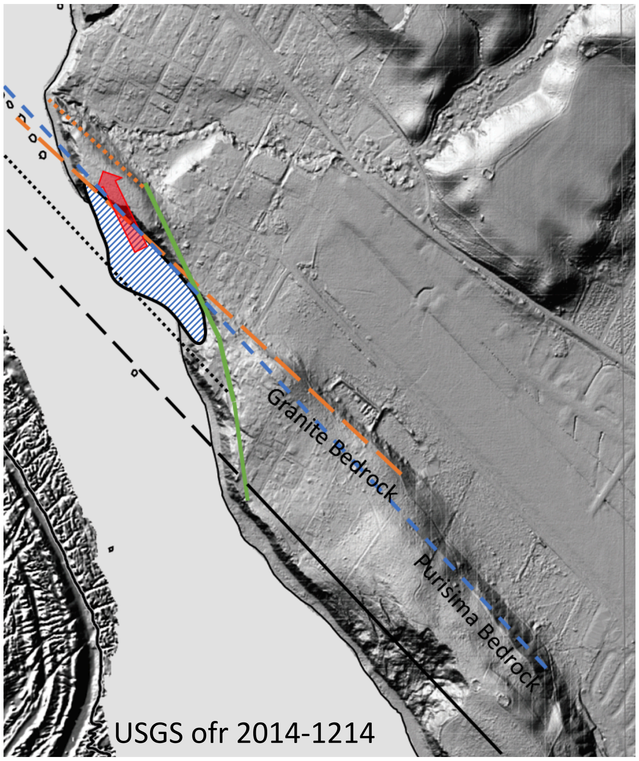

Figure 64: Original position of Fitzgerald Bluff (blue cross-hatched), aligned with the eastern scarp of PPB (orange and blue dashed lines), and its translation 317 ± 90 m along 332 ± 6° (red arrow) along the Distillery Fault (green line) to its current location (dotted orange line). Coeval translation of NW going MF fault included (black dashed to black dotted lines).

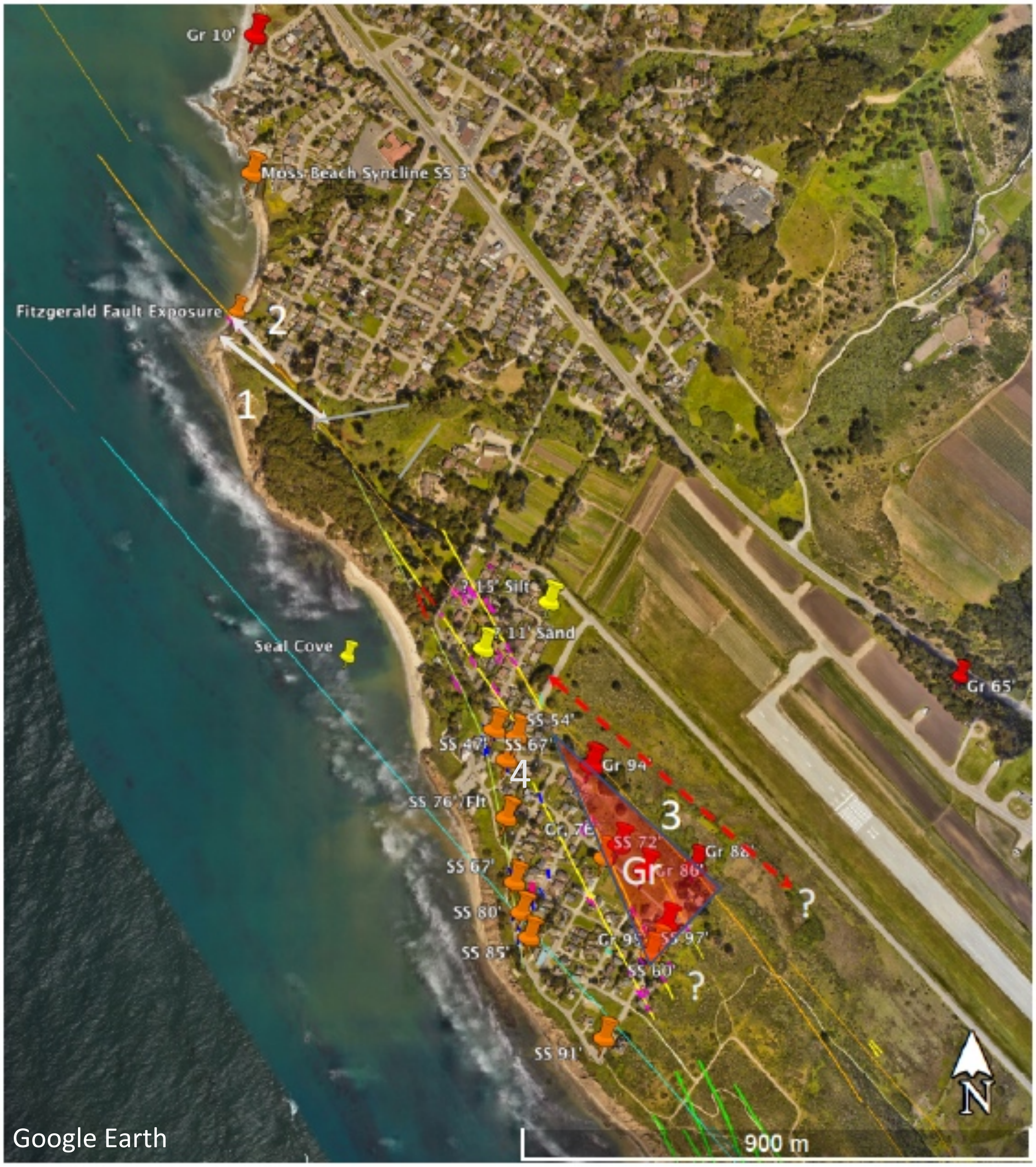

Figure 65: Locations of alternative piercing points. 1) San Vicente Creek offset, 2) Fitzgerald Fault vertical rise, 3) Granite bedrock against the Seal Cove Fault, 4) Granite bedrock against a releasing fault.

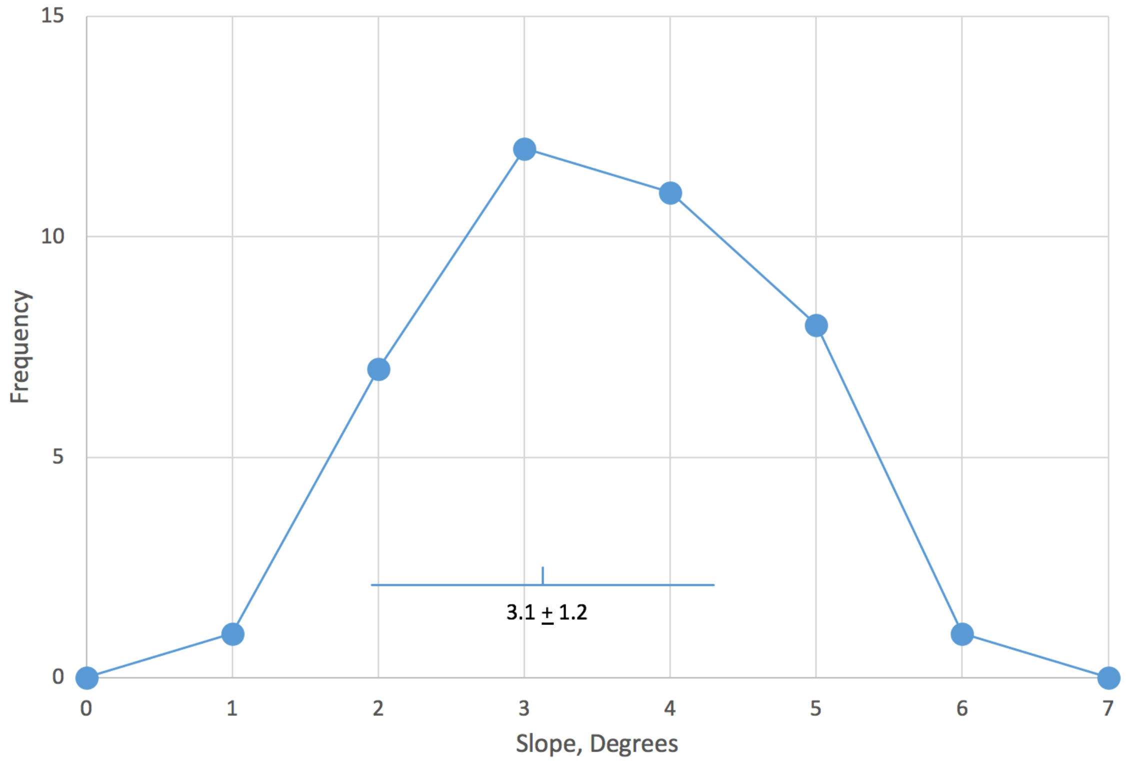

Figure 66: Histogram of wavecut platform angles in Purisima in modern PPB/HMB region.

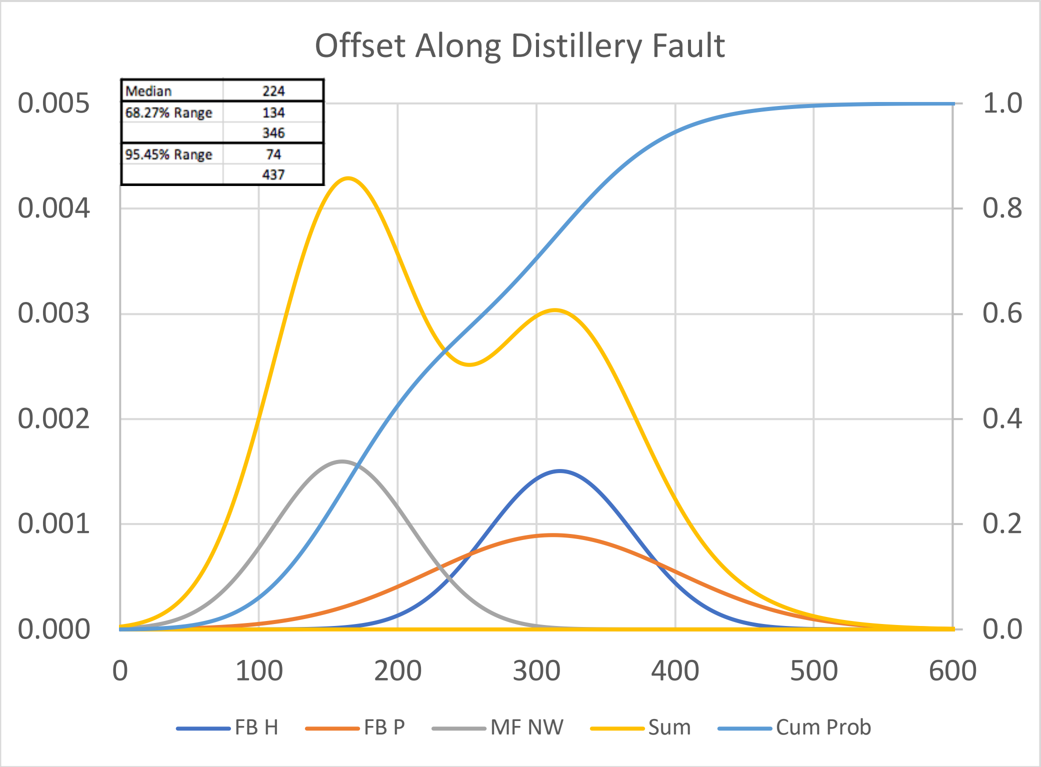

Figure 67: Probability density function of offset along the Distillery Fault based on two measurements of Fitzgerald Bluff offset and one of the NW extension of the MF.

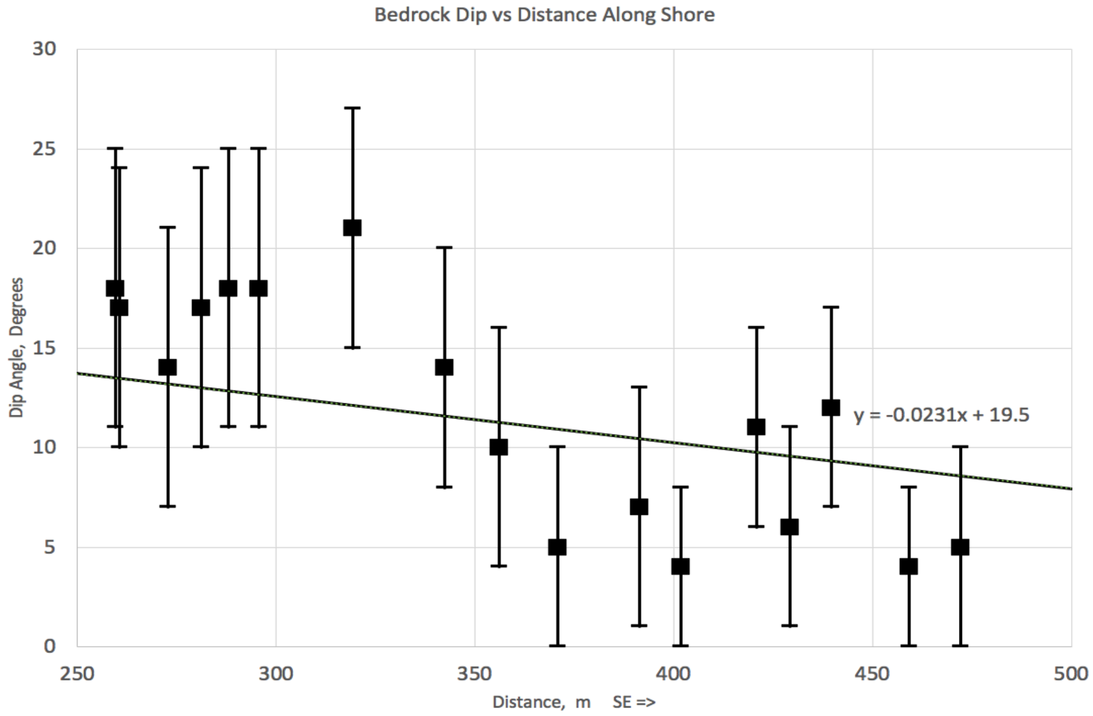

Figure 68: Dip along PPB in surf zone versus projected distance along the shore. A slope of -.0231 m/deg reasonably fits the data although is not here well constrained, see Appendix D for a more precise determination.

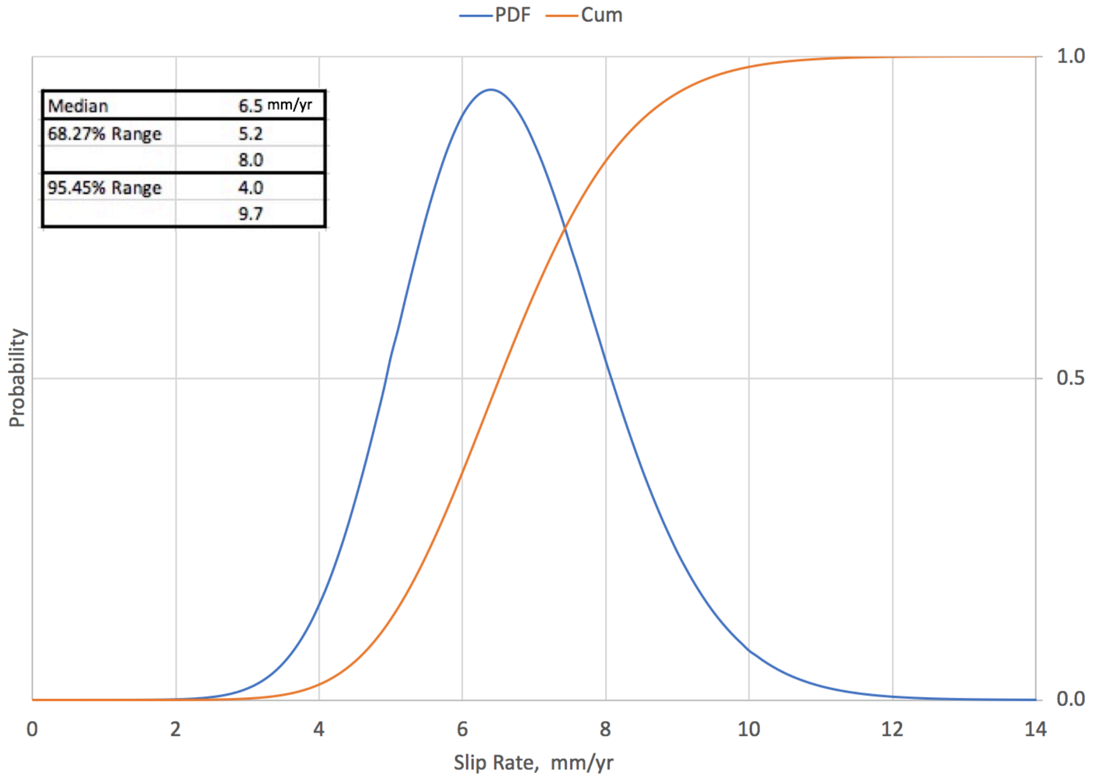

Median	6.5 mm/yr
68.27% Range	5.2
	8.0
95.45% Range	4.0
	9.7

Figure 69: Probability Density Function of slip rate on SGF-E determined from the rotation of the wavecut platform along the restraining bend.

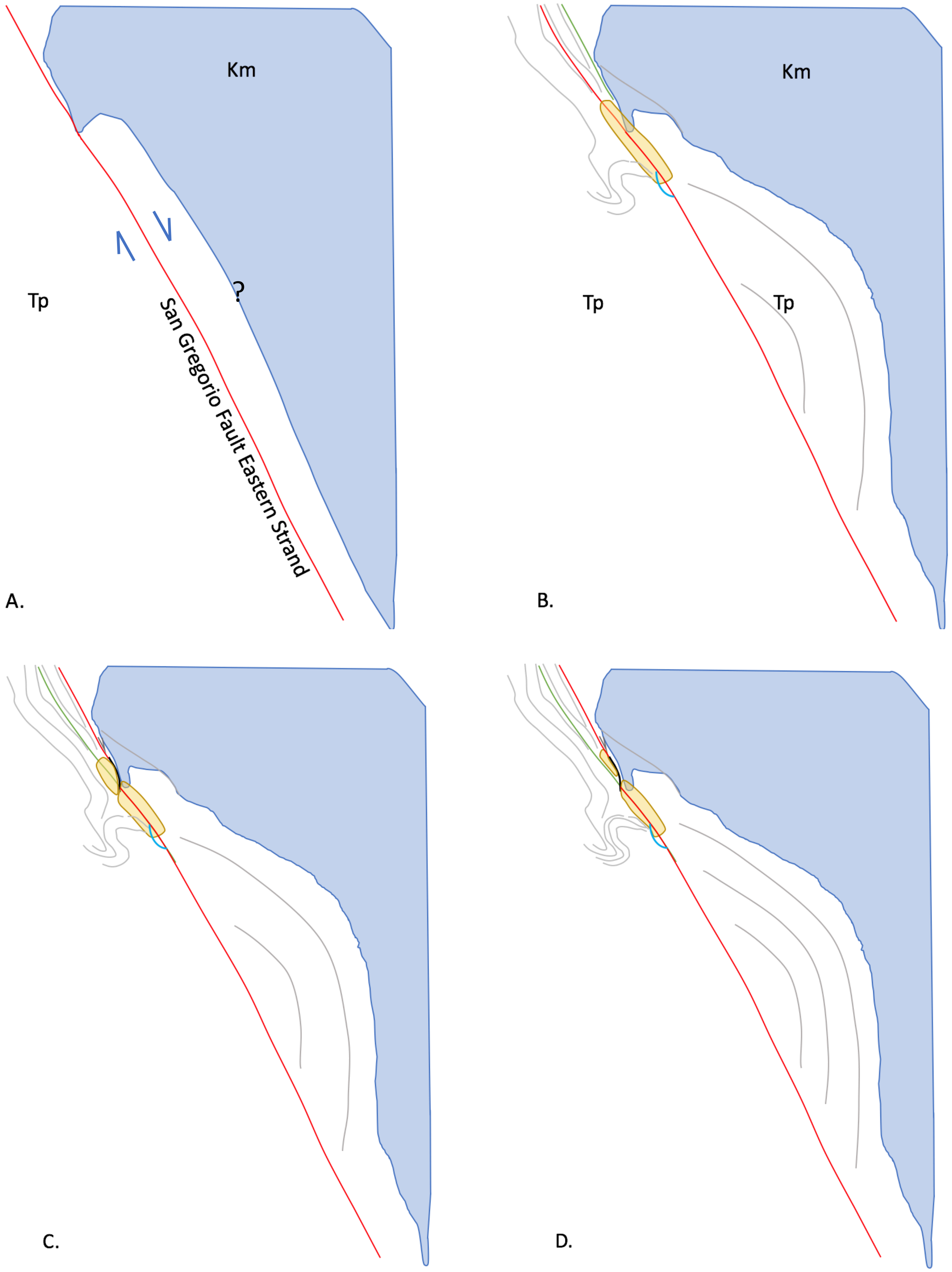

Figure 70: SGF-E fault progression from Miocene to Holocene. A) Miocene: Montara granite contacts SGF-E. B) Granite protrusion deflects fault forming restraining bend, extension deformation of HMB begins. C) Crossover faults develop. D) Holocene: Crossover faults displace Fitzgerald Bluff.

Figures for Appendix A:

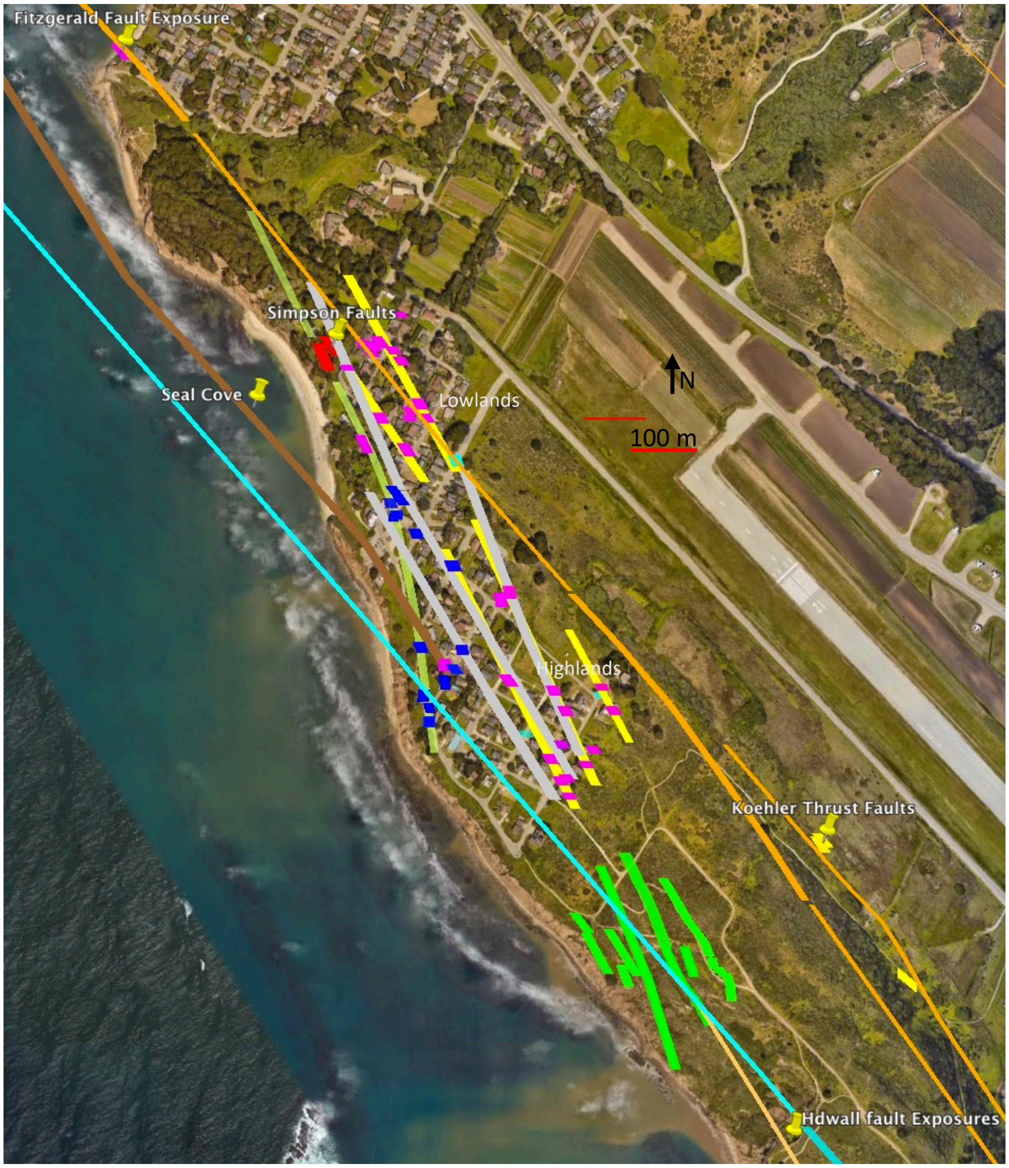

Figure A1: Mapped features in Seal Cove area of Moss Beach, California. Magenta lines: Consultant-identified faults from trenching reports. Long Yellow lines: Trends of consultant faults. Gray lines: Lineations from Leighton et al, 1971. Dark Blue lines: Right-lateral Riedel shears in roadbeds. Green lines: Gravity spreading ridges. Short Light blue lines are complementary pairs of arcuate extension cracks (Appendix C). Olive green line: Distillery Fault. Red lines: Simpson et al, 1997, faults. Short Yellow lines: Koehler et al, 2005, thrust faults. Long light blue line: Extrapolation of Middle Strand fault. Long Brown line: Middle Strand where it is shifted by offset along crossing faults. Orange lines: CGS A-P designated fault lines. Beige line: Extrapolation of West Wall Faults.

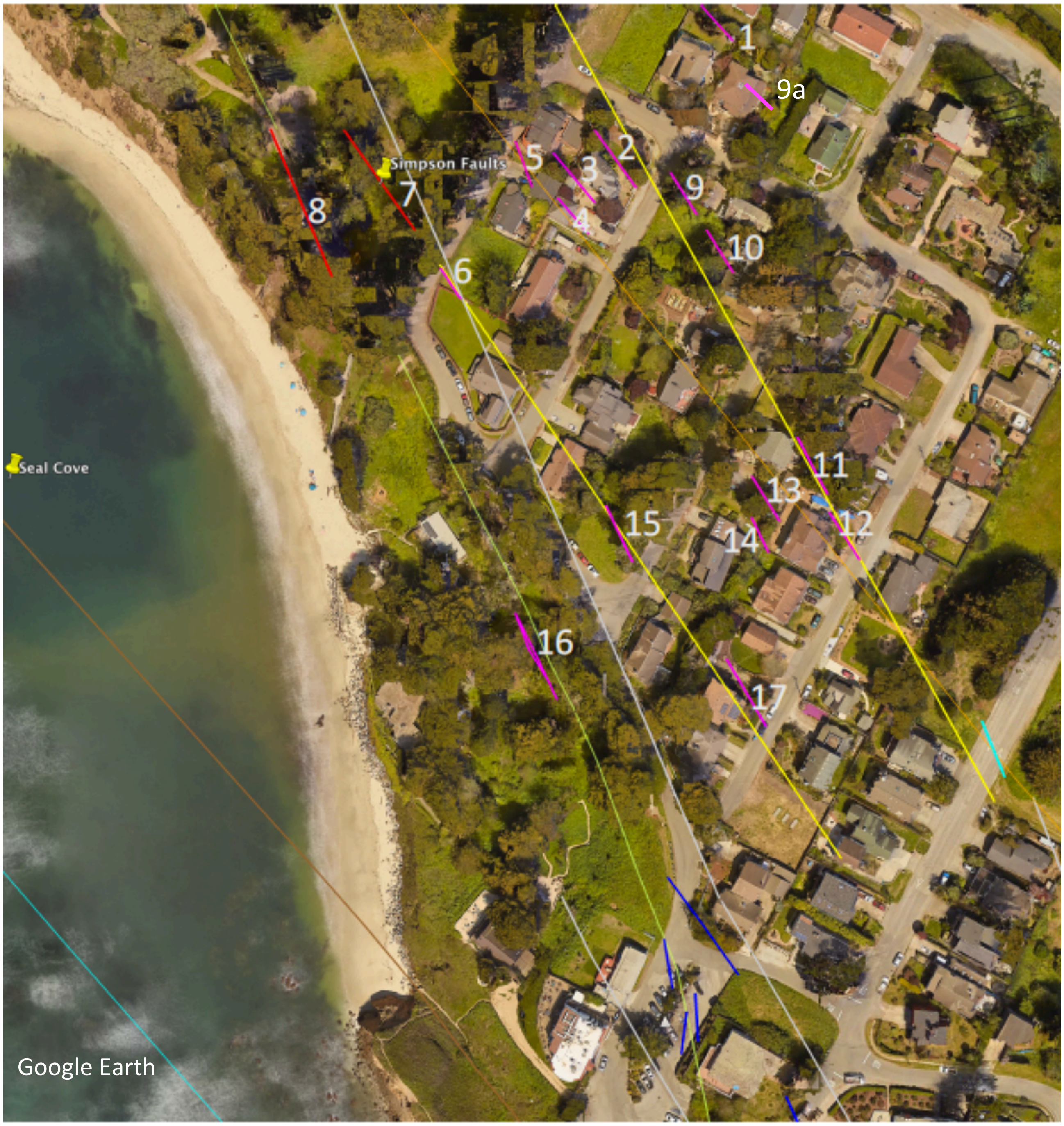

Figure A2: Expanded view of consultant faults in Seal Cove Lowlands. Lines are explained in Figure A1. Numbers correspond to consultant faults listed in Table A1.

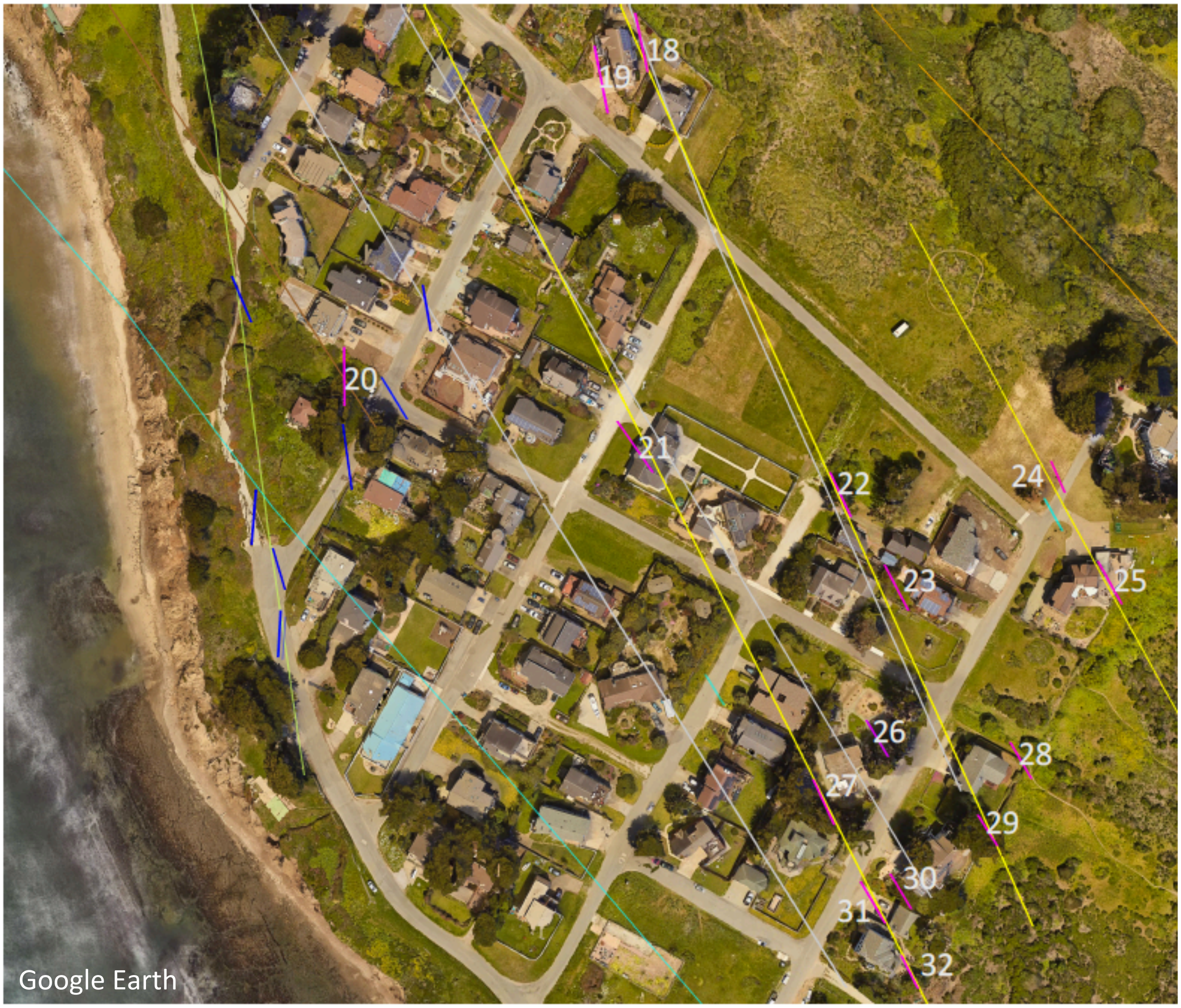

Figure A3: Expanded view of numbered consultant faults in Seal Cove Highlands. Lines are explained in Figure A1. Numbers correspond to consultant faults listed in Table A1.

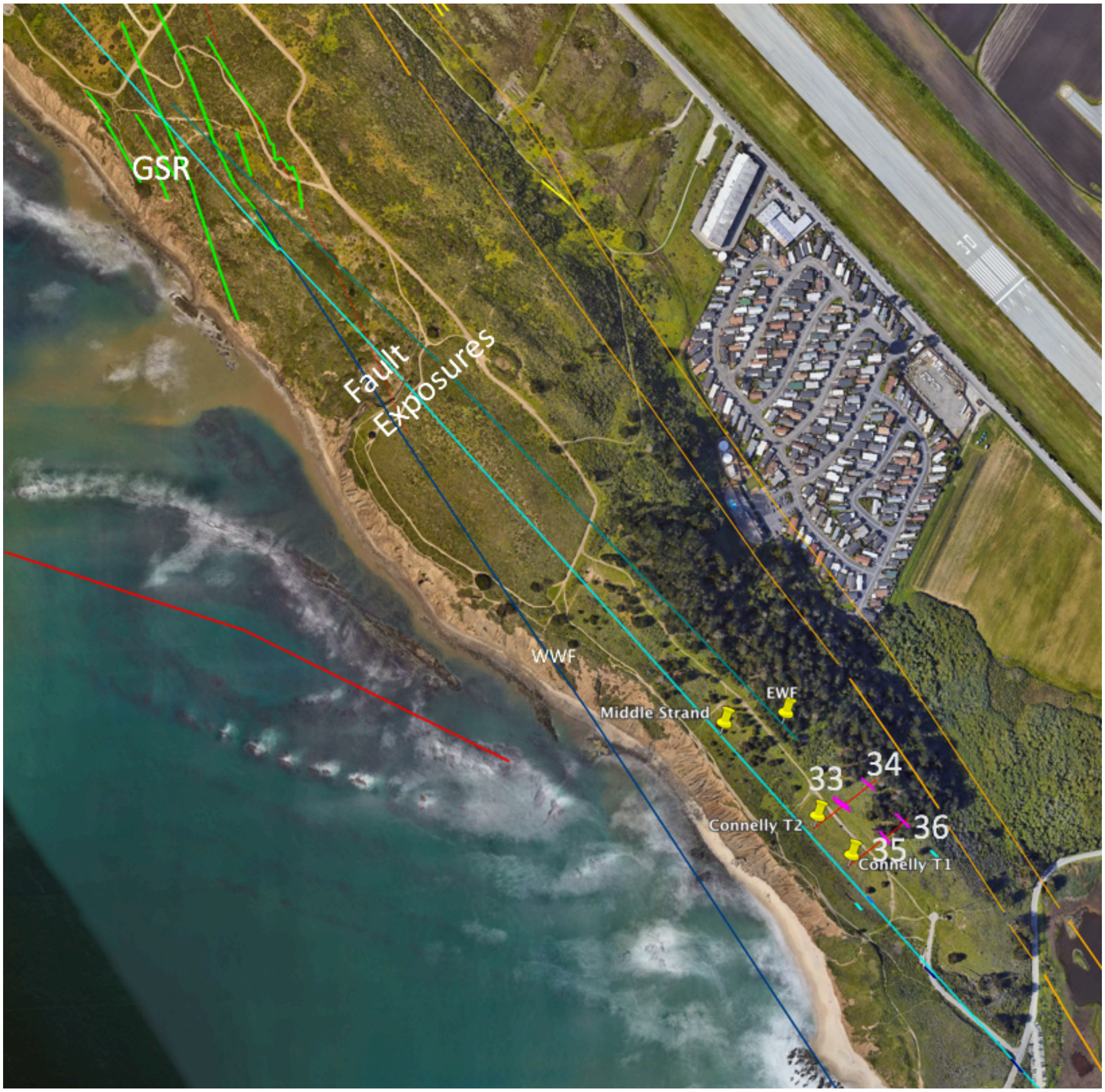

Figure A4: Expanded view of numbered consultant faults in Pillar Point Bluff. Lines are explained in Figure A1. Numbers correspond to consultant faults listed in Table A1. Fault 33 (actually two faults) is identified by Connelly and Rubin, 2001 as a dip slip fault, see Figure A5.

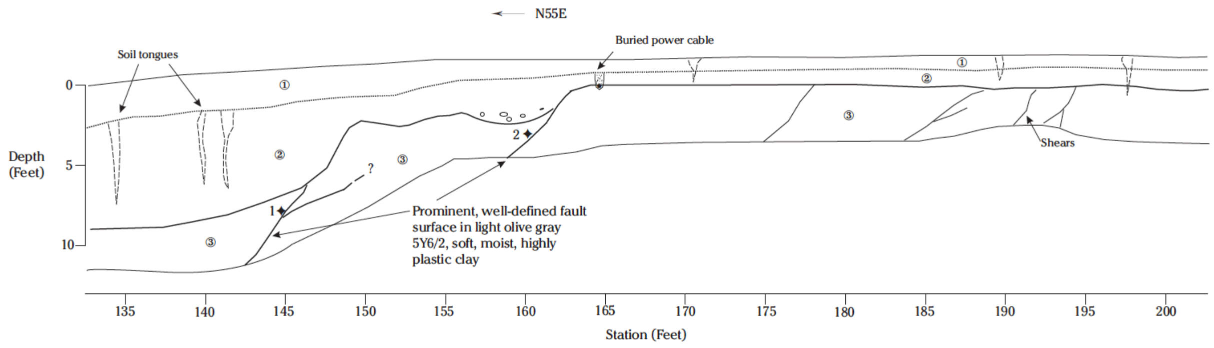

① clayey silt, black, 2.5Y2.5/1, slightly moist, soft to firm, abundant rootlets, low plasticity, poor soil development, gradual color change to grayish brown 2.5Y5/2 with depth, firm to stiff with depth (Topsoil)

② gravelly sandy silt, light olive brown, 2.5Y5/4, slightly moist, very stiff to hard, trace rootlets, some subrounded to well rounded pebbles and cobbles typically concentrated at bottom of unit (Terrace Deposit)

③ siltstone, light yellowish brown, 2.5Y6/4, with yellowish brown 10YR5/6 staining, very dense to hard, moderately weathered and closely fractured (Purisima Formation/Weathered Bedrock)

Symbols

……… gradational contact

– – – relatively sharp contact

—— very sharp contact

1✦ N57W54NE on fault surface, gray clay seam 1/8-1/4" thick, with faint slickensides oriented down dip

2✦ N56W46NE on fault, with wet, soft, highly plastic clay gouge zone on top of fault surface

Logged by Steven F. Connelly, C.E.G., and Ron Rubin, 1/29/01

Log of Trench 2

STEVEN F. CONNELLY, C.E.G.

Consulting in Engineering Geology

Pillar Point Property
Princeton-by-the-Sea
San Mateo County, California

Project #	Scale	Date	Figure
0103	1 Inch = 5 Feet	3/2/01	15

Figure A5: Figure from Connelly and Rubin, 2001 of southwest end of Trench 2 showing report of down dip-oriented slickensides on one component of fault number 33 in Figure A4.

Figures for Appendix B:

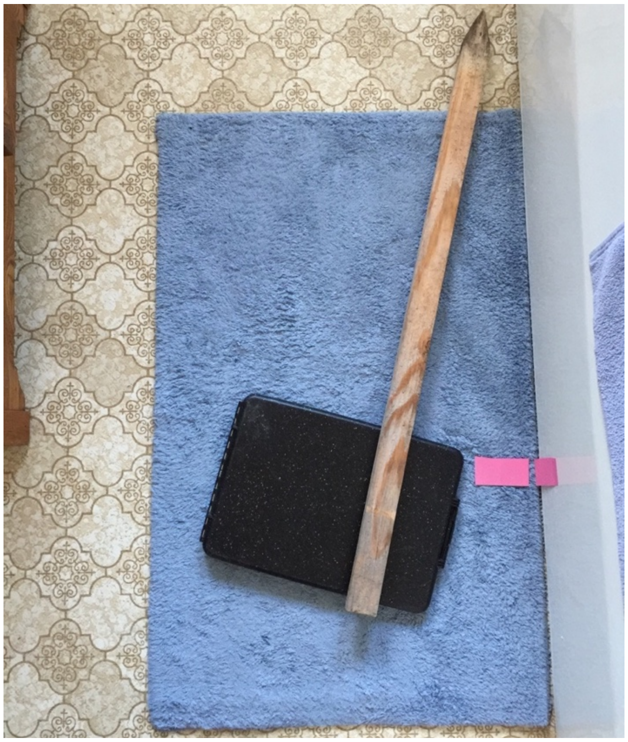

Figure B1: Setup and arrangement for demonstrating folding on a flexible medium pushed at a shallow angle against a restraining surface. Force is applied to black driving plate in direction indicated by stake. Pink markers used to indicate offset from starting point.

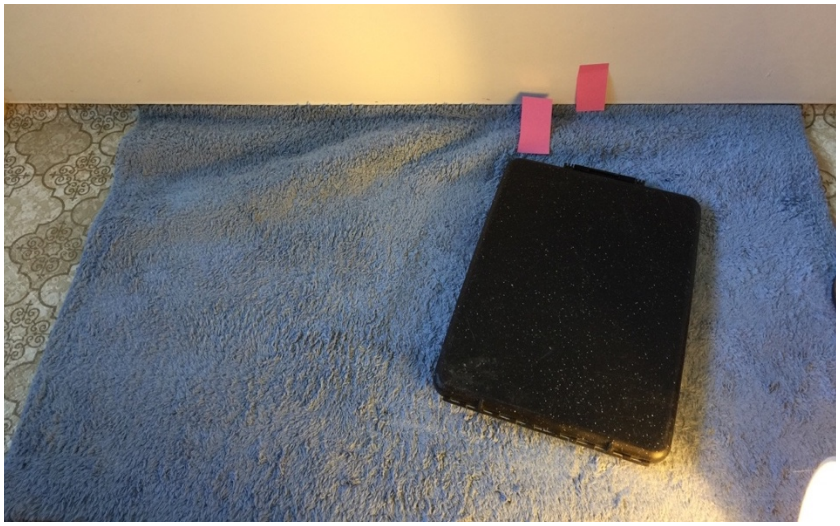

Figure B2: Initial offset. Two ridges start forming ahead of pusher. One ridge forms between pusher and restraint.

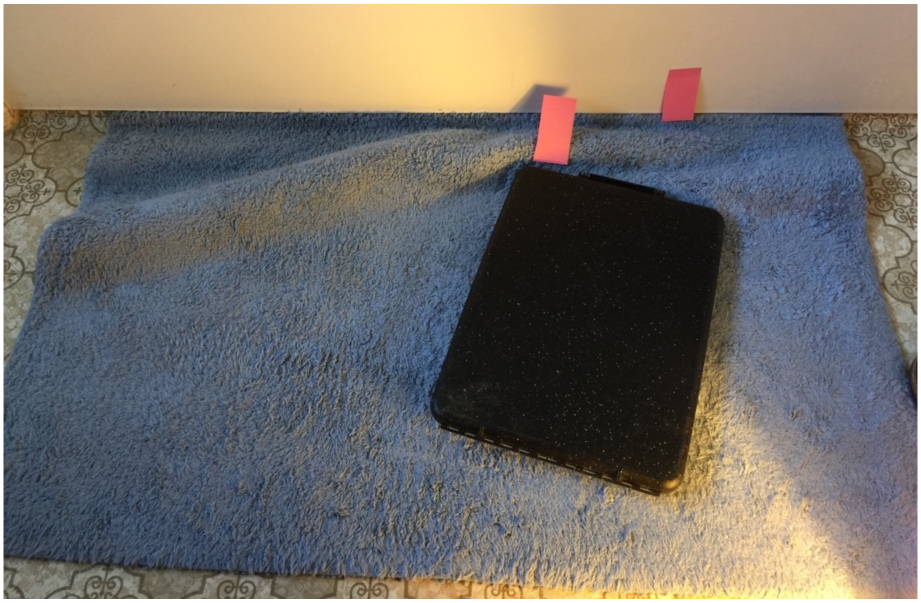

Figure B3: More offset, ridges increase in height. One furthest from restraint grows more than one closer to restraint.

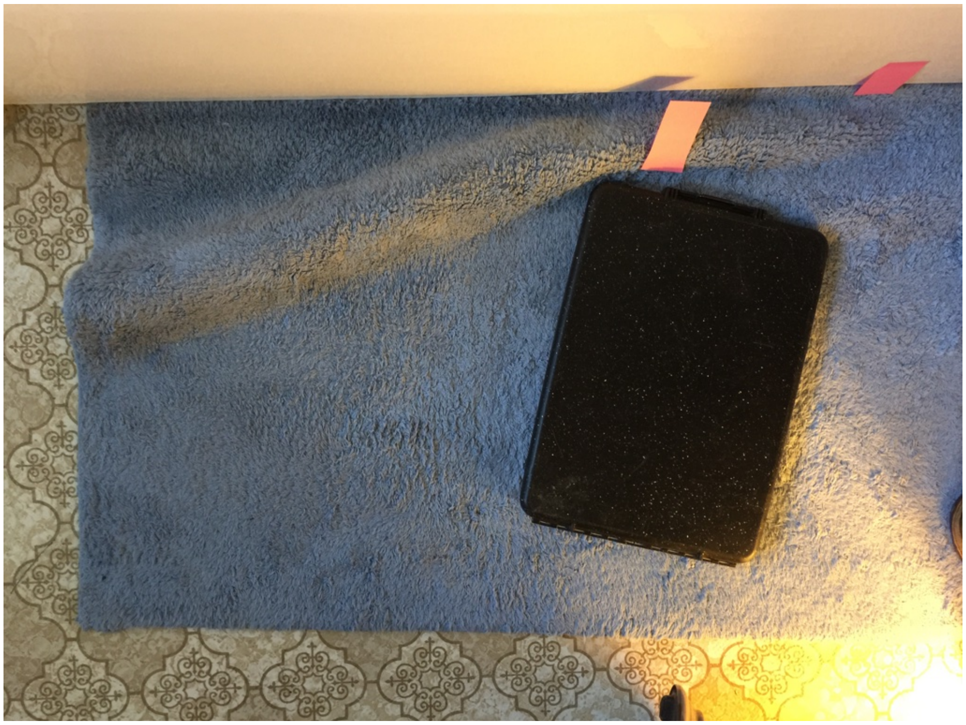

Figure B4: Top view of folded surface. Ridge closest to restraint has folding axis subparallel to restraint, axis for restraint furthest from restraint is slightly curved and fold amplitude is higher.

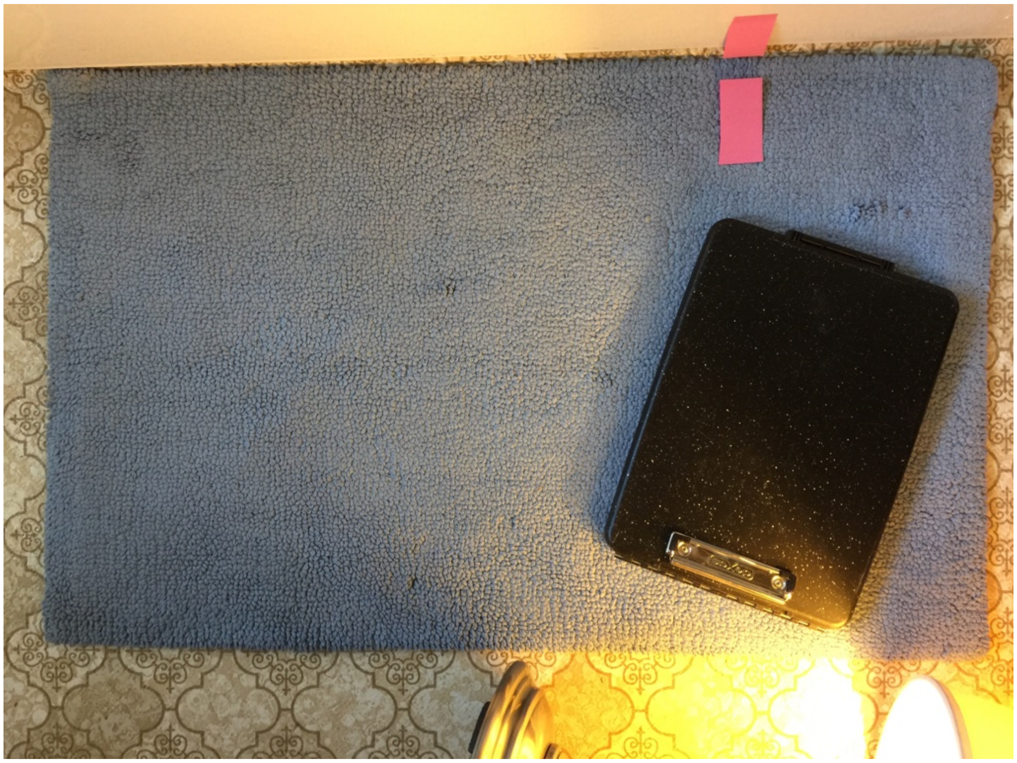

Figure B5: Beginning of another run. Pusher is further back on flexible medium.

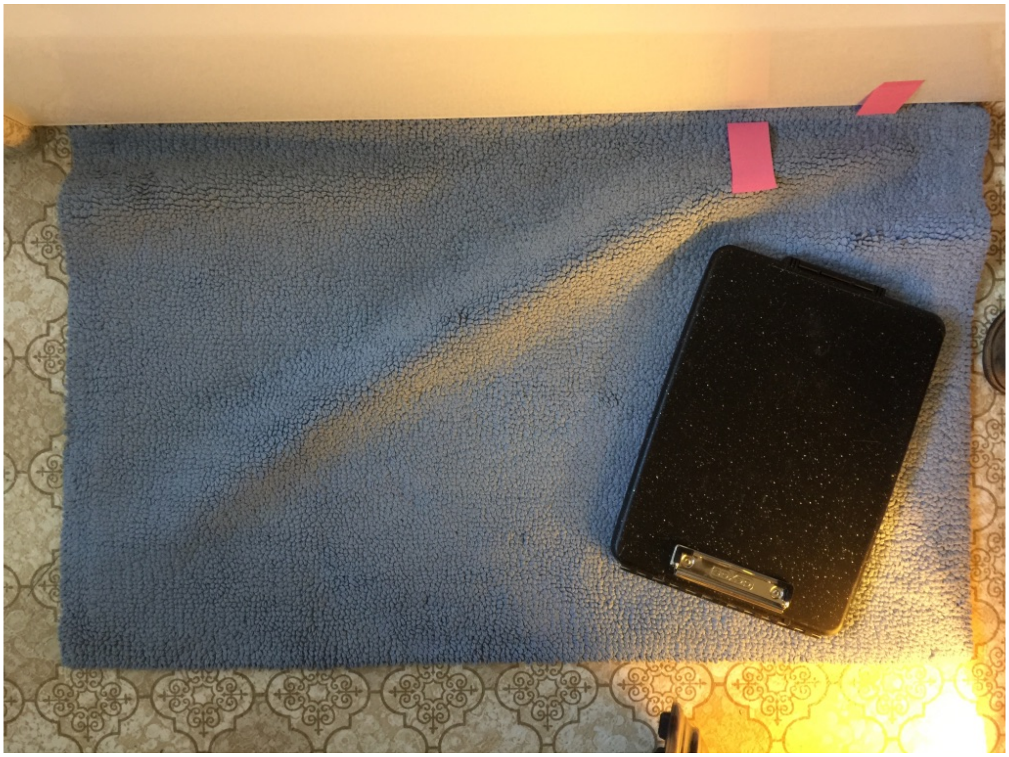

Figure B6: Top view after second run. Again, two ridges formed.

Figures for Appendix C:

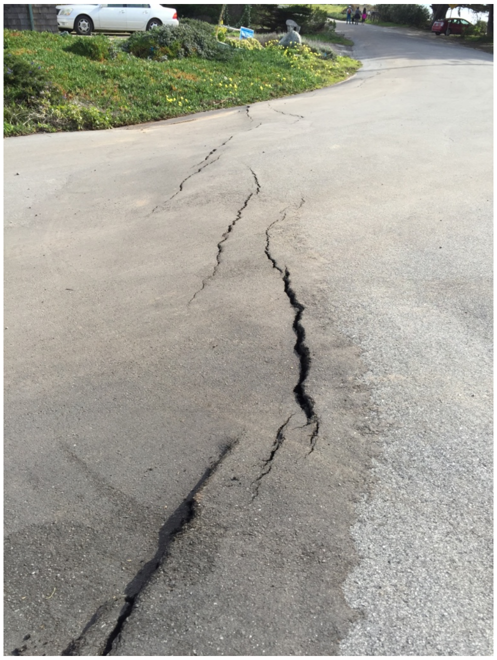

Figure C1: Riedel shears in asphalt road bed at corner of San Lucas Ave and Ocean Blvd; GPS Coordinates: 37^{o}, 30’, 54.1” N; 122^{o}, 30’, 42.6”W.

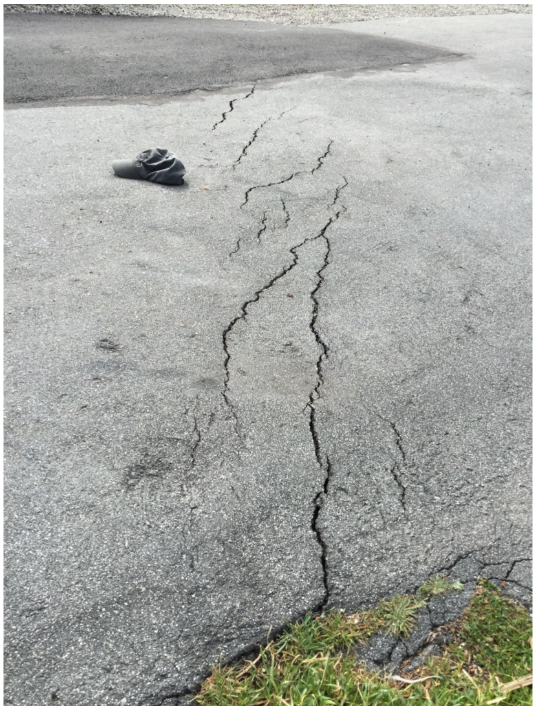

Figure C2: Riedel shears in asphalt road bed on Los Banos Ave west of Park Ave; GPS Coordinates: 37^{o}, 31’, 3.1” N; 122^{o}, 30’, 43.4”W.

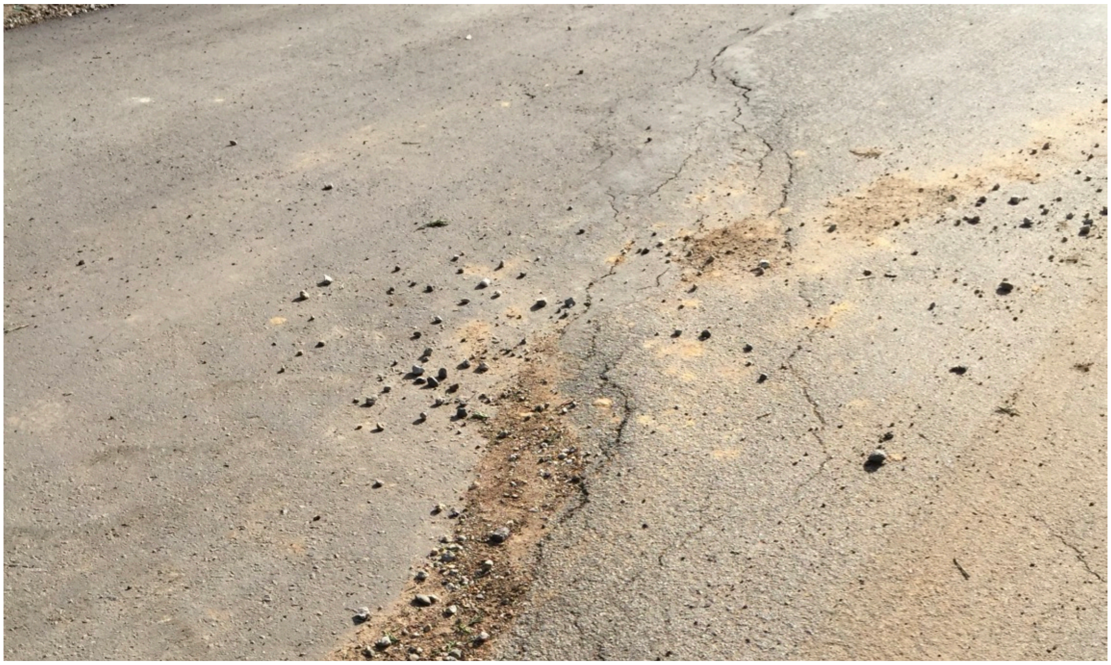

Figure C3: Riedel shears in asphalt road bed on San Lucas Ave between Ocean Blvd and Del Mar Ave; GPS Coordinates: 37^o, 30’, 55.2” N; 122^o, 30’, 41.6”W.

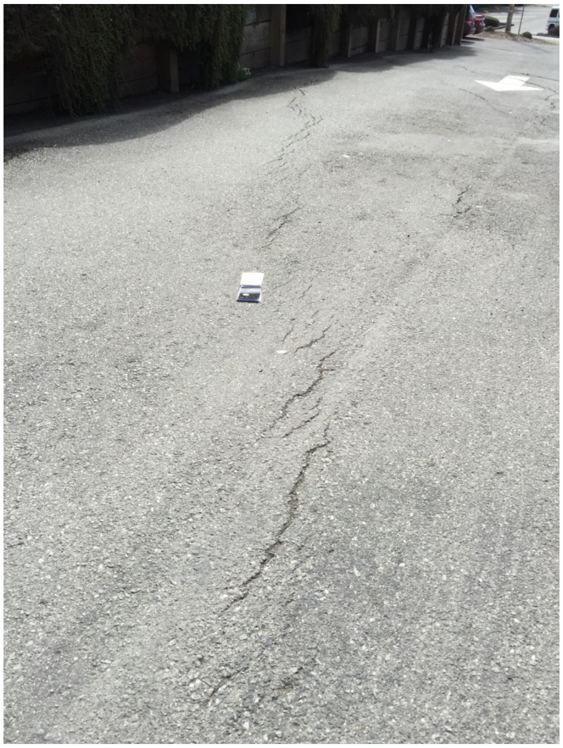

Figure C4: Riedel shears in asphalt road bed in south parking lot of The Distillery Restaurant; GPS Coordinates: 37^o, 31’, 4.1” N; 122^o, 30’, 44.7” W. Trend 356^o.

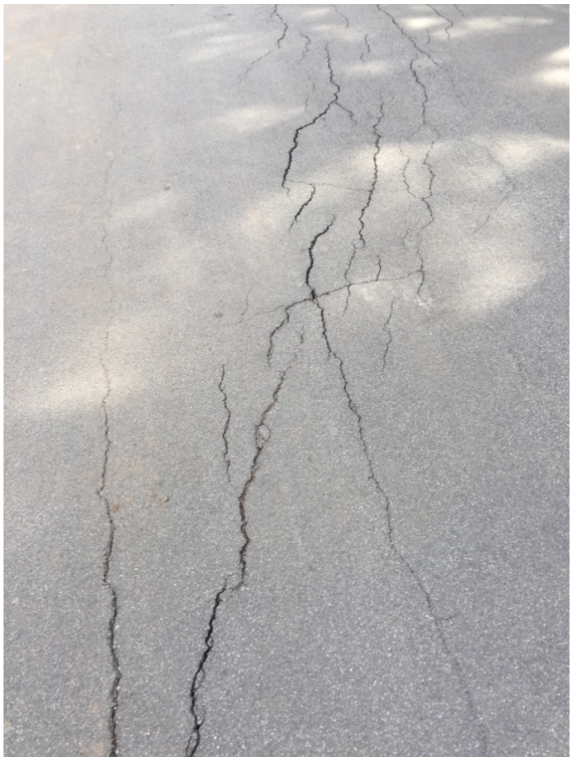

Figure C5: Possible Riedel shears in asphalt road bed on Ocean Blvd between San Lucas and Madrone Ave; GPS Coordinates: 37°, 30', 53.3" N; 122°, 30', 42.6"W.

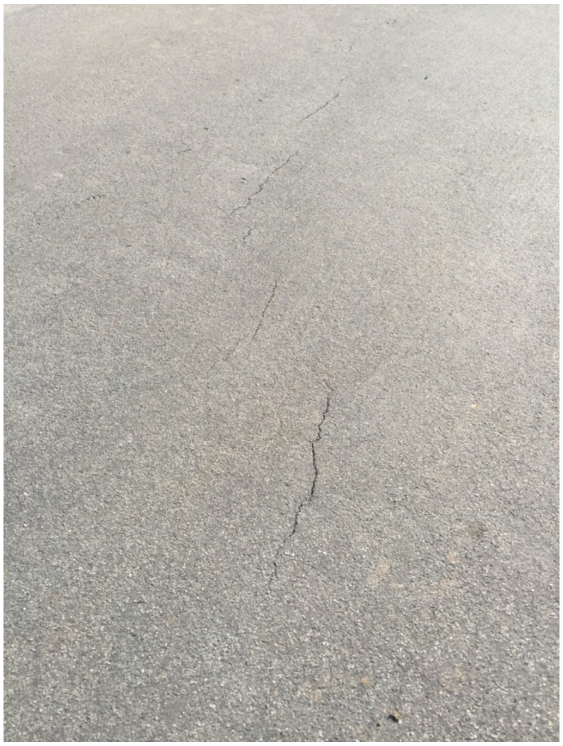

Figure C6. Possible Riedel shears in asphalt road bed on San Lucas Ave between Del Mar and San Ramon. GPS Coordinates: 37°, 30', 57" N; 122°, 30', 40.4"W

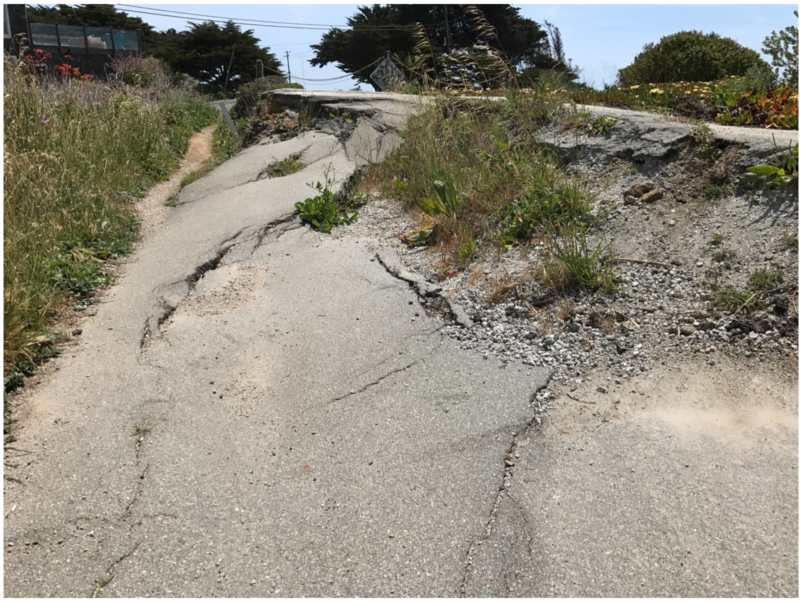

Figure C7: Horst/Graben subsidence and shears in abandoned Ocean Blvd road bed; GPS Coordinates: 37^{o}, 30’, 54.7” N; 122^{o}, 30’, 43”W. NW of photo in Figure C1.

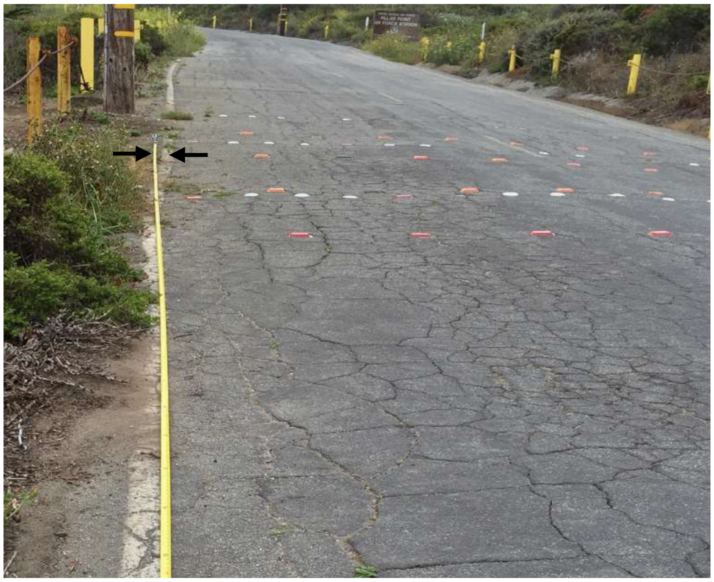

Figure C8: West Point Road south road line offset. GPS Coordinates: 37^{o}, 30’, 6.4” N; 122^{o}, 29’, 49.4”W.

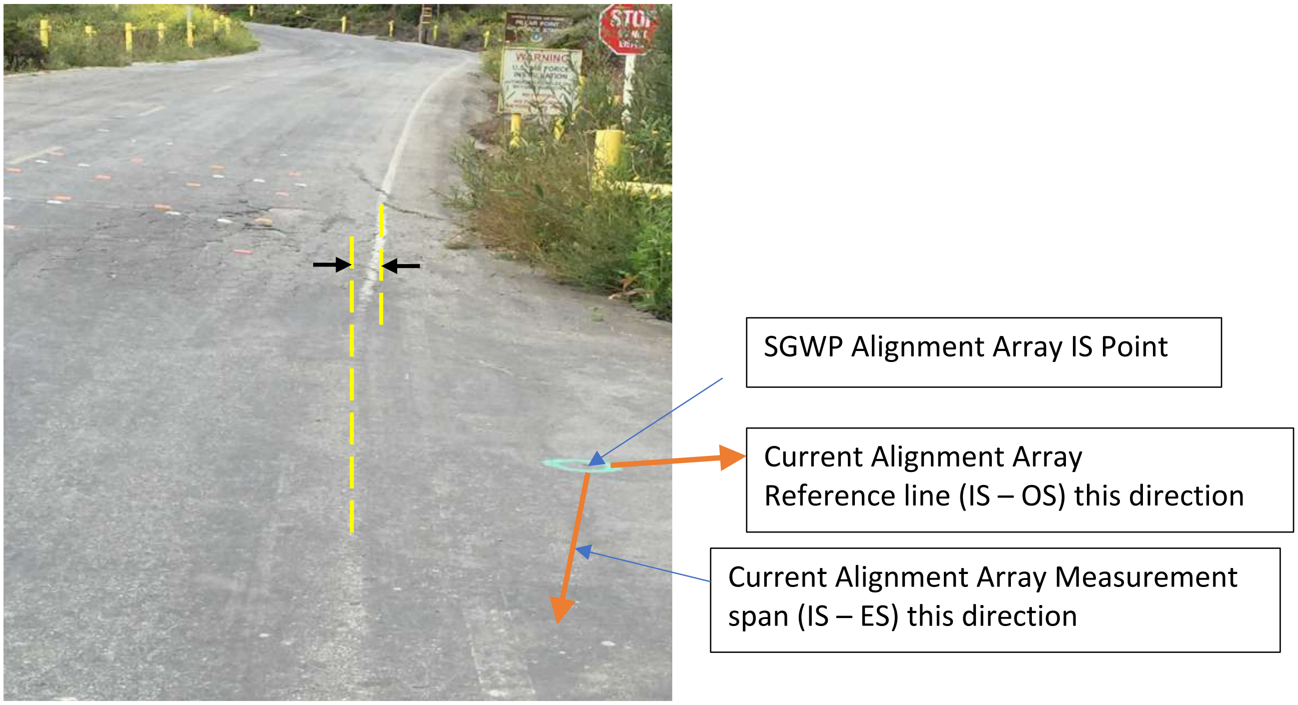
SGWP Alignment Array IS Point

Current Alignment Array Reference line (IS – OS) this direction

Current Alignment Array Measurement span (IS – ES) this direction

Figure C9: West Point Road north road line offset

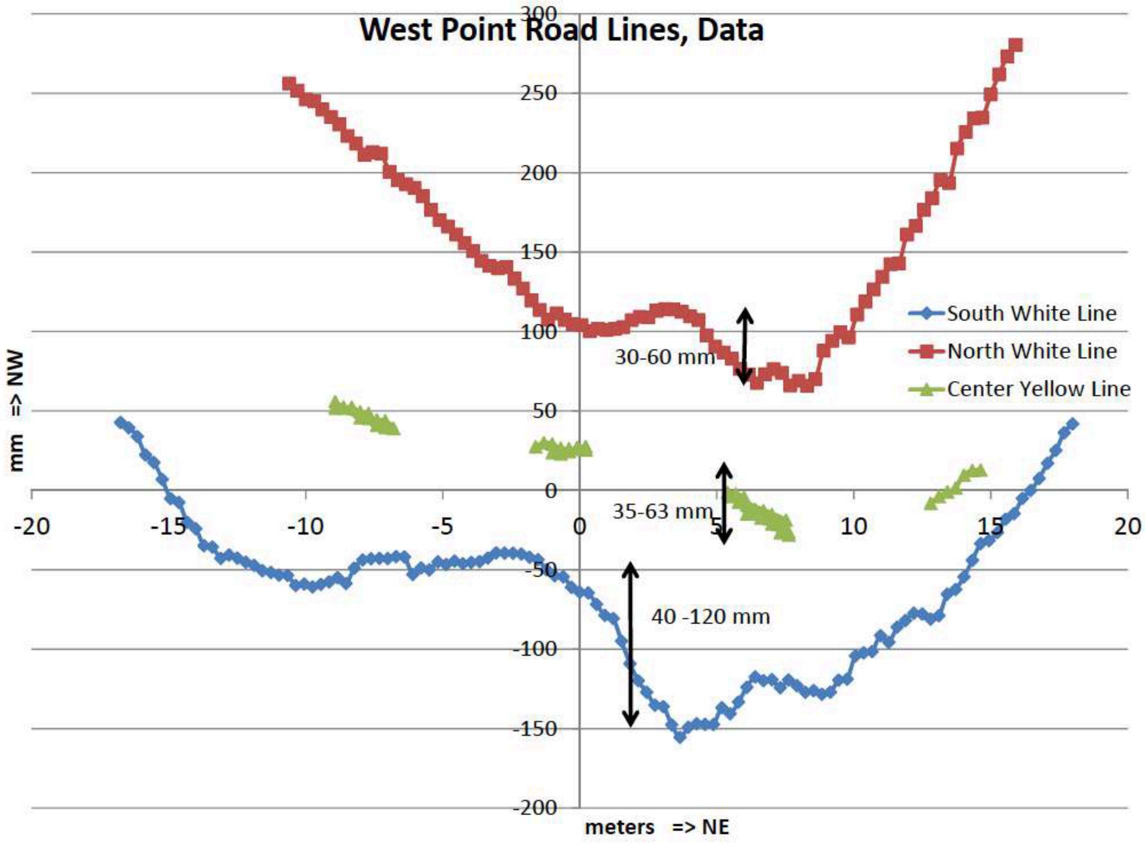

Figure C10: Measured offsets of the three West Point Road Lines. Offset = 30 to 63 mm (120 is discarded as being influenced by roadside slumping) over 17 ± 1 year, => 2.7 ± 1.0 mm/yr

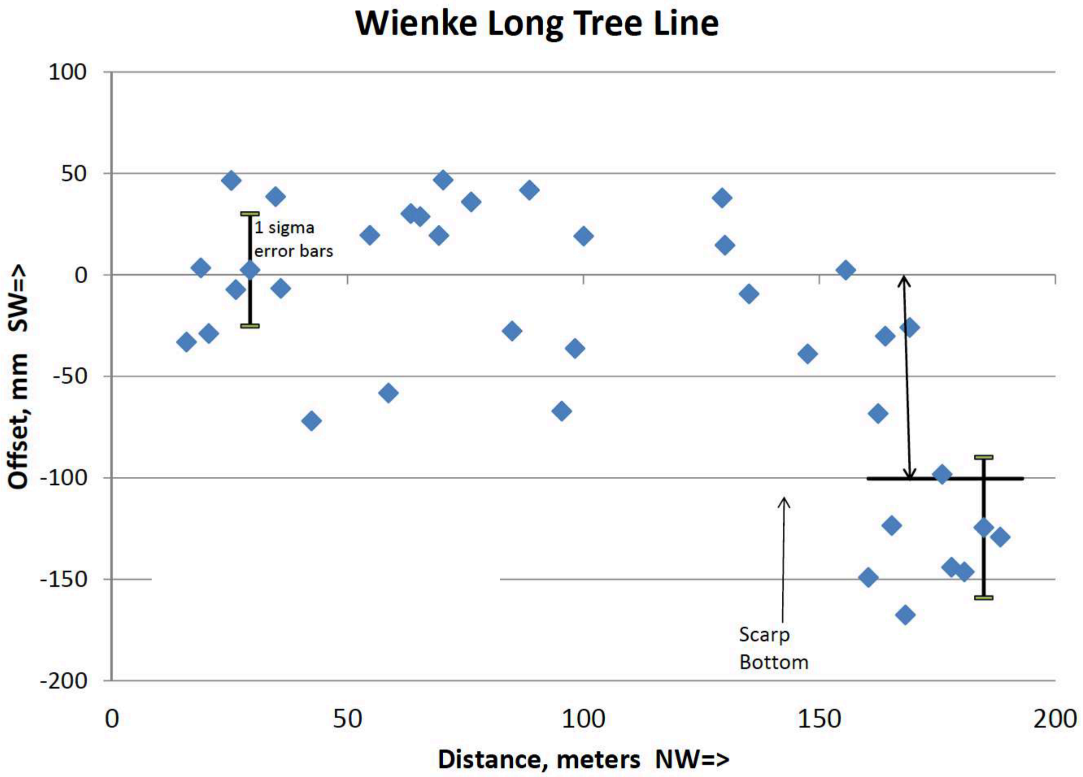

Figure C11: Measured offset on Wienke Long Tree Line ~100 – 130 mm. Time since planting ~ 103 years. Angle to Fault ~ 35^{o}. Calculated creep rate ~ 1.6 – 2.3 mm/yr.

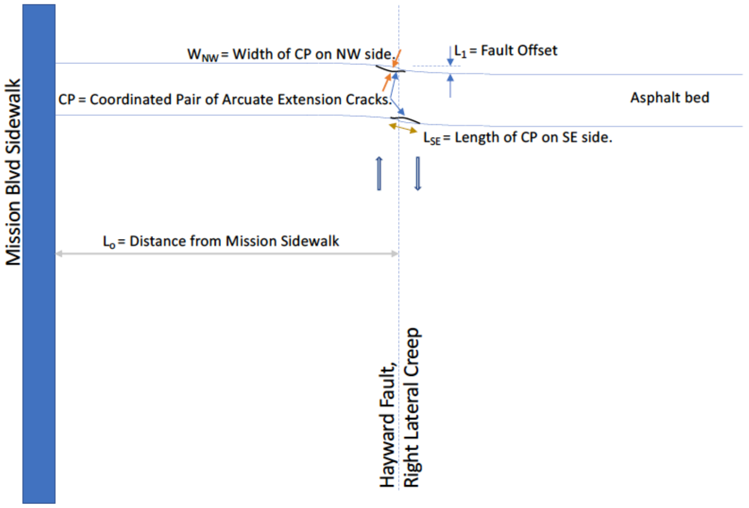
Mission Blvd Sidewalk
W_{NW} = Width of CP on NW side.
L_1 = Fault Offset
CP = Coordinated Pair of Arcuate Extension Cracks.
Asphalt bed
L_{SE} = Length of CP on SE side.
L_o = Distance from Mission Sidewalk
Hayward Fault, Right Lateral Creep

Figure C12: Schematic diagram of Coordinated Pair of Arcuate Extension Cracks (CP) showing parameters used in Table CI. Mission Blvd sidewalk reference is specific to the Hayward Fault in Hayward, Ca. Asphalt bed is any of indicated parking lots or roadbeds used for the measurements in Table CI.

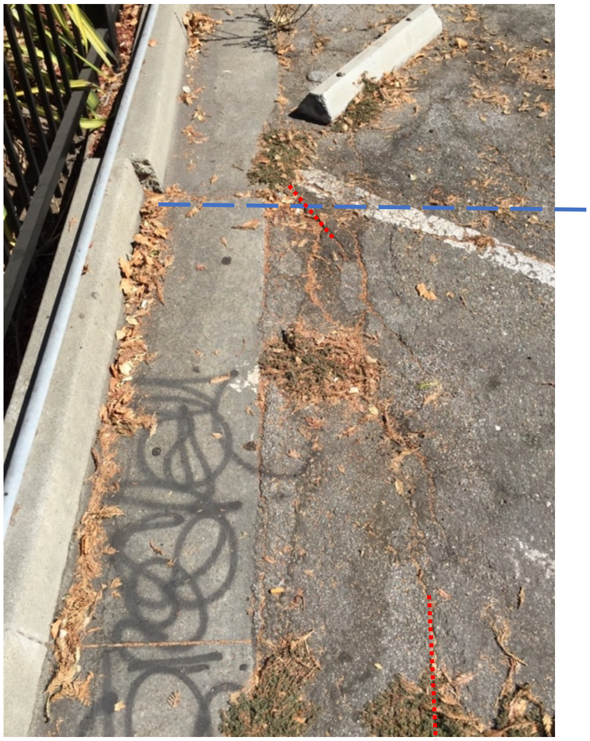

Figure C13: Typical arcuate crack straddling a fault along Hayward fault, parking lot between A&B streets in Hayward, Ca. Blue dashed line approx. fault line, red dotted line highlights the ends of the CP.

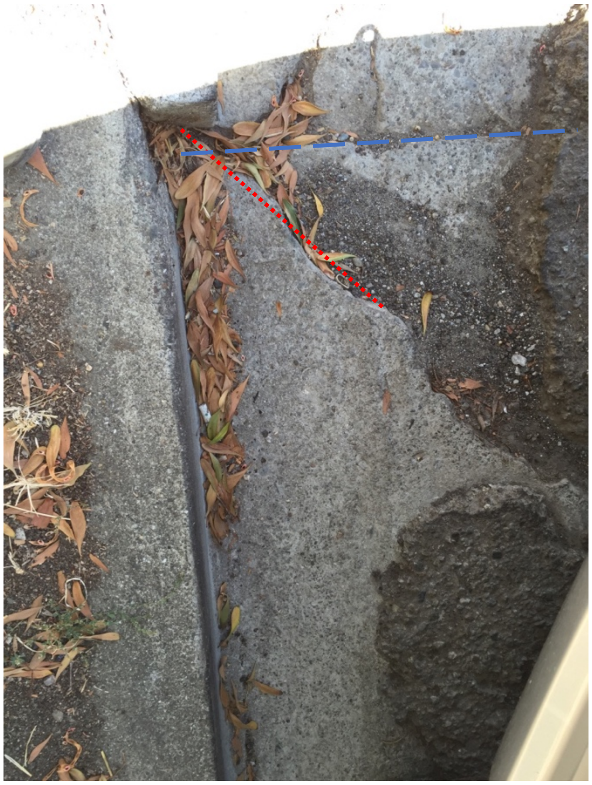

Figure C14: Arcuate crack straddling Hayward fault, Simon Str in Hayward, Ca. Blue dashed line approx. fault line, red dotted line is an end of a CP. Need better photo.

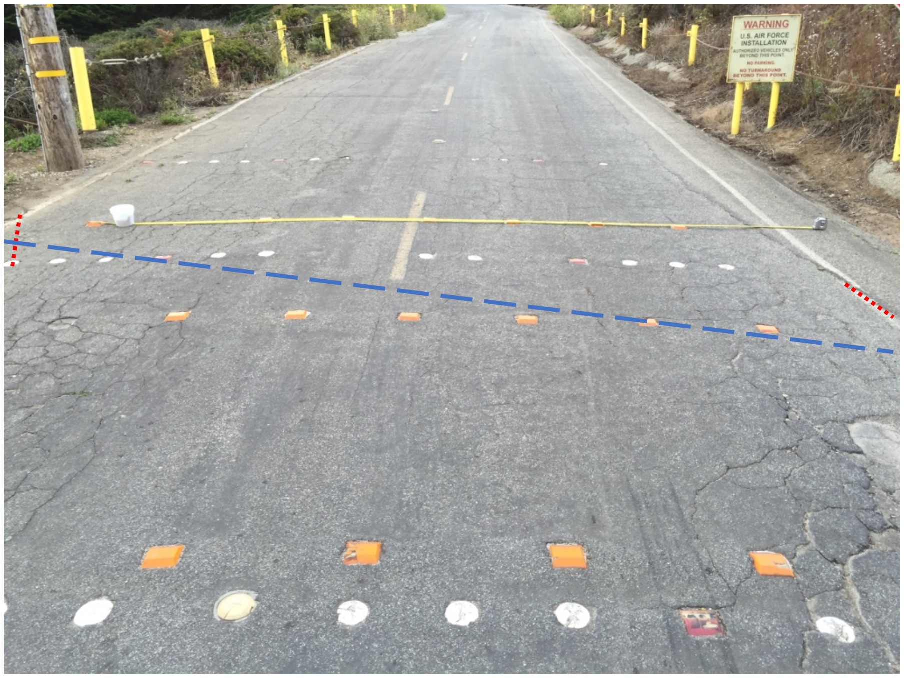

Figure C15: CPs found on West Point Road straddling the implied fault indicated by the road line offsets in Figure C10. Blue dashed line is approximate implied fault path. Red dotted lines mark part of CPs. Need better photo.

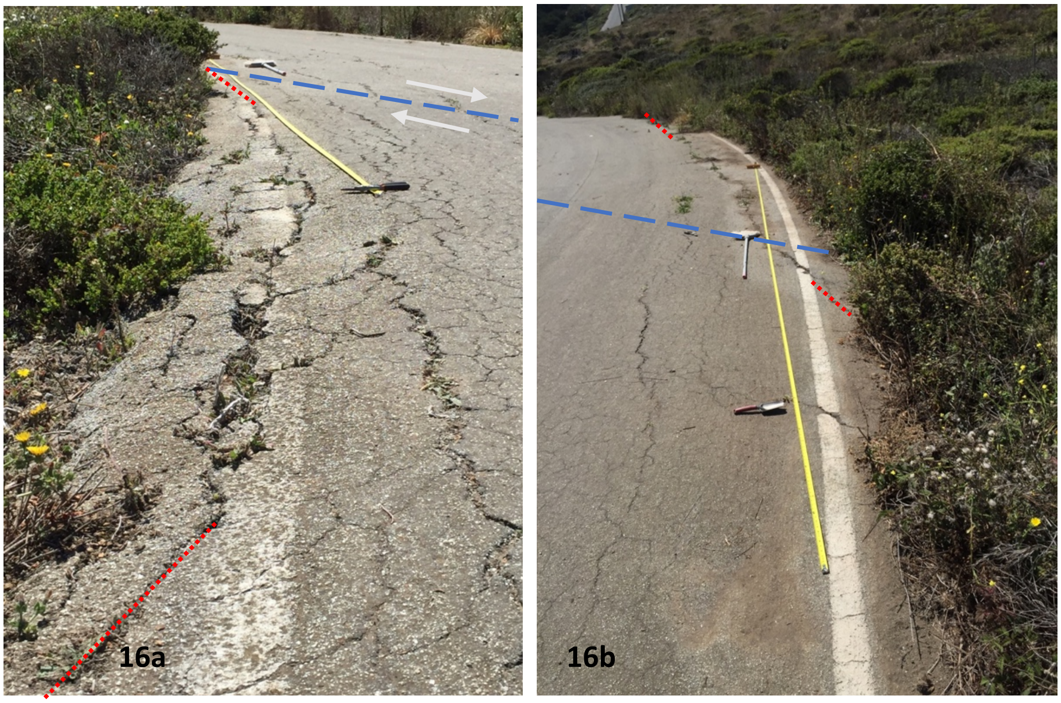

Figure C16a and b: CPs on the curved Service Road extending north from West Point Road, looking west. 16a is south side of road, 16b is north side of road. Blue dashed line is approximate fault path. Red dotted lines mark ends of CPs. 1.4 m long broom for scale.

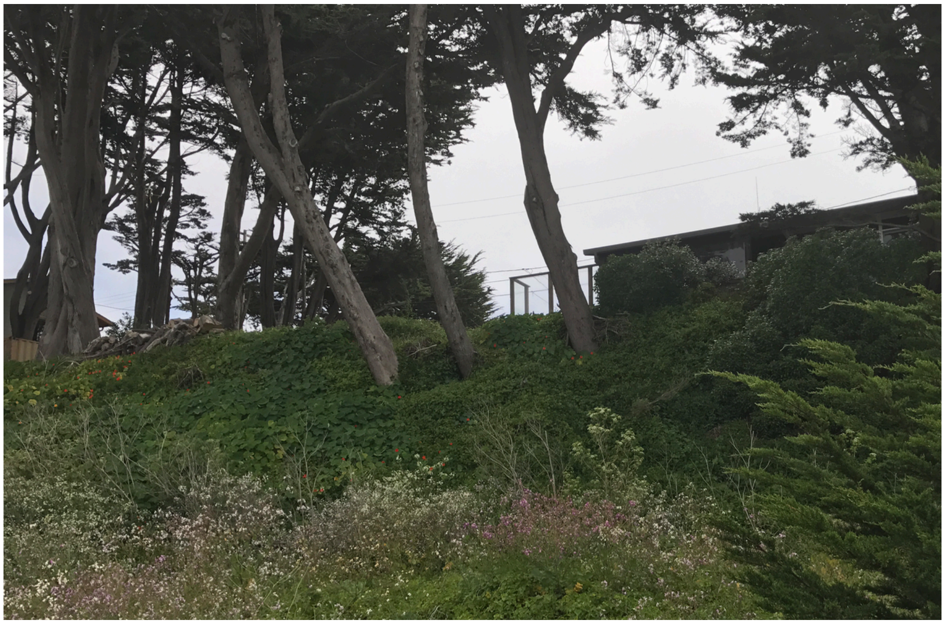

Figure C17: Three trees along the Distillery Fault scarp that are tilting at an oblique angle to the scarp gradient. View is perpendicular to strike.

Figures for Appendix D:

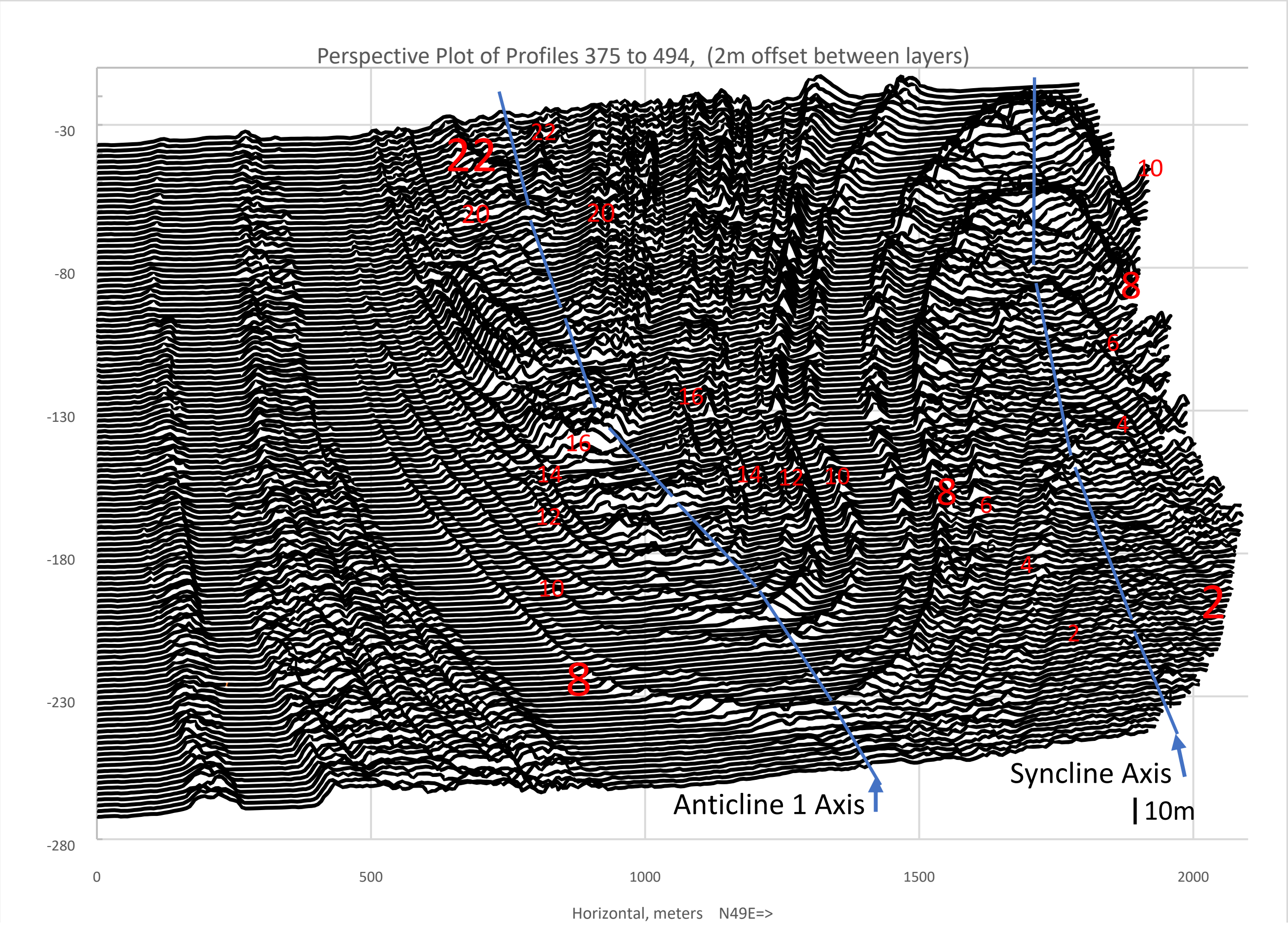

Figure D1: Bathymetry data of Bretz et al, 2014 is digitized along lines perpendicular to the Middle Strand fault thus vertical in this figure corresponds to 319^{o} azimuth. The data is plotted in simulated 3D by offsetting adjacent lines 2m, they are actually offset in the horizontal plane by 10m. Individual resistant layers are numbered in their vertical sequence with 1 being the highest of the exposed distinguishable layers. Note layer 8 is the folded layer exposed furthest west and is traceable throughout the structure. The structure west of layer 8 is uplifted, but not folded.

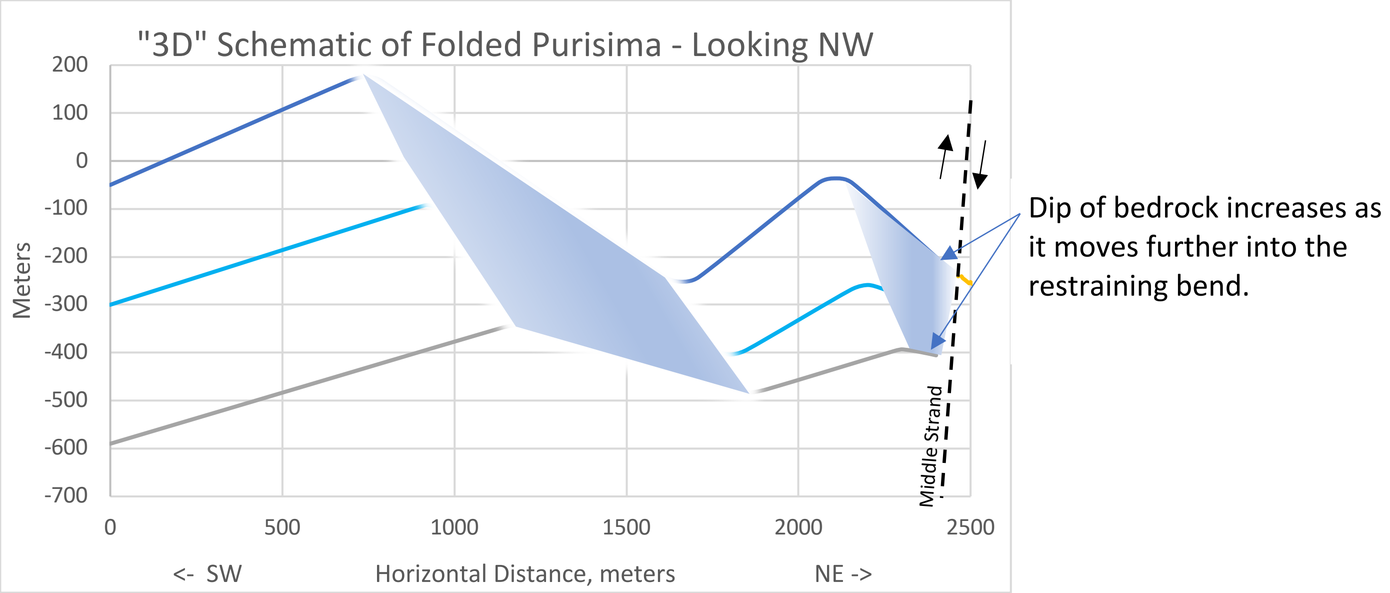
"3D" Schematic of Folded Purisima - Looking NW
Meters
200
100
0
-100
-200
-300
-400
-500
-600
-700
0
500
1000
1500
2000
2500
<- SW
Horizontal Distance, meters
NE ->
Middle Strand
Dip of bedrock increases as it moves further into the restraining bend.

Figure D2: A schematic of the folding to illustrate the objective of the folding model; which is to obtain the change in bedrock slope as a function of distance into the restraining bend.

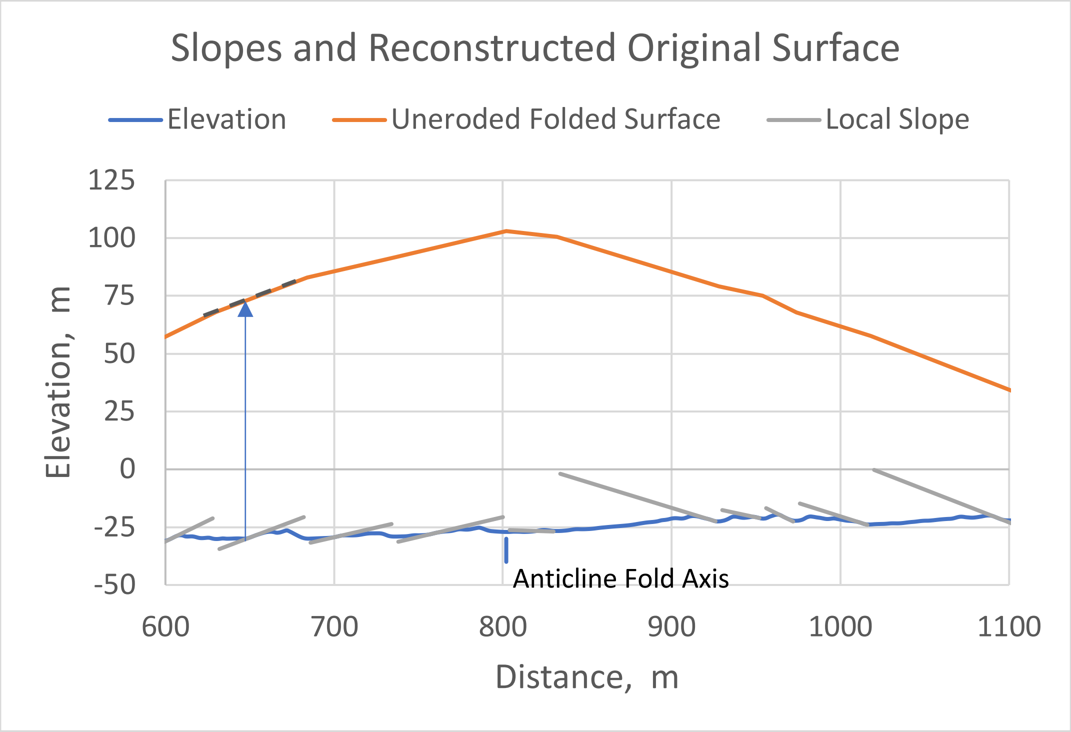

Figure D3: Method to reproduce the uneroded surface of the fold as explained in the text.

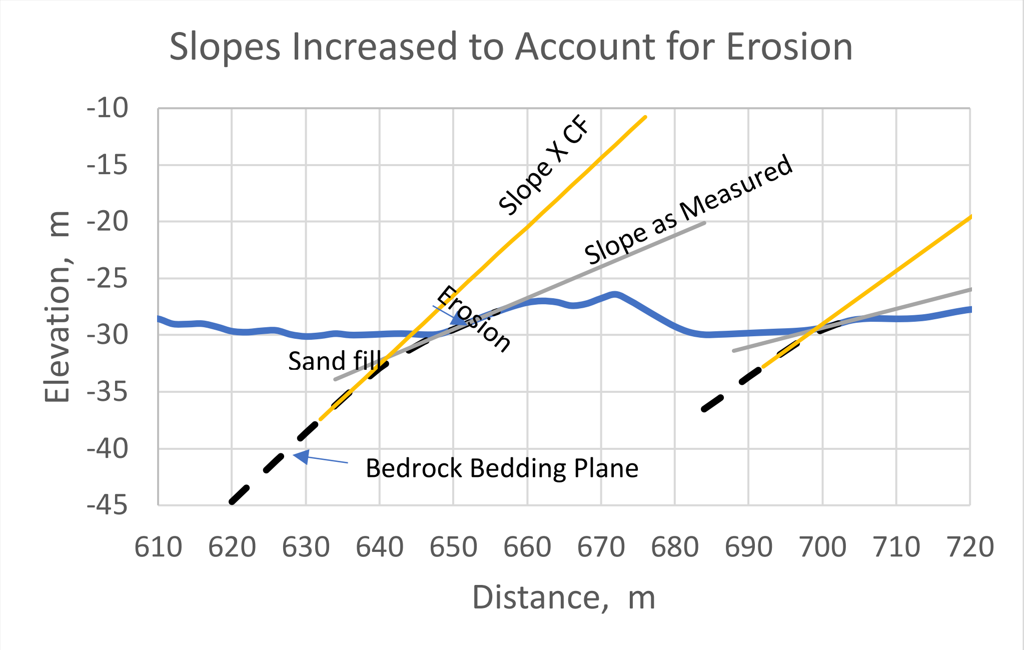

Figure D4: Expanded view of Figure 49 showing effect of erosion on the measured slope and the method to compensate that effect by multiplying the slope by a compensation factor, CF.

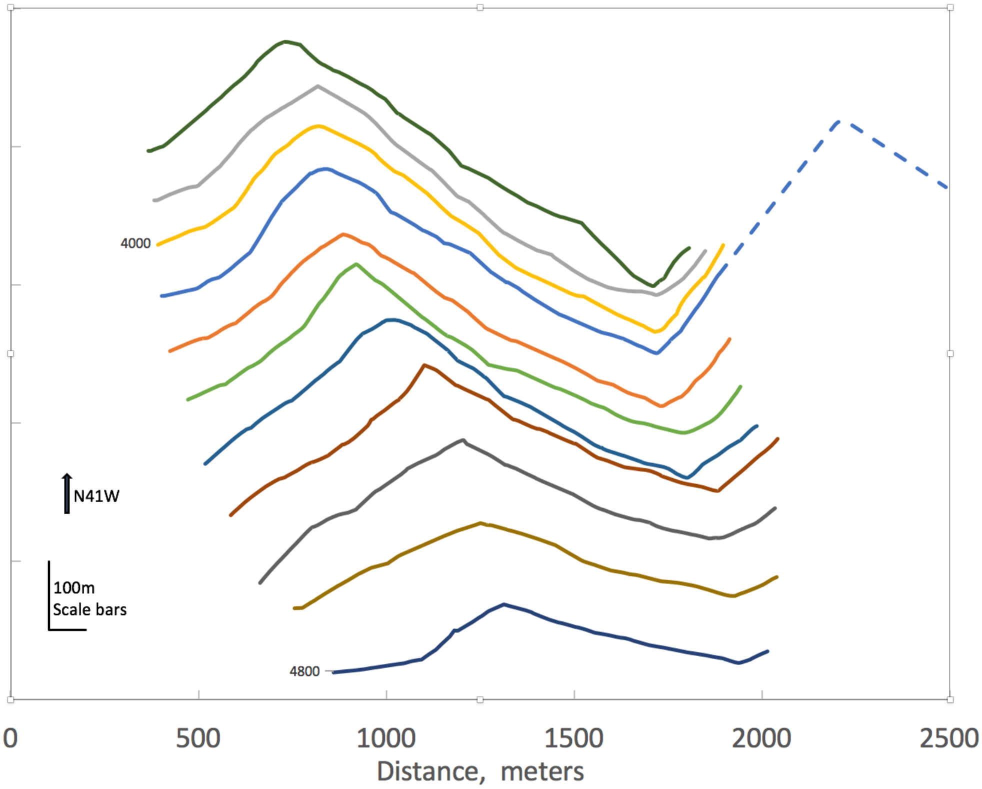

Figure D5: Reconstructed surface profiles plotted in pseudo 3D (each line is lowered 70 m compared to neighbor which is 100 m horizontally separated from it). Each profile is an average of 5 lines and uses two CFs (as explained in the text) of 2.1 and 1.3. Extrapolated sections to the anticline 2 axis and between that axis and the Middle Strand are included for line 4100 as explained in the text.

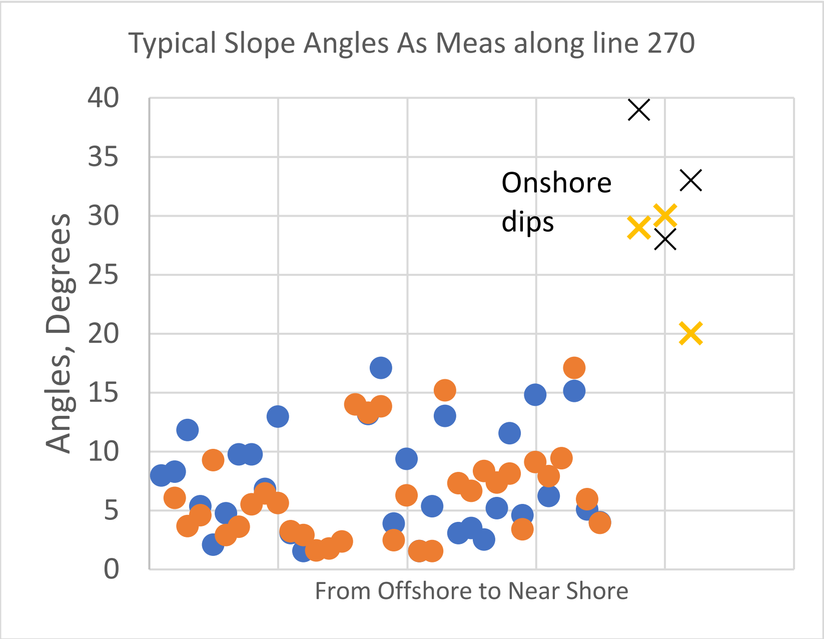

Figure D6: The slope of the erosional planes offshore from bathymetry data compared to the real dips of the bedding planes measured onshore of layers upsection.

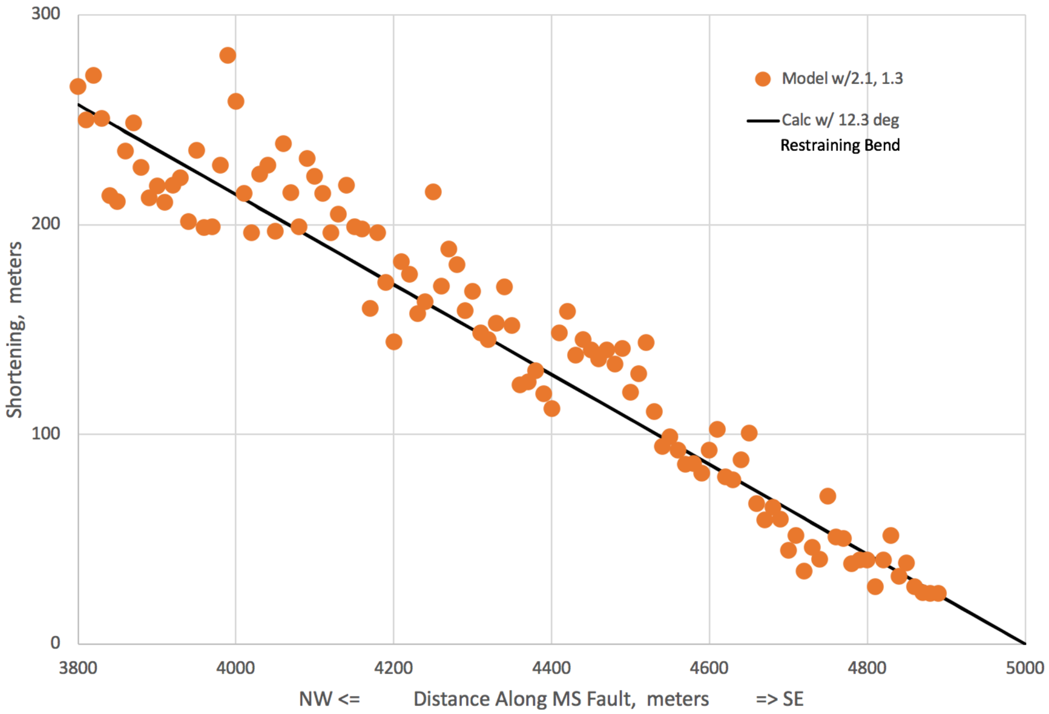

Figure D7: Shortening as a function of distance along the restraining bend. Black line is theoretical shortening required to accommodate a restraining bend of 12.3° starting at the 5000 m point. Orange points are results of the modeling using CF1 = 2.1, CF2 = 1.3. R^2 is .93.

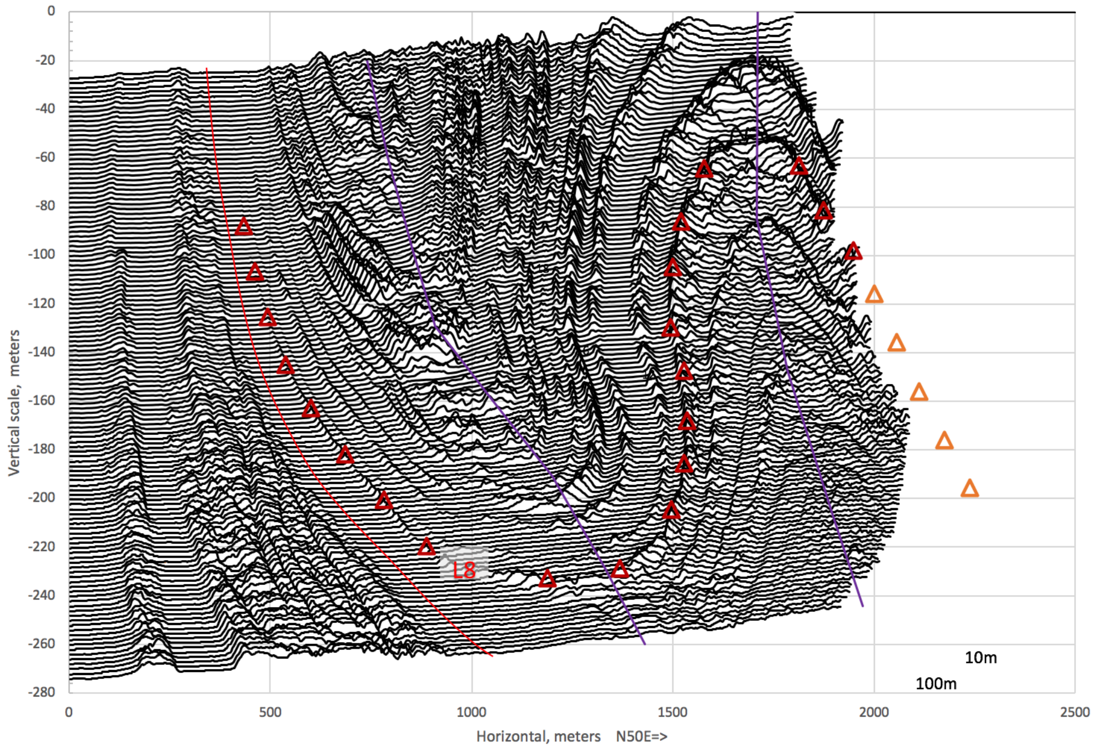

Figure D8: Location of the elevation measurements along layer 8 discussed in the text.

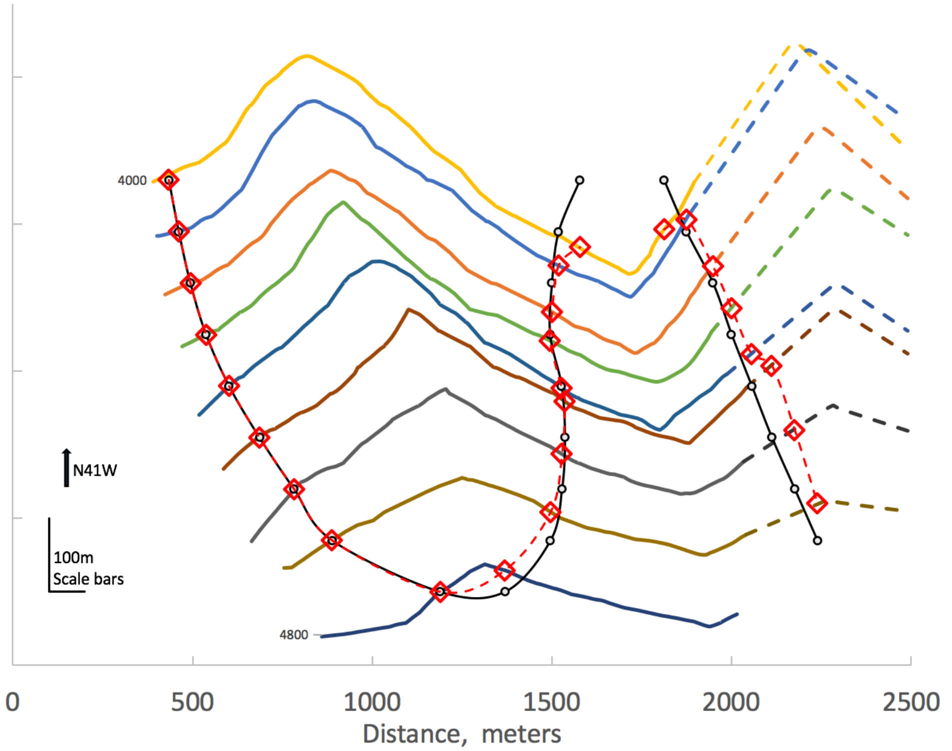

Figure D9: Reconstruction of profiles across the folds plotted in pseudo 3D including extrapolation to the near-shore anticline, dashed lines. Black line and circles are the actual locations and elevations of layer 8. Red diamonds with a dashed red line are model results at those locations when using CF1 = 2.1 and CF2 = 1.3.

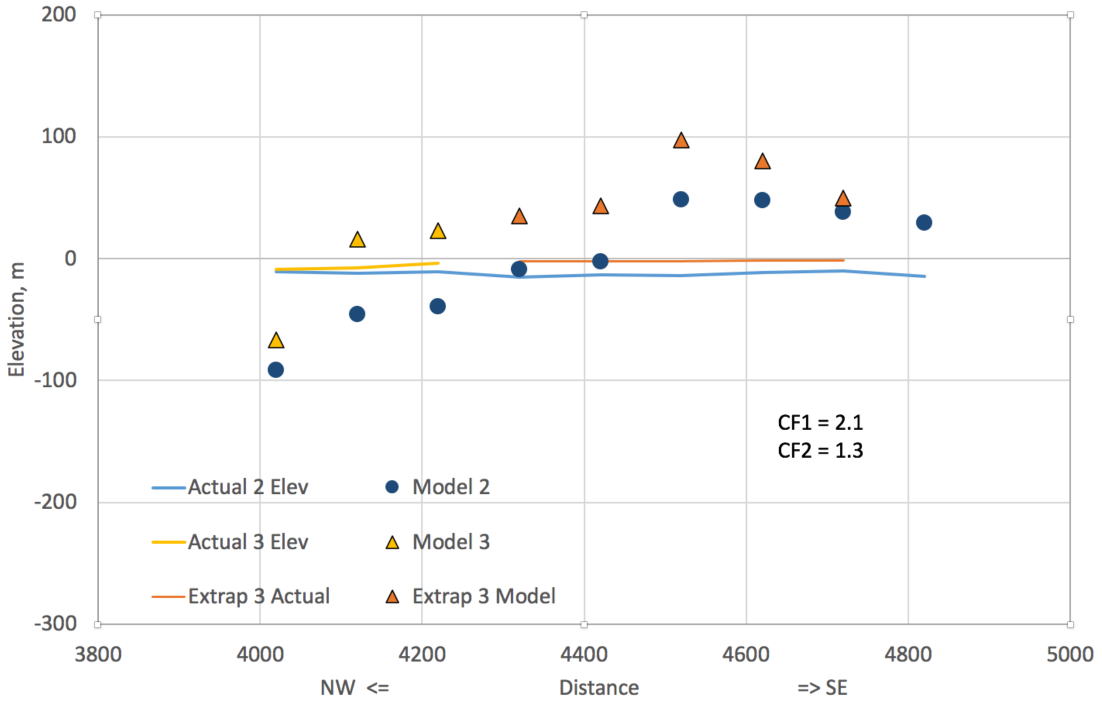

Figure D10: Elevations of actual and model results plotted looking northeast in Figure D9. "2" and "3" refer to the lines along the west side and east side of the syncline, respectively. Note the elevations at 4020 are not of layer 8.

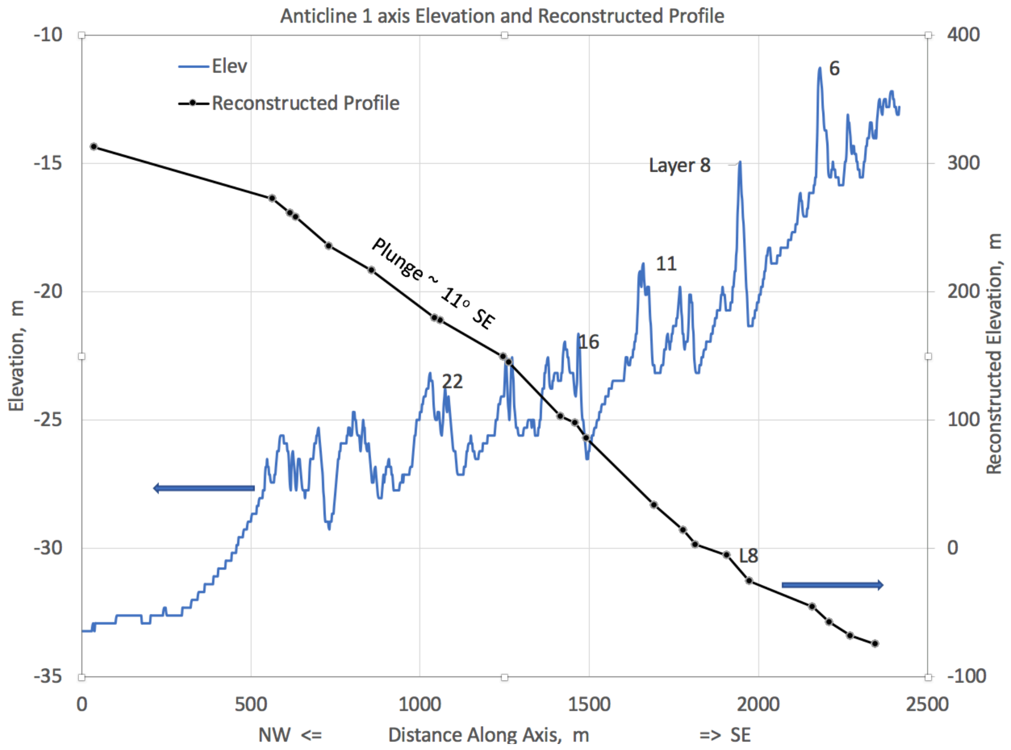

Figure D11: Elevation profile along the anticline 1 fold axis obtained from Google Earth and the reconstructed surface of layer 8 derived from that using no CF, (CF=1).

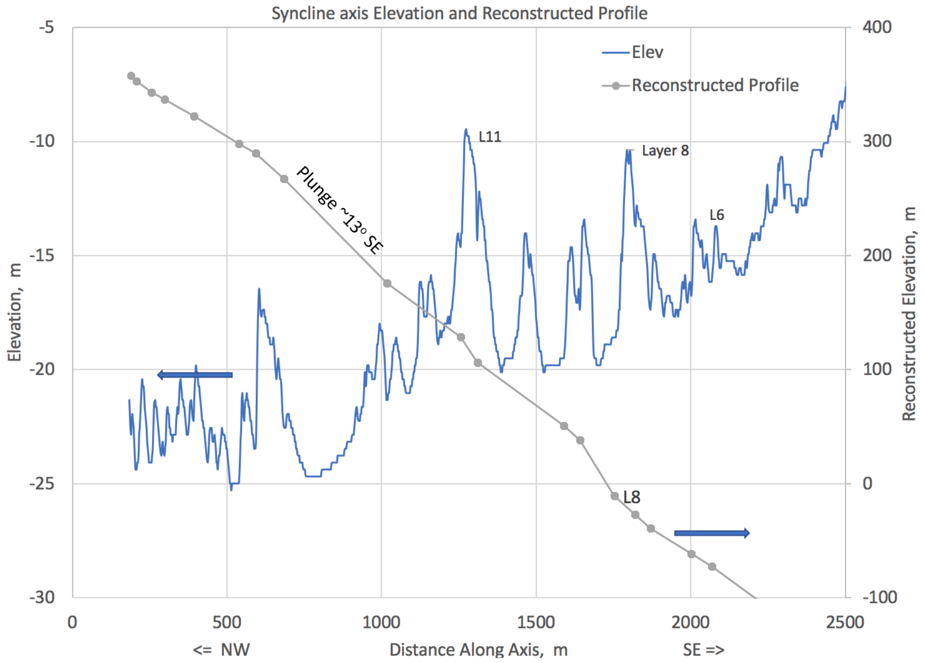

Figure D12: Elevation profile along the syncline fold axis obtained from Google Earth and the reconstructed surface of layer 8 derived from that using no CF.

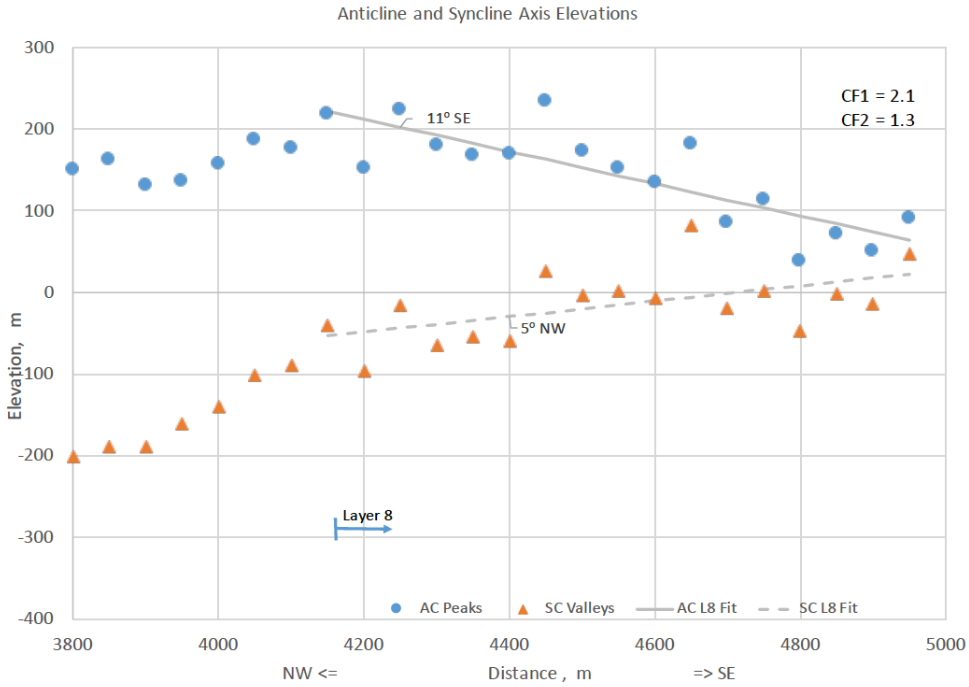

Figure D13: Peaks in the offshore anticline and valleys in the syncline from the model when using CF1 = 2.1 and CF2 = 1.3. To the right of about 4150 the points represent the modeled location of layer 8, to the left the points represent layers lower in the Purisima strata.

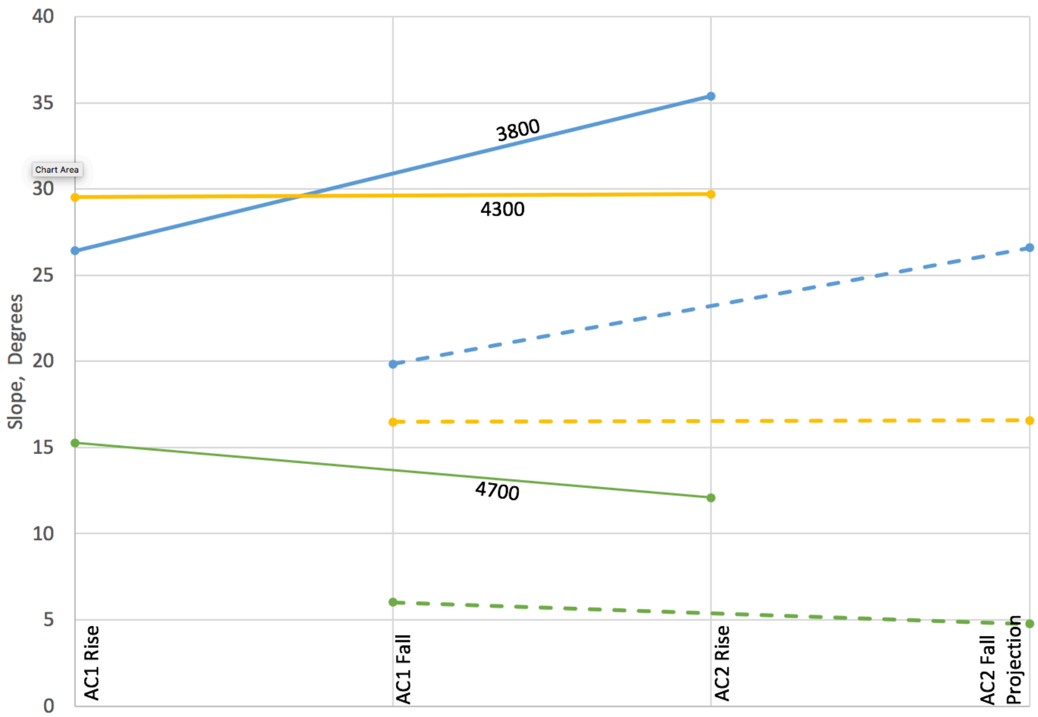

Figure D15: Method of extrapolating the angle on the east side of anticline 2. The ratio of Fall 2 angle to Fall 1, dashed lines, is made the same as the ratio of Rise 2 to Rise 1, solid lines of the same color. Three representative samples are shown for the lines indicated.

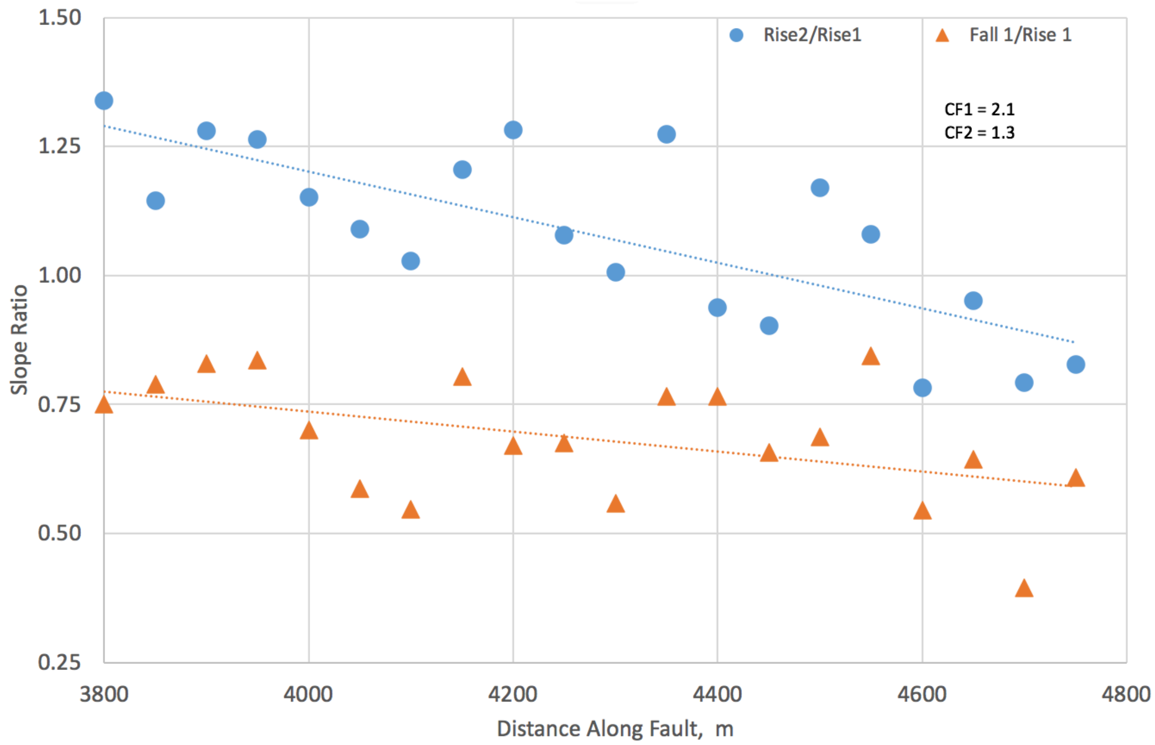

Figure D16: Ratio of slopes versus distance for the case of CF1 = 2.1 and CF2 = 1.3.

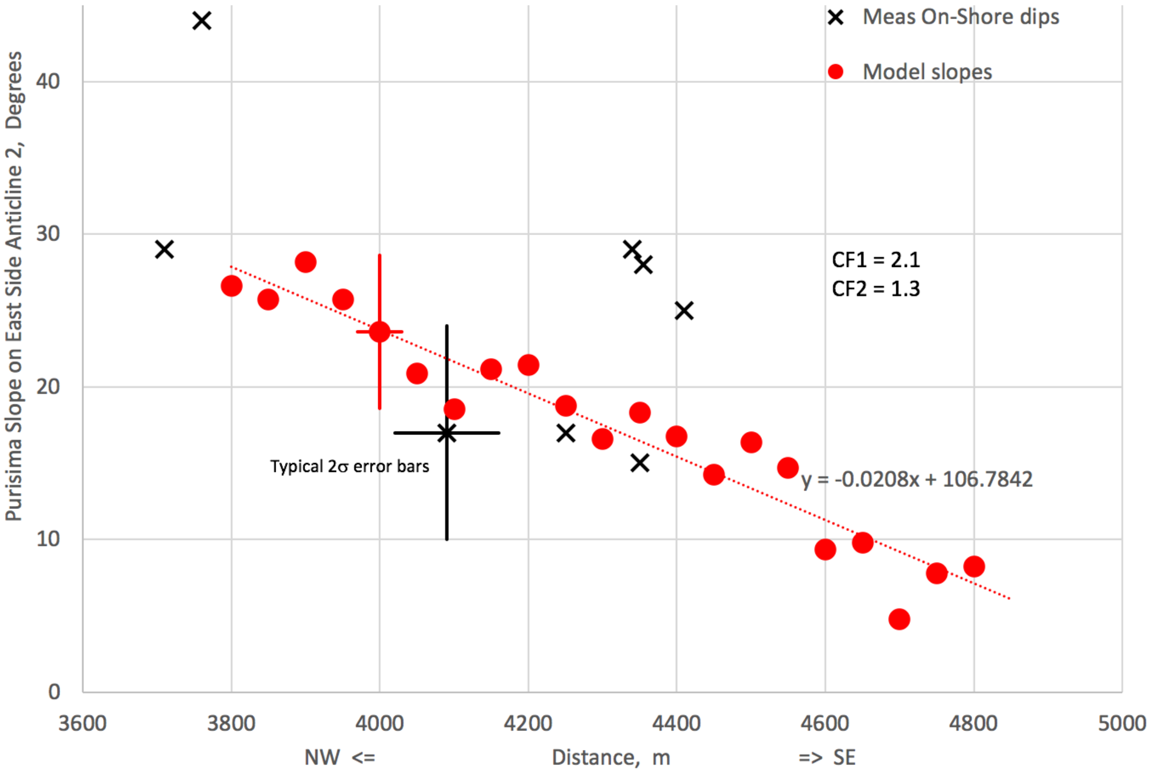

Figure D17: Purisima slope angle perpendicular to fault versus distance along the Middle Strand from the model when using CF1 = 2.1 and CF2 = 1.3 (red circles). Black crosses are measured on-shore dips on the same structural segment. The coefficient, -.0208, represents the change in angle along the fault in deg/m. R^2 is .92.

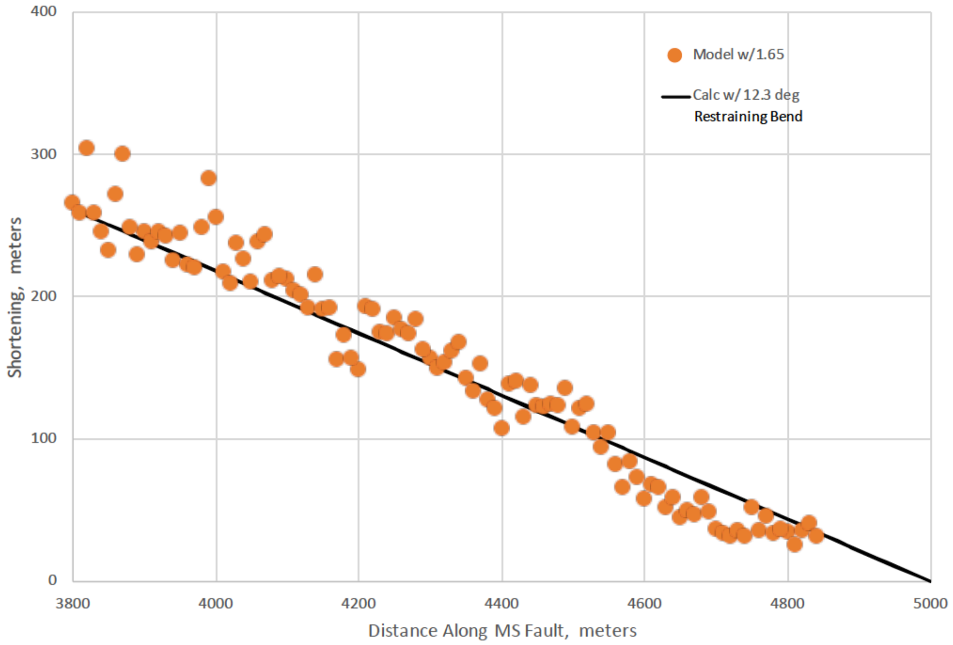

Figure D18: Shortening calculated for the case of a single CF of 1.65 along lines perpendicular to the MS fault as a function of distance along the fault. R^2 is .96.

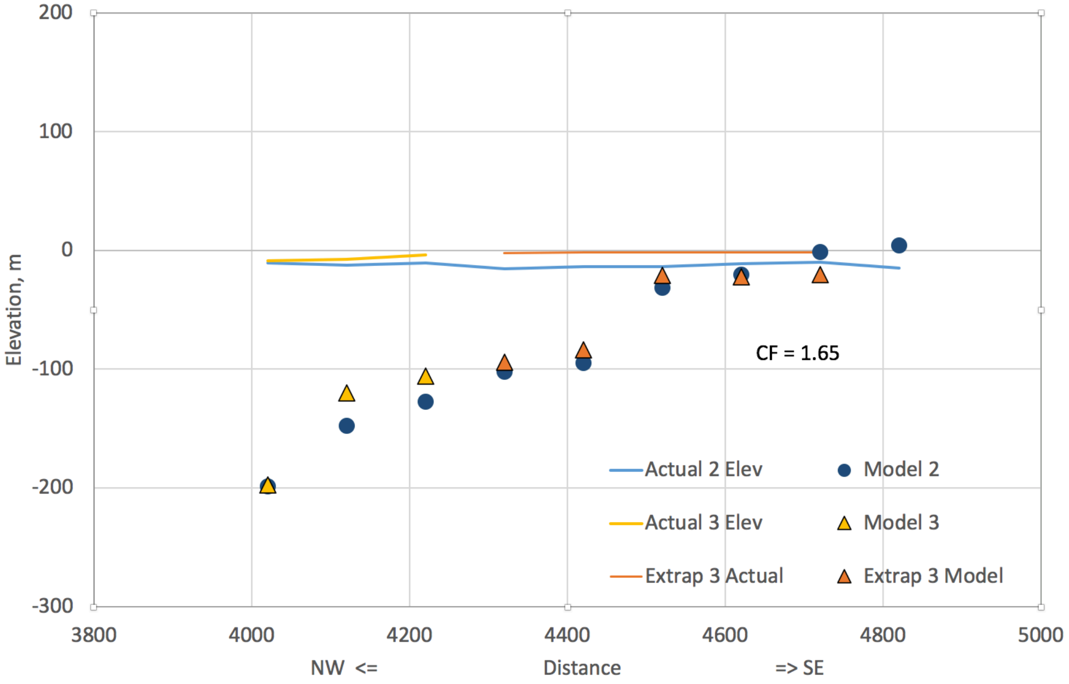

Figure D19: Elevation of Layer 8 from the reconstructed profiles with a single CF of 1.65 compared to measured elevations obtained from bathymetry data plotted as a function of distance along the fault. Locations of measurements are shown in Figure D8.

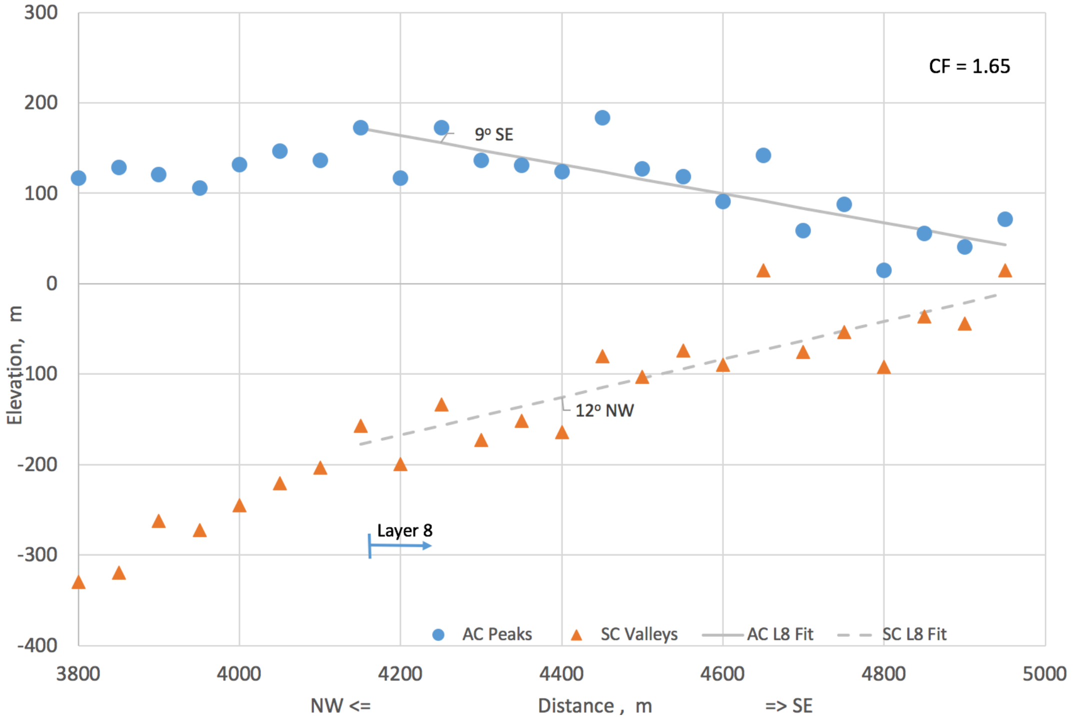

Figure D20: Peak and valley elevations for Anticline 1 and the Syncline from profiles using a single CF of 1.65. The fit lines are calculated only over the region where layer 8 is represented by the model calculations.

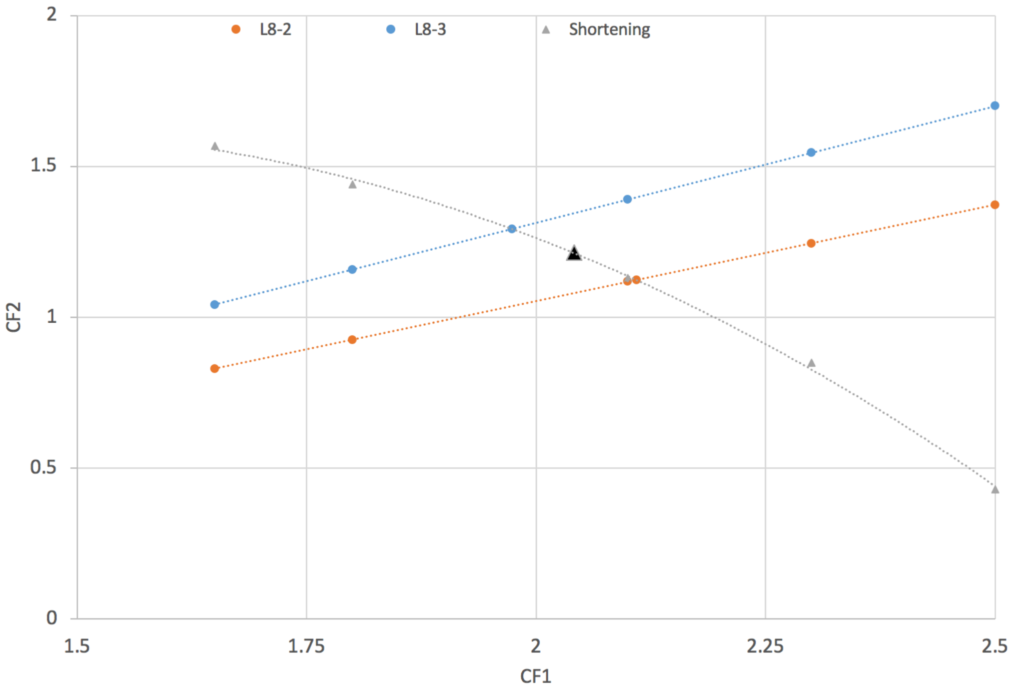

Figure D21: Optimizing CFs to the combination of shortening and layer 8 elevation profiles on the west (L8-2) and east (L8-3) sides of the syncline for one profile line at 4320 m. The Black triangle is the optimization point.

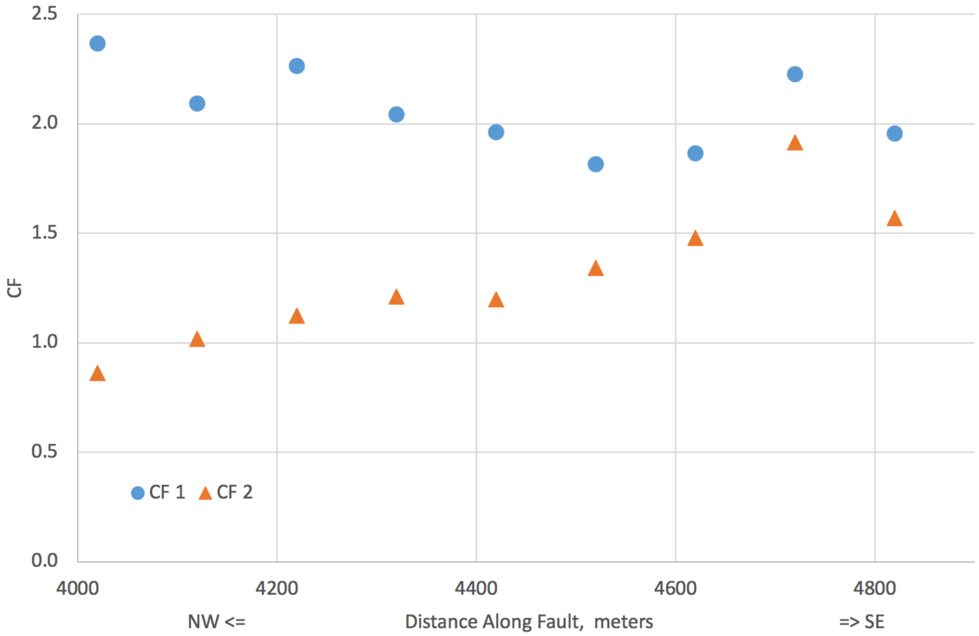

Figure D22: Coefficients obtained when optimizing each individual transect using shortening and layer 8 elevations. CF1, for oceanward facing slopes, tends to decrease going down the restraining bend, while CF2, for landward facing slopes, tends to increase.

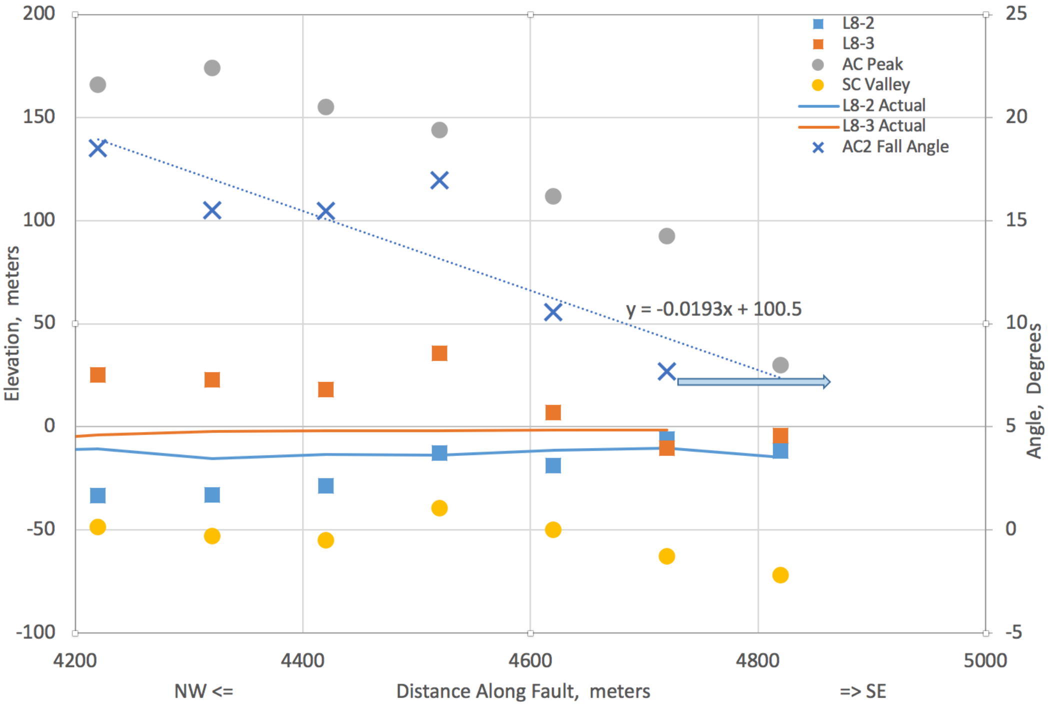

Figure D23: Results for layer 8 elevation on both sides of the syncline and along the anticline apex and the syncline valley when CFs are optimized for each individual transect. Included is the resulting bedrock angle on the east side of anticline 2 with the slope shown to be -0.0193 deg/meter.

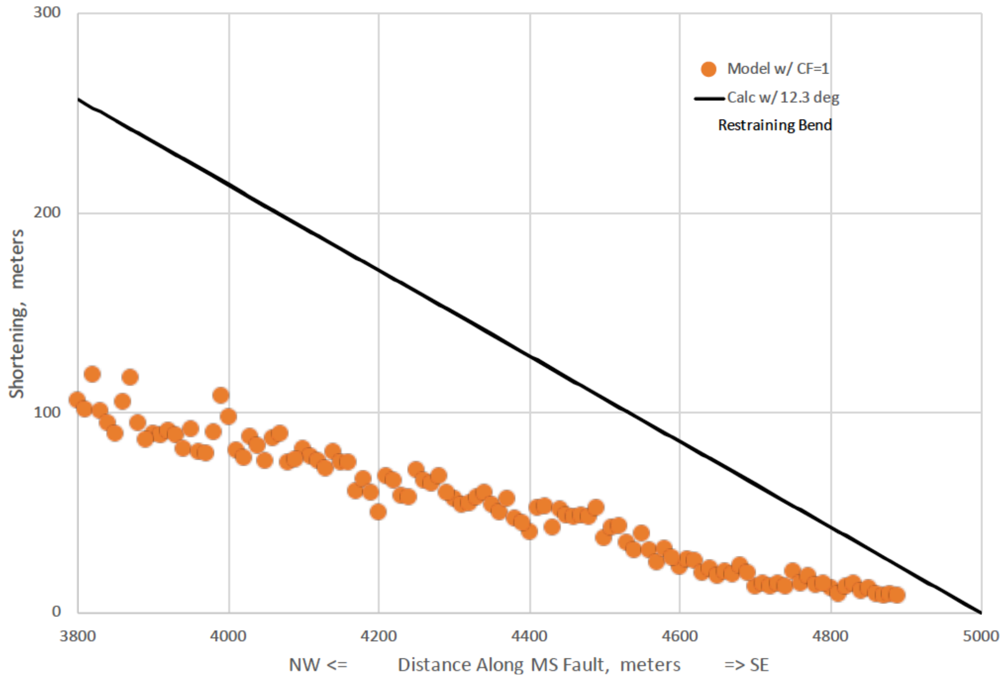

Figure D24: Shortening calculated from the model with no correction factors, (i.e. CF = 1). Measured values of shortening, orange points, are much lower than needed to accommodate the required shortening, the black line.

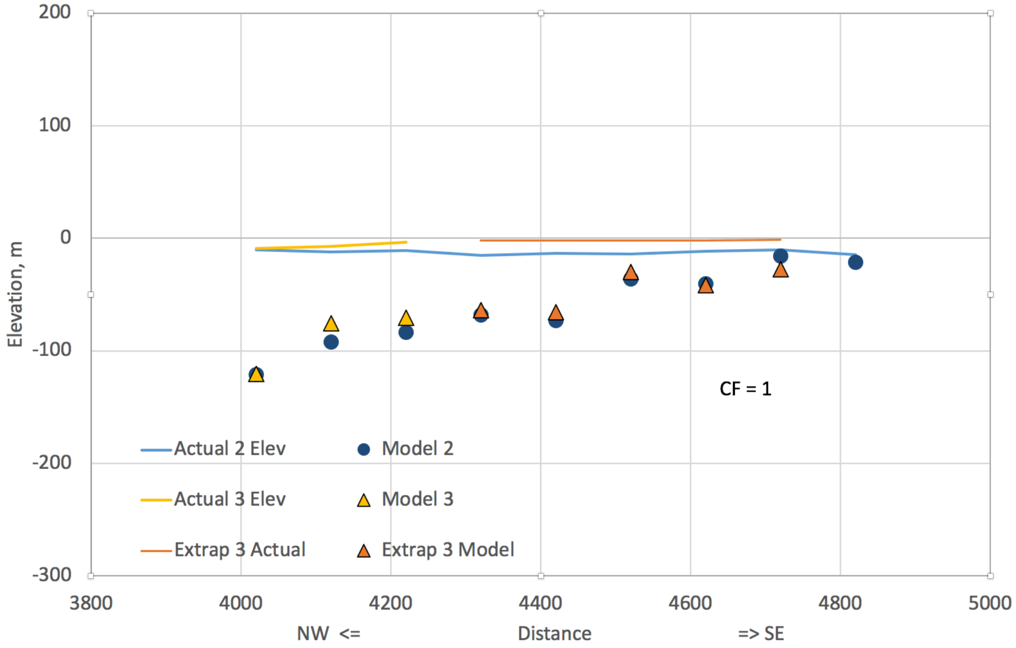

Figure D25: Layer 8 elevations calculated from the model with no correction factors, (i.e. CF=1). Solid lines are actual elevations of layer 8 where exposed, blue dots are from the model on the west side and yellow & orange triangles are on the east side of the syncline.

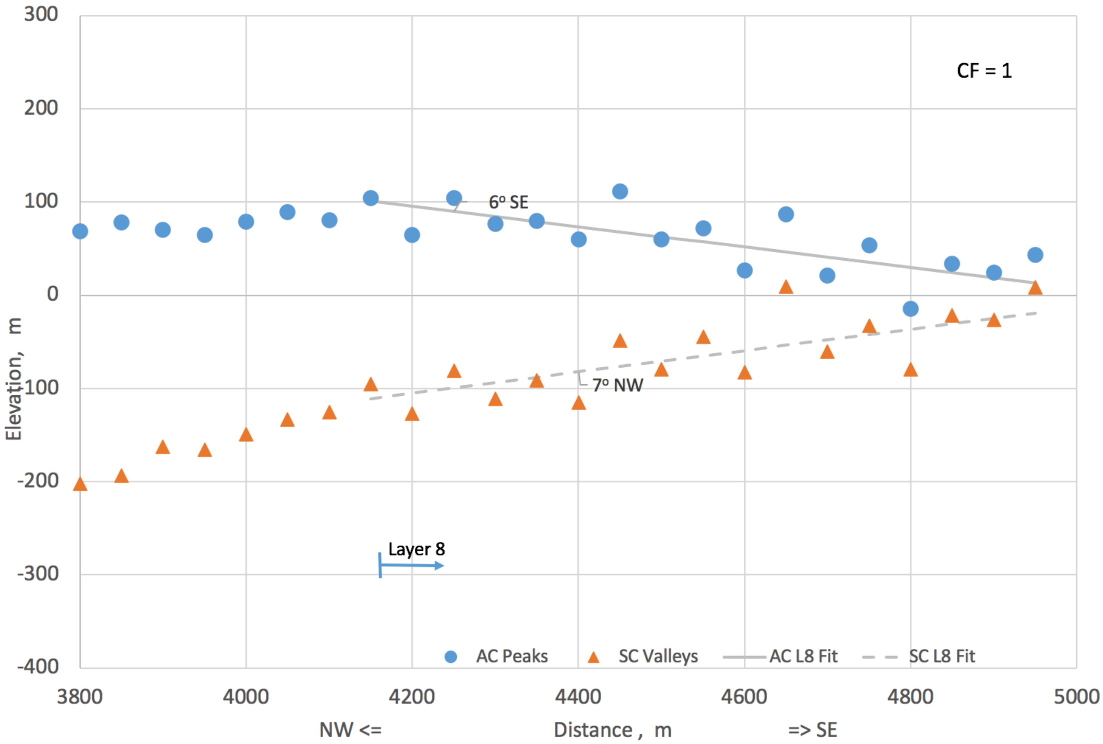

Figure D26: Anticline and Syncline Axes when using no correction factors, CF=1.

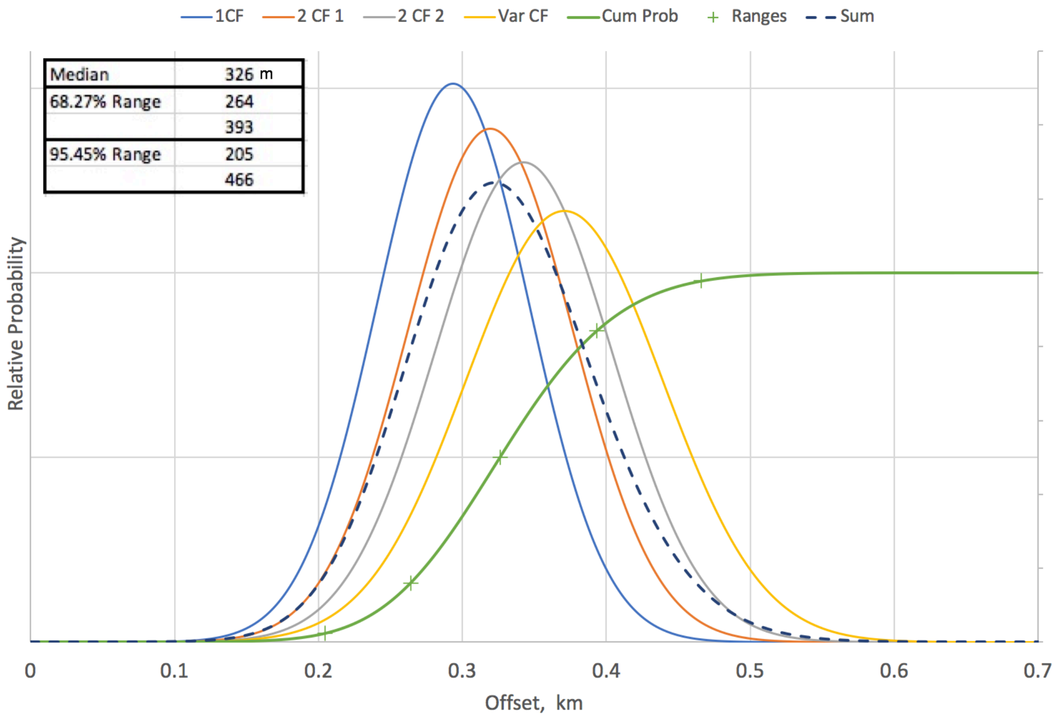

Figure D27: Offset probability density function distribution from summing results from four different folding model results listed in Table DI

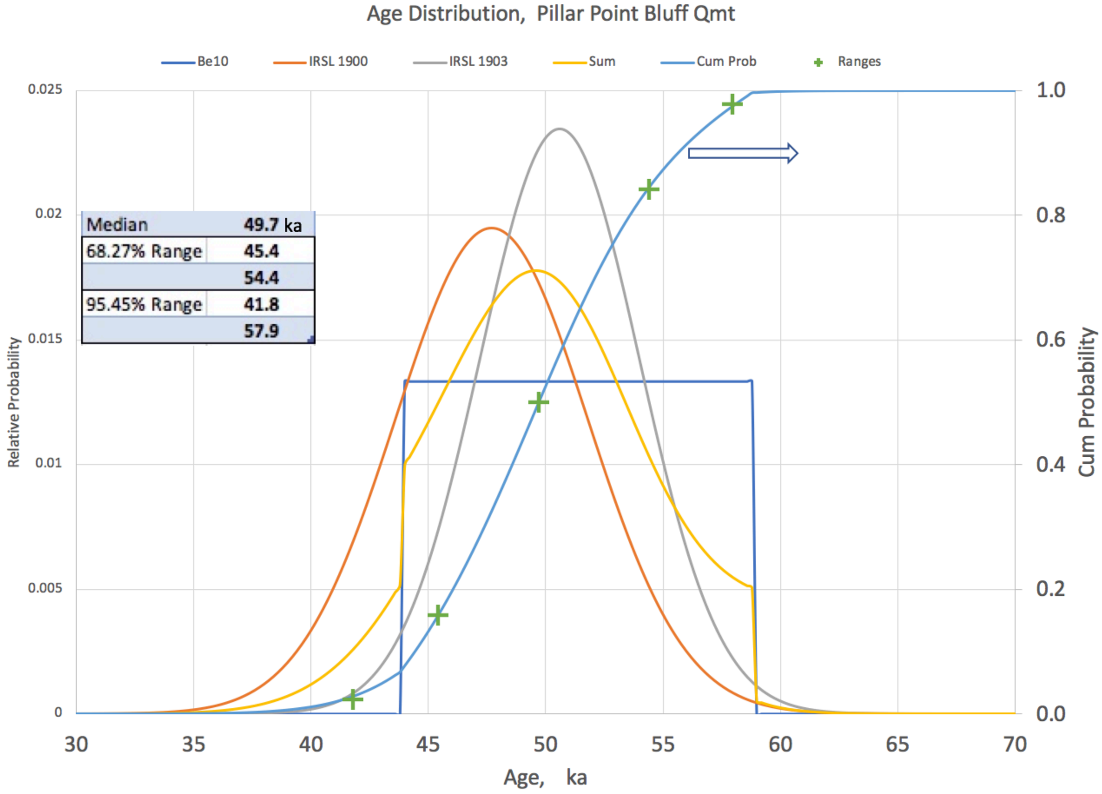

Figure D28: Age distribution function derived from a Be10 CRN depth profile, and two IRSL samples for Qmt sediments above the wavecut platform in Tp at Pillar Point Bluff.

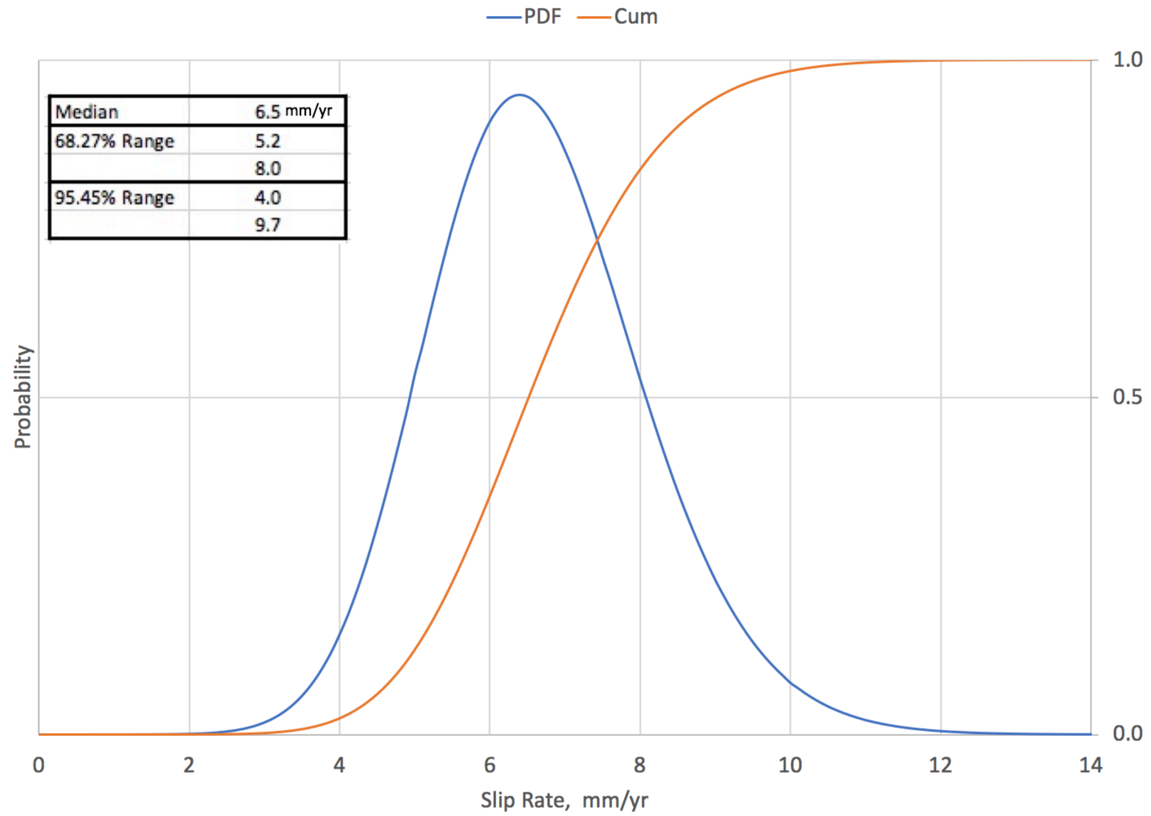

Figure D29: Probability density function for slip rate using offset density function in Figure D27 and dating density function as derived in Figure D28.

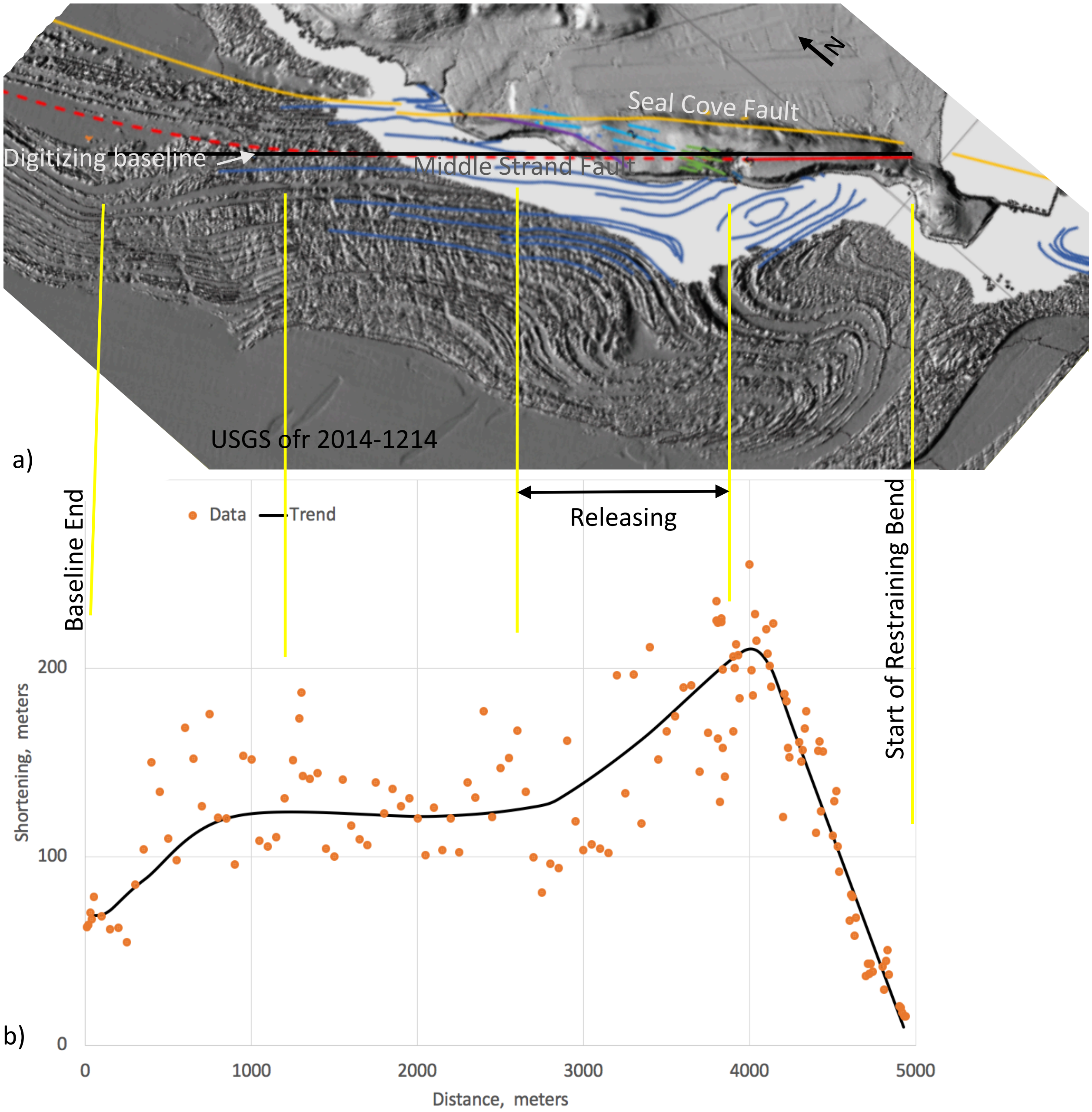

Figure D30: a) The bathymetry and lidar map from USGS 2014-1214 with additional structure and faults mapped in is aligned with b) the plot of shortening calculated by the model along the Middle Strand Fault. Pacific plate motion is from the right to the left for the calculated shortening.

Figures for Appendix E:

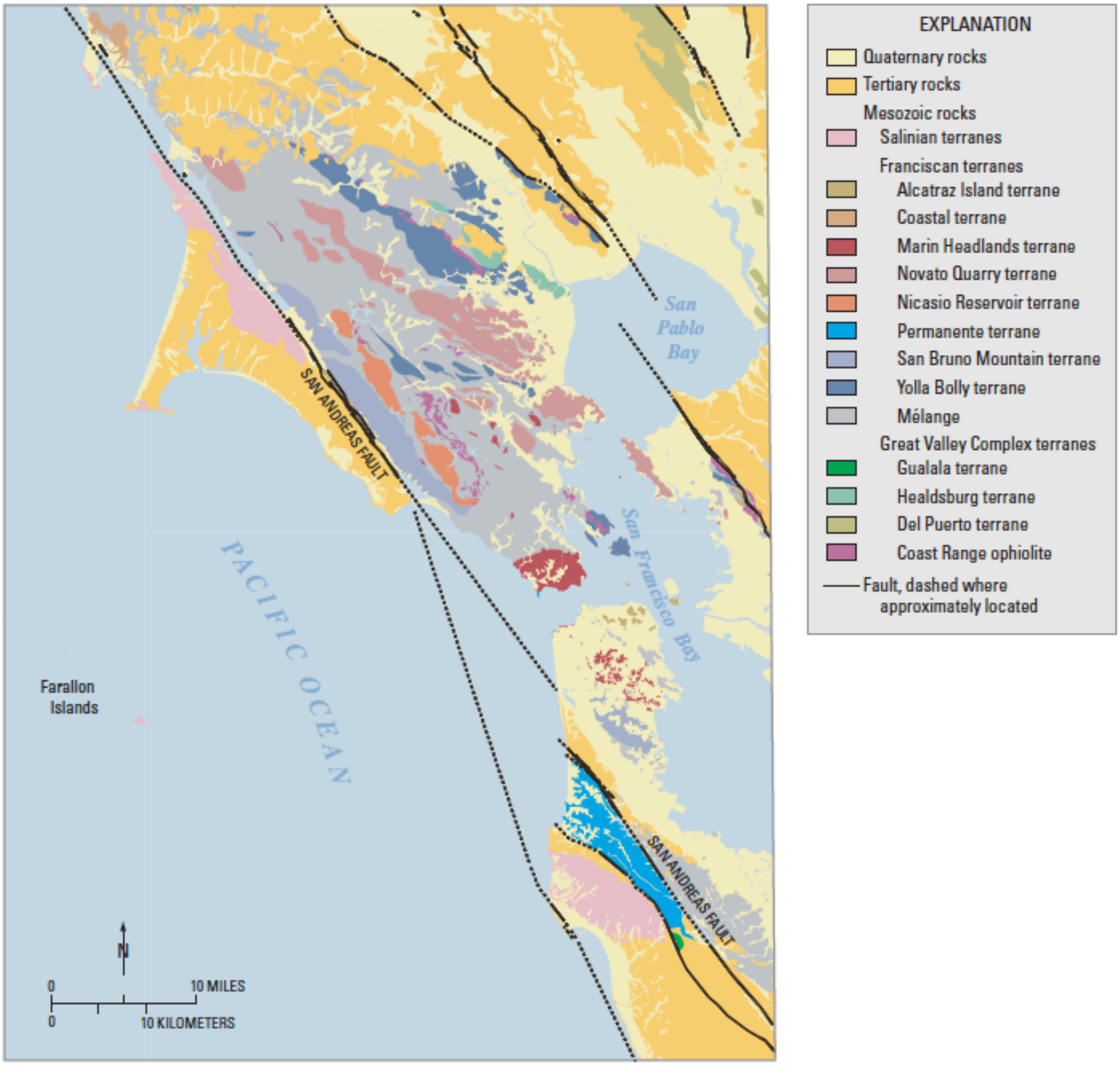

Terrane map of the San Francisco Bay region. Beneath the landscape of the bay region lie fragments of at least 17 different bedrock types that have been transported and juxtaposed by movement along faults. The major basement rock types can be ascribed to either the Franciscan terranes or the Salinian terranes. Rocks west of the San Andreas Fault are generally part of the Salinian terranes, whereas those east of the San Andreas Fault are generally part of the Franciscan terranes. These major terranes, separated by the San Andreas Fault, are composed of rock types that formed in very different geologic environments and some of which were transported long distances by tectonic motion to their present positions.

Figure E1: Figure and description from Ryan, Ross, and Graymer, USGS 037-046.

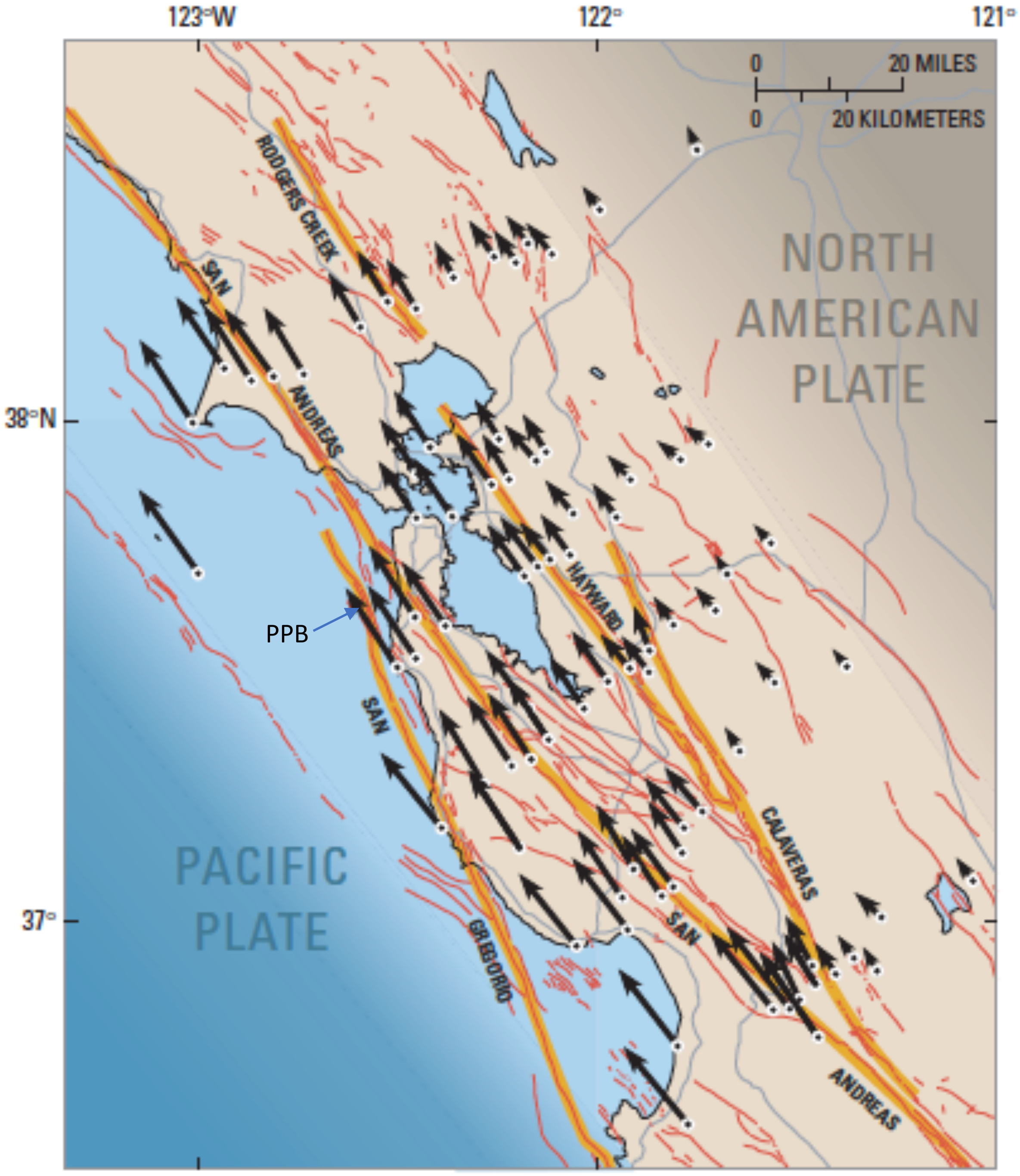

Figure E2: Another figure from Ryan, Ross, and Graymer, 037-046. Geodetic velocity vectors in SF Bay region. The vector at the PPB location has a similarly directed, but about 4 mm/yr larger amplitude, than that just inland from it. From: Page et al, 1999.

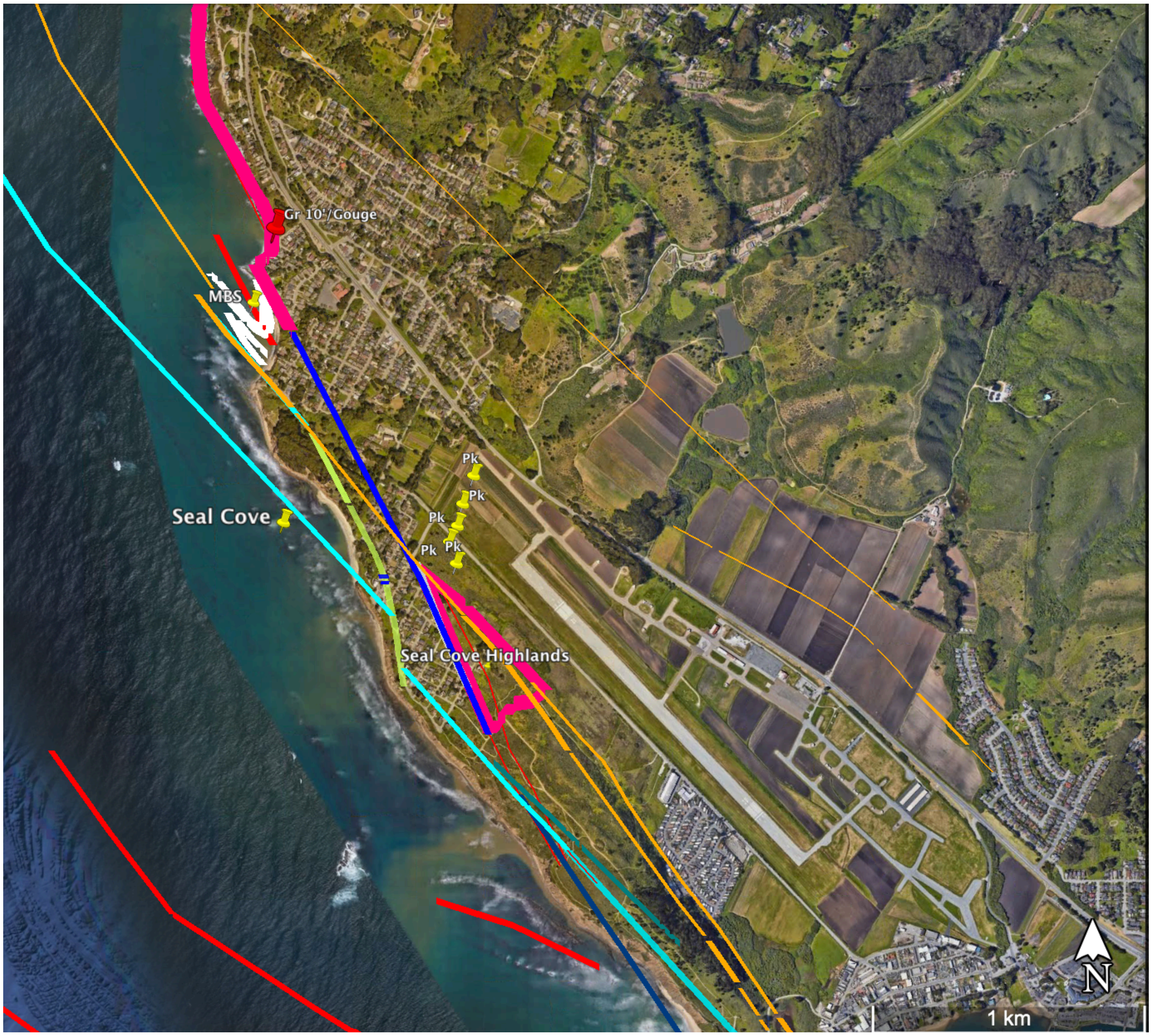

Figure E3: Granitic shoreline and known granitic bedrock in Seal Cove Highlands are outlined by wide pink lines. “Pk” Yellow markers are profile peaks along HMB terrace. Heavy dark blue line is possible western edge of granitic bedrock. MBS is Moss Beach Syncline where the red line is the fold axis which is subparallel to possible granite bedrock edge.

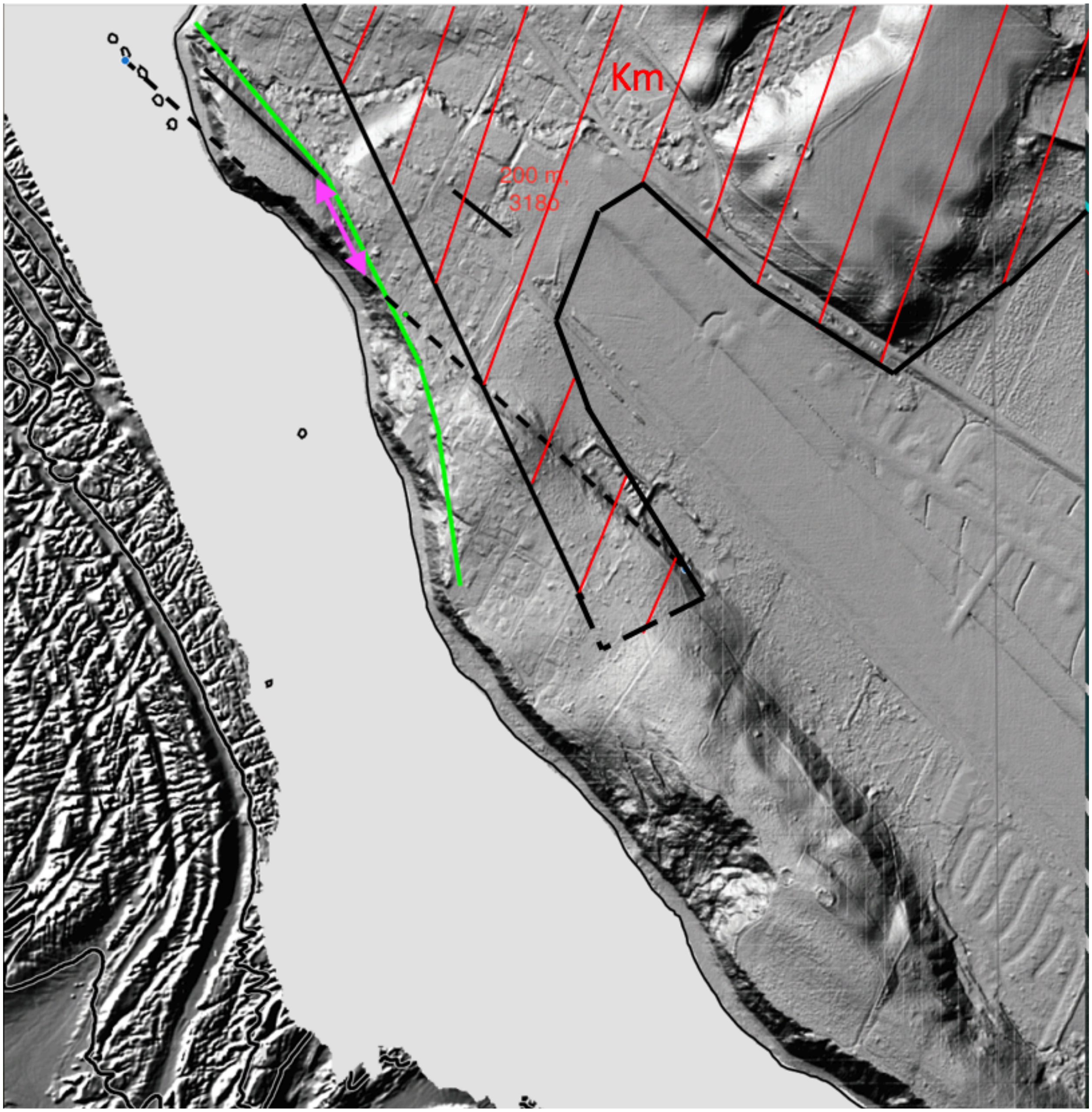

Figure E4: Estimated extent of granitic bedrock throughout Seal Cove including where it protrudes into PPB, red hatched area with black outline. The green line is the Distillery Fault.

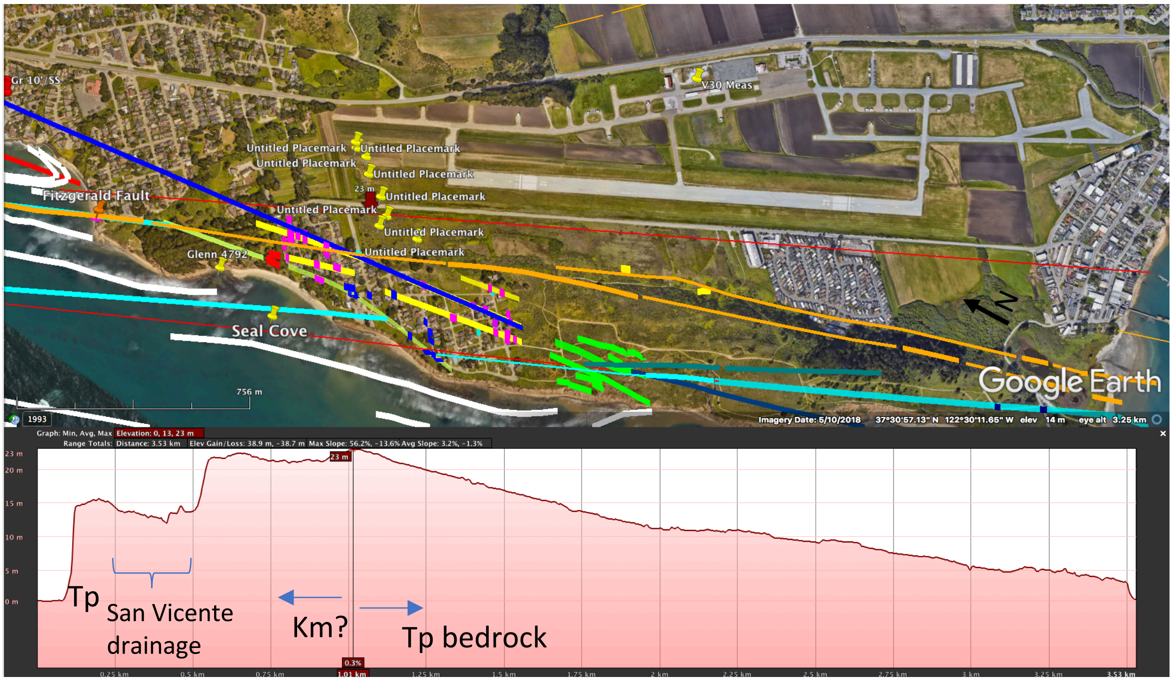

Figure E5: Google Earth elevation profile across Half Moon Bay terrace, parallel Airport Rd from Half Moon Bay to near the Moss Beach Syncline, red line in the map. The line of yellow markers on the map show the location of the slope break across the terrace. The airport runway azimuth is about 317°. The heavy blue line is the continuation of Consultant's Fault Trend 2 to the shoreline granite outcrop.

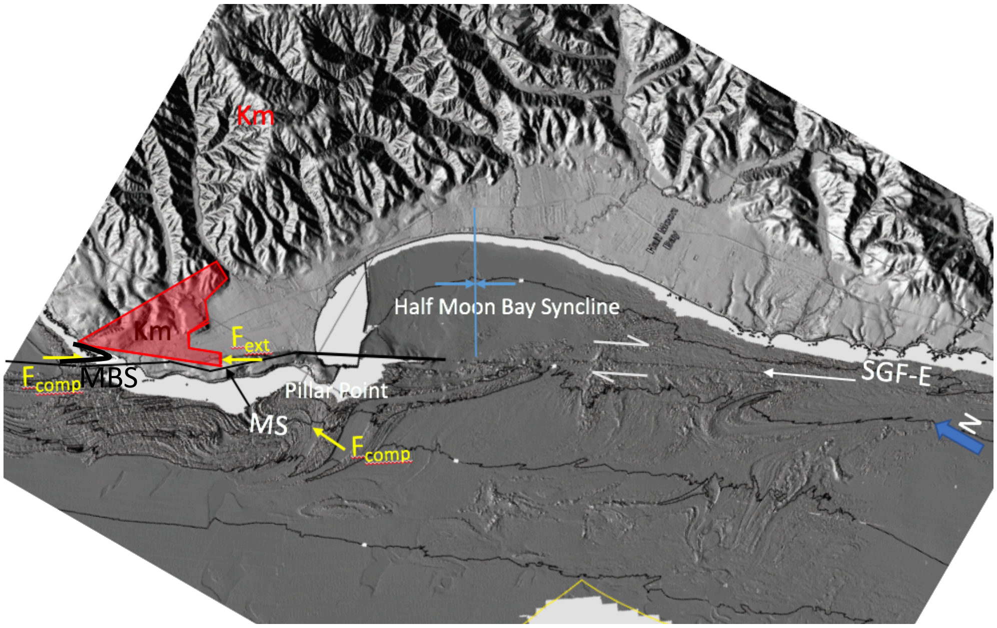

Figure E6: Schematic showing how a proposed Km spur protruding into PPB produces a restraining bend that in turn produces compressive forces causing folding west of Pillar Point Bluff, an extensive force producing the syncline across Half Moon Bay, and a compressive force producing Moss Beach Syncline, MBS.

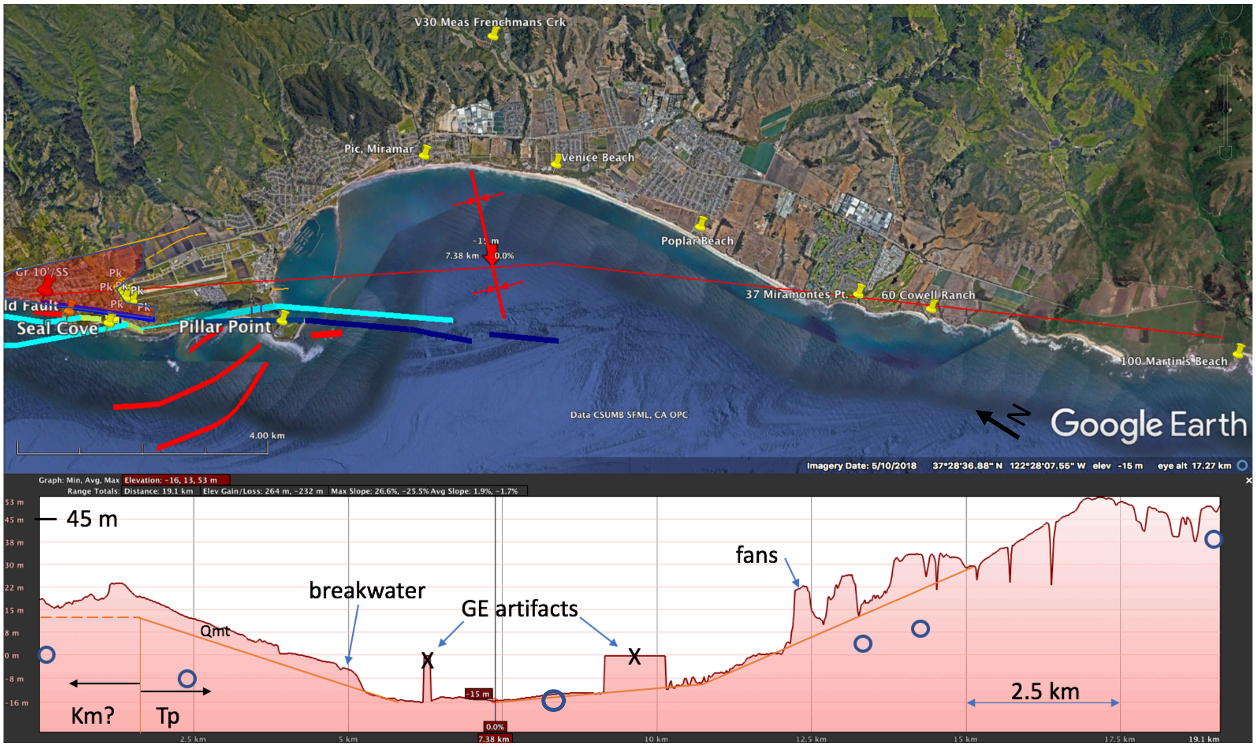

Figure E7: GE surface profile across HMB, (along red line in map), showing synclinal structure ending at a proposed Km bedrock on left, (red shaded area in map plus its continuation into the unshaded foothills). Blue circles in profile are Purisima elevations.

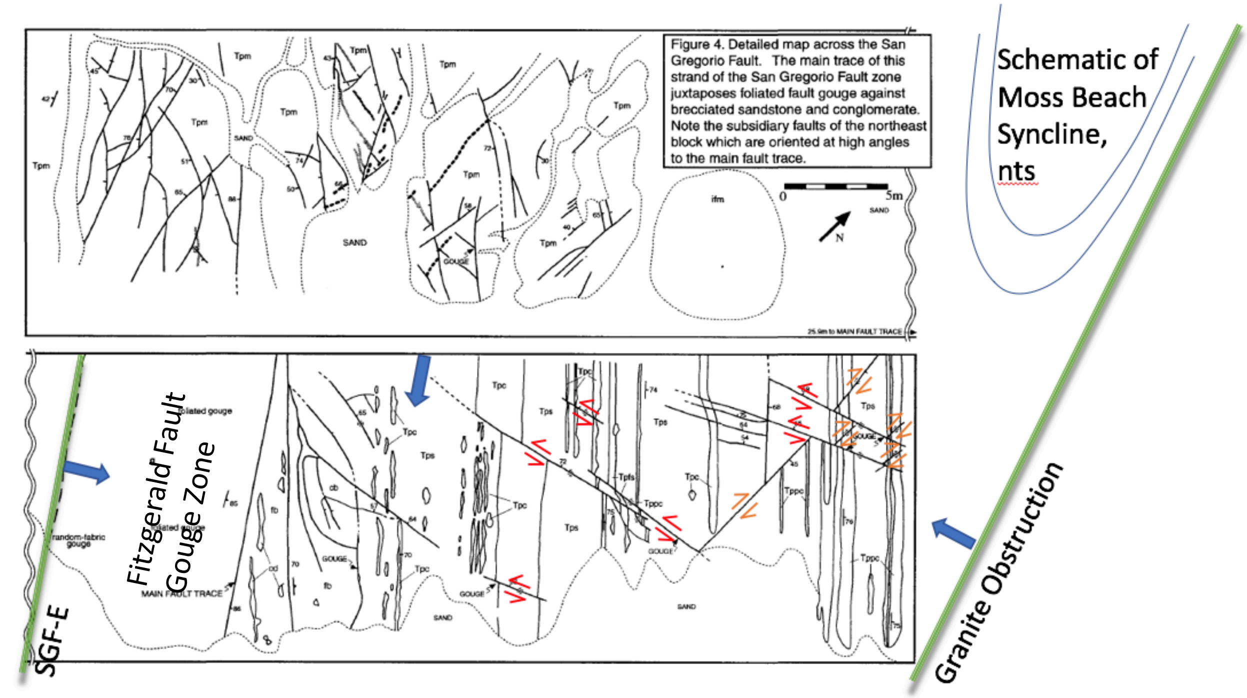
Figure 4. Detailed map across the San Gregorio Fault. The main trace of this strand of the San Gregorio Fault zone juxtaposes foliated fault gouge against brecciated sandstone and conglomerate. Note the subsidiary faults of the northeast block which are oriented at high angles to the main fault trace.
Schematic of Moss Beach Syncline, nts
Tpm
SAND
GOUGE
ifm
0
5m
N
25.9m to MAIN FAULT TRACE
Fitzgerald Fault Gouge Zone
foliated gouge
random-fabric gouge
MAIN FAULT TRACE
SGF-E
Tpc
Tps
Tpfs
Tppc
Granite Obstruction

Figure E8: Schematic of Moss Beach Syncline and environment. Copied and modified from Lohr et al, 2009. Sinistral offsets in red and dextral offsets in orange, result from the SE directed plate and confinement between the granite wall and the Fitzgerald Fault (SGF-E).

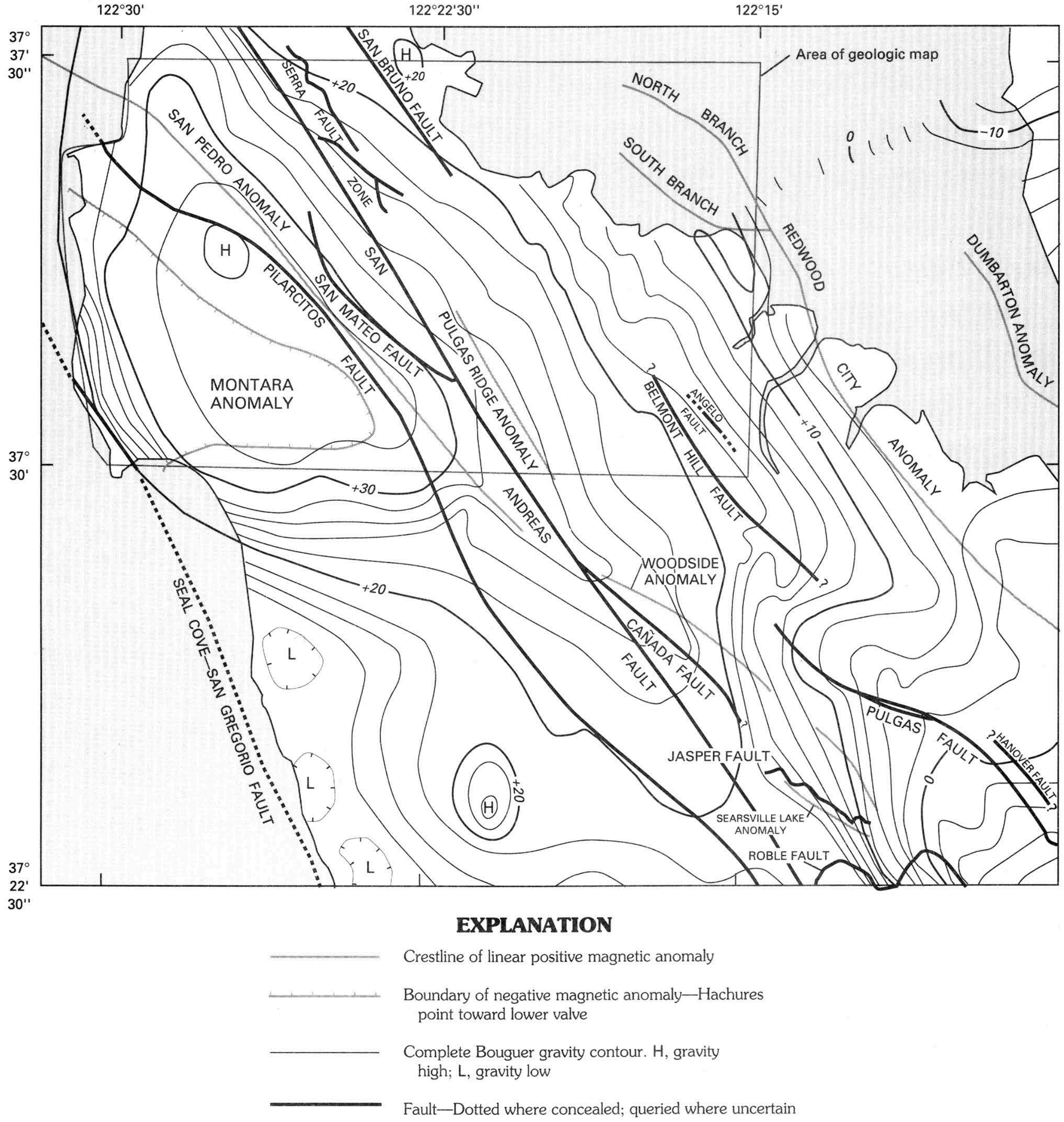

Complete Bouguer gravity contours, aeromagnetic anomalies, and principal faults in the study area and vicinity. Gravity data from Robbins and others (1982); contour interval 2 mGals. Aeromagnetic data from Brabb and Hanna (1981) and V.E. Langenheim and R.F. Sikora (unpub. data, 1991).

Figure E9. Gravity and magnetic map from Pampeyan, 1994. Gravity is elevated and steeply declining approaching PPB and indicates a possible slight bulge near northern end of PPB.

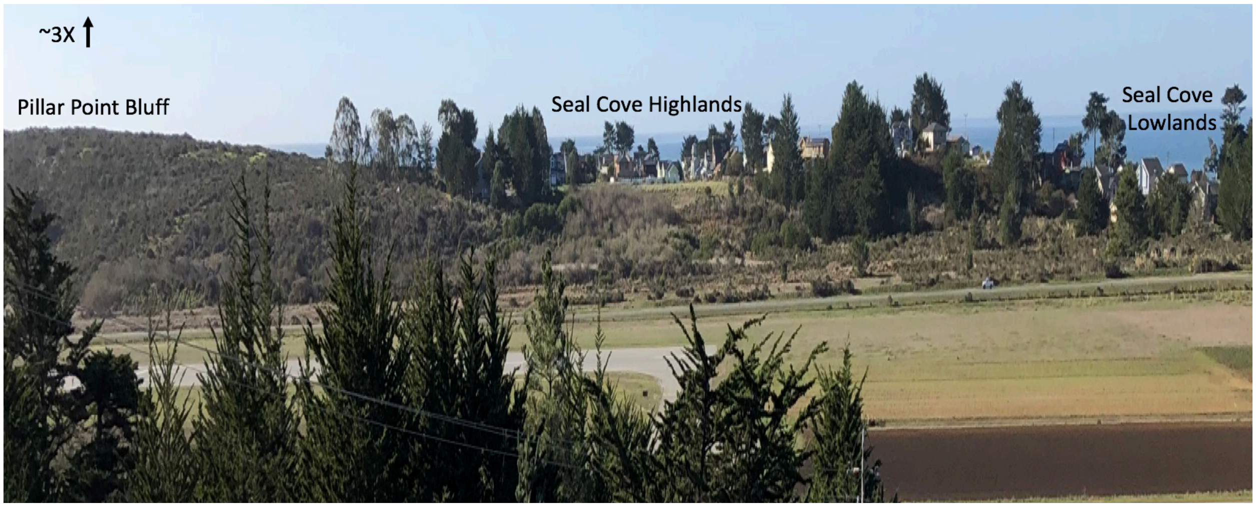

Figure E10: View of PPB, Highlands, and Lowlands looking southwest. View vertically expanded about 3X. Pillar Point Bluff has Purisima bedrock, Seal Cove Highlands has granitic bedrock, and Seal Cove Lowlands is assigned as a pull-apart basin.

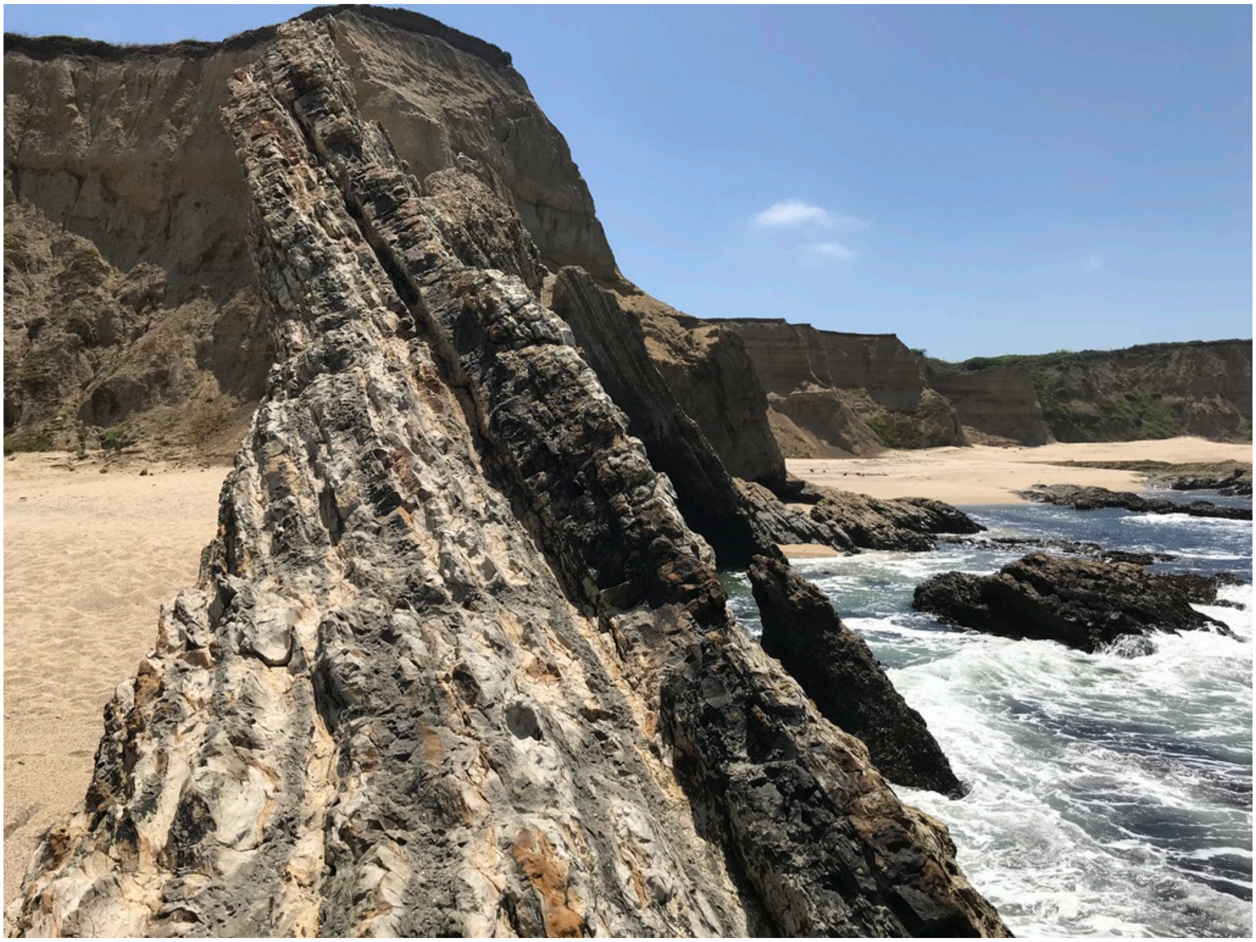

Figure E11: Tilted bedrock fault in surf zone at Cowell Ranch that probably results from extension. Striking 105°, dip 50° S.

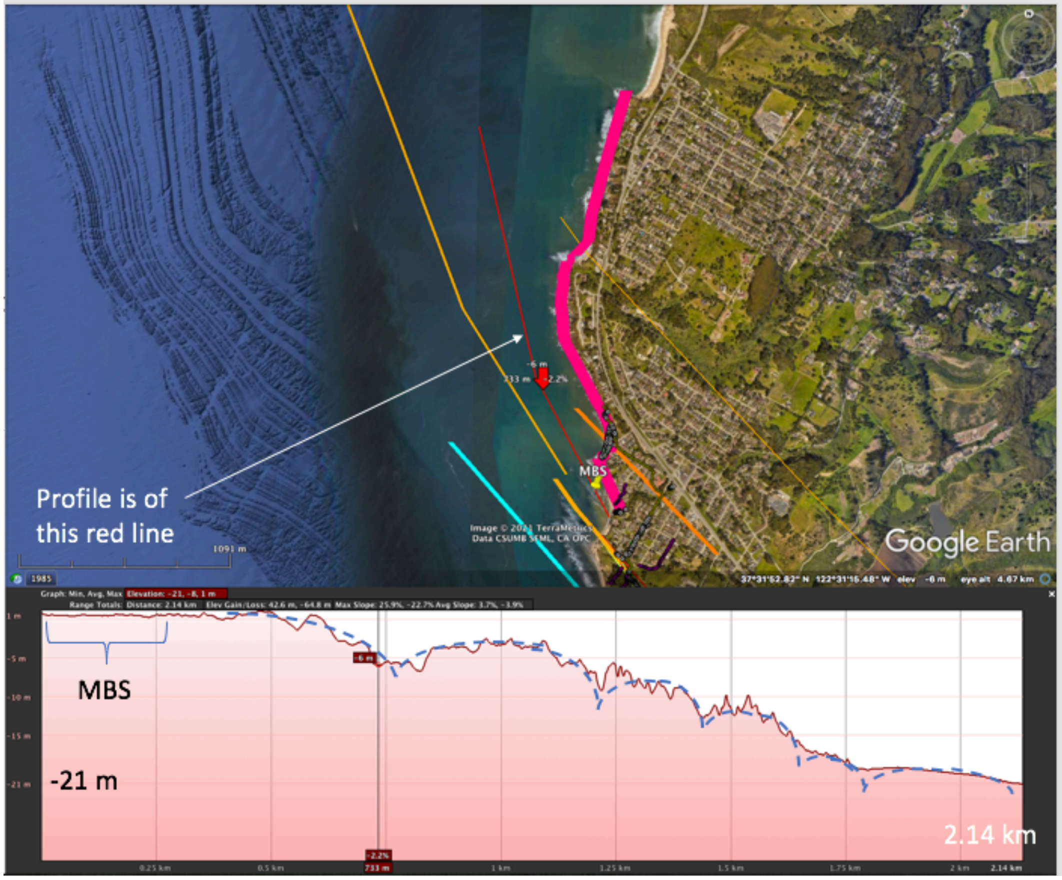
Profile is of this red line
MBS
1091 m
1985
Image © 2021 TerraMetrics Data CSUMB SFML, CA OPC
Google Earth
37°31'52.82" N 122°31'16.48" W elev -6 m eye alt 4.67 km
Graph: Min, Avg, Max Elevation: -21, -8, 1 m
Range Totals: Distance: 2.14 km Elev Gain/Loss: 42.6 m, -64.8 m Max Slope: 25.9%, -22.7% Avg Slope: 3.7%, -3.9%
1 m
-5 m
-10 m
-15 m
-21 m
-6 m
MBS
-21 m
2.14 km
0.25 km
0.5 km
-2.2%
733 m
1 km
1.25 km
1.5 km
1.75 km
2 km
2.14 km

Figure E12: Near-shore underwater profile going NNW from MBS. Profile suggests lobate folds (dashed blue line) characteristic of compression folding of thin sedimentary rock layers.

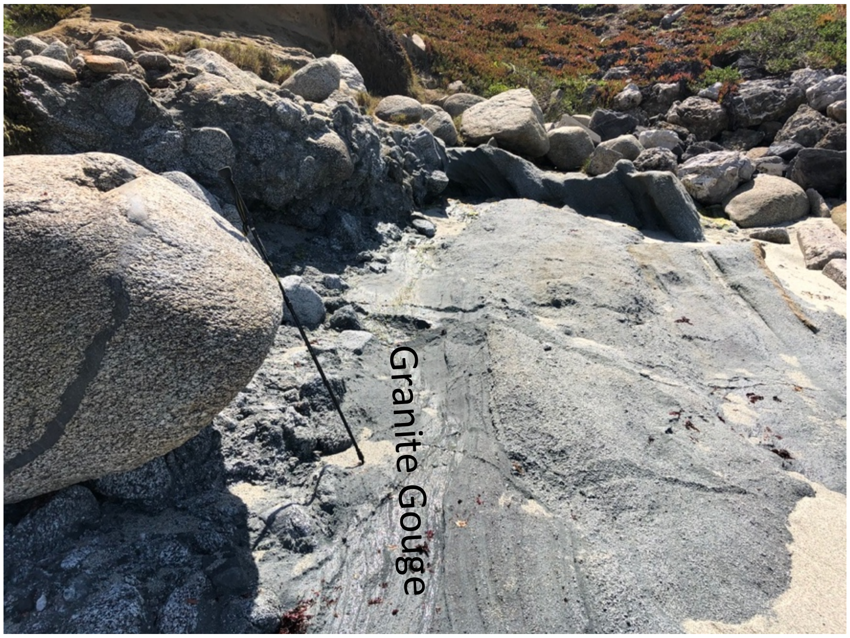

Figure E13: Granitic outcrop at beach north of Wienke Way in Moss Beach at north end of Figure 29 showing apparent striated fault gouge in granite bedrock.

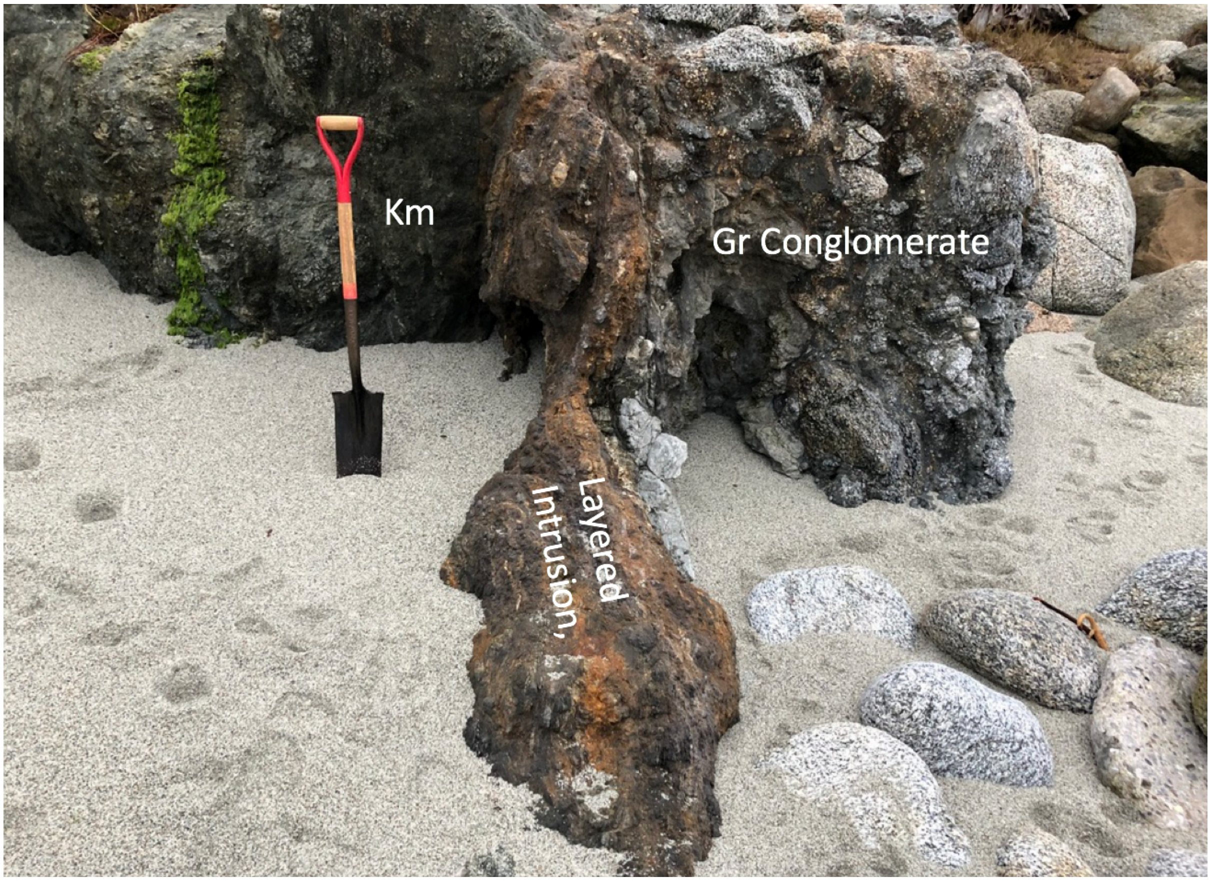

Figure E14: Montara granodiorite on left with a layered intrusive next to a granitic conglomerate.

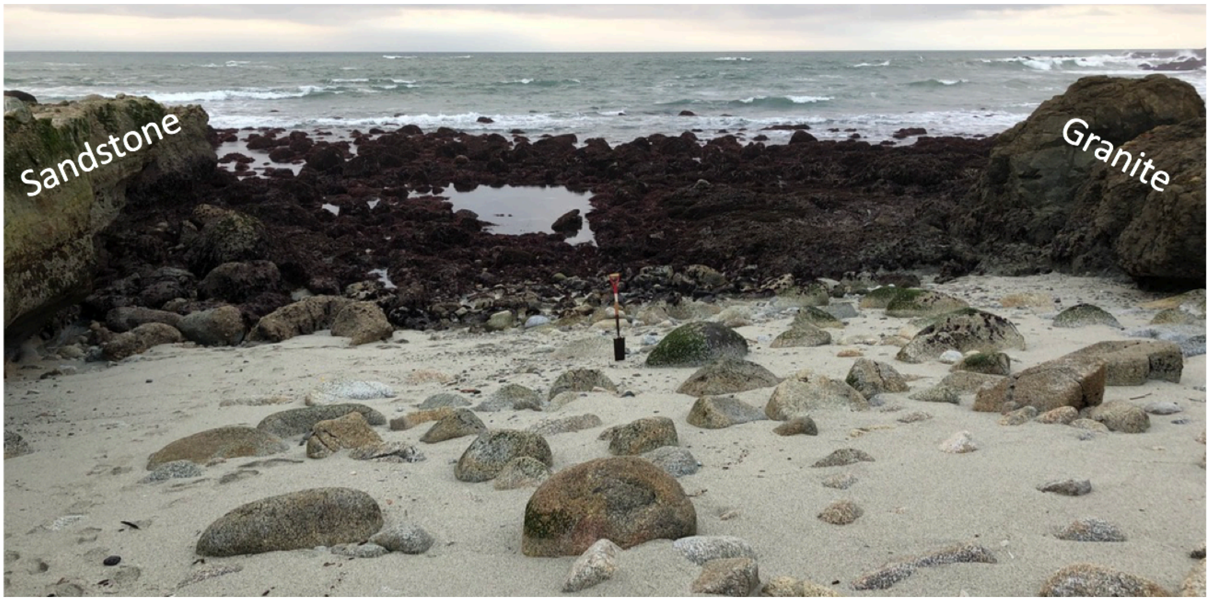

Figure E15: North Point Cove looking north with sandstone, presumably Tp, on left (west) and granite, presumably Km, on right. The main contact between the two passes through this cove and has been eroded. MBS lies adjacent to the west of this cove.

Figures for Appendix F:

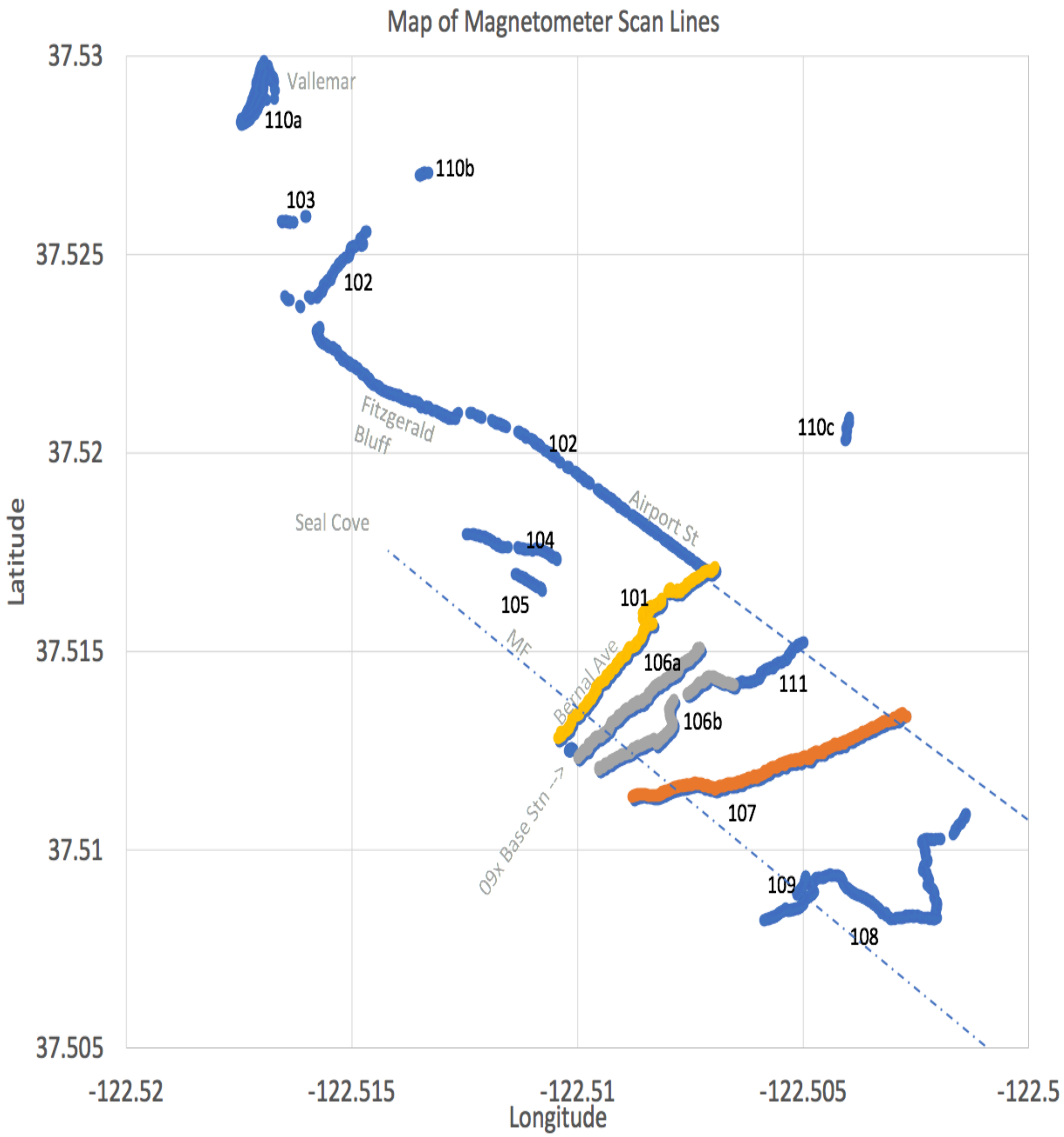

Figure F1: Map of magnetometer scans on Pillar Point Bluff and in Moss Beach. Line numbers indicate individual scans referenced in subsequent figures.

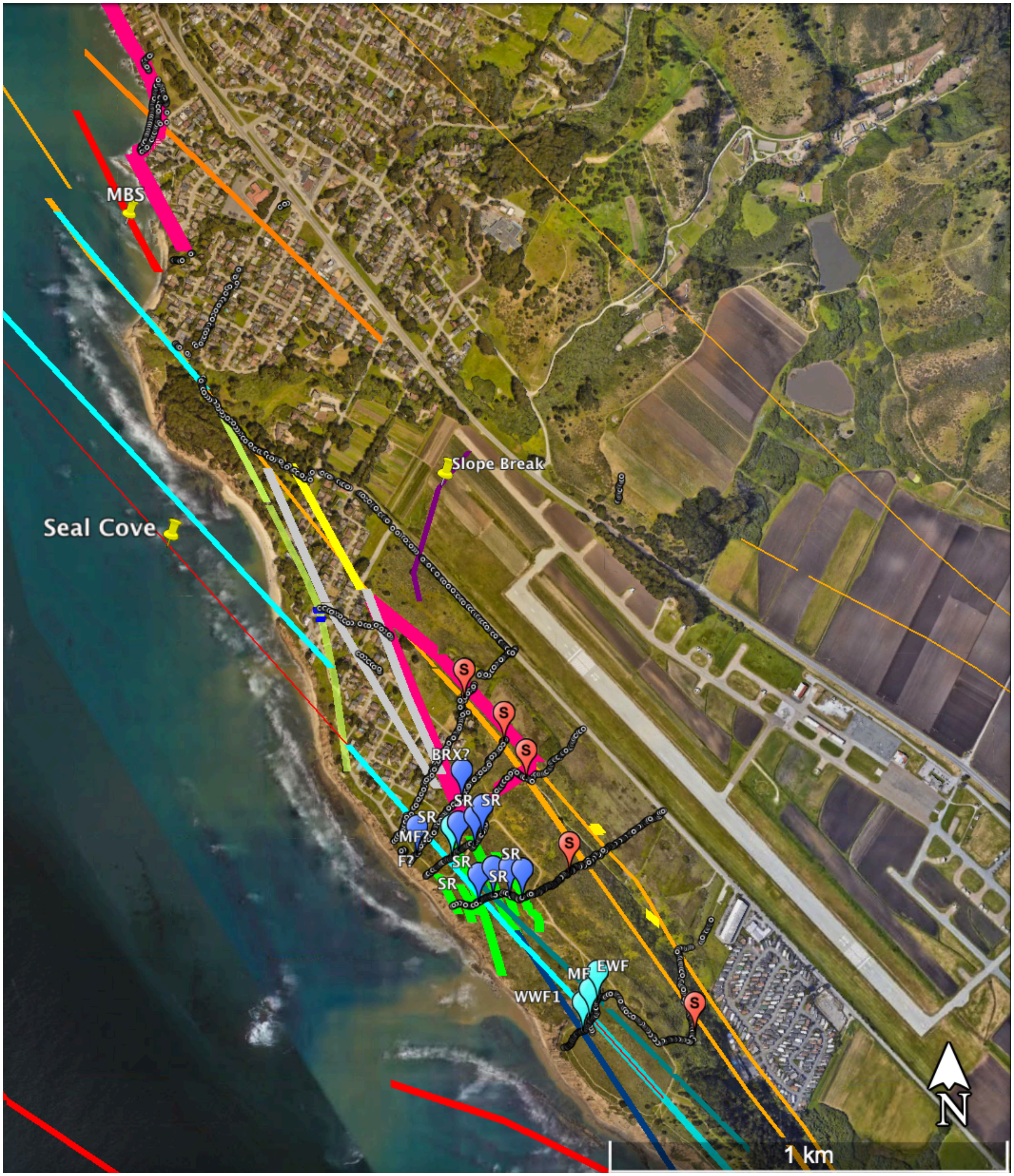

Figure F2: Google Earth image showing Magnetometer scans by small white in black circles. Markers indicate features identified in Figure F3.

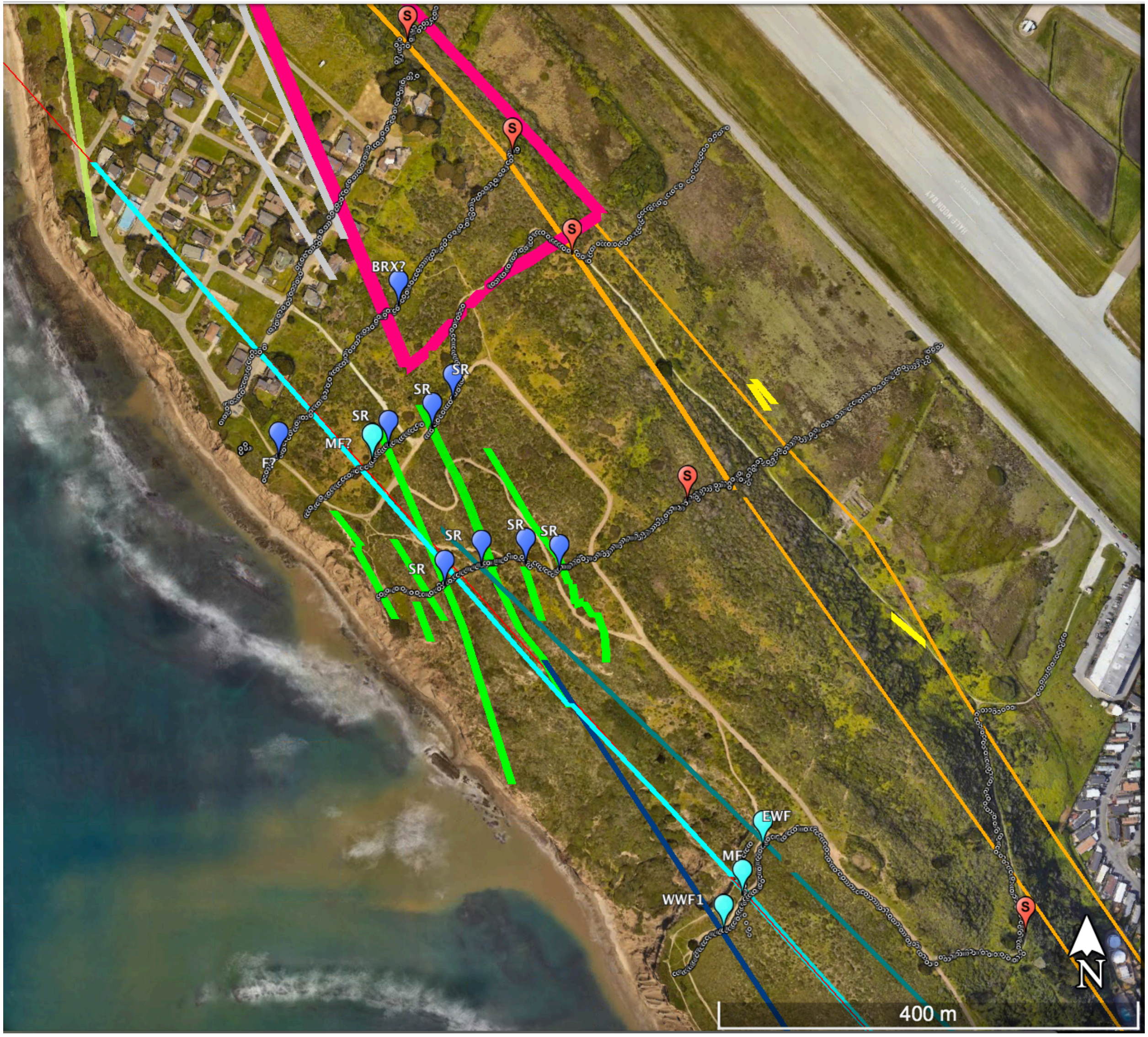

Figure F3: Google Earth expanded view of faults identified on magnetic scans on Pillar Point Bluff. Small gray circles trace magnetic scan paths and tear-drop markers identify peaks in magnetic anomaly. EWF, MF, and WWF1 align with exposed faults in headwall of landslide basin, SR align with faults called “spreading ridges”, “BRX?” is possible transition between bedrocks, red S identify scarp top anomaly peaks that are interpreted as dip slip faults.

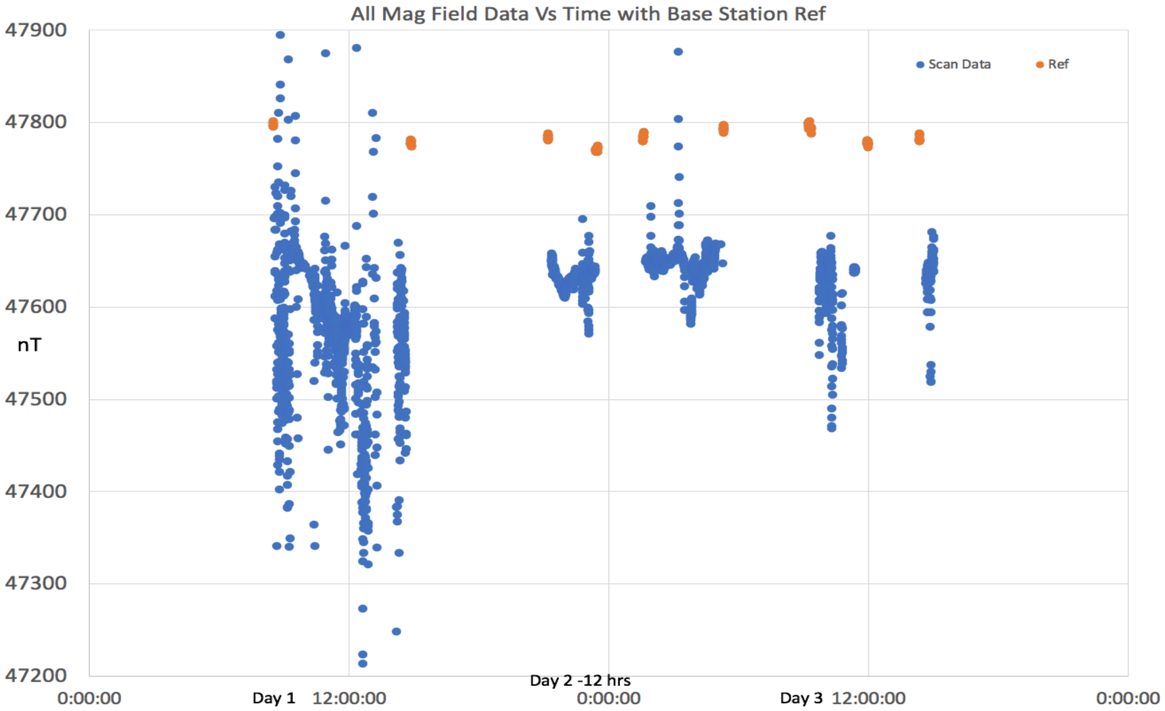

Figure F4: Time sequence of all Scans including base station reference data.

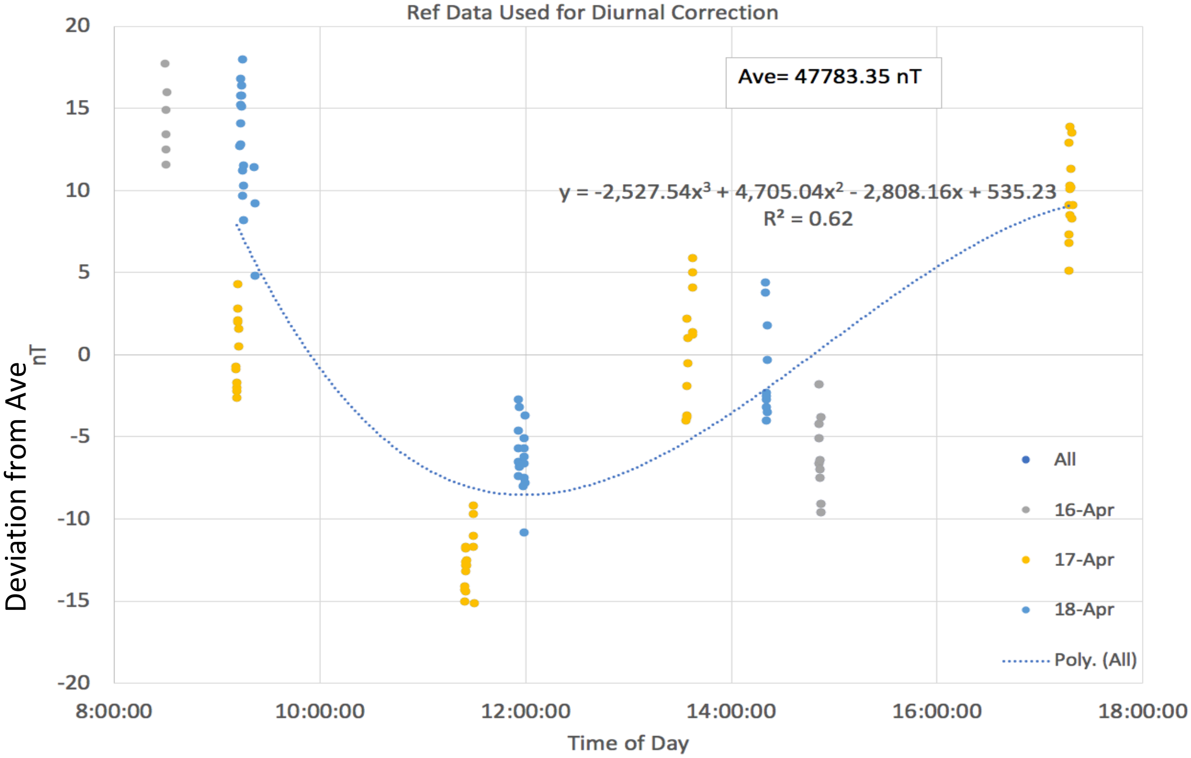

Figure F5: Base Station reference data over three days with single equation for diurnal correction of magnetic amplitudes.

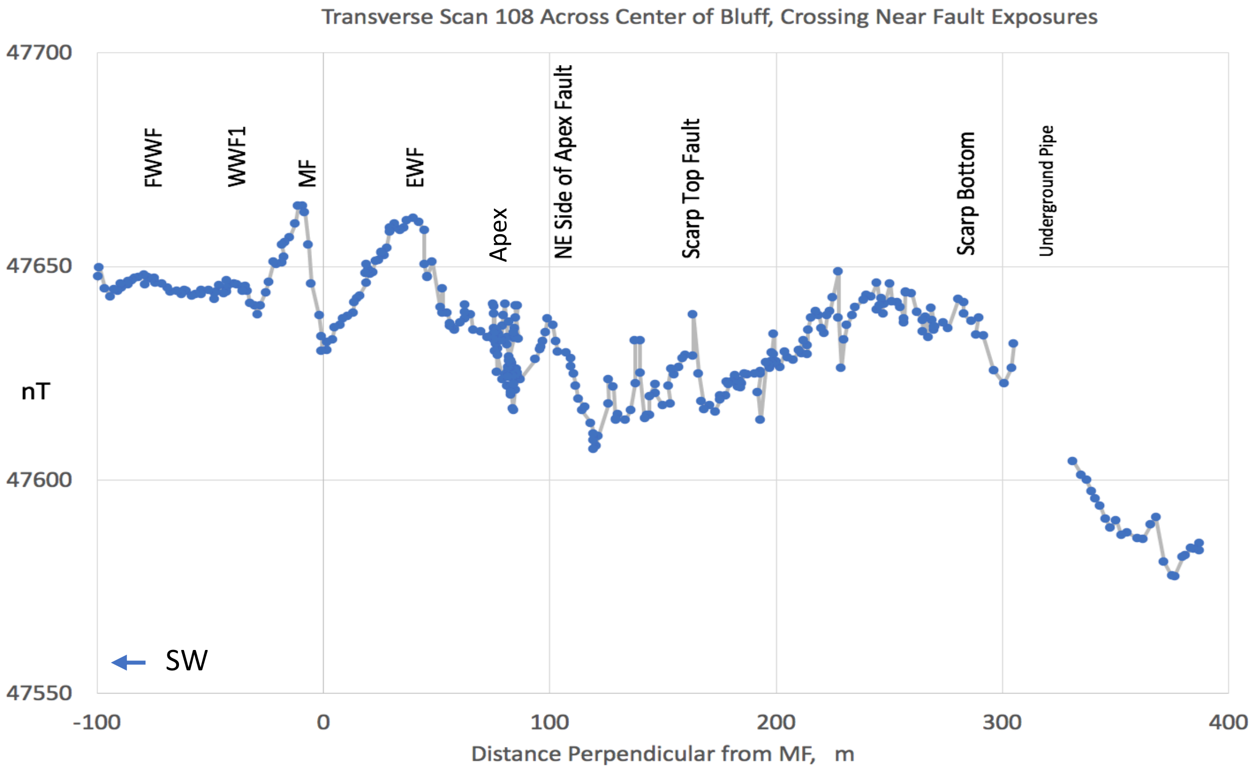

Figure F6: Transverse scan 108 crossing PPB just southeast of fault exposures.

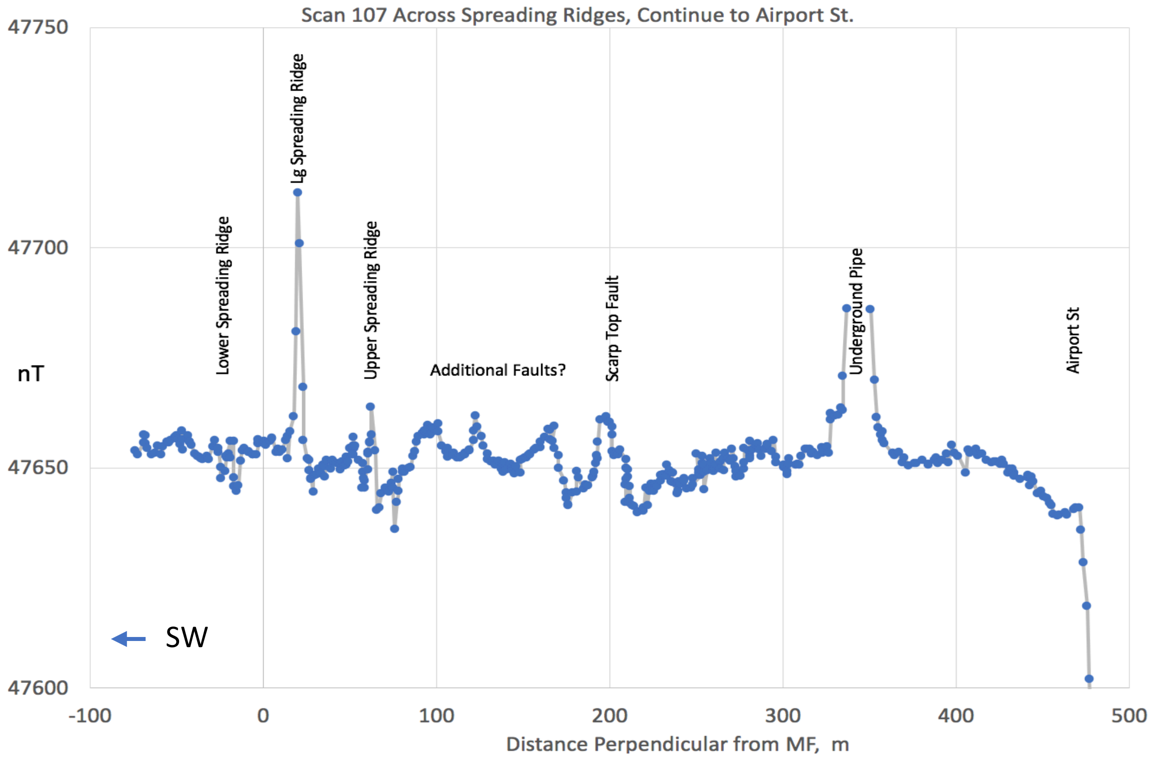

Figure F7: Transverse scan 107 across spreading ridges on Pillar Point Bluff continuing on to Airport St.

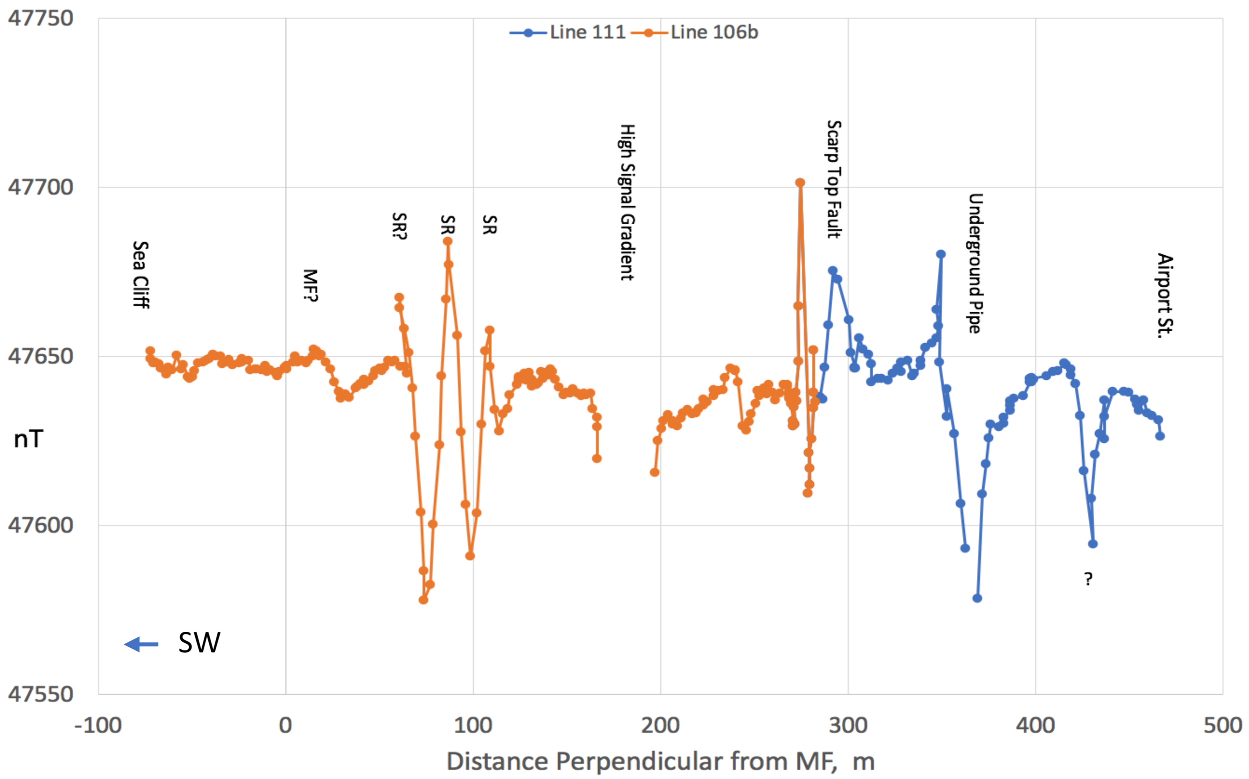

Figure F8: Transverse scans 106b and 111, south of 106a, partly along foot path.

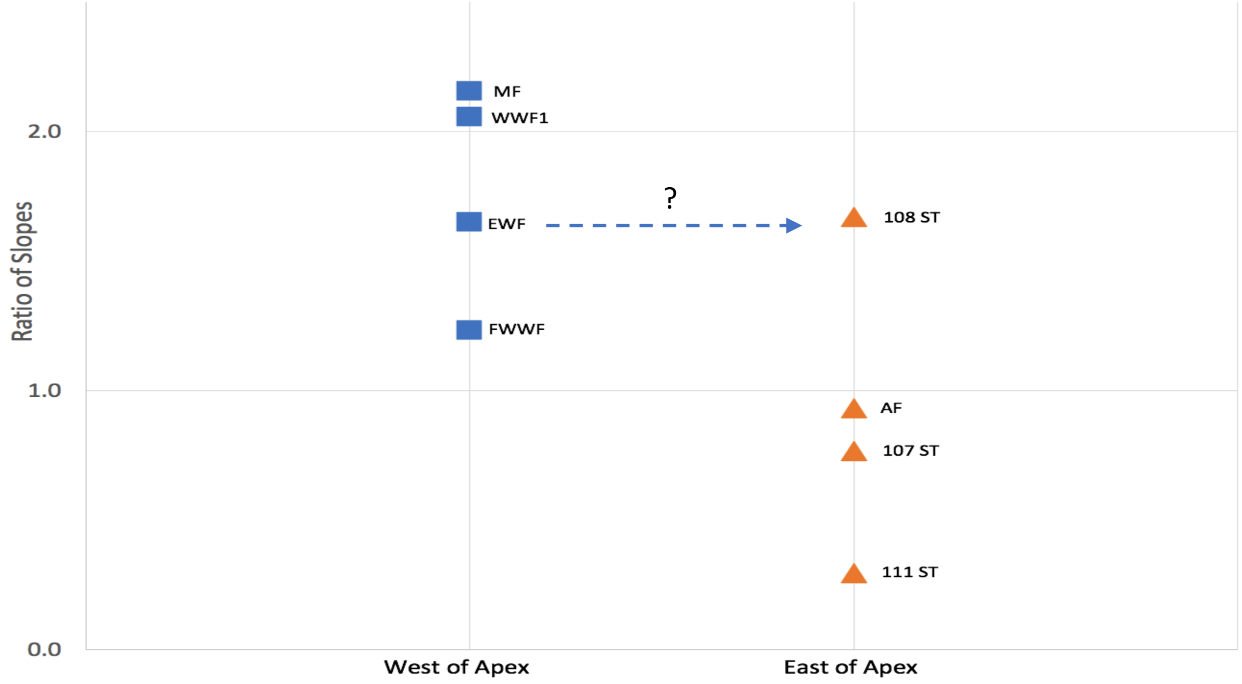

Figure F9a: Asymmetry of fault profiles (Ratio of East side slope/West side slope). Comparing faults west of Apex (strike-slip) to those on east side (dip-slip?).

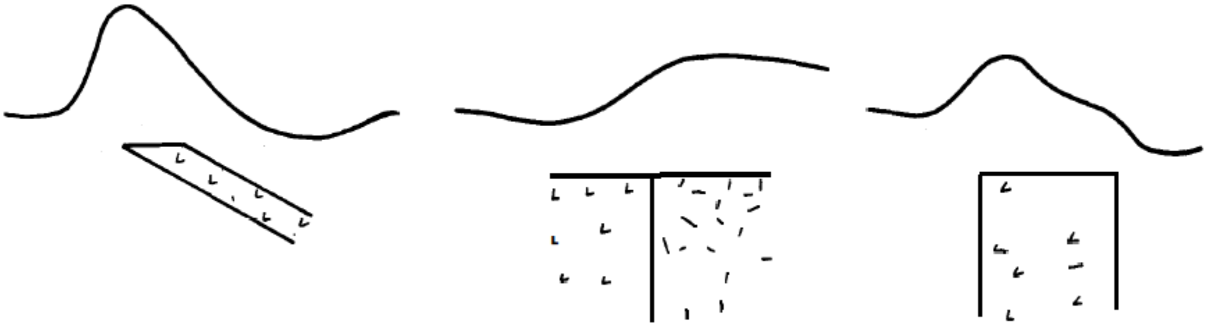

Figure F9b: Typical anomalies for simple geologic models, Figure copied from Breiner, 1999. Left figure may be typical for dip-slip fault on SCF. Right figure is representative of gouge in strike-slip fault. Center may be expected behavior at a granite to sandstone bedrock transition, all depend on orientation wrt earth's field and here assumes a right to left component in plane of page.

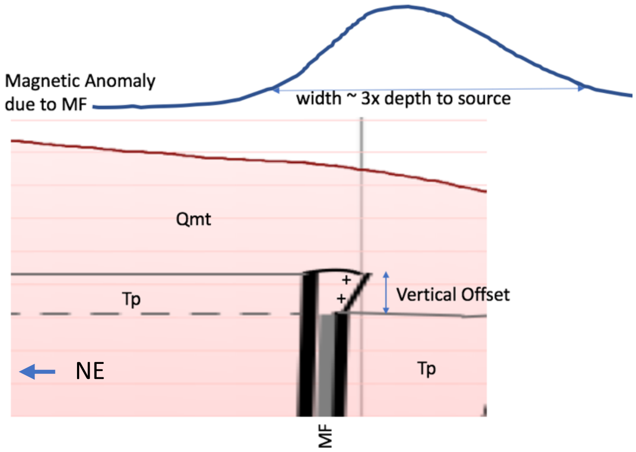

F9c:

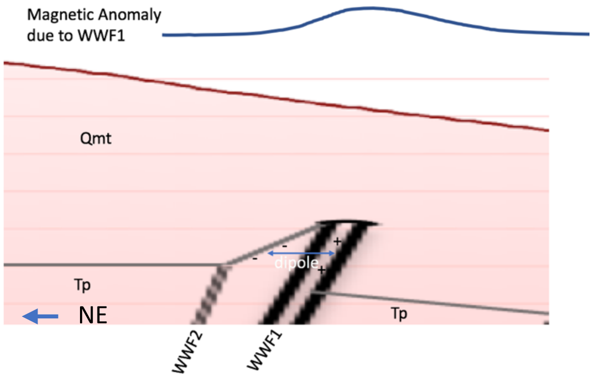

F9d:

Figure F9c: Schematic of magnetic arrangement at MF. View is looking southeast; Vertical offset appears responsible for magnetic anomaly above the MF fault. Earth's magnetic field is roughly in the plane of the figure.

Figure F9d: A dipole contribution likely causes the lower anomaly above WWF1.

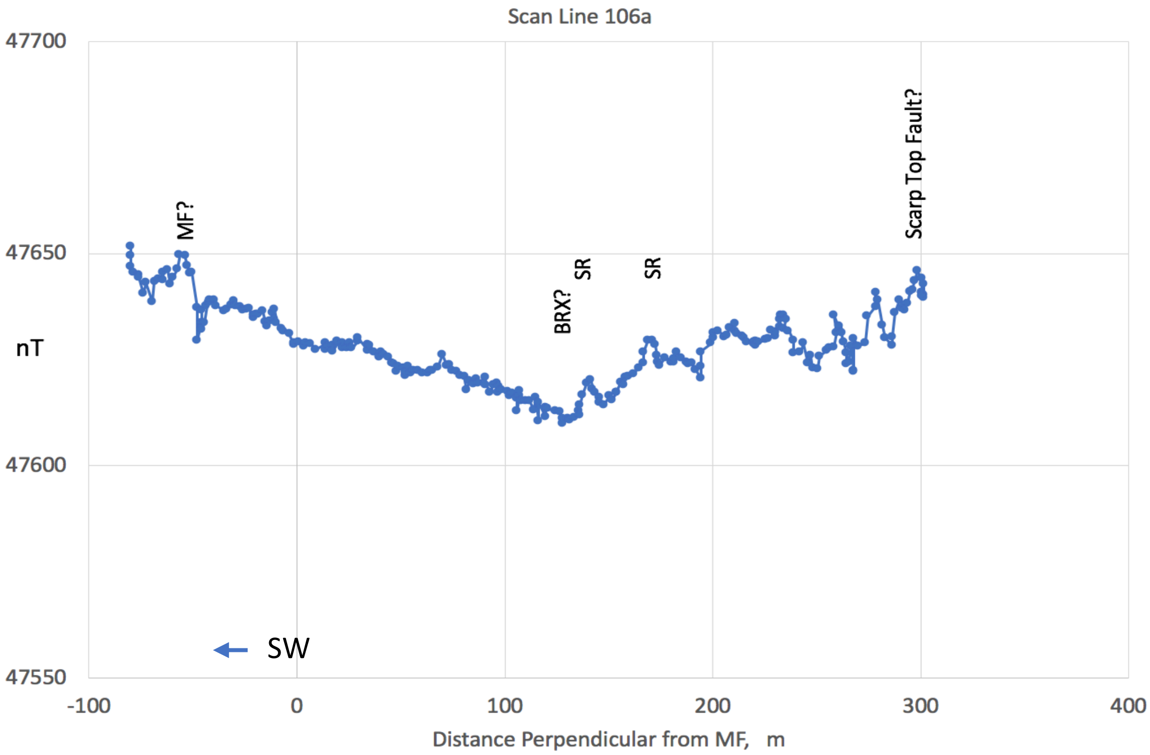

Figure F10: Transverse scan 106a, across undeveloped area south of Bernal.

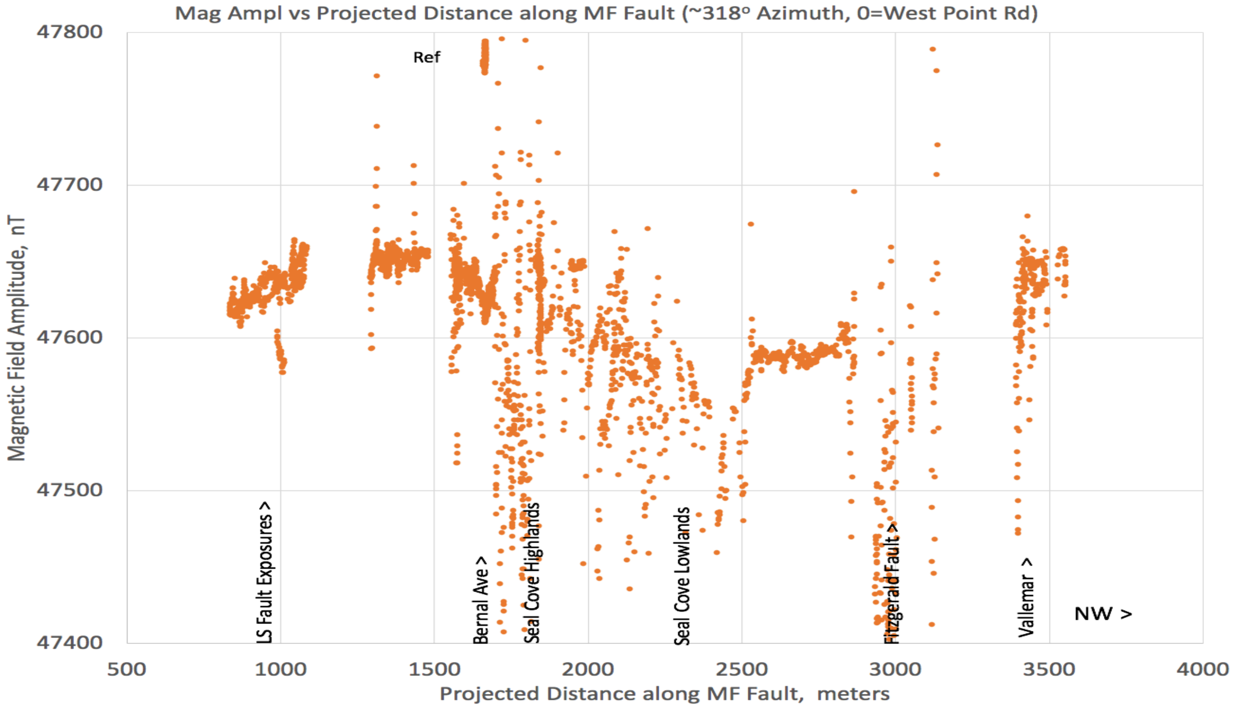

Figure F11: Magnetic field amplitude for all scans plotted along the length of MF.

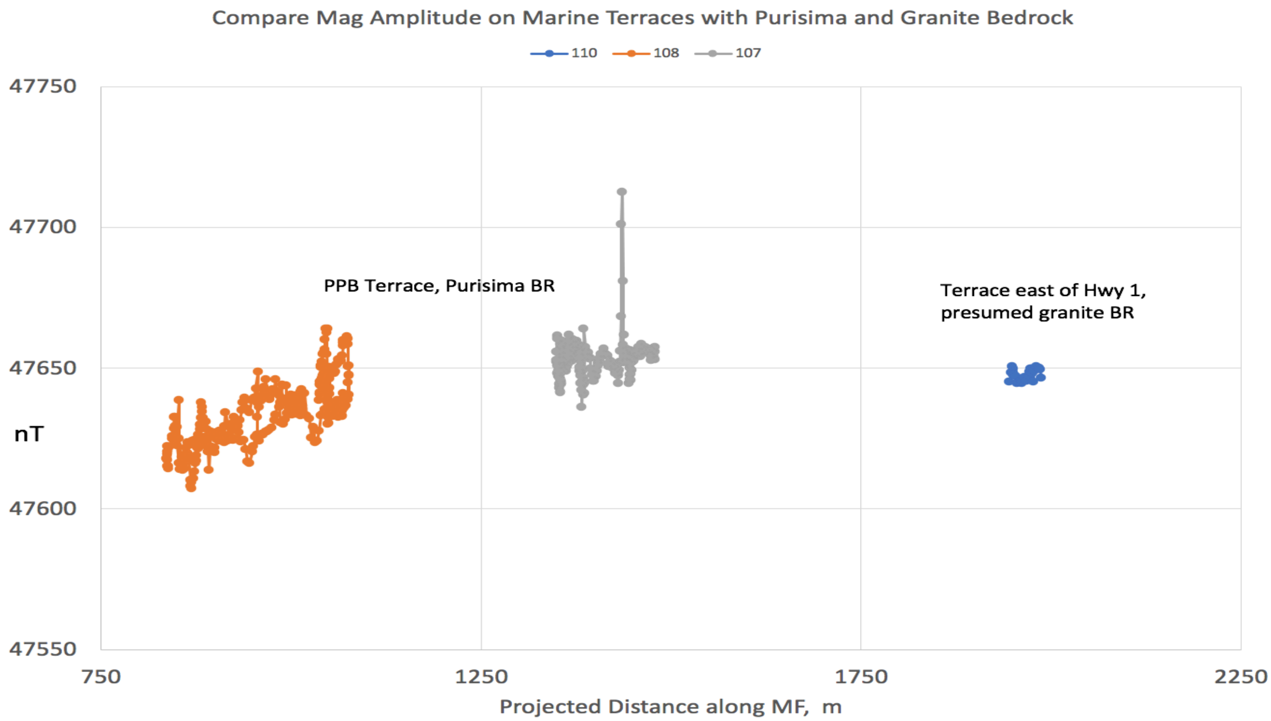

Figure F12: Comparison of magnetic amplitude on Marine Terraces underlain by Purisima sandstone and Montara Mountain granite bedrock.

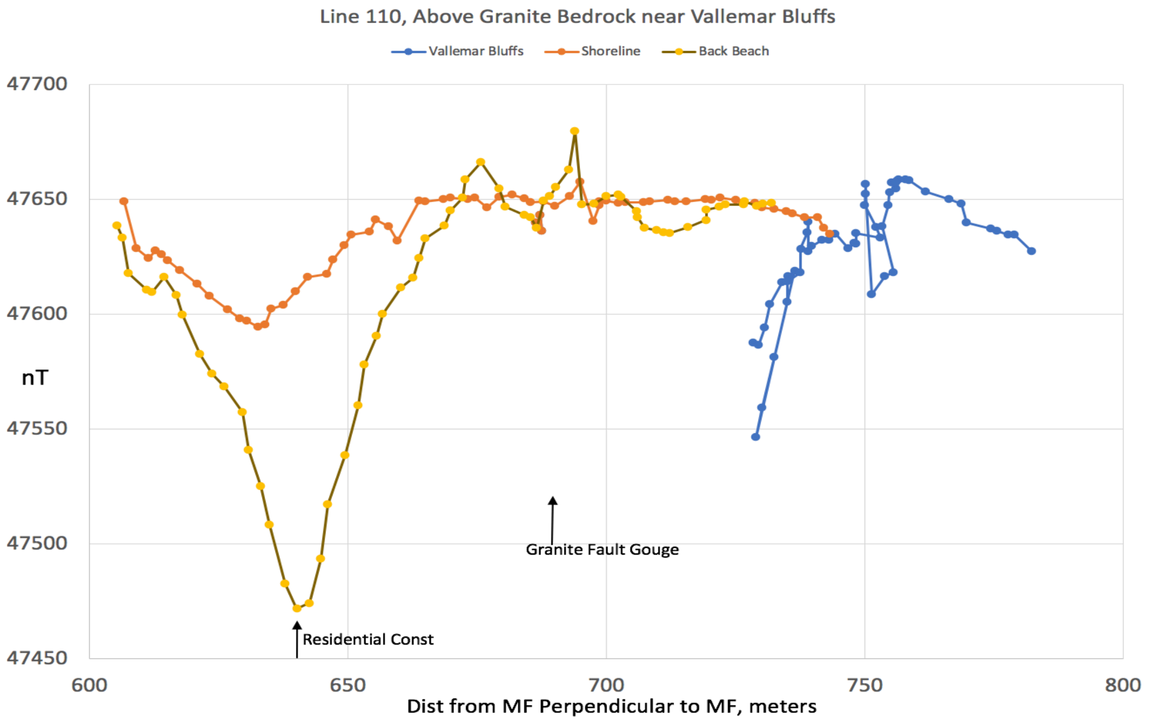

Figure F13: Scan 110a above granite bedrock in the Vallemar Bluffs vicinity.

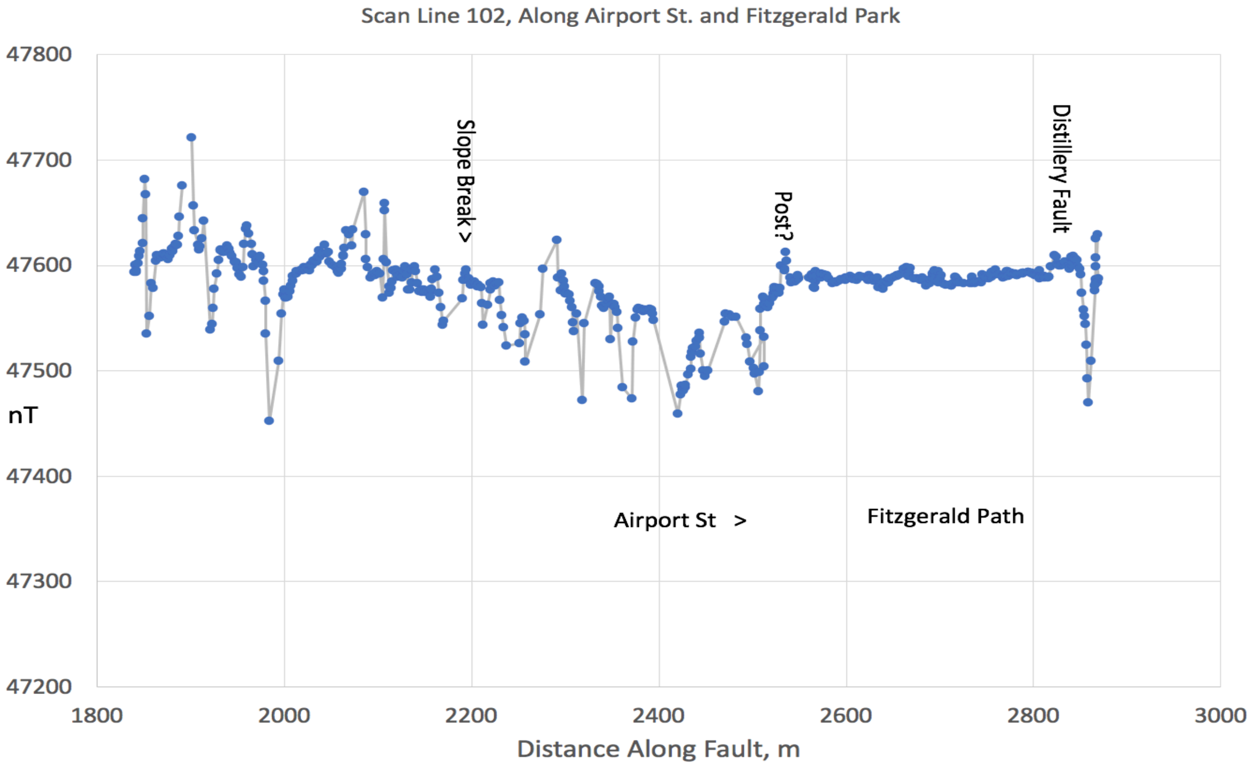

Figure F14: Scan 102 along Airport St to Fitzgerald Park Trail.

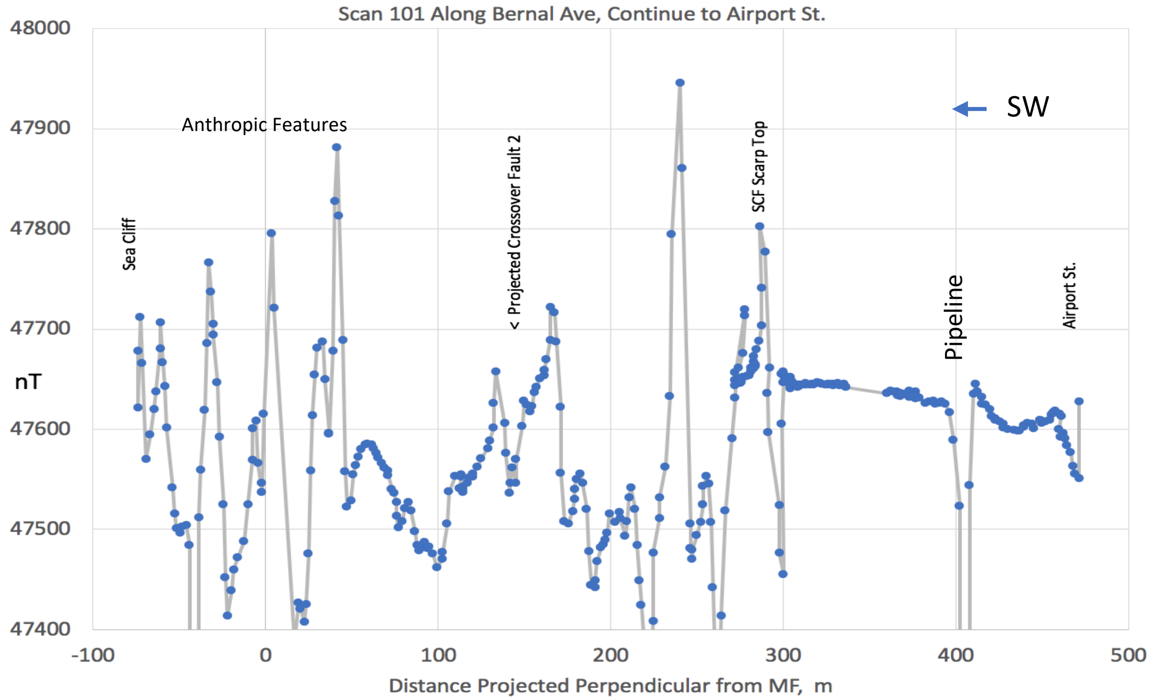

Figure F15: Scan 101 along Bernal Ave and continuing on to Airport St. Most large anomalies are from anthropic features, but NE of 270 m is mostly geologic.

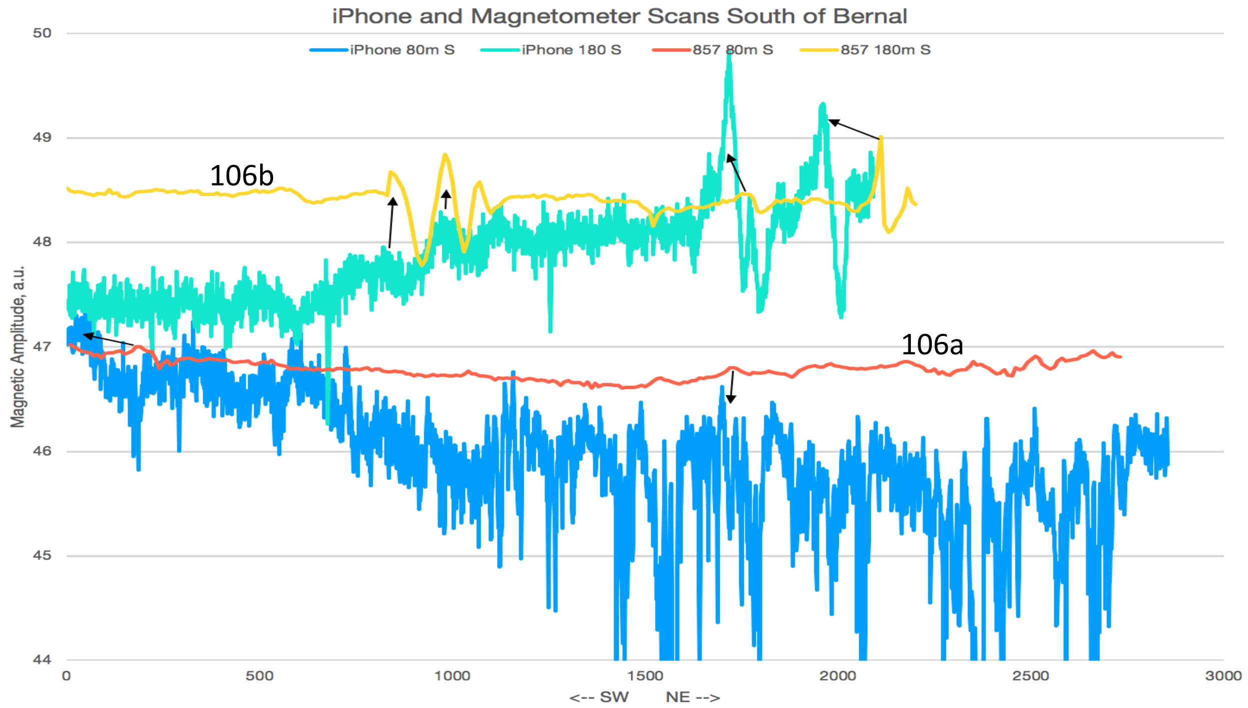

Figure F17: Comparison of iPhone 8 and magnetometer scans (106a and 106b). Paths are similar but not identical and horizontal scales are not the same.

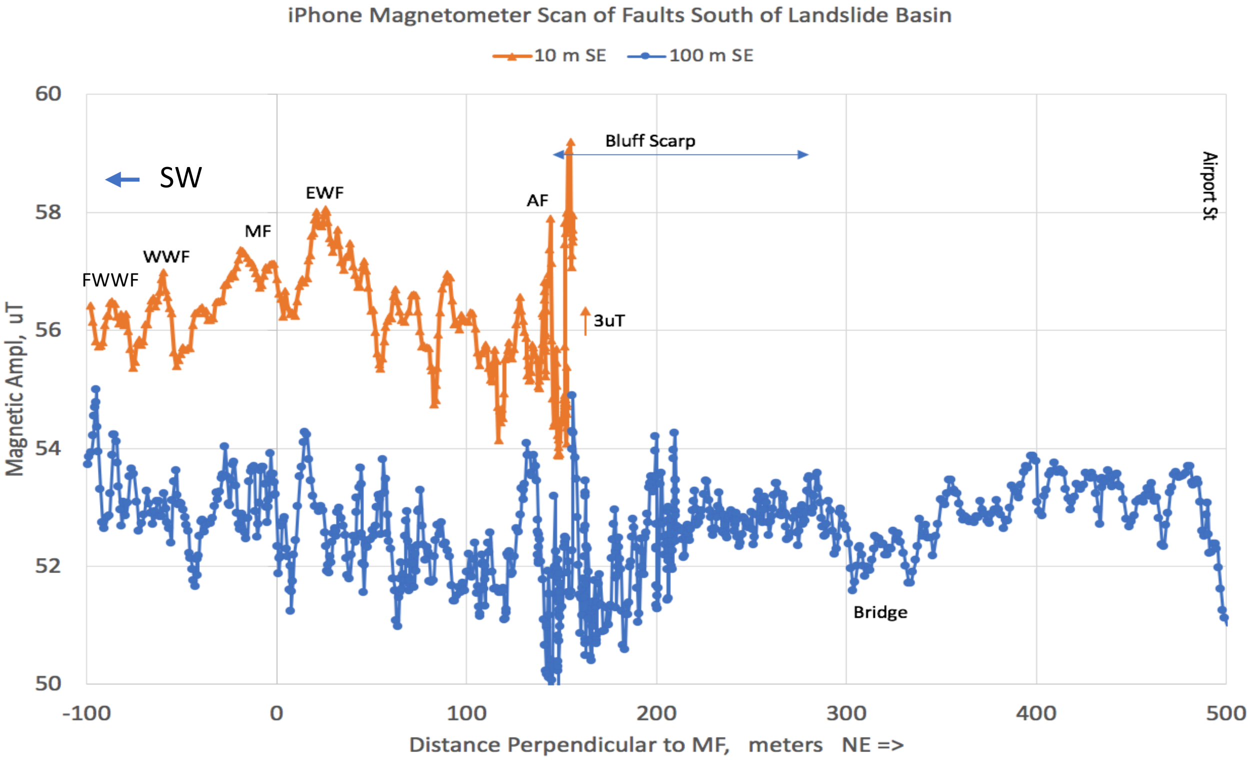

Figure F18: iPhone magnetometer scans across PPB about 10 m and 100 m SE of the Landslide basin’s southern headscarp.

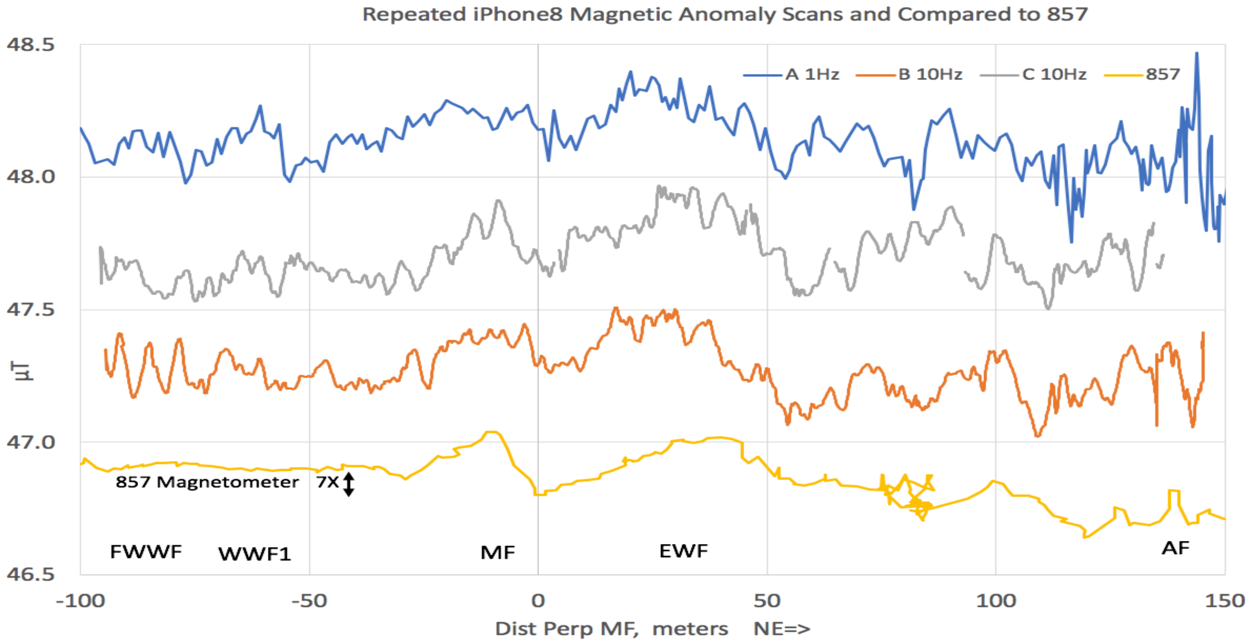

Figure F19: Repeatability of iPhone scans and their comparison to an expanded 857 magnetometer scan. Scan A is same as the 10 m SE scan in Figure F18, the other two use 10Hz scan rate with smoothing and follow a slightly different path east of EWF. Data offset vertically for clarity.

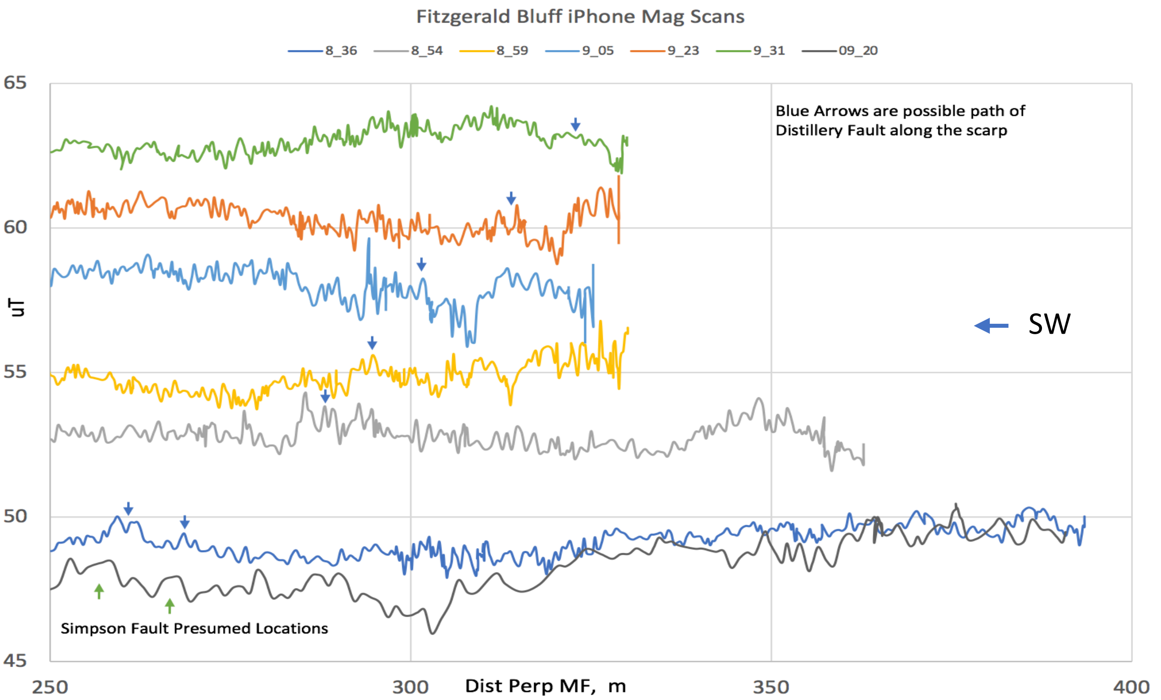

Figure F20: iPhone 8 magnetometer scans across Fitzgerald Bluff including near the Simpson faults' trench. Scans are vertically offset for clarity.

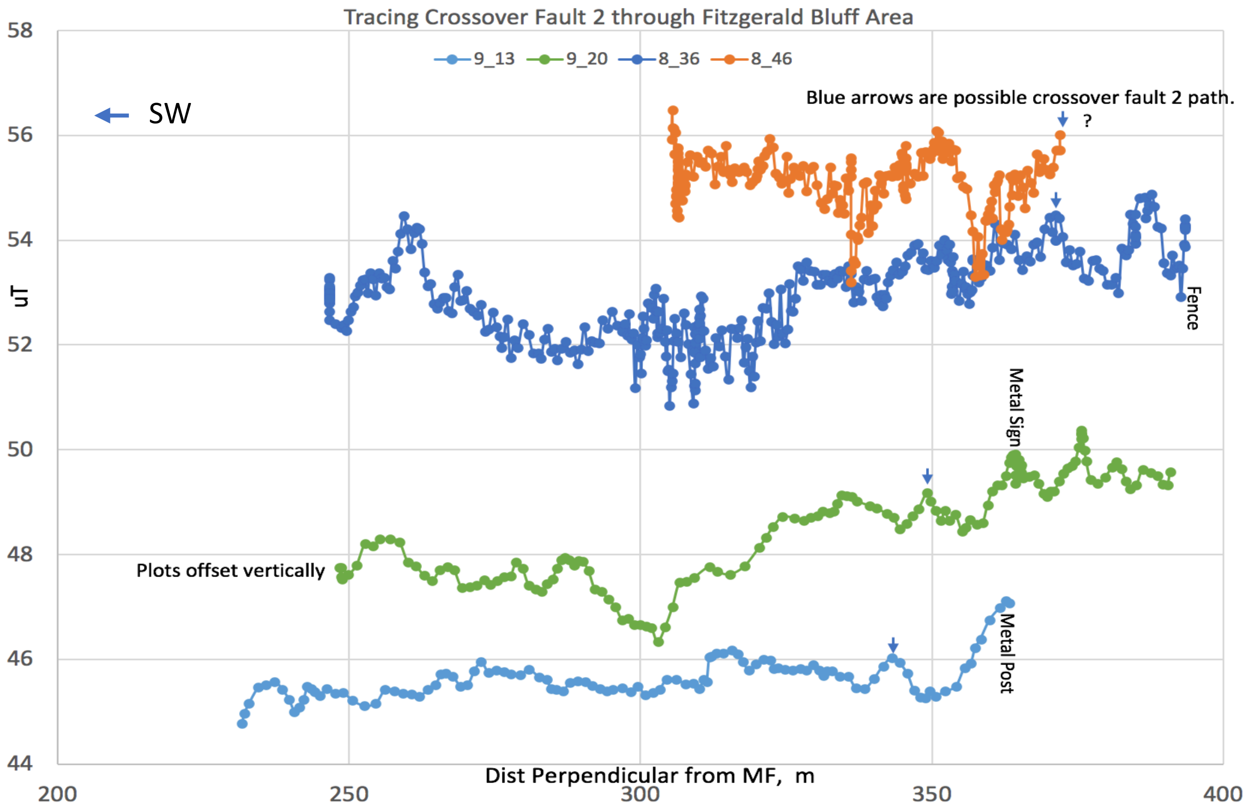

Figure F21: iPhone 8 magnetometer scans in area of Crossover Fault 2 Extension.

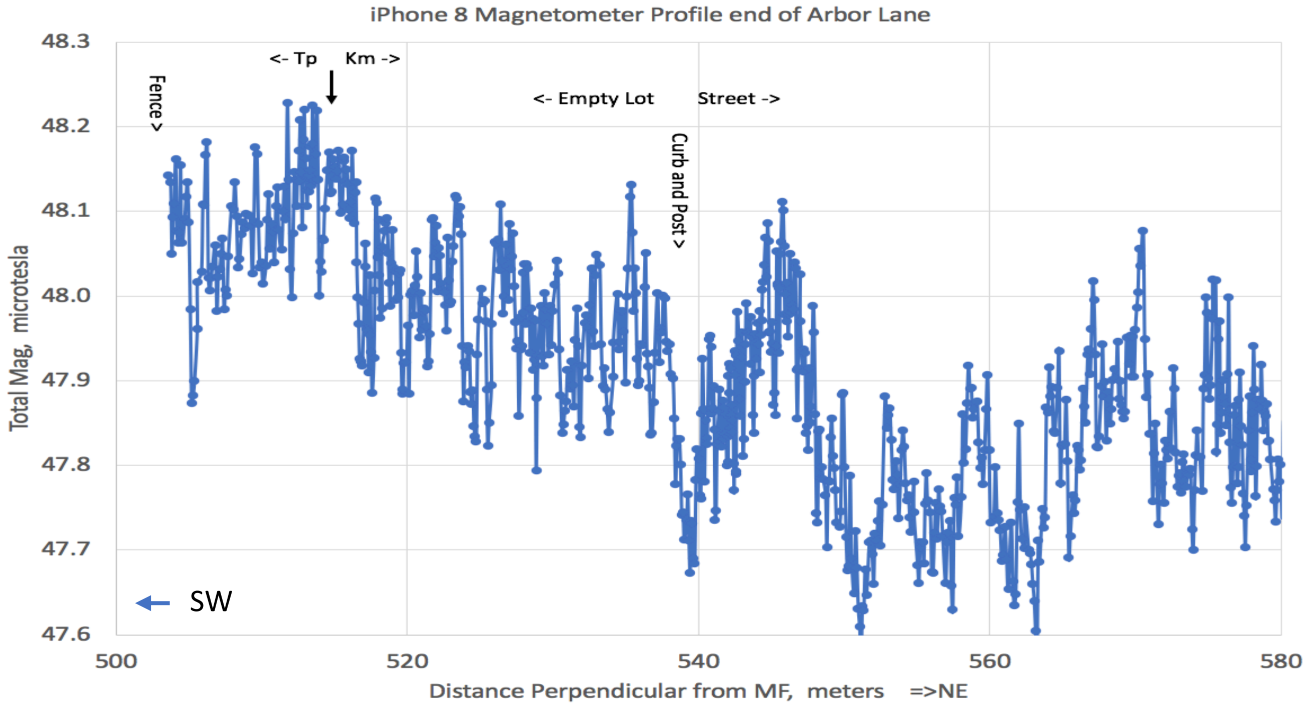

Figure F22: iPhone 8 profile along Arbor Lane and an empty lot that lies above expected Tp / Km interface. Structure along street is presumed to be anthropic.

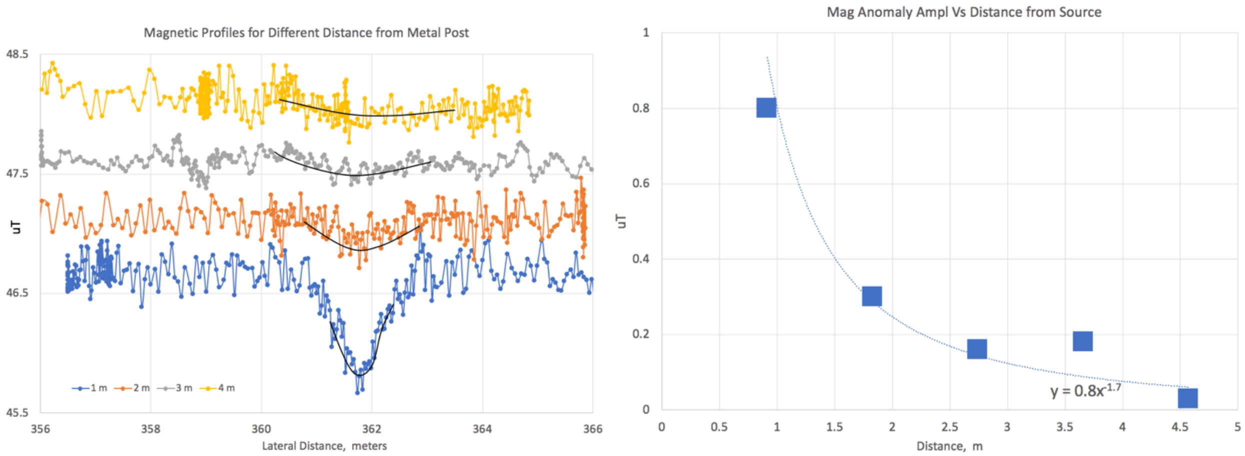

Figure F23: Magnetic anomaly amplitude versus distance from a metal post. Left figure shows each scan, right is max amplitude versus distance from post.

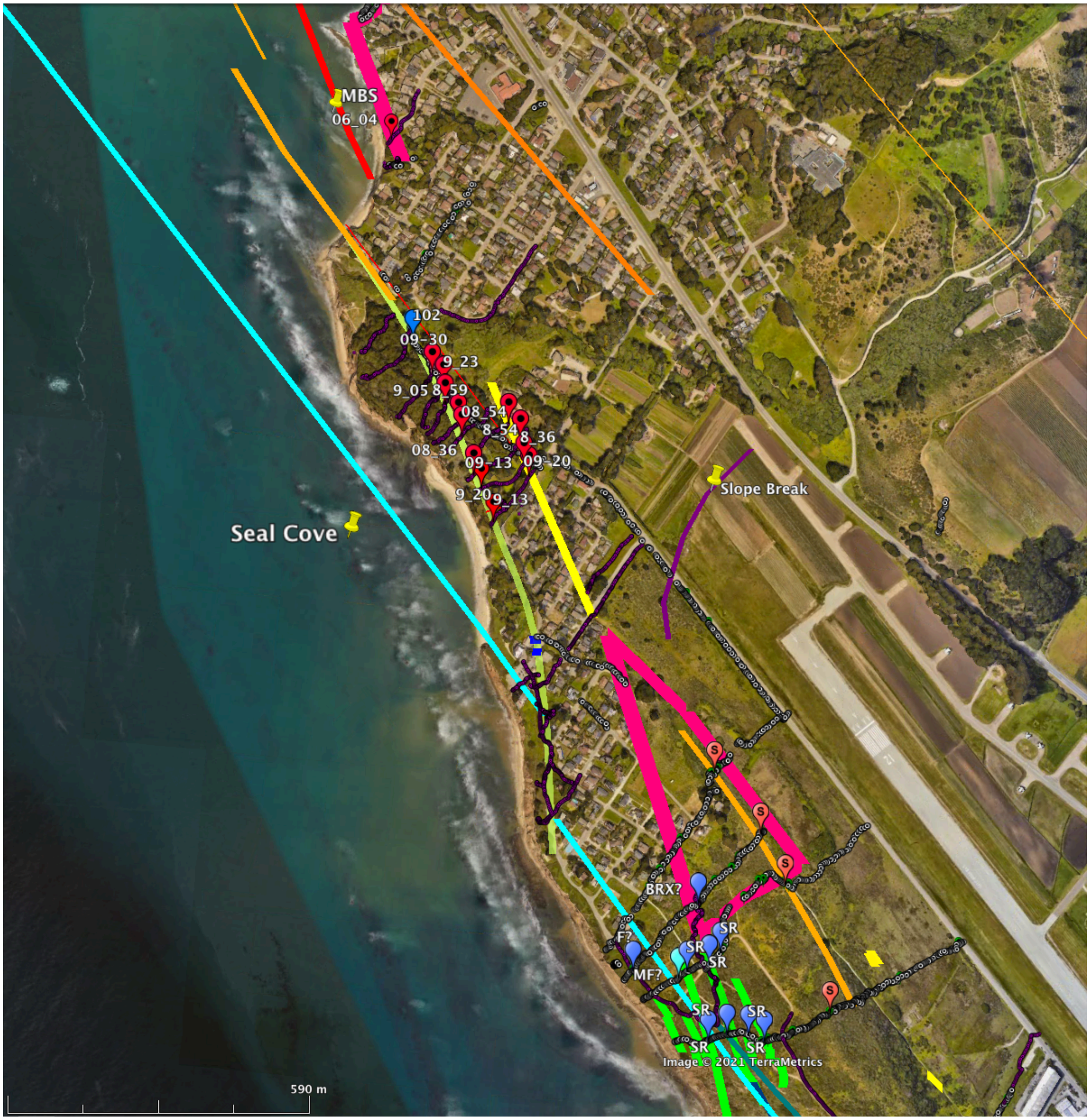

Figure F24: Faults from iPhone 8 magnetometer scans (red markers with black dots are unconfirmed) plotted on Google Earth map showing possible alignment with Crossover Fault 2 (yellow line), Tp/Gr transition near MBS, and Distillery Fault (light green line). Blue markers and the red "S" markers are faults identified by Magnetometer 857 scans.